Sandstone Reservoir Quality Studies: geochemistry and mineralogy of modern estuarine sediments as an analogue for ancient deeply, buried sandstone

UNIVERSITY OF LIVERPOOL

Thesis submitted in accordance with the requirements of the University of Liverpool for the degree of Doctor in Philosophy by

Dahiru D. Muhammed

January 2022

Dedication

This thesis is dedicated to the memory of my late father and my loving family.

Declaration

I declare that this thesis, which I submit for the degree of Doctor of Philosophy at University of Liverpool, is my own work, except where acknowledgement is made in the text, and not substantially the same as any work which has previously been submitted at University of Liverpool or any other institution for any degree, diploma or other qualification.

Table of Contents

List of figures

List of tables

1. Abstract

Sandstone Reservoir Quality Studies: geochemistry and mineralogy of modern estuarine sediments as an analogue for ancient deeply, buried sandstone

Understanding sediment depositional mineralogy and texture in sandstones reservoir quality prediction is increasingly challenging, these challenges are compounded in marginal marine settings owing to the to the complex interaction between tidal and riverine processes. The application of sedimentological and diagenetic models often fail to accurately predict reservoir quality in ancient and deep sandstone reservoirs, because the spatial and temporal variability of sandstone compositions are poorly-understood. This study focused on surface sediment (< 2 cm depth) samples and core (< 15 m depth) samples from the Ravenglass Estuary, NW England, and detailed geological mapping of the different estuary sub-depositional environments. Samples were analysed using portable XRF spectroscopy (pXRF), laser particle size analysis (LPSA), total organic carbon analysis, scanning electron microscopy (SEM-EDS) and statistical techniques. The distribution of geochemical elements, total organic carbon and grain size for surface sediments, were mapped at an unprecedented high-resolution using ArcGIS, in order to understand the controls on the distribution of elements, particularly Fe, and Fe bearing clay minerals. Holocene core samples were analysed to establish the controls on clay minerals and clay coats distribution patterns in the palaeo-sub-depositional environments of Ravenglass Estuary Holocene sediments. A novel automatic geochemical data-based classification approach was developed to predict palaeo-sub-depositional environments from core, through a combination of visual discrimination of gravel and vegetated surfaces and recursive partitioning routine (RPART) in R statistical software. The automatic classification approach was then applied to Holocene cores from the Ravenglass Estuary and an improved method was established to interpret palaeo-sub-depositional environments that compliments descriptive sedimentology and lithostratigraphic analysis. The result shows that the finest sediments in the central and upper estuary, have the highest concentration of Fe. Iron capable of producing Fe-rich grain coating minerals, was partly transported into the estuary as Fe-rich minerals, such as biotite and detrital chlorite, via the Esk arm of the estuary. However, Fe was also transported into the estuary as fluvially-transported complexes with organic matter, that were subsequently destabilised in the saline estuary and deposited during slack water conditions with the finest grained sediment. Clay minerals occur in the finer sediment as pore-filling or grain-coating and in coarser sediment clay minerals occur as grain coats and lithic grains. Clay minerals distribution vary greatly between the different sub-depositional environments while clay coat coverage increases with increasing clay fraction abundance. Provenance and depositional environments have played an significant role in controlling detrital

mineral and texture distribution in the Ravenglass Estuary but local geochemical processes of fluvial organic complexation and co-deposition and early-diagenetic mineral alteration in sub-depositional environment-specific locations have partly over-printed primary depositional features and provenance signals. This study shows that sediment mineralogy and texture that potentially affect reservoir quality, vary across different sub-depositional environments. However, burial diagenesis will affect the primary sediment mineralogy, and this in turn will affect reservoir quality; outer estuarine sediment with negligible clay coat coverage and clay fraction is likely to be extensively quartz cemented during deep burial. Mud-flat and mixed-flat sediments are likely to have low porosity and low permeability due to pore-filling clays that block pore-throats. Sand flat and tidal bars sediments, that in Ravenglass have >10% detrital coat coverage (within optimum range), and that contain chlorite-bearing lithic grains, can form diagenetic chlorite coats that can preserve anomalously high porosity in inhibiting quarts cementation, in deeply buried sandstone. Furthermore, knowledge of the distribution of minerals and elements is helpful in petroleum exploration and reservoir development in both deep and shallow reservoirs as clays (chlorite) can be good or bad, depending on the amount and the diagenetic setting. It is also of valuable in carbon capture and storage, and geothermal applications.

Acknowledgements

All Praise be to God almighty. My boundless affection and prayers will forever be with my parents for their guidance, prayers and support.

My profound gratitude goes to my dear family, for their noble support. Thank you and May God almighty rewards you with the best. YOU ARE MY HEROES.

My sincere appreciation goes to my main supervisor Prof. Richard H. Worden for his support and guidance, and for being there for me since day one. Thank you for making me, a better researcher. The time and effort you dedicated towards training and guiding, will be remembered forever.

My research and field partner Naboth Simon, I enjoyed a wonderful time and experience working with you. The support, friendship and ability to discuss ideas has been invaluable and has contributed immensely to this PhD.

I would also like to acknowledge all my colleagues in the Diagenesis Research Group, University of Liverpool, for their support and guidance.

And finally, a big thanks to my family and friends whom are very numerous to mention for always supporting me.

1. Introduction

Understanding the composition of sandstones for reservoir quality prediction is increasingly challenging, because the spatial and temporal variability of sandstone composition, a master control on reservoir quality, is poorly-understood (Ajdukiewicz and Lander, 2010). In addition, oil and gas are now being produced from ever deeper reservoirs making the hunt for anomalously good porosities and permeabilities increasingly important, as such more accurate determination of reservoir composition is now required for efficient reservoir characterisation, as incomplete or overly simplistic measurement of physical properties usually makes oil and gas project difficult. Reservoir quality studies in the oil and gas industry have led to improved production strategies for oil and gas fields (Rui et al., 2017); these improvements have been enabled through advances in laboratory analysis (e.g., SEM-EDS), and forward modelling (e.g., diagenetic modelling) (Worden et al., 2018a).

Reservoir quality in sandstones is controlled by different depositional and diagenetic processes; porosity and permeability are a function of depositional texture and mineralogy, while diagenetic processes such as dissolution, cementation and compaction tend to modify the primary texture (Worden and Burley, 2003). As porosity and permeability are kwown to decrease with increasing depth, a significant number of deep (4 km) sandstone reservoirs worldwide have anomalously high porosity and permeability (Bloch et al., 2002). Anomalous high porosity and permeability can be defined as being statistically higher than the porosity and permeability values occurring in typical sandstone reservoirs of a given lithology (composition and texture), age, and burial/temperature history. The major causes of anomalous high porosity and permeability were proposed decades ago (Bloch et al., 2002); however, assessing the controls and the prediction of anomalous high porosity and permeability occurrence in sandstones have rarely been addressed in published literatures, owing to the intrinsic complexity of the subsurface and limited information available (Jahn et al., 2008). The proposed major causes of anomalously high porosity are;

- The presence of grain coats of chlorite or microquartz (Dowey et al., 2012; Dowey et al., 2017; French and Worden, 2013; French et al., 2012), the prediction of anomalous high porosity associated with grain coats is dependent on the availability of empirical data sets (Dowey et al., 2012).
- The early emplacement of hydrocarbons (Sathar et al., 2012; Worden and Morad, 2000; Worden et al., 1998).
- The development of overpressure at shallow depth (Osborne and Swarbrick, 1999; Sheldon et al., 2003).

This thesis was designed to establish an understanding of sandstone reservoir quality through studying the geochemistry and mineralogy of modern estuarine sediments as an analogue for ancient and deeply buried sandstone. To fulfil this, three different studies are presented; the first part was designed to understand the controls on surface sediment geochemical compositions and their statistical relationships with estuarine present day sub-depositional environments, the second part looked at the influence of provenance, estuarine hydrodynamics, and surface active solutes such TOC and clay grade particles on the distribution of Fe, in understanding the distribution of Fe bearing minerals in the estuary, the third part was designed to better understand the distribution of clay minerals and clay coats in the Ravenglass Estuary paleo-sub-depositional environments.

The objectives of this introductory chapter include:

(i) Reviews on the mineralogical compositions of sandstones and their effect on reservoir quality.
(ii) Discuss why a modern-analogue approach was adopted for this research.
(iii) Highlight the previous research work conducted in this study area for reservoir quality studies.
(iv) Present the research aims and methods.
(v) Discuss the layout of the thesis.
(vi) Summarise key research questions.

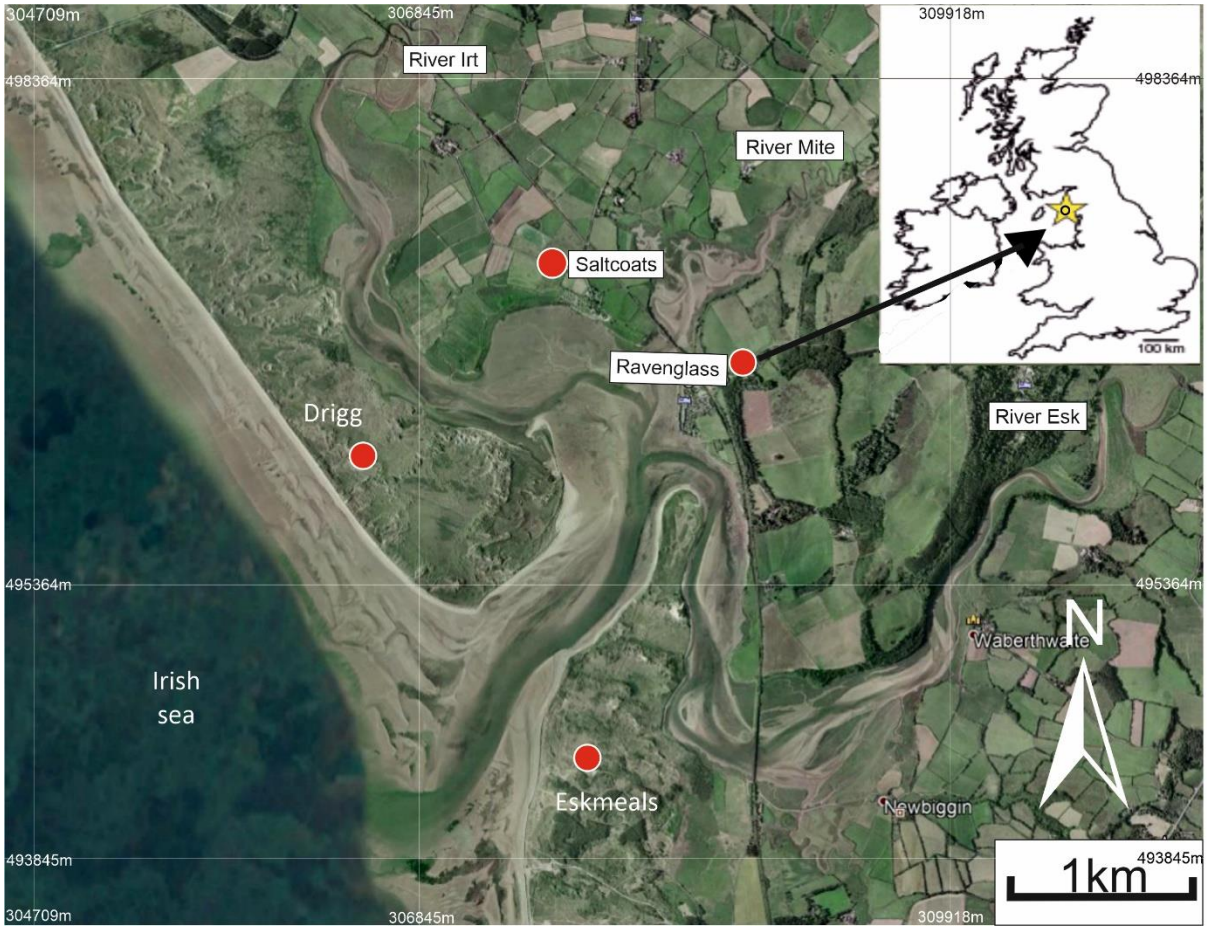

Figure 1.1; Aerial image showing the location map of the Ravenglass Estuary, NW, UK (sourced from google earth).

1.1 Background

1.1.1 Clay Mineralogy

Clay minerals are hydrated aluminium silicates with a particle size having an equivalent spherical diameter of < 2 µm (Worden and Morad, 2003). Clay minerals form a layered structure of tetrahedral sheet(s) linked through shared apical oxygens, to octahedral sheet. The Si^{4+} forms the central atom of the tetrahedral, while Al^{3+}, Fe^{3+}or Mg^{2+} occupy the octahedral sites (Worden and Morad, 2003). The bonding structure between one tetrahedral and one octahedral sheet in clays, is called a 1:1-layer silicate structure (e.g., kaolinite or berthierine). If two tetrahedral sheets sandwich one octahedral sheet, the bonded structure is called a 2:1-layer silicate (e.g., illite or smectite), while two tetrahedral sheets sandwiching one octahedral sheet with a hydroxyl interlayer forms a 2:1:1 structure (e.g., chlorite), (Worden and Morad, 2003). Generally, there are two types of octahedral sheets occurring

in clay mineral groups, dioctahedral and trioctahedral types. In dioctahedral 2:1 clays the octahedral sites are mainly dominated by trivalent central atoms, e.g. Al^{3+} or Fe^{3+}, while in trioctahedral clays, two-thirds of the octahedral sites are occupied by divalent central atoms, e.g. Mg^{2+} or Fe^{2+} (Fig. 1.2) (Madejova, 2003; Moore and Reynolds, 1997).

Clay minerals affect sandstones reservoir quality i.e. porosity and permeability, for example, chlorite coats inhibit quartz cement growth in deeply buried sandstones (> 80 to 100 ^{o}C) (Ehrenberg, 1993; Skarpeid et al., 2017; Stricker and Jones, 2016), mixed layer illite-smectite can cause pore space blockage and absorption of water (Worden and Morad, 2003), aggregates of kaolinite crystals can cause pore-throat blockage (Worden and Morad, 2003). Hence, the occurrence and distribution of clay minerals remain an important factor in controlling reservoir quality (Morris and Shepperd, 1982). Clay minerals are present in sandstone reservoirs in the form of thin layers, structural clasts, dispersed matrix and detrital coats, and also occurred as diagenetic clays in a form of pore-filling, pore-bridging and grain coat (Wilson and Pittman, 1977; Worden and Morad, 2003). Clay minerals composition and their relative abundance are controlled by weathering and provenance, while their distribution is controlled by depositional processes (Rao and Rao, 1995). In addition, the evolution of clay minerals is closely related to changes associated with sediment provenance and paleoenvironment (Dou et al., 2010), and relative contribution of fluvial inputs and weathering regimes (Thiry, 2000).

Weathering processes lead to the alteration of phyllosilicates, feldspar, pyroxenes, amphiboles and volcanic glass into different minerals such as illite, smectites, kaolinite, chlorite and vermiculite (Nesbitt and Young, 1989). This lead to predictable changes in rocks composition (Nesbitt and Young, 1989), and products (Chamley, 2013; Liu et al., 2009; Wilson, 2004). Notably the transformation of smectite into kaolinite, or mica minerals, illite, and chlorite into smectite via mixed-layers clays (Srodon, 1999), formation of illite from the felsic rich crystalline rocks, under dry climate (Weaver, 1989), and the hydrolysis of plutonic and metamorphic rocks, and biotite and feldspar to form detrital chlorite, and detrital kaolinite and smectites respectively (Chamley, 2013). Climatic conditions are the

major controls on the type and abundance of clay minerals during weathering regime (Chamley, 1989; Eberl et al., 1984; Rateev et al., 2008); under cold climate where mechanical weathering is dominant, chlorite and illite are the most abundant type of clay minerals (Chamley, 1989; Eberl et al., 1984; Rateev et al., 2008; Windom, 1976), whereas in warm and humid climate with intense chemical weathering, kaolinite is most abundant type of clay minerals (Chamley, 1989; Eberl et al., 1984; Rateev et al., 2008; Windom, 1976).

Clay diagenesis in sedimentary systems occur when either ductile argillaceous grains are subjected to compaction, or alteration of detrital silicates and authigenesis (precipitation from pore fluids) (Ketzer et al., 2003). For example, kaolinite is sensitive to geochemical environment (unstable in alkaline conditions) and increase in burial temperature can transform kaolinite to other form of clay mineral (Worden and Morad, 2003), also increase in temperature and pressure during burial may lead to the transformation of smectite into either chlorite or illite (De Segonzac, 1970; McKinley et al., 1999). In eogenetic realm, surface depositional facies and sequence stratigraphic show a direct relationship with clay minerals distribution (Ketzer et al., 1999; Worden and Morad, 2003). Mesogenetic clay minerals are strongly dominated by Illite and chlorite, and this usually developed at the later stage of eogenetic clay minerals, detrital feldspars and lithic grains transformation (Worden et al., 2020a; Worden and Morad, 2003). Mesogenetic changes can result from different controls and processes that include the time–temperature history, local eogenetic modifications, pore fluid geochemistry and the primary mineralogy and fabric (Worden and Morad, 2003).

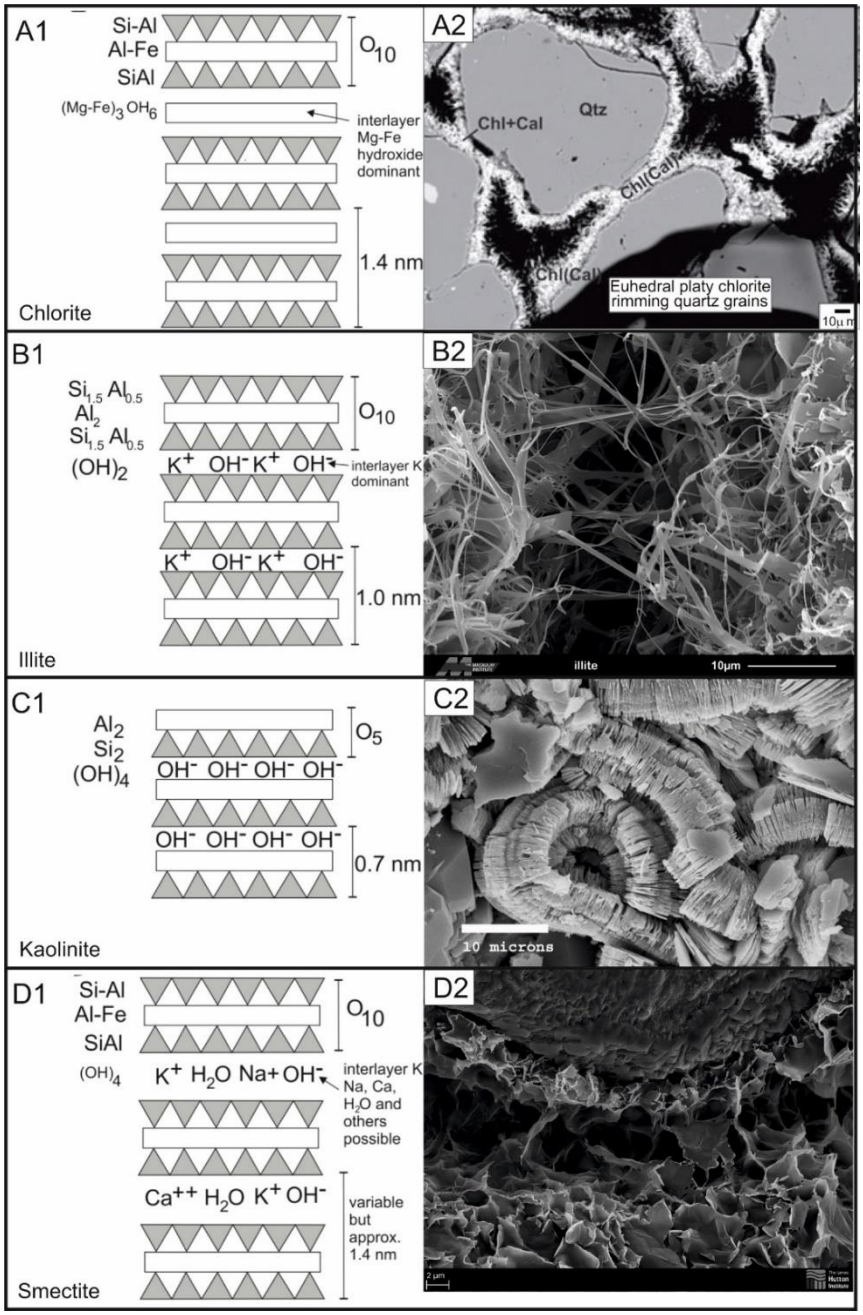

Figure 1.2; Schematic diagram showing the structure of common clay minerals in sandstone reservoirs, modified after Worden and Morad (2003), triangles represent tetrahedral layers, whereas bars represent octahedral layers. and SEM Images showing the morphology of different clay minerals in sandstones, (A1) chlorite, (A2) grain coating chlorite, (B1) illite, (B2) pore throat blocking fibrous illite, (C1) kaolinite, (C2) pore filling kaolinite, (D1) dioctahedral smectite, and (D2) pore throat blocking smectite.

1.1.2 Clay Mineral Groups

1.1.2.1 Chlorite

Chlorite can form from diagenesis, medium to low-grade metamorphism, and hydrothermal alteration, and it is present in silicic to ultramafic rocks (Worden et al., 2020a). Chlorite has a variable

chemical composition due to its crystal structure and the chemical diversity of its host rocks (Xie et al., 1997). The general formula for chlorite is given as $(Mg, Al, Fe)_{12}$ $[(Si, Al)_8O_{20}]$ $(OH)_{16}$, it has a structure of 2:1:1 with two octahedral sheets of cations (Al^{3+}, Fe^{3+}, Fe^{2+}, and Mg^{2+}), coordinated by hydroxyl interlayer (Fig. 1.2A1) (Worden and Morad, 2003). Two important diagenetic chlorite groups that occur on detrital grains as grain coats are Mg-rich varieties (clinochlore) and Fe-rich chlorite (chamosite) (Dowey et al., 2012). These mineral groups can also be present in both igneous and metamorphic rocks, resulting from intense hydrothermal alteration (Moseley, 1978; Young et al., 1986).

In most sedimentary deposits, chlorite occurs as a mesogenetic mineral where burial diagenesis (mesodiagenesis) led to chloritisation of Fe-rich silicate minerals (Worden and Morad, 2003), at burial depths greater than 2000 to 3000 m and temperatures greater than 60-100 ^{o}C (Burley and Macquaker, 1992; Ehrenberg and Boassen, 1993; Johnsson and Meade, 1990; Worden and Morad, 2003). Increasing temperature and pressure, changes in pore water chemistry, can have significance influence on chlorite distribution in sandstone reservoirs (Worden and Morad, 2003). Diagenetic chlorite can occur from the transformation of eogenetic kaolinite, haematite, berthierine and smectite (Dixon et al., 1989; Worden and Morad, 2003), destabilisation of organometallic complexes (Surdam et al., 1989) or the alteration of volcanic clasts and Fe–Mg-bearing detrital minerals, such as garnet, biotite or amphibole, where chlorite typically occur as grain replacements (Chang et al., 1986; De Ros et al., 1994; Morad and Aldahan, 1986; Pirrie et al., 1994; Remy, 1994). Siderite can also combine with kaolinite to form authigenic chlorite at burial temperatures of around 120 °C (Worden and Morad, 2003). Therefore, the early chlorite coats reported in many publications (Fig. 1.2A2) (Dowey et al., 2012; Dutton and Land, 1985; Longstaffe, 1993; Pittman and Lumsden, 1968) are likely the product of chloritisation of detrital grain-coats from eogenetic berthierine-odinite, smectite or kaolinite. Diagenetic chlorite grain coats can inhibit quartz overgrowths in deeply buried sandstone reservoirs; this can preserve porosity leading to anomalously high-porosity (Dowey et al., 2012; Ehrenberg, 1993; Saïag et al., 2016; Skarpeid et al., 2017; Stricker and Jones, 2016). The ability of chlorite to occlude

quartz cement growth, is defined by the extent and completeness of the clay coat (Ajdukiewicz and Larese, 2012; Billault et al., 2003; Lander et al., 2008). Conversely, an over-abundance of chlorite can have a negative effect on reservoir quality (porosity and permeability) by filling and blocking pore space and pore throats (Islam, 2009; Pay et al., 2000).

1.1.2.2 Illite

Illite is a general term for dioctahedral mica-like clay minerals found in sedimentary rocks (Pevear, 1999), although illite has more Si, Mg, and H_2O, and less tetrahedral Al and interlayer K than muscovite (Moore and Reynolds, 1997), the name can also be used for any clay mineral with 1-nm basal spacing identified by XRD analysis (Wilson, 1987). Illite is a K-rich dioctahedral 2:1 clay mineral with a general formula given as $K_yAl_4(Si_{8y},Al_y)O_20(OH)_4$, where y is less than 2, it comprises of one octahedral sheet sandwiched between two tetrahedral layers, where K is bound between each octahedra-tetrahedra-octahedra unit (Fig. 1.2B1) (Velde, 1985). Illite can occur in different forms such as flakes, filaments or hair-like crystals (Fig. 1.2B2), its morphology reflects the stacking patterns of the different layers that constitute illite crystal structure (Moore and Reynolds, 1997). The most common morphology of authigenic illite are thin laths; a notable example has is 90 Å thick, 0.5 to 1.0 nm long and 0.1 to 0.2 nm wide found in Permian Rotliegend sandstones of the North Sea (Ziegler, 2006). Illite with a platy morphology may also occur in sandstones; this type of illite tends to have lath-like or fibrous forms growing from the edges of the plates (Macchi, 1987). The illite varies greatly in terms of thickness, particle size and crystallinity, cation exchange capacity, and surface area (Inoue and Kitagawa, 1994; Nadeau et al., 1985; Środoń et al., 2000; Wilson et al., 2014).

Illite structure and composition are related to temperature and have significant influence on the sandstones reservoir quality (Jahren and Aagaard, 1992), for example sandstone with 25% total porosity may be reduces to approximately 0% porosity by diagenetic pore-filling illite that is less than 2 wt.% (Hurst and Nadeau, 1995). Illite also has the ability to preserve sandstone porosity in deeply-buried reservoirs, by inhibiting quartz cementation (Storvoll et al., 2002; Stricker et al., 2016), although

this behaviour of illite is the exception rather than the norm. In addition, the reaction of illite with CO_2 during reservoir management, for example enhanced oil recovery, releases Fe that will subsequently form siderite in the present of carbonate material (Worden and Morad, 2003). However, illite can significantly reduce permeability owing to it hair-like and fibrous morphology (Fig. 1.2B2); forming pore bridge and blocking pore throat (Lander and Bonnell, 2010; Yuan et al., 2015), enhancing sediment chemical compaction via aiding pressure dissolution and increasing quartz cementation (Oelkers et al., 1996; Worden et al., 2018a; Worden and Morad, 2003). Furthermore, illite and mixed mineralogy coats (for example, illite–chlorite–smectite) have also been reported in sandstones (Martinius et al., 2005; Oelkers et al., 1996; Storvoll et al., 2002; Stricker et al., 2016).

1.1.2.3 Kaolinite

Kaolinite represent a group of clay minerals with a structure of one tetrahedral layer linked to one octahedral layer by O-H-O bond (Fig. 1.2C1), with no interlayer cation, it has chemical formula of $Al_2Si_2O_5(OH)_4$ (Worden and Morad, 2003). The high temperature kaolinite group are called dickite and nacrite and they occur as small rhombic crystal (Brigatti et al., 2013). Kaolinite occurs in a form of stacked, booklets and vermicules, or as discrete aggregates forming a nearly well-crystallised mineral, the textural relationship between kaolinite and other sandstone components, and its euhedral nature indicates that kaolinite is diagenetic (Worden and Morad, 2003). Kaolinite particles may be distinctly elongated or have an irregular outline, and may show considerable variation in size (Wilson et al., 2014). Kaolinite textures range from fine grained vermicules with an individual plate diameter approximately 2 μm, to coarser grained vermicules with plate diameters of 40 μm and coarser compact crystal blocks (Hurst and Nadeau, 1995).

Kaolinite can affect sandstone reservoirs in different ways; blocking pore throats and reducing permeability (Kantorowicz, 1984), or lowering production rates when mobile kaolinite booklets accumulate in pore throats near the well-bore (Cerda, 1987). Kaolinite is also a precursor to the formation of chlorite coats in sandstones (Dowey et al., 2012), chloritisation of kaolinite typically

occurs at burial depths between about 3500 and 4500 m and temperature between 165-200^{o}C (Boles and Franks, 1979; Worden and Morad, 2003). The major sources of Fe for the chloritisation of kaolinite include siderite (Iljima and Matsumoto, 1982) and iron oxide (Curtis et al., 1985).

1.1.2.4 Smectite

Smectite have numerous possible forms, but the most common is lamellar aggregates that typically showed a honeycomb cellular arrangement under SEM examination (Wilson and Pittman, 1977). The differences between individual smectite clay groups are attributed to variability in external surface area, in addition to changes to the mineral due to swelling effects (Dogan et al., 2006; Katti and Katti, 2006; Wilson et al., 2014). Smectite is 2:1 clay mineral with a structure of one octahedral layer sandwiched between two tetrahedral layers and has a chemical formula $(0.5Ca, Na)_{0.7}(Al, Mg, Fe)_4(Si, Al)_8O_20(OH)_4\ nH_2O$ (Fig. 1.2D1) (Worden and Morad, 2003). The cations (Fe^{2+}, Fe^{3+}, Mg^{2+}, Ca^{2+}, Na^{+}) that form the smectite interlayers, are variably hydrated, and therefore smectites have the ability to swell when exposed to organic solvents, which may be absorbed by the cations in the interlayer space. Smectite generally represents an early stage of chemical weathering (Salem et al., 2000). Smectite can transform to different clay minerals or even serve as precursor to different forms of authigenic minerals in mesogenetic realm; dioctahedral smectite can transform to illite, with the addition of K^{+} (commonly sourced from K-feldspar dissolution) and trioctahedral smectite can undergo progressive transformation to mixed-clay and ultimately chlorite (McKinley et al., 2003; Worden and Morad, 2003). Dissolution of smectite and subsequent release of elements for illitisation, quartz cementation and zeolite growth also occur during smectite transformation during diagenesis (Boles and Franks, 1979). During the transformation of smectite to illite or muscovite, up to 25 wt.% of SiO_2 is liberated, assuming that Al is conserved (De Kamp, 2008). Smectites are commonly regarded as reservoir quality degrading clay minerals due to their abundant ineffective microporosity and also during expansion, smectite readily absorbs and incorporates water and organic material, and therefore alter the wettability of sandstone, potentially making the reservoir oil-wet (McKinley et al., 2003).

1.1.3 Clay Coats in Sandstone Reservoirs

Detrital coats are clay minerals, silt to clay-sized lithics and biological materials (e.g. diatoms) attached to a clastic grain, surrounding its outer surface forming a discontinuous coat (Dowey et al., 2017; Ehrenberg, 1993; Griffiths et al., 2018; Wooldridge et al., 2017a; Wooldridge et al., 2017b). They are composed of variable mixtures of different phyllosilicates minerals; chlorite, illite, kaolinite, berthierine, smectite and odinite (Dowey et al., 2017; Ehrenberg, 1993; Griffiths et al., 2018; Wooldridge et al., 2017a; Wooldridge et al., 2017b). Detrital coats are distributed at the surface or in near surface environment (Fig. 1.3), typically within the eogenetic realm (Ajdukiewicz and Larese, 2012; Bloch et al., 2002; Ehrenberg, 1993; Worden et al., 2020a; Worden and Morad, 2003). Diagenetic coats are formed through thermally-driven recrystallisation under low temperature (prior to burial) or from *in situ* growth when in contact with pore fluids during burial (Ajdukiewicz and Larese, 2012; Bloch et al., 2002; Ehrenberg, 1993; Worden et al., 2020a; Worden and Morad, 2003). The time and manner at which detrital coats transform to diagenetic coats have not been fully established in the literature, although numerous researchers have invoked a combination of the following mechanisms (Aagaard et al., 2000; Ajdukiewicz and Larese, 2012; Billault et al., 2003; Ehrenberg, 1993);

- Early attachment of detrital clay minerals to the surface of the sand grain prior to sediment compaction.
- The evolution of detrital clay coat to continuous diagenetic clay coat (if there is sufficient material available to support neoformation) prior to quartz cementation and feldspar alteration.
- Dissolution of clay coat precursor minerals and subsequent precipitation of authigenic clay-coat components.

Diagenetic coats are composed of two different layers; an inner platy-anhedral layer that is tangential to the grain surface (Fig. 1.3), and an outer euhedral layer that is perpendicular to the grain surface, the outer layer projects from the grain surface into the sediment pore space (Fig. 1.3) (Bloch et al.,

2002; Gould et al., 2010; Stricker and Jones, 2016). The inner diagenetic coats are made up of densely packed platy-anhedral crystals, typically of different clay mineral types (Fig. 1.3) (Bloch et al., 2002; Pittman et al., 1992). The outer authigenic coats, that form the continuous coat on the detrital coats, are made up of euhedral clay materials (Figs. 1.3) (Ajdukiewicz and Larese, 2012; Billault et al., 2003; Bloch et al., 2002; Gould et al., 2010; Pittman et al., 1992). The occurrence of detrital coats on the clastic grain is important for the development of authigenic coats, in shallow marine sandstones (Aagaard et al., 2000; Ajdukiewicz and Larese, 2012; Ehrenberg and Boassen, 1993; Worden et al., 2020a). The completeness (the fraction of grains surface area covered by attached clay minerals) of the coat on the clastic grain, exert significant control on the effectiveness of the clay coats to occlude quartz overgrowth (Ajdukiewicz and Larese, 2012; Bloch et al., 1997; Bloch et al., 2002; Ehrenberg, 1993; Lander et al., 2008; Skarpeid et al., 2017) (Figs. 1.2A2 and 1.3). In addition to coat completeness, clay coat mineralogy also affects the ability to occlude quartz overgrowths (Ajdukiewicz and Larese, 2012; Billault et al., 2003; Bloch et al., 2002; Ehrenberg and Boassen, 1993; Lander et al., 2008). Therefore, it has become imperative to understand the distribution of precursor, specific clay minerals and detrital clay coats and their mineralogy, in order to better understand and predict the occurrence and completeness of detrital clay coats, and their corresponding depositional settings.

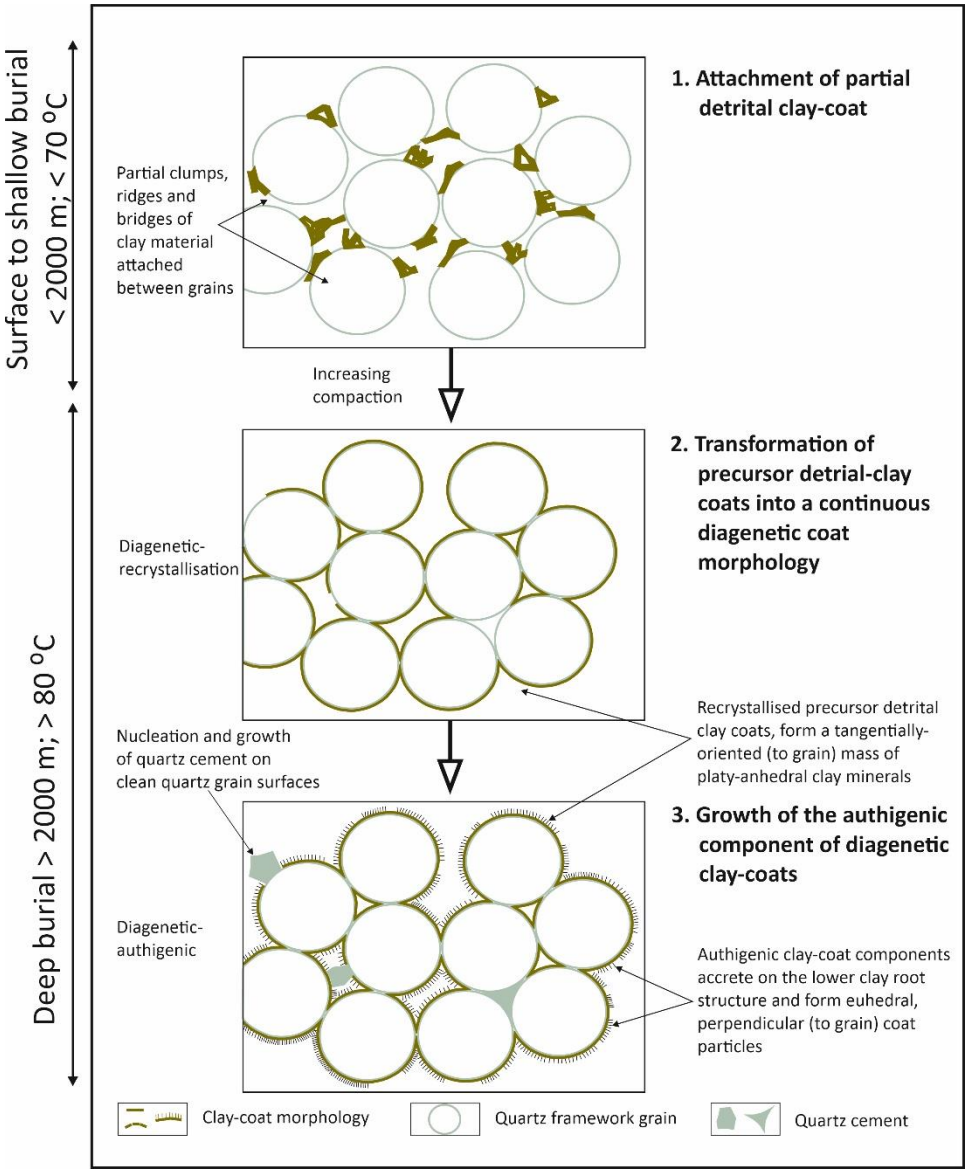

Figure 1.3; Schematic illustrations of diagenetic evolution in clay-coat timing and morphology from detrital-clay to diagenetic clay-coat phases, modified after *Wooldridge et al. (2019b).*

1.1.3.1 Significance of Chlorite Coats

Chlorite grain-coats play an important role in sandstones reservoir quality (Ajdukiewicz and Larese, 2012; Ehrenberg, 1993; Griffiths et al., 2018; Skarpeid et al., 2017; Worden and Burley, 2003; Worden et al., 2020a; Worden and Morad, 2003), because they have the ability to preserve anomalously high-porosity in deeply-buried sandstones reservoirs by inhibiting quartz overgrowth (Dowey et al., 2012). The initial mineral compositions of the detrital coats are the main control on diagenetic coats mineralogy (Worden and Morad, 2003), which in turn determines their effectiveness in inhibiting quartz cement. Clay coats tend to inhibit quartz overgrowths via two-step process;

- Clay coats will physically isolate the quartz cement from silica saturated pore fluid, thereby retarding initial quartz cement nucleation, this commonly observed at temperature between 80 to 115 ^{o}C (Ajdukiewicz and Larese, 2012).
- As the temperature approaches 115 ^{o}C to > 160 ^{o}C, isolated nanocrystals of quartz cement will begin to nucleate between the clay coat mineral particles, and, due to the increased temperature, the clay coat mineral particles will act as barrier (kinetic barrier) and therefore inhibit epitaxial quartz growth (Figs. 1.2A2).

Overall, the presence of clay coats will reduce the rate and volume of quartz cement growth, by isolating the quartz nanocrystals between the clay coat mineral particles, (Ajdukiewicz and Larese, 2012; Billault et al., 2003; Bloch et al., 2002).

The occurrence of detrital and diagenetic coats in sandstones, has been widely reported (Ajdukiewicz and Larese, 2012; Worden et al., 2020a; Worden and Morad, 2003). The ability of any given clay-coat to inhibit quartz growth is a function of its morphology and completeness (Fig. 1.3), and mineralogy (Ajdukiewicz and Larese, 2012). Clay coats that limit the nucleation area on detrital quartz grains, to reduce quartz cementation, are chlorite and illite coats (Ehrenberg, 1993; Pittman et al., 1992). Anomalously high porosity reported in deeply buried sandstone reservoirs are commonly associated with chlorite coats (Dowey et al., 2012). Chlorite occurs as platy crystals, this morphology makes chlorite a better clay coat to inhibit quartz cement than illite, which has fibrous hair-like crystals morphology (Figs. 1.2B2) (Ajdukiewicz and Larese, 2012; Worden and Morad, 2003). Chlorite coats can occur in a form of a thin lining that has minor blocking effect on pore throats (Figs. 1.3) (Bloch et al., 1997; Ehrenberg and Boassen, 1993). The presence of chlorite is of great significance to sandstone reservoir quality because of its ability to form thin coats on sand grains and prevent quartz cementation, thereby leading to anomalously high in porosity deeply buried sandstone reservoirs (Worden et al., 2018a; Worden et al., 2020a). In addition, there are also mixed mineralogy coats such as illite–chlorite–smectite that occur in sandstone reservoirs, found within the marginal marine settings, that may positively influence reservoir quality (Table 1), notable example include; sandstone reservoirs in Norwegian Continental Shelf (Martinius et al., 2005; Storvoll et al., 2002), sandstone

reservoirs in Ordos Basin, China (Luo et al., 2002), reservoirs in Ghawar Field, Saudi Arabia (Al-Ramadan et al., 2004), and in the Permian, Bonaparte Basin, Australia (Saïag et al., 2016). Mixed clay mineral coats also occur in modern sedimentary deposits of Ravenglass Estuary, England (Griffiths et al., 2018; Griffiths et al., 2019a; Griffiths et al., 2019b; Wooldridge et al., 2017a; Wooldridge et al., 2017b; Wooldridge et al., 2019a; Wooldridge et al., 2018), Gironde Estuary, France (Virolle et al., 2021; Virolle et al., 2019a; Virolle et al., 2019b; Virolle et al., 2020), and Anllons Estuary, Spain (Dowey et al., 2017), also in an experiment by (Duteil et al., 2020; Matlack et al., 1989).

Table 1.1; Collation of examples of sandstones that contain chlorite and berthierine grain coats.

Authors	Formation	Basin	Country
Armitage et al. (2010), Tudge et al. (2014)	-	Timimoun Basin	Algeria
Saïag et al. (2016)	Upper Cape Hay Formation	Bonaparte Basin	Australia
Anjos et al. (1999), Bahlis and De Ros (2013)	Itajai-Acu Formation	Santos Basin	Brazil
Gould et al. (2010), Pe-Piper and Weir-Murphy (2008)	Missisauga Formation	Scotian Basin	Canada
Hornibrook and Longstaffe (1996)	Clearwater Formation	Western Canada Basin	Canada
Ma et al. (2017)	Shiqianfeng Formation	Bohai Bay Basin	China
Cao et al. (2018), Peng et al. (2009), Sun et al. (2014), Yu et al. (2016)	T_3x or Xujiahe Formation	Sichuan Basin	China
Fan et al. (2017), (Xiang et al., 2016), Zhu et al. (2017)	Yanchang Formation	Ordos Basin	China
Mu et al. (2015)	Lista Formation, Heimdal Member	Danish Basin	Denmark
Hillier et al. (1996)	Rotliegend Formation	North German Basin	Germany

Table 1.1; continued

Authors	Formation	Basin	Country
Huggett et al. (2015)	Mahim Formation	Mumbai Basin	India
Humphreys et al. (1994)	Keutapang Formation	North Sumatra Basin	Indonesia
Aagaard et al. (2000), Ehrenberg (1993), Ehrenberga et al. (1998), Hillier and Velde (1992), Jahren et al. (1998), Martinius et al. (2001), Griffiths et al. (2021)	Tilje, Tofte and Garn Formations	Haltenbanken	Norway
Churchill et al. (2017), Skarpeid et al. (2017)	Cook Formation	North Sea	Norway
Line et al. (2018)	Kobbe and Snadd Formations	Barents Sea Basin	Norway
Berger et al. (2009)	Goru Formation	Indus Basin	Pakistan
Al-Ramadan et al. (2004), Saner et al. (2006)	Jauf Formation	Arabian Basin	Saudi Arabia
Barshep and Worden (2021)	Corallian sandstone	Weald Basin	UK
Stricker and Jones (2018), Weibel (1999)	Skaggerak Formation	Central Graben	UK and Denmark
Pittman and Lumsden (1968), (Spoetl et al., 1994)	Spiro Member, Savanna Formation	Arkoma Basin	USA
Ryan and Hillier (2002)	Sundance Formation	Bighorn Basin	USA
Grigsby and Langford (1996), Grigsby (2001))	Vicksburg Formation	Gulf of Mexico Basin	USA
Ajdukiewicz et al. (2010), Dixon et al. (1989))	Norphlet Formation	Gulf of Mexico Basin	USA
Dutton et al. (2018), Ryan and Reynolds (1996), Ryan and Reynolds (1997), Thomson Thomson (1979), Thomson (1982)	Tuscaloosa Formation	Gulf of Mexico Basin	USA

1.1.4 Other rock Forming Minerals and Diagenesis

1.1.4.1 Quartz

Quartz typically constitutes the major mineral group of sandstones, granitic rocks and their metamorphic equivalents (MacKenzie and Adams, 1994). The rate of mechanical compaction in sandstones, which reduces sandstone porosity during burial, is controlled by detrital quartz abundance in relation to clay mineral abundance (rigid grains vs ductile grains). Mechanical compaction can be the dominant control on porosity-loss in sandstones. Authigenic quartz cement, which is often second major control on porosity-loss in sandstones (Lander et al., 2008; Worden and Morad, 2000; Worden and Morad, 2003), typically starts to develop at temperatures in excess of 70 to 80 °C (Worden and Burley, 2003). Quartz cement develops when the kinetic barrier to the supply, transport and growth of quartz has been overcome (Lander et al., 2008; Worden and Morad, 2000). Silica is supplied into the system through variety of ways; amorphous silica (from e.g. volcanic glass or *Rhaxella perforate* sponge spines), alteration of feldspars to clay minerals, transformation of smectite into illite or chlorite during burial diagenesis, pressure dissolution of quartz grains and large scale re-distribution of silica (Worden and Morad, 2003). Therefore, a well sorted clean sand (minimal clay-size matrix), which is typically regarded as having good reservoir potential during hydrocarbon exploration, may become extensively cemented by quartz overgrowths during deep burial, which in turn will reduce its porosity and permeability (Worden et al., 2020a). The presence of a few percent of clay minerals as grain coats in sandstone reservoir, particularly chlorite, may inhibit quartz cement and preserve porosity in deeply buried sandstone (Bloch et al., 2002; Worden et al., 2020a). Microcrystalline quartz coats may also preserve porosity in deeply-buried sandstones by inhibiting quartz cement growth (Aase et al., 1996; French and Worden, 2013; French et al., 2012; Worden et al., 2012). Microcrystalline quartz cement typically originates from the dissolution and subsequent precipitation of siliceous micro-organisms such as sponge-spicules and diatoms. Other publications have proposed that quartz overgrowths can also be inhibited by early oil emplacement (Marchand et al., 2000; Worden et al., 2018b; Worden et al., 1998), and early development of pore fluid

overpressure (Osborne and Swarbrick, 1999; Stricker and Jones, 2016; Stricker et al., 2016). However, this remains contentions in the broader reservoir quality community.

1.1.4.2 Feldspar

Feldspars are among the most abundant rock-forming minerals in the Earth's crust and the two main types of feldspar mineral group are alkali feldspars (K-feldspar) and plagioclase feldspars. The composition of alkali feldspars ranges between orthoclase (KAlSi3O8) and albite (NaAlSi3O8), while that of the plagioclase feldspars ranges between albite (NaAlSi3O8) and anorthite (CaAl2Si2O8). The abundance of plagioclase has been reported to exceed that of K-feldspar (Bloch and Helmold, 1995). Feldspars influence both the mechanical and chemical properties of sandstones, and they play a significant role in diagenetic processes that affect reservoir quality (Bloch and Helmold, 1995; Chuhan et al., 2001; Griffiths et al., 2016; Morad et al., 2010). For example, feldspars supply reactants during diagenesis (Bloch and Helmold, 1995), and enhance efficient grain packing owing to their lower mechanical strength, which results in grain fracturing and broader grain size distribution, thus causing significant loss in porosity and permeability (Griffiths et al., 2016). The chemical composition of different feldspar minerals can have significant influence on sediment mineralogy during diagenesis. For example, the albitisation of calcic-plagioclase releases Ca^{2+} and Al^{3+} that may lead to the formation of carbonate and clay mineral cements, whereas the albitisation of K-feldspar releases potassium that may lead to the creation of illite cements (Morad et al., 2010). In addition, K-feldspar and kaolinite are unstable at temperatures above 70 °C (Worden and Burley, 2003), and their co-deposition may lead to the formation of illite and quartz cements during deep burial diagenesis, as reported by Chuhan et al. (2001) in the Garn formation of Norwegian North-Sea. The replacement of K-feldspar in sandstone can occur at depths of burial between 1500 to 4500 m and temperature between 50 to 150 °C (Wilkinson et al., 2001), or extensive alteration at depths > 2500 m (Worden and Burley, 2003).

Chemical weathering of feldspar minerals can affect sediment mineralogy, pore fluid chemistry, and porosity and permeability (dissolution pores) in sandstone reservoirs (Ehrenberg and Jakobsen, 2001).

Migration process and precipitation of the by-products of mineral dissolution are important in the evolution of sandstone reservoirs (Stoessell and Pittman, 1990; Thyne et al., 2001). In shallow and marginal marine sediments, feldspars are commonly subjected to extensive meteoric water-flushing (subsurface weathering) typically at depths < 100 m (Bjorlykke, 1998). The occuranve of CO_2 in sandstones resulting from enhanced oil recovery, through carbon capture and geological storage, may also lead to feldspar dissolution (Ehrenberg and Jakobsen, 2001). Meteoric water-flushing during telogenesis (uplift) may also lead to feldspar dissolution and subsequent clay minerals formation (Bjorkum et al., 1990). The by-products that resulted from the total- or part-dissolution of feldspar in the sandstones framework (detrital grains, matrix or diagenetic-cements), are mainly clay minerals and authigenic quartz (Emery et al., 1990; Schmidt and McDonald, 1979).

The development of secondary porosity in both shallow and deeply buried sandstones has also been attributed to feldspar dissolution (Burley, 1986; Dutton and Loucks, 2010; Huang et al., 2003; Surdam et al., 1984; Wilkinson et al., 1997). However, other studies have argued about the possibility of feldspar dissolution in creating significant high secondary porosity in sandstone, for example Yuan et al. (2015) reported that most rock-forming minerals in clastic rocks, have low-solubility (e.g. feldspars), and therefore minerals dissolution and flushing in sandstones is unlikely to occur in sufficient quantities to create significant secondary porosity. Cement of clay minerals and authigenic quartz in sediment pore spaces, forming as by-products of feldspar dissolution may lead to porosity and permeability reduction, for example illite cements and feldspar overgrowths associated with mineral dissolution in sandstone reservoirs of the Brent Group in Gulffaks Field, northern North Sea, have been reported by Ehrenberg and Jakobsen (2001).

1.1.4.3 Carbonates

The main carbonate minerals are aragonite ($CaCO_3$), calcite ($CaCO_3$), dolomite ($CaMg(CO_3)_2$) and siderite ($FeCO_3$). Aragonite is metastable and usually dissolves and recrystallises to calcite in shallow marine sandstones (MacKenzie and Adams, 1994). The occurrence of shells in shallow marine may

lead to the dissolution and subsequent precipitation of eogenetic calcite as nodules or discrete layers, this can affect porosity and permeability (Hendry et al., 1996; Morad et al., 2010; Wilkinson, 1991; Worden and Burley, 2003). However, carbonate cements may preserve depositional porosity by reducing mechanical compaction through strengthening the sediment framework (Bjorlykke, 2010; Morris et al., 2006). Carbonate cements that commonly form during eodiagenesis and mesodiagenesis are calcite, dolomite and siderite (Worden and Burley, 2003), these minerals can react with other aluminosilicate minerals under different physiochemical conditions; e.g., at burial temperatures > 120 °C kaolinite react siderite to form authigenic chlorite (Worden and Morad, 2003). Carbonate precipitation in sandstones may result from mass influx of highly soluble carbonate materials from nearby carbonate-rich lithologies (Worden and Burley, 2003). Therefore, it is vital to understand the relationship between reservoirs and the surrounding geological deposits above and below it. Siderite precipitation occurs under reducing conditions when there is high aqueous bicarbonate activity and low aqueous sulphide activity (Berner, 1980), for example in a humid, warm (subtropical to temperate) environment, pore waters are slightly acidic diluted with Ca^{2+} and HCO^{3-} (Worden and Morad, 2003).

1.1.4.4 Iron Sulphides/Other Fe-Minerals

The distribution of iron in sedimentary deposits is controlled by provenance, pH-Eh conditions, the extent of diagenetic alteration and grain size (Hylander et al., 2000). Fe-minerals in sedimentary deposits include (detrital) biotite, Fe-oxides and hydroxides, ilmenite, heavy minerals such as garnet, pyroxene and amphibole, Fe-bearing muscovite, (eogenetic) smectite, glauconite, celadonite, berthierine, odinite, verdine, (mesogenetic) chlorite and other non-silicate minerals include Fe-rich calcite, ankerite, pyrrhotite, magnetite, siderite and pyrite (Worden and Morad, 2003).

Iron-sulphide is an Fe-rich sulphide that typically originates from the bacterial reduction of aqueous sulphate, when sea water inundates the coastal region (Daneshvar and Worden, 2017). Fe-sulphides include pyrite, marcasite and pyrrhotite, are found in modern marginal-marine sediments. Iron-sulphide is less common in brackish and freshwater systems due to lower concentrations of dissolved

sulphate ions (Morad et al., 2010). The high concentrations of aqueous SO_4^{2-} in estuarine settings may lead to the growth of Fe-sulphides due to bacteria sulphate reduction, in the sediment column or in the guts of creatures (Needham et al., 2006; Worden et al., 2006). Pyrite is formed under reducing condition with the supply of marine aqueous sulphate in the presence of organic matter (Tucker, 2001). The formation of pyrite significantly affects the availability of Fe by sequestering the Fe, this limits the amount of Fe available for the formation of berthierine, odinite and Fe-chlorite during diagenesis. Therefore, it is necessary to understand the distribution of Fe-sulphides in modern sediments in understanding the potential ingredients available for the formation of burial-diagenetic Fe-minerals. The primary depositional environments for the occurrence Fe-rich precursor clay minerals include estuarine and marine-pro-deltaic environments (Baker et al., 2000; Dowey et al., 2012; Ehrenberg and Boassen, 1993; Worden and Morad, 2003), deltaic-lacustrine environments (Luo et al., 2002) and fluvial incised-valley settings (Dowey et al., 2012; Morad et al., 2010).

1.1.4.5 Oxides

Oxides are present in igneous, metamorphic and sedimentary rocks as accessory minerals. such as rutile, ilmenite and hydroxides; the hydroxides typically occurred where alteration and weathering are pervasive (Deer, 1978; Delvigne, 1998; Dyar et al., 2008). Oxides occur in sedimentary rocks as products of mineral alteration of pre-existing rocks and as resistant detrital grains in sediments (secondary) (Lindsley, 2018). Oxides are also present in soils and sediments, as amorphous material or biogenic oxide; Mn(IV) oxides and/or oxyhydroxides are formed where microbial activity produces mineral compounds through oxidation of bioavailable transition metals (Tebo et al., 2004). In most weathered terrains, the different Fe-phases are dominated by secondary hydrous oxides such as ferrihydrite (Fh), akaganeite ($Fe^{3+}O(OH,Cl)$), feroxyhyte ($Fe^{3+}O(OH)$), goethite (FeO(OH), lepidocrocite (y- FeO(OH) and limonite (FeO (OH)-n-H2O) (Hansel et al., 2004; Taylor and Konhauser, 2011). However, primary oxides may also account for some types of Fe minerals, and highly oxidised Fe (ferric) may form hydroxide or sesquioxides coats on grains (Worden and Morad, 2003). Oxides are of great significance as they may serve as source of metals such as Fe and Al during diagenesis (Griffiths

et al., 2018; Griffiths et al., 2019a; Worden et al., 2018a; Worden et al., 2020a; Worden and Morad, 2003), and are widely used in heavy mineral stratigraphic correlation (Morton et al., 2011; Verhaegen, 2020). The widespread occurrence of Fe-Ti oxides coupled with their ability to incorporate additional cations into their structure has made them a very useful tool in geochemical studies of sedimentary deposits (Dare et al., 2014; Dupuis and Beaudoin, 2011; Knipping et al., 2015; Nadoll et al., 2014)

There are single element oxides developing, for example rutile (TiO_2), or two or more oxides may combine to form double element oxides, for example ilmenite ($FeTiO_3$) (Bowles, 2021). Oxide mineral formed from two or more elements, additional elements may enter the mineral structure in substitution for those that are characteristic of the mineral (Bowles, 2021). Oxide minerals are categorised based on their site of cation distribution and crystal structure (Bowles et al., 2011; Scheinost, 2005). The two main classes are simple oxides (XO, X_2O, XO_2, and X_2O_3), complex oxides (XY_2O_4), and hydroxides (OH^{1-}); these classes can be further subdivided into periclase group, zincite group, hematite group, rutile group, spinel group, and goethite group (Deer, 1978; Wenk and Bulakh, 2016). Silicate minerals are distinguishable from oxide minerals, because of readily definable structure of oxygen atoms covalently bonded to an atom of another element like silicon (Bowles, 2021). Minerals containing H_2O or -OH (hydroxyl group) component instead of O_2 are referred as hydroxides, while a mineral containing both hydroxyl and oxygen is known as an oxyhydroxides (Deer, 1978; Dyar et al., 2008; Wenk and Bulakh, 2016).

1.1.5 Geochemical Elements

The definition encompasses the classification of elements in various ways based on their abundance, behaviour, and distribution in the Earth (Lee, 2018). Geochemical elements have been qualitatively classified into major, minor and trace elements (Lee, 2018).

The major elements that dominate the earth and make the majority of minerals present in the Earth are: oxygen, hydrogen, carbon, sodium, magnesium, aluminium, silicon, potassium, calcium, sulphur, titanium and iron, these elements are typically present at > 1,000 ppm (Krauskopf and Bird, 1967; Lee,

2018). Major elements can be associated with a single mineral, or with several minerals, they dictate the mineralogy in sediments and sedimentary rocks and thus, regarded as the major rock-rocking elements (Krauskopf and Bird, 1967).

The minor elements are typically present between the range of 1000-100 ppm and include: phosphorous, manganese, fluorine, chlorine, barium, strontium, chlorine, vanadium, chromium, rubidium and boron (Krauskopf and Bird, 1967). These minor elements may locally occur as unique minerals (e.g. phosphate or halite), or as trace element in a major rock forming mineral, where they substitute a major element (e.g. by solid solution), for example Ba and Sr can replace Ca in carbonate and sulphate minerals (Krauskopf and Bird, 1967; Lee, 2018; Wedepohl, 1995).

Trace elements are not essential to the definition of a sediment or rock, nor directly influence their bulk properties (Krauskopf and Bird, 1967). They either occur passively as dissolved constituents, as a minor amounts of accessory phases or a dominant mineral-forming element in a trace mineral (e.g. Zr in zircon) (Krauskopf and Bird, 1967). Trace elements include all other naturally occurring elements that are present at low concentration (<100 ppm) in sediments and sedimentary rocks. Some trace elements are economically important, or helpful for provenance studies of sediments and sedimentary rocks, including zirconium, thorium, uranium, lead, zinc, tin, antimony, arsenic, bromine, iodine, and the rare earth elements (La to Lu of the lanthanide series) (Lee, 2018). A single element can be a major element in one rock and be a trace element in another, for instance, during petrogenetic processes an element initially occurs at trace levels and can eventually become concentrated enough to be at major or minor level (Lee, 2018).

An important aspect regarding the distribution of elements in sediments and sedimentary rocks, is understanding the compositions of the dominant minerals that accommodates the various elements. The mobility of elements, elemental substitution and solid solution in minerals, tend to play major roles in the positioning and distribution of element within the range of compositions of the dominant minerals (Pauling, 1960; Shannon, 1976).. The ionic radius and charge (valence state) need to be

broadly similar, for a trace element substitution into a crystal lattice to occur, preferably the ionic radius should be within 10 % and same ionic charge, the difference in charge cannot exceed +/- 1, for substitution to occur (Pauling, 1960; Shannon, 1976). Element relative solubility determines its mobility in a sedimentary succession, and the degree of isochemical diagenesis in any sedimentary processes. Immobile elements such as Al, Ti and Fe are highly insoluble in aqueous solution (Warren and Smalley, 1994) and are thus part of a closed geochemical system. In such an isochemical medium, the distribution of immobile elements helps the definition of sediment provenance and supply at the time of deposition. Mobile elements such as Na, Cl and K, are relatively soluble in aqueous solution, and their distribution in a sedimentary rock can be used to infer material flux, as well as the initial composition of the sediment. It is noteworthy that there are rare occurrence of quartz-cemented veins in sedimentary basins (Worden et al., 2016), while the SiO_2 solubility is relatively low at temperatures recorded in most sedimentary basins and therefore, Si is also considered to be isochemical, especially at temperatures below 80-100°C (Worden and Morad, 2000).

Iron is a major element that occurs in a form of either Fe^{2+} or Fe^{3+}, at the Earth's surface (Ure and Berrow, 1982). Fe^{2+} commonly occurs as a remnant of olivine, pyroxene, amphibole and biotite, while Fe^{3+} is present in a form of iron oxides and hydroxides, as a by-product of weathering (Ure and Berrow, 1982). During weathering, the distribution of Fe-minerals is largely controlled by the pH-Eh, and the initial oxidation state of the Fe compounds (Ure and Berrow, 1982). In oxidising and alkaline conditions, Fe is likely to be precipitated, whereas in acid and reducing conditions Fe compounds are likely to undergo dissolution (Kabata-Pendias, 2004). The mobility of Fe is largely controlled by the solubility of the Fe^{3+} and Fe^{2+} amorphous hydrous oxides and, to some extent, the formation of other Fe compounds, such as phosphates, sulphides and carbonates, may greatly modify Fe mobility (Kabata-Pendias, 2004).

1.1.5.1 Geochemical data in the study of sediments

Portable X-ray fluorescence spectroscopy (pXRF) is a rapid, non-destructive technique that provide element concentration data. The use of pXRF for geochemical data analysis has developed significantly over the last decade owing to its ease of use, speed of analysis and an acceptable level of precision (Gazley et al., 2011; Kenna et al., 2011; McLaren et al., 2012; Morris, 2009; Rowe et al., 2012; Weindorf et al., 2012). Recent development in pXRF devices have made it possible to replicate numerous conventional analytical approaches in determining both major, minor and trace elements chemistry of sediments and sedimentary rocks (Potts, 2008; Turner et al., 2015). pXRF has been used for a wide range of geochemical applications such as lithogeochemical exploration (Benn, 2012), mineral abundance studies in core sediments (Marsala et al., 2012), studies of mineral enrichment in ores (Le Vaillant et al., 2016), geological reconnaissance and mapping (Young et al., 2016), element distribution in modern sediments (Emmerson et al., 1997), geochemical characterisation and provenance determination of sediments (Martins et al., 2012), and linking mineralogy to elemental distribution (Ross et al., 2014; Yuan et al., 2014).

pXRF has numerous advantages in relation to other multi-element analysis techniques, such as inductively coupled plasma mass spectrometry (ICP-MS). pXRF is fast with low operational cost, rapid in situ analysis, versatile and allows the analysis of numerous elements simultaneously in both sediments and sedimentary rocks (Holler et al., 2009; Nagata et al., 2001). Other important techniques such as whole rock neutron activation analysis, inductively coupled plasma atomic emission spectrometry and inductively coupled plasma mass spectrometry (ICPMS), ion microprobe, atomic absorption spectrophotometry, and electron microprobe analysis have all been in used in geochemical analysis of sediments and sedimentary rocks.

The application of sediment geochemical data to understand sedimentary processes has been widely employed, due to the sensitivity of some trace elements that can be used to identify minor components not easily recognised with petrographic analysis (Armstrong-Altrin et al., 2004; Garver et

al., 1996); the concentration of trace elements, such Zr and Th, provide insight into the sedimentological origin, lithological and grain size variation, redox and depositional conditions of siliciclastic sediments (Dypvik and Harris, 2001). The concentration of major elements have been used to classify clastic sediments (Herron, 1988), and to understand the processes controlling their distribution (Vital et al., 1999). Geochemical data are also helpful in understanding sedimentary environments in relation to sedimentary provenance (Andersson et al., 2004), lithology (Herron, 1986; Herron, 1988), weathering effect and intensity (Mongelli et al., 2006), paleoclimate and paleoenvironment (Andersson et al., 2004; Nesbitt and Young, 1982), geochemical correlation (Aehnelt et al., 2013; Craigie, 2015a; Craigie, 2015b; Craigie, 2016; Craigie et al., 2016a; Craigie et al., 2016b; Craigie and Rees, 2016), organic-rich sediments (by proxy) (Dahl et al., 2013; Rider and Kennedy, 2011; Swanson, 1961), and hydrothermal or metasomatic processes (Pirajno, 2005).

The geochemical composition of clastic rocks reflects an interplay between multiple variables; source area, weathering, transportation, physical sorting, and diagenesis (Cox and Lowe, 1995; Fralick and Kronberg, 1997; McLennan et al., 1993; Meinhold et al., 2007). Clastic sediments are typically not at thermodynamic equilibrium and so can have a large number of discrete mineral phases (Worden et al., 2018a), that far exceed their expected of attainment of the phase rule. A consequence of this is that a given element can be associated with several minerals (or phases) in a clastic sedimentary system. Bulk geochemistry of primary sedimentary deposits is related to mineral distribution (Zwingmann et al., 1999), the mineralogical composition of modern sediments in marginal marine settings are quartz, plagioclase, K-feldspar, calcite, dolomite, biotite, muscovite, illite, chlorite, smectite, kaolinite and some accessory minerals such haematite, pyrite, siderite, ilmenite, rutile, apatite and zircon, as reported by numerous researchers for example; Gironde estuary in France (Virolle et al., 2021; Virolle et al., 2019a; Virolle et al., 2019b; Virolle et al., 2020), Anllons Estuary in spain (Dowey et al., 2017) and Ravenglass Estuary (Daneshvar and Worden, 2017; Griffiths et al., 2018; Griffiths et al., 2019a; Griffiths et al., 2019b; Wooldridge et al., 2017b).

Table 1.2; The chemical composition of the dominant sedimentary rock forming minerals

Mineral	**Formula**	**Mineral**	**Formula**
Quartz	SiO_2	Apatite	$Ca_5(PO_4)_3(OH)$
K-feldspar	$KAlSi_3O_8$	Rutile	TiO_2
Albite	$NaAlSi_3O_8$	Ilmenite	$FeTiO_3$
Plagioclase	$Na_{0.5}Ca_{0.5}Al_{1.5}Si_{2.5}O_8$	Goethite	$FeO(OH)$
Anorthite	$CaAl_2Si_2O_8$	Haematite	Fe_2O_3
Analcime	$NaAlSi_2O_6.H_2O$	Gypsum	$CaSO_4.2H_2O$
Chabazite	$(CaK_2Na_2)_2(Al_2Si_4O_{12})_2.12H_2O$	Anhydrite	$CaSO_4$
Heulandite	$(CaNa)_5Al_9Si_{27}O_{72}.26H_2O$	Strontianite	$SrSO_4$
Kaolin	$Al_2Si_2O_5(OH)_4$	Barite	$BaSO_4$
Muscovite	$KAl_3Si_3O_{10}(OH)_2$	Calcite	$CaCO_3$
Muscovite-impure	$K_{1.95}Na_{0.05}Al_{2.2}Ti_{0.05}Si_{3.3}O_{10}(OH)_2$	Dolomite	$CaMg(CO_3)_2$
Biotite	$K(Mg,Fe^{2+})_3AlSi_3O_{10}(OH)_2$	Fe-dolomite (ankerite)	$CaMg_{0.63}Fe_{0.37}(CO_3)_2$
Illite	$K_{0.65}Al_{2.65}Si_{3.35}O_{10}(OH)_2$	Siderite	$FeCO_3$
Smectite	$(NaCa)_{0.7}(MgFe)_2AlSi_3O_{10}(OH)_8$	Rhodochrosite	$MnCO_3$
Chlorite-clinochlore	$Mg_5Al_2Si_3O_{10}(OH)_8$	Pyrrhotite	FeS
Fe-Mg chlorite	$Fe_{2.5}Mg_{2.5}Al_2Si_3O_{10}(OH)_8$	Pyrite	FeS_2
Chlorite-chamosite	$Fe_5Al_2Si_3O_{10}(OH)_8$	Halite	$NaCl$

1.2 Research Outline, Aims, Objectives and Questions

1.2.1 Modern Analogue Approach

Depositional environments play a significant role in the formation of Fe-rich minerals in sediments (Dowey et al., 2012). The distribution of eogenetic clay minerals is strongly related to primary depositional site and can be used to predict the evolution of clay minerals during burial, if the initial sediment composition is known (Griffiths et al., 2018; Griffiths et al., 2019a). The main components

of Fe-rich clay minerals (Fe-, Al- and Si-oxides) are largely insoluble in aqueous solution, and therefore the diagenetic transformation of Fe-bearing clay minerals during burial is largely isochemical (closed-system) process; the issue of mass influx of these sparingly soluble, materials into sandstones during diagenesis can be ruled out (Worden et al., 2020a). It is noteworthy that sedimentary deposits in modern environments have not been employed in establishing a detailed understanding, by analogy, of the distribution of clay minerals in sandstone reservoirs (Worden et al., 2018a; Worden and Morad, 2003). Previous research on sandstone reservoir compositional and textural (e.g. detrital clay coat coverage distribution), has been conducted using four established methods.

(1) Core studies, typically collected from oil and gas fields, can be used to understand the distribution of sandstones composition and texture (Aagaard et al., 2000; Ajdukiewicz and Lander, 2010; Al-Ramadan et al., 2004; Ehrenberg, 1993; Gould et al., 2010; Martinius et al., 2001; Saïag et al., 2016). Data collected during core studies can be spatially-limited and usually associated with high-levels of uncertainty on the diagenetic history, and also defining the exact initial depositional environments is challenging.

(2) The study of outcrops is regarded as a useful analogue (Musial et al., 2012); for example it allows the full coverage of the study area with fewer issues in spatial resolution associated with core-based approach. However, outcrops typically undergo weathering-related alteration due to exposure to atmospheric conditions, and therefore, information on sediment mineralogy and texture may not be well-preserved.

(3) Experimental studies can provide useful information on sediment composition and texture (Ajdukiewicz and Larese, 2012; Billault et al., 2003; Duteil et al., 2020; Needham et al., 2004; Pittman et al., 1992; Worden et al., 2006). However, up-scaling and extrapolation from small-scale experiment to the formation scale remains challenging.

(4) A modern-analogue approach can be helpful as the exact depositional-environment is known. Modern analogues provide a detailed understanding of the primary depositional settings as well as transport processes and provenance and can allow full coverage of the study area. The major challenges in adopting modern analogue approach is the ability to model the dataset in simulating burial diagenesis (e.g., to model compaction and mineral-alteration). With recent development of forward-diagenetic models, it is possible to make predictions of potential mineral-alterations, using well-established burial-diagenetic pathways (Fig. 1.4).

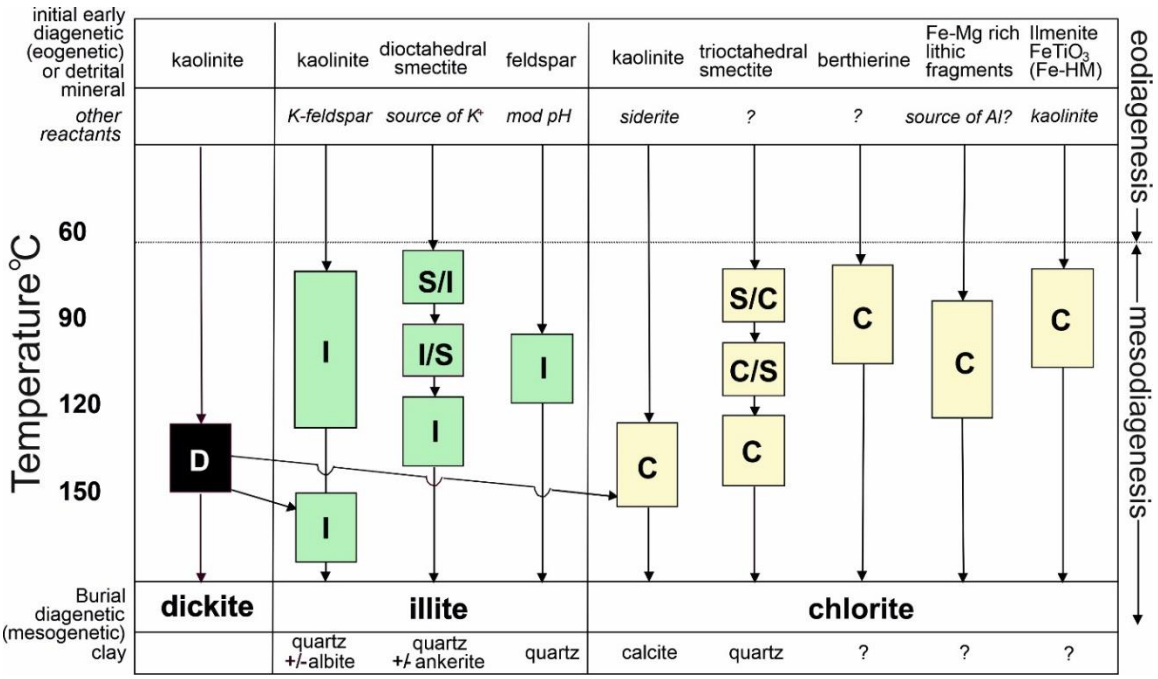

Figure 1.4; Common mesogenetic pathways for clay minerals in sandstones, edited from Worden and Morad (2003). Where; D is dickite, S is smectite, I is illite and C is chlorite. Randomly stratified mixed-layer clay minerals are named accordingly: S/I is mixed-layer smectite-illite dominated by smectite; I/S is the same mineral mixture dominated by illite.

In recent years, modern analogue studies have been employed to understand the distribution of sandstone composition and texture (e.g., predicting chlorite distribution and detrital clay coat) in clastic reservoirs for example, in the Ravenglass Estuary, England, UK (Daneshvar and Worden, 2017; Griffiths et al., 2018; Griffiths et al., 2019a; Griffiths et al., 2019b; Wooldridge et al., 2017a; Wooldridge et al., 2017b; Wooldridge et al., 2019a; Wooldridge et al., 2019b; Wooldridge et al., 2018), in the Gironde Estuary, France (Virolle et al., 2021; Virolle et al., 2019a; Virolle et al., 2019b; Virolle et al.,

2020), and in the Anllons Estuary, Spain (Dowey et al., 2017). For summaries of previous research conducted using a modern analogue approach, see Table 1.4 and 1.5.

Table 1.3; Previous examples of modern estuarine analogue studies.

Authors	Method	Main objective and analysis	Main conclusion	Environment	Country
Virolle et al. (2020)	XRD, carbon 14 (^{14}C) and Macdiff software.	Understanding the Reservoir quality	Tidal sand bars of the outer estuary funnel have the optimum coated grain content and are potentially the best reservoirs in deeply buried sandstones.	Gironde Estuary	France (South West)
Virolle et al. (2021)	XRD and SEM	Analyzed Berthierine and Chlorite clay-coat of shallow (400–1000 m) sandstones.	At shallow depth low temperature (<40 ^{o}C) berthierine coats, causes the inhibition of quartz overgrowths.	Paris Basin	France
Duteil et al. (2020)	Cryo–scanning electron and atomic force microscopy, wet chemical assays and Fourier transform infrared spectroscopy.	Laboratory experiments to simulate clay-coated quartz sands as an analogue to modern and ancient estuarine sands.	Detrital coats could be considered as biosignatures of biofilm development and EPS production in past environments, in ancient estuarine sandstone.	Experiment	France
Virolle et al. (2019a)	SEM-EDS, XRD and Leica EM HPM 100.	The analysis of composition and distribution of clays along modern estuary.	Tidal bars and heterolithic point bars are good targets for clay coats and potentially good reservoirs in deeply buried sandstones	Gironde Estuary	France (South West)
Virolle et al. (2019b)	XRD and SEM.	Relationship between facies and chlorite coat occurrences.	Detrital minerals and clay coats are prerequisite for the formation authigenic Fe-rich chlorite coats in estuarine sandstones.	Gironde Estuary	France (South West)

Dowey et al. (2017)	Electron and light microscopy, laser granulometry, and XRD.	Understanding the occurrence and distribution of clay coats on grains	Clay coat distribution on grains are primarily controlled by sediment transport and deposition processes.	Anllons Estuary	Spain (North West)

1.3 Estuaries

An estuary is a seaward stretch of a drowned valley that tends to accumulate sediments transported by both fluvial and marine processes; sediment deposited in an estuary is influenced by tidal, wave and fluvial processes (Dalrymple et al., 1992). The seaward outer estuary is dominated by tidal and wave action; the central part of an estuary is dominated by mixed energy, the landward inner estuary is dominated by river action (Dalrymple and Choi, 2007; Dalrymple et al., 1992), due of their intermittent to nearly constant subaerial exposure (Ainsworth, 2005; Tucker, 2009). In the inner part of estuaries, a seaward fining trend is commonly observed with silt and clay grade increasing toward the margins of the central and inner estuary (Griffiths et al., 2019a), while along the outer estuary, is a landward fining trend resulting from the transgression of reworked sediment and sediments deposited by wave erosion and longshore drift, from nearby coast (Castaing, 1970; Dalrymple and Choi, 2007). Also about 75% of fluvially-transported clay and silt are trapped in estuaries, with the remaining 25% transported on to the shelf, this resulted in trapping of different mineral types (Allen, 1972; Castaing and Allen, 1981). These trapped sediments tend to have a high preservation potential during marine transgression (Boyle et al., 1974; Boyle et al., 1977; Dalrymple et al., 1992).

Estuaries in general contain a wide range of depositional sub-environments that are dominated by tide, river and wave actions (Dalrymple and Choi, 2007). These depositional sub-environments play a significant role in the distribution of sediment texture and mineralogy, due to their inherent physio-chemical conditions that are largely influenced by the sediment water chemistry, water influx and evaporation rate, temperature and atmospheric oxygen, plant-derived CO_2, and organic matter content (Worden and Morad, 2003). Estuaries are influenced by both fluvial and marine processes that collectively control mineral distribution pattern (Berner and Berner, 2012). Estuarine deposits are

typically complex due numerous factors acting simultaneously, including water circulation, grain size variation, sediment mineralogy and geochemistry (De Lazzari et al., 2004). The complexity of these sediments results from the range of biological, chemical and physical processes occurring in the estuaries; for example, estuarine water salinity is controlled by the seasonal variations of the fluvial discharge and the neap-spring tidal ranges (Allen, 1972; Barrie et al., 2015) and increases seaward. Salinity variation also influences the organism population and diversity (Buatois et al., 2005; Pemberton, 2001).

In an estuarine settings, the redistribution of deposited sediment is controlled primarily by hydrodynamic processes, the physical forces of river flow, wave energy and twice-daily tidal actions (Dalrymple and Choi, 2007). Sediment deposited in marginal marine settings can be in a state of nonequilibrium and therefore, remain geochemically active owing to the accumulation of surface-active material typically organic matter, and contain physically stable sediment to form active micro- and macro-biological communities (Berner and Berner, 2012). The formation of minerals *in-situ* in pore waters through direct growth (neoformation), and the transformation of detrital minerals through modification by ion exchange or cation rearrangement (Aller and Aller, 1998; Berner, 1980; Feininger, 2013), tends to occur in an estuarine environment. These aforementioned processes usually take place immediately after deposition, within the depositional environment (Berner, 1980; McIlroy et al., 2003; Worden and Burley, 2003; Worden and Morad, 2003). Furthermore, there are numerous reports of early-diagenetic mineral alteration in an estuarine settings (Daneshvar and Worden, 2017; Griffin and Ingram, 1955; Grim and Johns, 1954; Nelson, 1960; Powers, 1957) and biologically-mediated processes (McIlroy et al., 2003; Needham et al., 2004; Worden et al., 2006). For example, a study conducted on marginal marine sediment revealed an alteration of clay minerals with depth, and the present of biogenic silica (Aller and Michalopoulos, 1999; Michalopoulos and Aller, 1995; Michalopoulos and Aller, 2004; Michalopoulos et al., 2000). Diagenetic processes that are synonymous with estuarine depositional environments include the formation of kaolinite and/or illite from feldspar alterations, the transformation of mixed-layer chlorite to Fe-rich chlorite and the precipitation of

gibbsite as a result of kaolinite dissolution and alteration (Daneshvar and Worden, 2017; Drever and Zobrist, 1992; Huang, 1993; Velde and Church, 1999; Worden and Morad, 2003).

The distribution pattern of clay minerals in estuaries is controlled by estuary hydrodynamics, the physical and chemical condition of water, grain-size sediments distribution and physical sorting of clay minerals (Caliani et al., 1997; Förstner and Wittmann, 2012; Griffiths et al., 2018; Griffiths et al., 2019b). Processes active during deposition and bio-sediment interaction, such as burrowing, also play a vital role in clay mineral distribution at the surface (Griffiths et al., 2018). Flocculation and accumulation of suspended sediments in estuaries affect the physio-chemical properties of clay minerals such as exchange capacity (Fig. 1.5) (Boyle et al., 1977). The role of organic matter is also significant in determining the mineralogical distribution of clay in estuaries (Venkatramanan et al., 2013). Clay mineral assemblages present in estuaries are mainly dominated by chlorite, kaolinite, illite, smectite and, less frequently, by gibbsite (Griffiths et al., 2018; Venkatramanan et al., 2013).

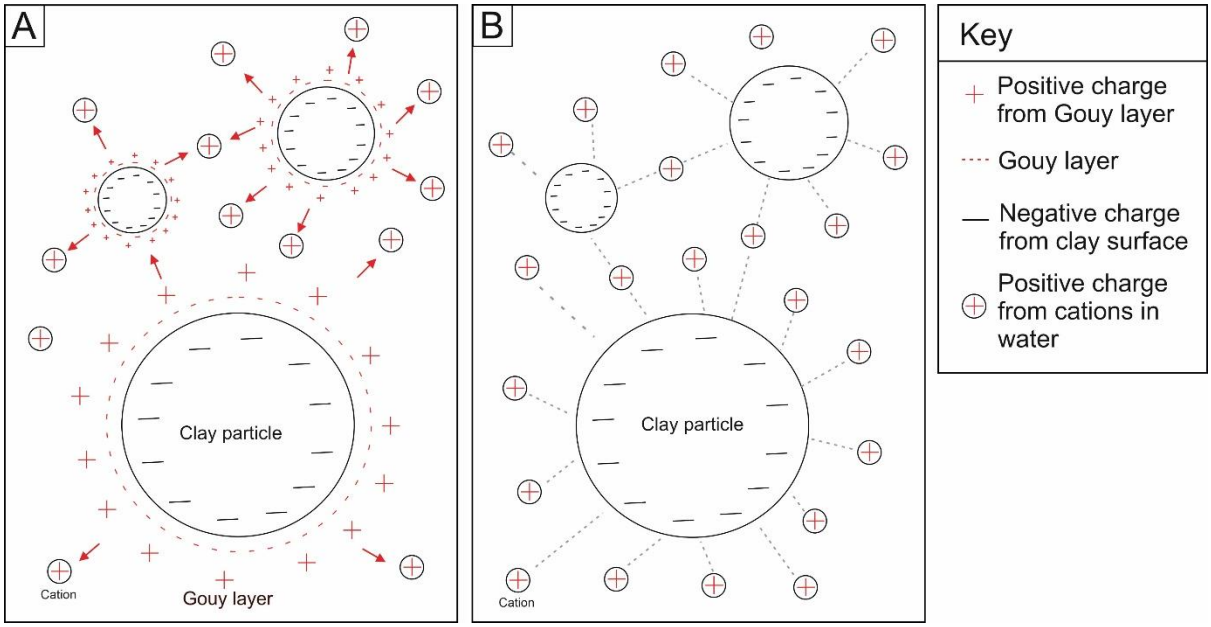

Figure 1.5; A schematic of electrostatic repulsion and attraction. (A) In freshwater systems, the presence of the Gouy-Chapman layer prevents cations from bonding to the surface of the negatively charged clay. (B) In saline water when this layer is destroyed, due to the increase in cation concentrations, the negative surface area of the clay particle is able to accept cations from the water. When polyvalent cations bond to more than one clay particle.

1.3.1 Ravenglass Estuary

The Ravenglass Estuary covers an area of about 5.6 km^2 and situated on the west coast of Cumbria in northwest England, UK (Fig. 1.1). It is a macro-tidal estuary with a maximum recorded tidal range of ~ 7.55 m; up to about 86 % of the area of the estuary is exposed at low tide (Bousher, 1999; Griffiths et al., 2018; Griffiths et al., 2019a; Griffiths et al., 2019b; Lloyd et al., 2013; Wooldridge et al., 2017a; Wooldridge et al., 2017b). The estuary has a brackish, river- and tide dominated inner basin, its central area has mixed-energy with near-seawater salinity dominated by Saltcoats tidal flat, while outer estuary is dominated by seawater with wave and/or tidal currents and covers the main tidal channel, estuary mouth and the foreshore. The estuary stretches eastward (landward) up to the tidal reaches of the Rivers Mite, Irt and Esk, and seaward, it is connected to the Irish Sea through a 500 m-wide tidal inlet that flows between two dune-topped coastal spits (Drigg and Eskmeals Spits). Sediments are fed into the estuary via the Rivers Mite, Irt and Esk with a reported average flow-rates of 0.4, 3.4, and 4.2 m^3s^{-1} respectively (Bousher, 1999). The post-glacial Holocene record of Ravenglass sediments shows nearly 10,000 years of deposition, these sediments were deposited above Devensian glacial till that was underlain by either peat deposits or fluvial gravel beds (McGhee et al., 2021). The Devensian glacial till and the peat deposits have distinctive clasts of the underlying bedrocks, thus allowing the discrimination of various lithostratigraphic units and the ice-movement patterns (Merritt and Auton, 2000). The relative sea level changes that resulted in this stratigraphic shift is associated with glacio-eustatic sea-level change and spatially-variable glacio-isostatic crustal-rebound during the deglaciation period (Lloyd et al., 2013; Merritt and Auton, 2000).

The estuary is regarded as a complete fluvial to marine transect for sediment routing system with a well-established link between sediment source(s) and sinks. According to Kelly et al. (1991), the Ravenglass Estuary can be classified as tide- and wave-dominated with a shallow bathymetry that causes frictional effects and promotes strong tidal-asymmetry, thus having a longer outward ebb tidal-flow than inward flood tidal-flow. The presence of barrier spits and the mud-rich central basin indicate

the influence of wave action, these Drigg and Eskmeals barrier-coastal spits shelter the estuary from wave-action but the estuary is exposed to periodic tidal currents as result of the macro-tidal regime (Griffiths et al., 2019a). The development of the Ravenglass Estuary as a mixed energy system with shared morphologies of both tides and waves, is likely due to one or more of:

- Strong tidal currents that extend beyond the central basin into the inner estuary, and resulted in the development of extensive tidal bars and tidal dunes (Griffiths et al., 2019a).
- The development of ebb-tidal delta at the later stage of estuary filling and this tends to weaken the significance of the energy-minimum in the central part of the estuary (Posamentier and Walker, 2006).
- Where tidal energy becomes dominant, coastal sands have been transported further up the estuary, and therefore, the initial muddy central basin will become sand rich tidal channels (Dalrymple et al., 1992).

The impact of anthropogenic activities in the Ravenglass Estuary is insignificant, because of the sparse population of its surrounding environment. However, the effect of population on the natural environment is profound. Pretty much all of the UK, including Ravenglass, is not 'natural'. E.g. the present of sheep farms bordering the estuary along the salt coat, and that means the vegetation is partly as a result of farming practices. Additionally, the construction of railway bridge in 1868 led to the expansion of the salt marsh, thereby protecting the lower reaches of River Mite from tidal currents (Carr and Blackley, 1986). Numerous research studies have been conducted on this estuary, in terms of sedimentary systems and processes, stratigraphy evolution and valley infills, detrital clay and clay coats; their origin, mineralogy and distribution, and estuarine sediment elemental composition (Daneshvar, 2015; Daneshvar and Worden, 2017; Griffiths et al., 2018; Griffiths et al., 2019a; Griffiths et al., 2019b; McGhee et al., 2021; Muhammed et al., 2022; Simon et al., 2021; Wooldridge et al., 2017a; Wooldridge et al., 2017b), and so this represents an ideal field site to study the effect of clay mineralogy and clay coats in modern sediment for reservoir quality predictions, as an analogue for ancient and deeply buried sandstone petroleum reservoirs.

1.3.2 Geological Setting and Provenance

Ravenglass sediments were sourced from different bedrock types and Quaternary drift-deposits. The source area is dominated by the Ordovician Borrowdale Volcanic Group (BVG), Devonian Eskdale Granite and Cambrian Skiddaw Group slate; a small area of Triassic Sherwood Sandstone Group at the west of the drainage area is largely covered by drift (Fig. 1.6). Granitic-sourced sediments are transported into the estuary via the River Esk, while the andesite-sourced sediments are transported into the estuary via the River Irt (Daneshvar and Worden, 2017; Griffiths et al., 2018; Griffiths et al., 2019a; Griffiths et al., 2019b).

The Eskdale Granite is the largest exposed intrusion in Cumbria (Soper, 1987) and forms part of the Lake District Batholith along the western-margin of the Lake District massif (Quirke et al., 2015). Hydrothermal mineralisation has caused a significant chlorite alteration of the mafic silicates and plagioclase (Moseley, 1978; Quirke et al., 2015; Rundle, 1979; Young et al., 1986). The Sherwood Sandstone Group locally known as the St Bees Sandstone Formation is a fluviatile sandstone sequence, it is feldspathic sandstones (Strong et al., 1994) dominated by detrital quartz, subordinate feldspar, muscovite and biotite, albite, and carbonate clasts (Barnes et al., 1994a; Strong et al., 1994), with heavy minerals; zircon, tourmaline, apatite, anatase and rutile (Strong et al., 1994). The Ordovician Borrowdale Volcanic Group is present in the Lake District in two different outcrops; the older exposure in the north-west and the younger exposure in the south-east (Entwisle et al., 2005). These extrusive rock suites are comprised of subduction-related K-rich, calc-alkaline basalt, andesitic-rhyolitic volcanic lavas, sills and pyroclastic rocks, and constitute the central part of the Lake District massif (Millward, 2004; Quirke et al., 2015). Quirke et al. (2015) reported that, during the Caledonian Orogeny the Borrowdale Volcanic Group was subjected to regional sub-greenschist facies metamorphism at about 395 Ma, leading to nine stages of hydrothermal activity that formed a complex zones of alteration with some variable amounts of haematite vein (Entwisle et al., 2005; Milodowski et al., 1998). The Skiddaw Group is a fine-grained (pelitic) sedimentary rocks that has been weakly metamorphosed (Merritt and Auton, 2000).

Quaternary drift-deposits dominate the lowland geology, they are composed of glacial till, peat, and glacial-lacustrine deposits (Griffiths et al., 2018; Griffiths et al., 2019a; Griffiths et al., 2019b; Merritt and Auton, 2000). The estuary is characterised by the present of knolls of glacial till, exposed across the entire region, peat is also present and is mostly occured on top of the glacial (Lloyd et al., 2013).

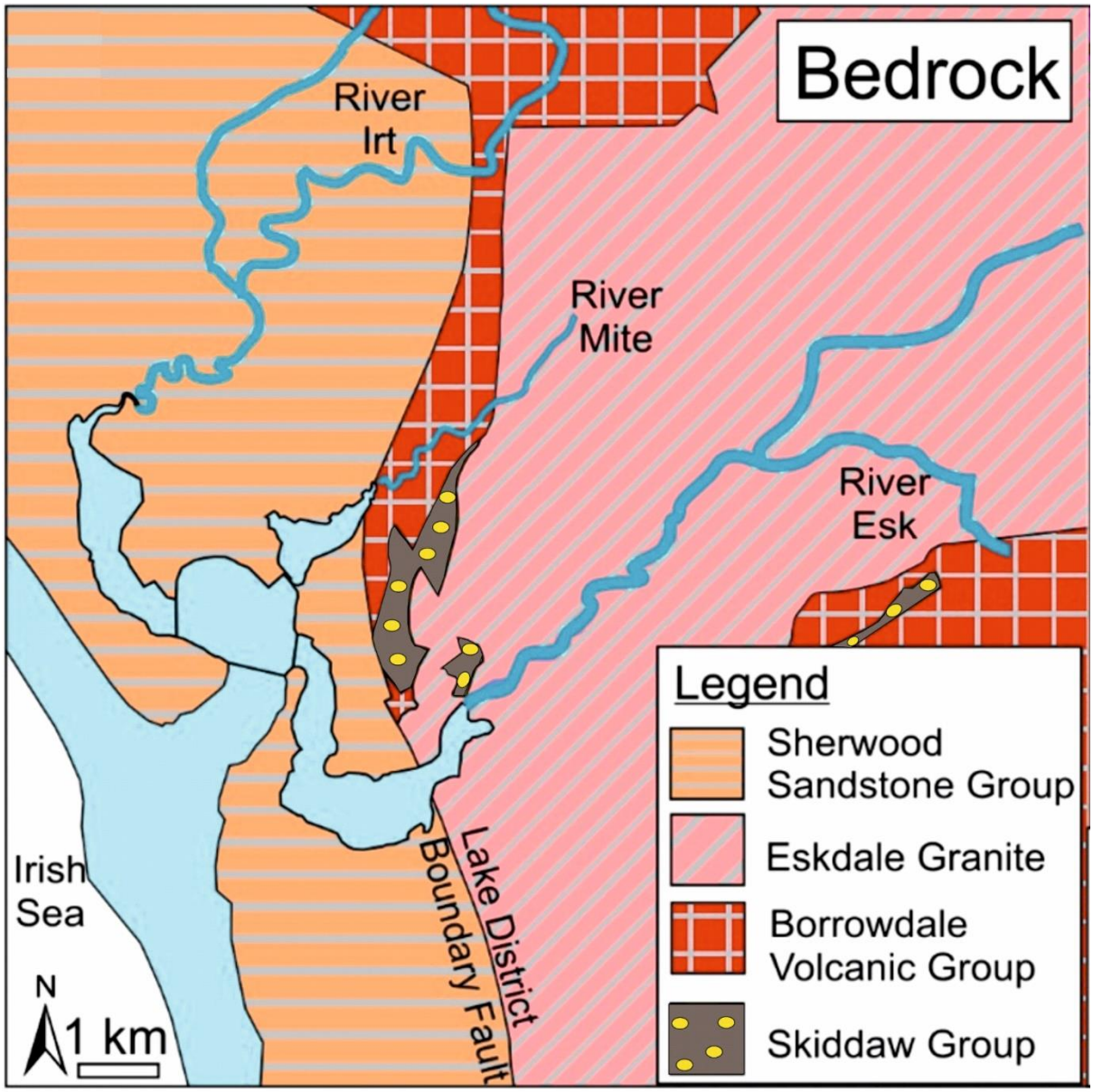

Figure 1.6; Geological setting of the Ravenglass Estuary, UK, showing the bedrock geology

1.3.3 Previous work on Ravenglass Estuary

The Ravenglass Estuary Holocene sediments have been extensively studied in terms of sedimentary systems and processes, sediment textural and compositional variability, stratigraphic evolution and valley infill, detrital clay and clay coats; their origin, mineralogy and distribution (Table 1.5).

Table 1.4; Summary of previous work on Ravenglass Estuary using modern analogue approach.

Authors	Method	Main objective and analysis	Main Conclusion
(Muhammed et al., 2022)	XRF analysis, ArcGIS and statistical analyses	Distribution of estuarine sediment elemental composition and discrimination of sub-depositional environment.	A novel automatic geochemical data based classification scheme was developed using a combination of visual analysis, and RPART.
McGhee et al. (2021)	Facies analysis of geotechnical cores and carbon 14 dating.	Understanding the lateral and vertical stacking patterns relative to the sea-level changes.	The best-connected (up to 1 km) reservoir-equivalent sands belong to the more stable channels.
Simon et al. (2021)	Grain size analysis, ArcGIS and statistical analyses	Distribution of textural parameters in the estuary and discrimination of sub-depositional environment.	A novel automatic textural classification scheme was developed using a combination of visual analysis, PCA and RPART.
Verhagen et al. (2020)	Flume experiments, SEM-EDS and BSEM.	Determine the stability of detrital grain-coats during sediment transport.	Detrital clay coats in estuary are remain stable during sediment transport.
Griffiths et al. (2019b)	XRD, LPSA, ArcGIS and statistical analyses	Controls on the distribution of clay minerals and clay coat in estuary depositional environment.	Tidal bars and dunes are rich in chlorite and likely to form authigenic clay coats in deeply-buried sandstones.
Wooldridge et al. (2019b)	SEM, SEM-EDS and Petrog statistical software.	Study the extent and the volume of clay minerals coating grain surface.	The novel clay-coat quantification techniques are applicable to modern and ancient sandstones.
Wooldridge et al. (2019a)	SEM-EDS, ArcGIS and Statistical analyses.	Distribution of clay minerals across estuarine sediments.	The grain-coating chlorite is highest in sand-flat and tidal-bar environments.

Table 1.5; continued

Wooldridge et al. (2018)	SEM, SEM-EDS, LPSA and Petrog statistical software and Statistical analyses.	Controls on clay-coat coverage and clay-coat mineralogy.	Infiltration and bioturbation have weak effect on the distribution clay-coat coverage in near-surface sediments.
Griffiths et al. (2018)	XRD, ArcGIS and statistical analyses	To understand the compositional variation and distribution in modern estuarine sands.	The distributions of quartz, feldspar, carbonates, and clay minerals are controlled by the grain size of specific minerals and estuarine hydrodynamics.
Griffiths et al. (2018)	Core analysis, XRD and Clay-Coat Coverage study.	Lithofacies, Fe-sulphide, and precursor detrital-clay-coats and clay-minerals distribution in near surface sediments	The distribution of clay coats and clay-minerals are controlled by processes active during deposition and bio-sediment interaction in the near surface of the primary depositional environment.
Wooldridge et al. (2017b)	XRD, SEM, SEM-EDS, ArcGIS and statistical analyses.	The distribution and origin of clay-coats in surface sediment.	Clay-bearing inner-tidal-flat-facies sands have the best RQ potential.
Wooldridge et al. (2017a)	SEM, environmental SEM, Raman spectroscopy and Petrog statistical software.	Study biofilm abundance and quantify the percentage of clay coat coverage.	In modern marginal marine systems, clay coats on grains, are primarily formed from adhesive biofilms.
Daneshvar and Worden (2017)	XRD, SEM and SEM-EDS analysis.	Mineral composition and distribution within estuarine modern sediments.	Feldspar controls clay distribution and Detrital Fe minerals seem to be locally replaced by pyrite

1.4 Research questions

- What elements are dominant within the surface sediment in the Ravenglass Estuary?
- What is the elemental abundance and distribution in the estuary?
- What controls elemental abundance and distribution patterns in the Ravenglass Estuary?
- Do specific estuarine sub-depositional environments have characteristic element concentrations?
- Can pXRF data be used to discriminate estuarine sub-depositional environments (both present-day and palaeo)?
- Can pXRF analysis be used to discern provenance in estuarine sediments?
- What are the different types of Fe present in these estuarine sediments?
- What factors control the distribution and accumulation of Fe in the estuarine sediments?
- Can pXRF analysis be used as a proxy for mineralogy in the estuarine sediments?
- What is the dominant sediment mineral assemblage and how does it affect clay mineral distribution within the palaeo-sub-depositional environment?
- How are clay minerals distributed? What controls clay-mineral distribution patterns?
- Is it possible to predict the distribution of clay minerals and detrital clay coat as a function of sub-depositional environments in the Ravenglass Estuary?

1.5 Organisation of the Thesis

Following the introductory chapters, the bulk of the thesis is presented in three main chapters that have been, or will be, submitted to journals for publication. Chapters two and three have been submitted to the international journals; Geosciences and Minerals respectively, while chapter four is intended to be submitted to Sedimentary Geology. The outline of each chapter, publication status, and work contribution from other authors are listed below. The final chapter synthesises the finding reported and presents ideas for further work in this research area.

1.5.1 Geochemistry of Sub-Depositional Environments in Estuarine Sediments: Development of an Approach to Predict Palaeo-Environments from Holocene Cores

Publication status: *Accepted for publication (currently in press): "Geosciences"*

Aim: To study sediment elemental compositional data of estuarine sub-depositional environments and determine if they can be used to predict sub-depositional environment with statistically significant differences.

Outline: In this chapter, a new way to automatically classify a known sub-depositional environment of surface sediment and to use this classification model to predict paleo-sub-depositional environment of estuarine sediment from cores, was presented. This study involved using a ten-fold classification of present day sub-depositional environments of 470 surface sample in Ravenglass Estuary, NW England, UK. The elemental composition of each sample was then determined using a portable XRF device. A novel automatic classification scheme based on geochemical data, was developed using a combination of visual discrimination of gravel and vegetated surfaces and a recursive partitioning routine (RPART) in Rstudio. The newly developed classification scheme was successfully applied to a 5 m Holocene core, drilled on present day vegetated tidal bar, and the paleo-sub-depositional environments of the Holocene estuarine sediments was interpreted.

Author contributions:

Dahiru D. Muhammed: Developed and executed the research, designed the paper, planning and undertaking detailed ground-surveys and sample collection, and performed analyses.

Richard H. Worden: Primary PhD supervisor. Responsible for providing guidance and support during the field and laboratory work and also from the industry, funding the project and defining fieldwork site (Ravenglass Estuary, UK). Provided in-depth discussions and detailed manuscript review.

Naboth Simon: Helped perform field work, undertook detailed ground-surveys and sample collection, and aided in sample analysis.

James E. P. Utley: Field assistant. Aided in sample collection. In-depth discussions and manuscript review.

Iris T. E. Verhagen: Secondary PhD supervision. Aided in project planning and detailed manuscript review.

Rob Duller: Discussions and detailed manuscript review.

Joshua Griffiths: Worked with the sub-contractor during the drilling of the geotechnical (long) cores in the estuary. Discussions and detailed manuscript review.

Luke J. Wooldridge: Worked with the sub-contractor during the drilling of the geotechnical (long) cores in the estuary. Discussions and detailed manuscript review.

1.5.2 Provenance and geochemistry of modern estuarine sediment

Publication status: *Submitted and returned for correction after first review and revision: "Minerals"*

Aim: To study the provenance, accumulation and distribution of Fe in the Ravenglass Estuary as function of sub-depositional environment, grain size, clay minerals and organic matter concentration, in order to understand distribution of Fe-bearing clays

Outline: In this chapter, the effect of grain size, clay minerals and organic matter on the accumulation and distribution of Fe in modern estuarine sediment was presented. This study employed the application of XRF, grain size, total organic carbon, minerals and statistical analyses, on surface sediment collected from 497 sites in Ravenglass Estuary, NW England, UK. This study shows that Fe increases from the river to the estuary with some local variations and then gradually decreases seaward, the Fe concentration is highest in tidal flat sediments, where Fe is present as a fine-grained material, probably as an oxide or hydroxide, that is associated with elevated organic carbon concentrations. The fine-grained Fe may be brought into the estuary as fluvially-derived metal-organic complexes that are destabilised in the saline waters of the estuary and settle out as floccules or coats on sand grains. Fe is also present in detrital Fe minerals including chlorite, biotite, Fe-bearing white mica, and minor Fe-oxides that are mainly present within lithic grains. The distribution and accumulation of Fe in the estuarine sediments are controlled by hinterland lithology and degree of weathering, sediment grain size, organic enrichment of the supplied sediment, and local estuary hydrodynamic conditions. Geochemical data can be used to help discern the different hinterland lithologies and can also be used as a proxy for what minerals might develop in estuarine sediment, i.e., during eo- or meso-diagenesis.

Author contributions:

Dahiru D. Muhammed: Developed and executed the research, designed the paper, planning and undertaking detailed ground-surveys and sample collection, and performed analysis.

Richard H. Worden: Primary PhD supervisor. Responsible for providing guidance and support during the field and laboratory work and also from the industry, funding the project and defining fieldwork site (Ravenglass Estuary, UK). Provided in-depth discussions and detailed manuscript review.

Naboth Simon: Helped perform field work, undertook detailed ground-surveys and sample collection, and aided in sample analysis.

James E. P. Utley: Field assistant. Aided in sample collection. In-depth discussions and manuscript review.

1.5.3 Understanding the distribution of clay minerals in modern estuarine sediment based on geochemical classification of environments and petrographic analysis.

Publication status: *In preparation for submission to Sedimentary Geology*

Aim: To study sediment mineralogy and paleo-sub-depositional environment, deposited during Holocene period, in an estuarine environment, and to investigate the relationship between clay abundance, clay coat and mineral alteration and early diagenetic processes.

Outline: In this chapter, a geochemical-based classification scheme was employed to define palaeo-sub-depositional environments from cores using bulk element geochemistry, SEM-EDS-, grain size-, and image-analysis to understand the distribution of different clay mineral types and clay coats. The dominant minerals of the inner estuary sediments are quartz, K-feldspar, plagioclase, muscovite, biotite, illite, chlorite, kaolinite, and smectite. Clay mineral distributions vary greatly between the different sub-depositional environment; chlorite is relatively most abundant in the sand flat and tidal inlet and is likely to occur as clay forming grain coat or as lithic grain in coarser sediment, kaolinite is relatively most abundant in the mixed flat, smectite is relatively most abundant in the ebb-tidal-delta, north foreshore and tidal inlet, illite is relatively most abundant in the salt-marsh and mud flat. Clay occur as either pore-filling or grain-coating material in the salt-marsh and mud flat, with over 40% coat coverage. In the mixed flat, sand flat and tidal bar sediment, clay is mostly present as grain coat with coat coverage of as much as 40%. The tidal inlet, foreshore and ebb-tidal-delta have a coat coverage of as much as 5%. Clay coat coverage increase with increasing clay fraction abundance. Sand flat and

tidal bars sediments, that in Ravenglass have >10% detrital coat coverage (within optimum range), and that contain chlorite-bearing lithic grains, can form diagenetic chlorite coats that can preserve anomalously high porosity in inhibiting quarts cementation, in deeply buried sandstone. The distribution patterns of sediment mineralogy and different clay mineral types in the Ravenglass Estuary Holocene core, are primarily controlled by the grain size and estuarine hydrodynamics. Post-depositional processes, particularly early-diagenetic mineral alteration appeared to have influenced clay-mineral distribution patterns, in the coarser sediment of Ravenglass Holocene cores, via mineral alteration of feldspar grains.

Author contributions:

Dahiru D. Muhammed: Developed and executed the research, designed the paper, planning and undertaking detailed ground-surveys and sample collection, and performed analysis.

Richard H. Worden: Primary PhD supervisor. Responsible for providing guidance and support during the field and laboratory work and also from the industry, funding the project and defining fieldwork site (Ravenglass Estuary, UK). Provided in-depth discussions and detailed manuscript review.

Naboth Simon: Helped perform field work, undertook detailed ground-surveys and sample collection, and aided in sample analysis.

James E. P. Utley: Field assistant. Aided in sample collection. In-depth discussions and manuscript review.

Iris T. E. Verhagen: Secondary PhD supervision. Aided in project planning and detailed manuscript review.

Joshua Griffiths: Worked with the sub-contractor during the drilling of the geotechnical (long) cores in the estuary. Discussions and detailed manuscript review.

Luke J. Wooldridge: Worked with the sub-contractor during the drilling of the geotechnical (long) cores in the estuary. Discussions and detailed manuscript review.

1.6 Methods

1.6.1 Field-Based Mapping and Surface Sample Collection

Based on geomorphological mapping criteria, together with the use of aerial imagery and grain size analysis, eleven sub-depositional environments across the estuary have been mapped (Fig. 2). The sub-depositional environments are gravel beds, vegetated surfaces, barrier spits, tidal flats (sub-divided into mud flat, mixed flat and sand flat), tidal bars, tidal inlet, backshore, foreshore, ebb-tidal-delta. The subdivision of tidal flats was based on laboratory-derived sand percentages, modified from a scheme initially proposed by Brockamp and Zuther (2004), where: 90-100% sand is sand flat, 50–90% sand is mixed flat, and 15–50% sand is mud flat. The small area occupied by the backshore deposits, the diminutive number of samples collected (two) in this sub-depositional environment, and also its low preservation-potential, has led to the exclusion of backshore deposits in this study. Surface sediment (from < 2 cm below the surface) was sampled from 497 sites covering the entire estuary and the coast. Sediment samples were placed in airtight plastic bags (< 100 ml) in the field and dried in the laboratory prior to XRF, grain size and TOC analyses.

1.6.2 Holocene Cores

Sediment cores were drilled through the Holocene succession as far as the Ravenglass Glacial Till Member, under tender by Geotechnical Engineering Ltd (GEL) (McGhee et al., 2021). Prior to the core drilling, detailed desk studies were conducted to estimate the depth to glacial till based on previous reports (Assinder *et al.*, 1985; Kershaw *et al.*, 1990; Halcrow Group, 2013; Coast & Area, 2015), and environmental impact assessment was conducted to ensure the protection of biodiversity species such as natterjack toads and great crested newts, the assessment was conducted under the supervision of an independent ecologist, in conjunction with Natural England. Core drilling was carried out during periods of low tides for accessibility and safety reasons. The geotechnical drilled cores were acquired with a Geotechnical Engineering Limited (GEL) light-weight “Pioneer” rotary rig, and the choice of this rig was due to the soft nature of the sediment surface. The drilled cores were retrieved

in a series of 12 cm diameter, 1 m long, semi-rigid plastic liners for protection against oxidation and sample degradation, and easy transport. Each segment of the sediment core (1 m) was sliced and photographed wet and air-dried for sedimentary logging and subsequent analysis at the University of Liverpool. Detailed sedimentary logging of each core segment, at a scale of 1:5, was carried out and different lithofacies were characterised based on grain size distribution, colour, sedimentary structures present, bed thickness, presence of roots and shell fragments, bioturbation extent and type. All cores were sampled every 5 cm for pXRF and LPSA analyses, using techniques described in this section.

1.6.3 XRF Analysis

All sediment samples from the Ravenglass Estuary were analysed using a handheld Thermo Scientific Niton +XL3t GOLDD XRF spectrometer (pXRF) to measure the abundance of major, minor and trace elements. The pXRF equipment is a self-contained, energy dispersive XRF spectrometer with a variable intensity energy source (6-50 kV, 0-200 μA) Ag anode X-ray tube. It is equipped with a factory-calibrated, GOLDD (Geometrically Optimised Large Area Drift Detector) detection system, optimised by the manufacturer for low detection limits, and high-precision measurements of more than 40 elements. Sediment samples were prepared by air drying whole sediment samples in a 50 mm petri dishes which was then placed 2 mm from the pXRF detector. Problems of horizontal and vertical heterogeneity of the sample, variable moisture and surface roughness, associated with core-based, "point and shoot" pXRF studies (Carr et al., 2008; Chou et al., 2010; Gutiérrez-Ginés et al., 2013; Weindorf et al., 2012) have here been avoided (Argyraki et al., 1997).

Despite concentrations for 40 elements being reported by the pXRF, only 12 elements were present in all samples. These elements are Al, Si, K, Ca, Ti, Fe, Mn, Rb, Sr, Zr, Ba and Cs. Other elements were variably present at concentrations above the element-specific detection limit, but these could not easily be incorporated into any scheme to interrogate the relationship between composition and sub-depositional environment.

The determined limit of detections of the instrument for Al, K, Ca, Ti, Fe, Mn, Rb, Sr, Zr, Ba and Cs are listed in Table 1.6 The instrument's high precision and accuracy was validated by replicating the XRF analysis, on a single sample 30 times, the average and standard deviation of Al, K, Ca, Ti, Fe, Mn, Rb, Sr, Zr, Ba and Cs are listed in Table 1. Each analysis was conducted, for 150 seconds, in "Test All GEO" mode; this combines mining and soil modes which thus permits the determination of major and trace elements. The optimum analysis time of 150 seconds was selected by repeating analysis of one sample for different replicate durations in order to identify when there was no significant improvement in the reported uncertainty.

Table 1.5; Factory reported detection limit for some key elements plus mean and standard deviations of one sample analysed 30 times to assess credibility of reported concentration data.

Element	Reported detection limit (ppm)	Mean of 30 repeat analyses from one sample (ppm)	Standard deviation of 30 repeat analyses from one sample (ppm)
Al	2000	64099	1685
K	250	18234	145
Ca	70	2610	46
Ti	6	2477	92
Fe	25	11837	90
Mn	30	172	19
Rb	6	70	1
Sr	8	73	2
Zr	3	352	3
Ba	50	487	18
Cs	12	85	4

1.6.4 Grain Size Analysis

Prior to grain size analysis, coarse materials and organic matter were removed, because the Laser Particle Size Analyser (LPSA) only accepts sediment clasts that are up to 2 mm in size and below, and the relative mass of the > 2 mm fraction and that of the coarse fraction were recorded. Organic matter was removed using established laboratory procedures for sample digestion; the organic matter was digested using 30 mL of 6 % hydrogen peroxide on about 10 to 20 mL of sediment sample, in a 100 mL

Pyrex beaker, then heated at 70 °C on a hotplate placed in a fume cupboard to aid digestion. The organic digestion process was repeated where sediment organic matter was at a relatively high concentration, until all the organic content are digested. Grains < 2 mm were separated from the sample using a sieve and then this fraction was analysed for grain size distribution using Laser Particle Size Analysis (LPSA) with a Beckman Coulter LS13 320 counter. A small amount of Calgon was added to convert the dried sediment into a paste for mixing and homogenisation, prior to analysis (Simon et al., 2021). The LPSA data were analysed using GRADISTAT© software (Blott and Pye, 2001), to define grain size parameters of the sediment.

1.6.5 TOC Analysis

Surface sediments were sampled with a screw neck vial (15-mm diameter) and immediately oven dried. The dried samples were crushed into powder with an agate mortar and pestle. Total organic carbon analysis of sediment was undertaken using a Thermo Scientific Flash Smart Organic Elemental Analyser after vapour phase de-carbonation using 12N Analar Grade HCl, following Yamamuro and Kayanne (1995). Two-point daily calibration was performed using High Organic Sediment Standard OAS (Elemental Microanalysis Ltd). Results for the standards were within uncertainty limits of certified value which are Carbon 7.17 % +/- 0.09 %, Nitrogen 0.57 % +/- 0.02 %.

1.6.6 Mineral and Grain Coat Analysis

Sediment mineralogy was determined using automated mineralogy using SEM-EDS analysis. SEM-EDS was undertaken using a FEI WellSite QEMSCAN®, which comprises a scanning electron microscope combined with energy dispersive spectrometers. The QEMSCAN operates with a 15-kV electron beam and two Bruker EDS detectors, to measure primary and secondary backscatter electrons, with the brightness indicating the sample density while the surface signal defines atomic weight. The QEMSCAN system has an electronic processing unit for integrating scanned data using a software suite (iDiscover) that includes Species Identification Protocols (SIPs) which uses a mineral chemical database, stored in the system library, to provide information regarding the chemical and mineral

compositions of the samples. The SEM-EDS analysis defines sediment mineralogy in a fully quantitative way; it divides each sample into a series of 2 mm × 2 mm fields and analyse each field individually. SEM-EDS analyses were conducted on carbon-coated polished thin sections. Data were collected with user-defined step sizes of 2 µm to ensure that all the clast sizes were analysed, the resolution of the output is dependent upon the step size selected at the time of data collection. The output is a mineral map that contain the summary of the fully quantitative mineralogical content of the analysed sample, in addition to textural information.

Backscattered electron (BSE) and scanning electron microscopy (SEM) imaging was carried out using a Hitachi TM3000 table-top SEM. This was undertaken to ascertain mineral alteration, coats and textural relationships. The detrital clay coat coverage was determined using a qualitative method recently proposed by Wooldridge et al. (2017b). The clay-coat coverage on individual sand grains was estimated by carrying out SEM analysis of 200 sand grains, on a 1 cm diameter stub, the stub stubs were examined in backscattered electron (BSE) imaging mode. Traverse across each sample was created from the BSE images in order to produce a representative image of approximately 200 grains analysed within each sample. Bin classes defined by Wooldridge et al. (2017b) were adopted for this study: Class 1; complete absence of clay coats, Class 2; less than half of the grains have a small (~ 1 to 5%) surface area of attached clay coats, Class 3; every grain exhibits at least ~ 5 to 15% clay-coat coverage, Class 4; extensive (~ 15 to 30%) clay-coat coverage on the majority of grains, and Class 5; greater than 30% surface area covered by clay coats on every grain.

1.6.7 Measuring clay-coat coverage: Petrog

Clay coat coverage was quantified using a new perimeter tool developed in Petrog software by Wooldridge et al. (2019b). The new tool allows the quantification of clay-coat grain coverage on imported SEM petrographic images. To quantify clay coat coverage at a very high resolution, 2,160 backscattered electron microscope images; approximately 60 sand grains per sample (thin section) and at least 1 grain per image, were captured using the SEM, and all the SEM images of a single sample

(thin section) were imported for each analysis. The perimeter tool was used to define the total perimeter length of a grain and then to identify the length that is covered by attached clay-coat material manually, to calculate the percentage perimeter of the grain covered by clay-coat material. Any form of web or lump of clays, surrounding a sand grain without any single or continuous contact, was not regarded as attached clay-coat.

1.6.8 Statistical Multivariate Analysis

Multivariate statistical techniques are powerful tools commonly used to investigate variability in large datasets (Cheng et al., 2006; Grunsky and Smee, 1999; Klovan, 1966; Michael et al., 2013). Although concentration maps of elements are displayed, there is a risk that dilution by quartz will dominate the variation patterns of non-quartz minerals. To evaluate the more meaningful *relative* abundance of elements, a range of indices (e.g., X/(X+Y)) and ratios (e. g. X/Y) have been employed and mapped.

1.6.8.1 Spatial Mapping

Spatial distribution maps of elements and element indices were generated using ArcGIS software, via an inverse distance weighted (IDW) interpolation function. The IDW approach has low mean prediction errors and high correlations between predicted and measured values (Zarco-Perello and Simões, 2017). IDW was also selected to avoid the automatic generation of physically-meaningless negative concentrations, such as are produced by spline-based interpolation methods, and to avoid the formation of valleys or ridges (Watson and Philip, 1985). A polyline in ArcGIS was drawn down the long axes of the Drigg and Eskmeals Spits, to separate the marine data from estuarine data when performing the interpolations (Griffiths et al., 2019a).

1.6.8.2 ANOVA and Post-Hoc Tukey

Analysis of Variance (ANOVA) tests were used in R statistical software (R Core Team, 2016), to investigate the statistical significance of geochemical differences between various pairs of sub-depositional environment. Following ANOVA, a post-hoc Tukey's honestly significant difference (HSD) test was then employed, using R statistical software (R Core Team, 2016), to determine which

individual depositional environment were statistically different from one another as a function of elemental indices. The difference between each pair, for each elemental index, is defined as being significant if the “p” value is less than 0.01 (R Core Team, 2016; Scheffe, 1999).

1.6.8.3 Boxplots and classification trees

Univariate analysis of geochemical indices, split by sub-depositional environment, was undertaken using boxplots produced using ggplot2 in RStudio (Wickham, 2016). The Recursive Partitioning and Regression Tree (RPART) package (Therneau and Atkinson, 2019), available in R statistical software (R Core Team, 2016), was used to characterise the sediment geochemical signatures (continuous data) into sub-depositional environments (categorical data).

The RPART routine allows the development of a classification tree by using one or more variable (in this case, elemental indices) to find the optimum splits of the dataset, into different categories (e.g., sub-depositional environment) (Simon et al., 2021).

2. Geochemistry of Sub-Depositional Environments in Estuarine Sediments: Development of an Approach to Predict Palaeo-Environments from Holocene Cores

2.1 Abstract

In the quest to use modern analogues to understand clay mineral distribution patterns to better predict clay mineral occurrence in ancient and deeply buried sandstones, it has been necessary to define palaeo sub-environments from cores through modern sediment successions. Holocene cores from Ravenglass in the NW of England, United Kingdom, contained metre-thick successions of massive sand that could not be interpreted in terms of palaeo sub-environments using a conventional descriptive logging facies analysis. We have therefore explored the use of geochemical data from portable X-ray fluorescence analyses from whole-sediment samples, to develop a tool to uniquely define the palaeo sub-environment based on geochemical data. This work was carried out through mapping and defining sub-depositional environments in the Ravenglass Estuary and collecting 497 surface samples for analysis. Using R statistical software, we produced a classification tree based on the surface geochemical data from Ravenglass that can take compositional data for any sediment sample from the core or the surface and define the sub-depositional environment. The classification tree allowed us to geochemically define ten out of eleven of the sub-depositional environments from the Ravenglass Estuary surface sediments. We applied the classification tree to a core drilled through the Holocene succession at Ravenglass, which allowed us to identify the dominant paleo sub-depositional environments. A texturally featureless (massive) metre-thick succession, that had defied interpretation based on core description, was successfully related to a palaeo sub-depositional environment using the geochemical classification approach. Calibrated geochemical classification models may prove to be widely applicable to the interpretation of sub-depositional environments from other marginal marine environments and even from ancient and deeply buried estuarine sandstones.

2.2 Introduction

Reservoir quality studies in the petroleum industry have led to improved production strategies for oil and gas fields (Rui et al., 2017). The improvement in production due to reservoir quality studies has been enabled through advances in downhole logging (e.g., NMR), laboratory analysis (e.g., SEM-EDS), and forward modelling (e.g., diagenetic modelling) (Worden et al., 2018a). Sedimentary facies analysis should be employed in reservoir quality studies (Haile et al., 2018; Zahid et al., 2016), because the primary characteristics of sediment typically influence the way sediment fabric and mineralogy change during diagenesis (Chan, 1985). Sedimentary facies are distinguishable units of sedimentary deposits, each with a unique set of characteristics developed during a specific mode of sediment transport and deposition (Anderton, 1985). The environment of deposition of clastic sediment has a profound impact on sediment characteristics, because it influences grain size, sorting, degree of bioturbation, clay infiltration, water composition, in situ mineral processes, and water flux (Worden et al., 2018a).

Dalrymple and Choi (2007) suggested that estuarine sediments are uniquely complex because of the interplay of a wide variety of processes that give rise to a suite of specific depositional environments. Reservoir quality prediction in ancient estuarine and mixed fluvial–marine clastic sediments therefore presents a challenge (Martinius et al., 2005). These problems are compounded by the presence of multiple sediment sources (variable hinterland geology as well as sediment sourced from the sea), the spatial and temporal variability in sediment transport related to the interaction of tidal and riverine processes, and the susceptibility of these environments to evolve as a result of relative sea-level change (Dalrymple and Choi, 2007). We advocate that, given the complexity of ancient estuarine and mixed fluvial–marine environments, a multi-disciplinary and quantitative approach is required to generate robust interpretations. Geochemical approaches offer a practical way to effectively characterise and interpret estuarine and mixed fluvial–marine sediments, which may be linked to reservoir quality analysis of ancient and deeply buried strata because sediment geochemistry influences the mineral processes during diagenetic transformations (Primmer et al., 1997).

Estuaries are strongly influenced by the fluvial and marine processes that together control mineral and elemental distribution patterns (Berner and Berner, 2012). Estuaries tend to act as sinks for elements such as Fe and Mn due to flocculation, a process by which colloidal particles come out of suspension to sediment under the form of flocs, or flakes, due to a change of water composition (Boyle et al., 1977). Accumulated floccules of Fe and Mn can be flushed out of the estuary during storm events (Coynel et al., 2007) and during longer-term episodes of relative sea-level fall (Audry et al., 2006; Dabrin et al., 2009; Elbaz-Poulichet et al., 1987a; Lanceleur et al., 2013). In the United Kingdom, the site of the current study, modern estuaries tend to act as sinks rather than sources for elements such as Fe and Mn because tidal and flocculation processes limit river output to the ocean (Dyer, 1997).

Although the bulk geochemistry of primary sediment is considered to control the mineralogical architecture of petroleum reservoirs (Zwingmann et al., 1999), our knowledge of the abundance and concentration of rock-forming elements (i.e., the elements that comprise rock-forming minerals) in surface sediments is limited (Smith et al., 2009). Geochemical analysis of sediments can unlock some of the challenges in basin analysis, for example the interpretation of sediment provenance and differentiation of specific depositional environment (Meinhold et al., 2007).

Unlike rocks that are at, or close to, thermodynamic equilibrium, such as most metamorphic rocks (Yardley, 1989), clastic sediments are typically distant from thermodynamic equilibrium. Clastic sediments can have a large number of discrete mineral phases (Worden et al., 2018a) that far exceed that expected of attainment of the phase rule. A consequence of this is that a given element can be associated with several minerals (or phases) in a clastic sedimentary system. The composition of surface sediment is controlled by a number of factors including the geology of the hinterland, climatic conditions, the vigour and distance of sediment transport, and the redox conditions at the site of deposition (Fralick and Kronberg, 1997).

There is a broad relationship between clastic sediment grain size and its geochemical composition (Flood et al., 2016) because phases in fine-grained sediment fractions, i.e., clay minerals, hydroxides and sesqui-hydroxides, tend to concentrate elements such as Al, Mn and Fe. In contrast, coarse-grained fractions tend to enrich Si and elements, such Zr and Ti, which are concentrated in heavy minerals (Berner and Berner, 2012). In the field of sedimentology, the application of grain size distribution to determine sedimentary environment, is well established (Folk, 1966; Folk, 1968). In this study, we have attempted to discriminate estuary sub-depositional environments using geochemical signatures derived by portable X-ray fluorescence spectrometry (pXRF).

The use of pXRF spectrometers in exploration and environmental geochemistry has developed significantly over the last decade owing to its ease of use, speed of analysis and an acceptable level of precision for sedimentary rocks (Gazley et al., 2011; Morris, 2009; Rowe et al., 2012) and soils (Kenna et al., 2011; McLaren et al., 2012; Weindorf et al., 2012). pXRF spectrometers have been applied successfully in surface sediment characterisation (Plourde et al., 2013). Recent developments have allowed pXRF to be used for the analysis of 42 major, minor and trace elements (Turner et al., 2015). The detection limits of pXRF are commonly sufficient for many geochemical analyses. pXRF can detect element concentrations ranging from high percentages down to few parts per million; this allows monitoring of many elements in sediment (Potts, 2008). However, pXRF suffers from low sensitivity for some elements, e.g., magnesium has a high detection limit (typically > 1000 ppm) (Rollinson, 2014).

Portable XRF has been used for a wide range of geochemical applications such as lithogeochemical exploration (Benn, 2012), mineral abundance studies during studies of oil field core (Marsala et al., 2012), studies of mineral enrichment in ores (Le Vaillant et al., 2016), geological reconnaissance and mapping (Young et al., 2016), assessment of metal distribution in modern sediments (Emmerson et al., 1997), geochemical characterisation and provenance determination of sediments (Martins et al., 2012), and linking mineralogy to elemental distribution (Ross et al., 2014; Yuan et al., 2014). We here introduce a novel approach for sedimentary sub-environment classification and prediction using pXRF

data from the Ravenglass Estuary in NW England. This is an area previously studied as a modern analogue for ancient estuarine and mixed fluvial–marine sediments (Daneshvar, 2015; Daneshvar and Worden, 2017; Griffiths et al., 2018; Griffiths et al., 2019a; Griffiths et al., 2019b; Simon et al., 2021; Wooldridge et al., 2017a; Wooldridge et al., 2017b). The Ravenglass Estuary offers a wide range of estuarine sub-depositional environments that are relatively pristine and easily accessible. The main aims of this study were to understand surface sediment geochemistry across the Ravenglass Estuary sub-depositional environments, assess compositional differences between sediments from sub-depositional environments, develop a geochemical method to classify sub-depositional environments and use the classification to predict sub-depositional environments from core samples. This new approach to the classification of sub-depositional environments has been applied to the core drilled into the Holocene succession in the Ravenglass Estuary to reveal palaeo-sub-depositional environments.

This study addressed the following research questions:

1. What elements are dominant within the surface sediment in the Ravenglass Estuary?

2. What controls elemental abundance and distribution patterns at Ravenglass?

3. Do specific estuarine sub-depositional environments have characteristic element concentrations?

4. Can surface pXRF data be used to discriminate subsurface estuarine sub-depositional environments?

2.3 Study Area: The Ravenglass Estuary

The Ravenglass Estuary is situated on the west coast of Cumbria in northwest England, UK and covers an area of approximately 5.6 km^2 (Figure 2.1). The estuary is macro-tidal with a maximum recorded tidal range of ~7.55 m; up to approximately 86% of the area of the estuary is exposed at low tide

(Bousher, 1999; Griffiths et al., 2018; Griffiths et al., 2019a; Griffiths et al., 2019b; Lloyd et al., 2013; Wooldridge et al., 2017a; Wooldridge et al., 2017b). The estuary extends eastwards up to the tidal reaches of the Rivers Mite, Irt and Esk and is connected to the Irish Sea through a single tidal inlet 500 m in width that flows between two, dune-topped coastal spits (Drigg and Eskmeals Spits). The coastal spits shelter the estuary from wave-action, but the estuary has strong tidal currents as result of the macro-tidal regime. The Rivers Mite, Irt and Esk have average flow rates of 0.04 m^3s^{-1} , 0.34 m^3s^{-1} , and 0.42 m^3s^{-1}, respectively (Bousher, 1999). Kelly et al. (1991) classified the estuary as tide- and wave-dominated and 'dual-funnelled' and described the shallow bathymetry which causes frictional effects and promotes strong tidal-asymmetry, with a longer outward ebb tidal-flow than inward flood tidal-flow. The impact of anthropogenic activities on the Ravenglass Estuary is relatively low because the surrounding environment is sparsely populated. However, the construction of the Esk and Mite railway bridges in 1868 led to expansion of salt marsh due to added localised sheltering from tidal currents (Carr and Blackley, 1986).

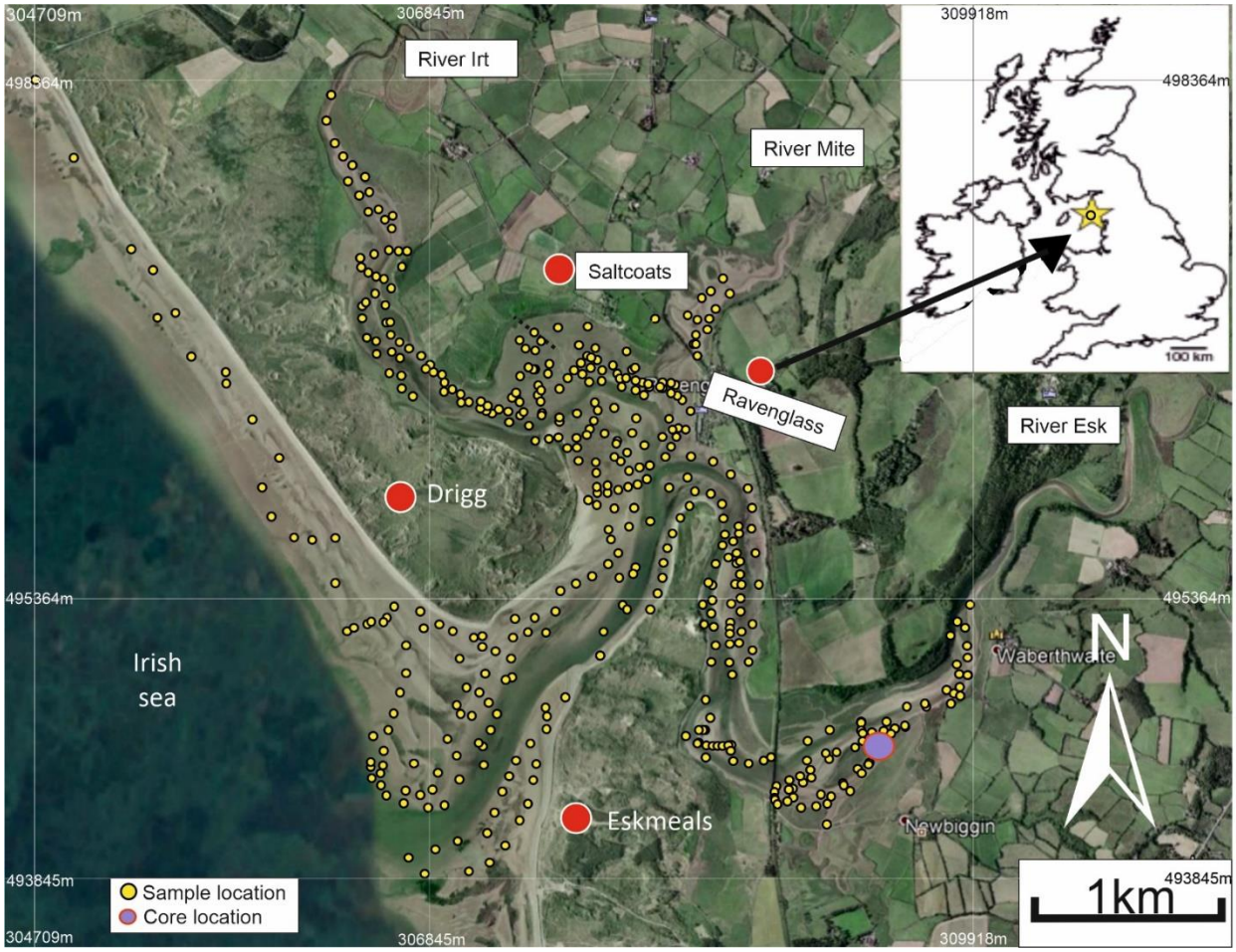

Figure 2.1; Location map of the Ravenglass Estuary, north-west England with an inset map showing the location of the estuary in the UK. The yellow dot shows the distribution of surface-sediment sample site (<2 cm) used for XRF analysis and the purple dot shows the distribution of surface-sediment sample site (<2 cm) used for XRF analysis and the purple dot shows the location of the geotechnical core.

The inner estuary contains brackish water and has moderate fluvial influences from the Rivers Irt, and Esk (Figures 2.1 and 2.2). The central part of the estuary, containing Saltcoats tidal flat, has mixed energy (fluvial, tide and wave-influenced) with near-seawater salinity (Figures 2.1 and 2.2). The outer estuary is dominated by seawater with wave and/or tidal currents; this covers the main tidal channel, estuary mouth and the foreshore (Figures 2.1 and 2.2).

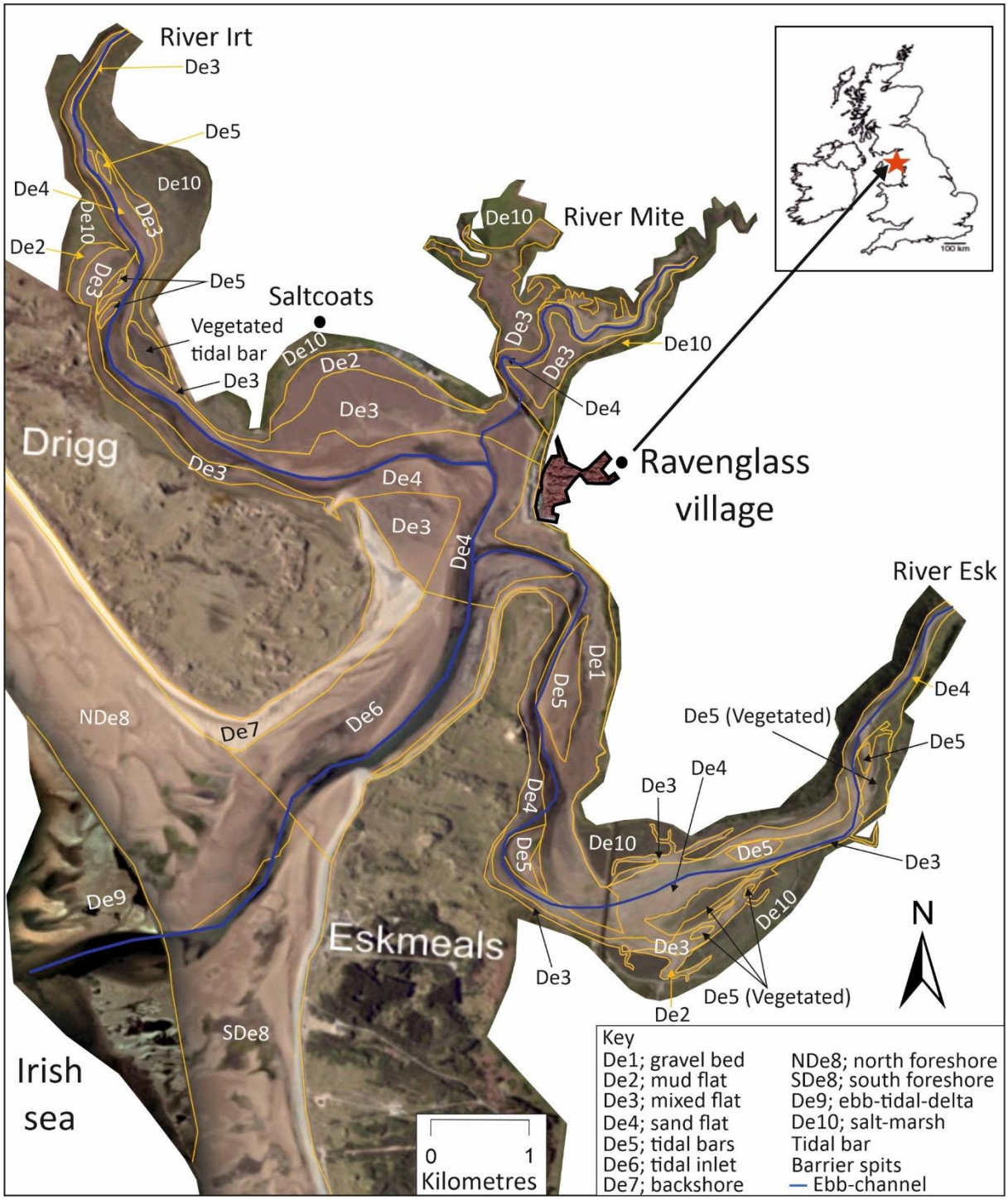

Figure 2.2; Distribution of estuarine sub-depositional environments mapped across the Ravenglass Estuary. These sub-depositional environments are labelled; De1, gravel bed; De2, mud flat; De3, mixed flat; De4, sand flat; De5, tidal bars; De6, tidal inlet; De7, backshore; De8, foreshore (northern and southern sites); De9, ebb-tidal delta; and De10, salt marsh.

Sedimentary deposits are fed into the estuary via the Rivers Mite, Irt and Esk. The sediments drain from a range of different bedrock types and Quaternary drift-deposits. The hinterland geology is comprised of Ordovician Borrowdale Volcanic Group (BVG), Devonian Eskdale Granite and Cambrian

Skiddaw Group slate; a small area of Triassic Sherwood Sandstone Group at the west of the drainage area is largely covered by drift. Quaternary drift-deposits are dominated by glacial diamicton, peat, and glacial-fluvial-lacustrine deposits (Griffiths et al., 2018; Griffiths et al., 2019a; Griffiths et al., 2019b; Merritt and Auton, 2000). Eskdale Granite-sourced sediment was transported into the estuary via the River Esk, while BVG andesite-sourced sediment was transported into the estuary via the River Irt (Daneshvar and Worden, 2017; Griffiths et al., 2018; Griffiths et al., 2019a; Griffiths et al., 2019b). The post-glacial, Holocene record represents approximately 10,000 years of deposition (McGhee et al., 2021). The estuary has been extensively studied in terms of sedimentary systems and processes, detrital clay mineralogy and distribution, detrital clay coat origin, mineralogy and distribution (Daneshvar, 2015; Daneshvar and Worden, 2017; Griffiths et al., 2018; Griffiths et al., 2019a; Griffiths et al., 2019b; Wooldridge et al., 2017a; Wooldridge et al., 2017b) and so represents an ideal field site to answer the research questions set out in the introduction.

2.4 Samples and Methods

2.4.1 Field-Based Mapping and Samples Collection

Based on geomorphological mapping criteria, together with the use of aerial imagery and grain size analysis, we have mapped eleven sub-depositional environments across the estuary (Figure 2.2). The sub-depositional environments are gravel beds, vegetated surfaces, barrier spits, tidal flats (sub-divided into mud flat, mixed flat and sand flat), tidal bars, tidal inlet, backshore, foreshore, ebb-tidal delta (Figure 2.2). The subdivision of tidal flats was based laboratory-derived sand percentages, modified from a scheme initially proposed by Brockamp and Zuther (2004), where: 90–100% sand is sand flat, 50–90% sand is mixed flat, and 15–50% sand is mud flat.

We sampled surface sediment (from <2 cm below the surface) from 497 sites covering the entire estuary and the coastal portion of the system (Figure 2.1). Sediment samples were placed in airtight plastic bags in the field and dried in the laboratory prior to geochemical pXRF analysis.

2.4.2 Grain Size Analysis

Grain size analysis was undertaken solely to differentiate the sediments of the tidal flats into mud-, mixed- and sand-flat sub-depositional environments. Grains <2 mm were separated from the sample using a sieve and then this fraction was analysed for grain size distribution using laser particle size analysis (LPSA) with a Beckman Coulter LS13 320 Counter. Organic matter was removed using established laboratory procedures for sample digestion. A small amount of Calgon was added to convert the dried sediment into a paste for mixing and homogenisation, prior to analysis (Simon et al., 2021). The LPSA data were analysed using GRADISTAT© to define grain size parameters of the sediment.

2.4.3 Multi-Element Analyses Using Handheld Niton +XL3t GOLDD pXRF Spectrometer

All sediment samples from the Ravenglass Estuary were analysed using a handheld Thermo Scientific Niton +XL3t GOLDD XRF spectrometer (pXRF) to measure the abundance of major, minor and trace elements. The pXRF equipment is a self-contained, energy dispersive XRF spectrometer with a variable intensity energy source (6–50 kV, 0–200 μA) Ag anode X-ray tube. It is equipped with a factory-calibrated, GOLDD (Geometrically Optimised Large Area Drift Detector) detection system, optimised by the manufacturer for low detection limits, and high-precision measurements of more than 40 elements. Sediment samples were prepared by air drying whole-sediment samples in a 50 mm Petri dishes which was then placed 2 mm from the pXRF detector. Problems of horizontal and vertical heterogeneity of the sample, variable moisture and surface roughness, associated with core-based, “point and shoot” pXRF studies (Carr et al., 2008; Chou et al., 2010; Gutiérrez-Ginés et al., 2013; Weindorf et al., 2012) have here been avoided (Argyraki et al., 1997).

Despite concentrations for 40 elements being reported by the pXRF, only 12 elements were present in all samples. These elements are Al, Si, K, Ca, Ti, Fe, Mn, Rb, Sr, Zr, Ba and Cs. Other elements were variably present at concentrations above the element-specific detection limit, but these could not

easily be incorporated into any scheme to interrogate the relationship between composition and the sub-depositional environment.

The reported limit of detections of the instrument for Al, K, Ca, Ti, Fe, Mn, Rb, Sr, Zr, Ba and Cs are listed in Table 2.1. The instrument's high precision and accuracy was validated by replicating the pXRF analysis, on a single sample 30 times, the average and standard deviation of Al, K, Ca, Ti, Fe, Mn, Rb, Sr, Zr, Ba and Cs are listed in Table 2.1. Each analysis was conducted, for 150 s, in "Test All GEO" mode; this combines mining and soil modes which thus permits the determination of major and trace elements. The optimum analysis time of 150 s was selected by repeating analysis of one sample for different replicate durations in order to identify when there was no significant improvement in the reported uncertainty.

Table 2.1; Factory reported detection limit for some key elements plus mean and standard deviations of one sample analysed 30 times to assess credibility of reported concentration data.

Element	Reported Detection Limit (ppm)	Mean of 30 Repeat Analyses from One Sample (ppm)	Standard Deviation of 30 Repeat Analyses from One Sample (ppm)
Al	2000	64,099	1685
K	250	18,234	145
Ca	70	2610	46
Ti	6	2477	92
Fe	25	11,837	90
Mn	30	172	19
Rb	6	70	1
Sr	8	73	2
Zr	3	352	3
Ba	50	487	18
Cs	12	85	4

2.4.4 Spatial Mapping

Spatial distribution maps of elements and element indices were generated using ArcGIS software, via an inverse distance weighted (IDW) interpolation function. The IDW approach has lower mean prediction errors and high correlations between predicted and measured values (Zarco-Perello and Simões, 2017). IDW was also selected to avoid the automatic generation of physically-meaningless negative concentrations, such as are produced by spline-based interpolation methods, and to avoid the formation of valleys or ridges (Watson and Philip, 1985). A polyline in ArcGIS was drawn down the long axes of the Drigg and Eskmeals spits, to separate the marine data from estuarine data when performing the interpolations (Griffiths et al., 2019a).

2.4.5 Statistical Multivariate Analysis

Multivariate statistical techniques are powerful tools commonly used to investigate variability in large datasets (Cheng et al., 2006; Grunsky and Smee, 1999; Klovan, 1966; Michael et al., 2013). Although we will display concentration maps of elements, there is a risk that all we will display is greater or smaller amounts of element dilution by SiO_2 due to variable quantities of the dominant mineral, quartz. To evaluate the more meaningful relative abundance of elements, we have calculated a range of indices (e.g., X/(X+Y)) and mapped these values. We choose not to use ratios as they vary from infinitely large to infinitely small; also, multi-order of magnitude ranges are difficult to map and present problems for machine learning approaches. We have avoided indices of elements that are strongly autocorrelated due to their geochemical similarity (e.g., K and Rb; Ca and Sr; Fe and Mn). We produced a correlogram (available on request) using R statistical software to identify the presence of strong element correlations (e.g., K and Rb) and to high-grade elements of the greatest non-correlation that reveal most about the geochemical variability of the estuary. The indices we have employed are: K/(K+Si), K/(K+Al), K/(K+Ca), K/(K+Ti), K/(K+Mn), K/(K+Sr), Sr/(Sr+Rb), Ca/(Ca+Fe), and Mn/(Mn+Sr); maps and boxplots of these indices will be presented. These elemental indices were selected as they were the ones that subsequent machine learning (recursive partitioning) employed

to differentiate sub-depositional environments (see later text in Section 2.6.3.2). However, we have also mapped the spatial distributions of Fe/(Fe+Ti), K/K+Fe) and Al/(Al+Fe), because Fe is of relevance to the understanding of Fe-clay minerals in the estuary.

2.4.5.1 ANOVA and Tukey's Post Hoc Test

Analysis of variance (ANOVA) tests were used in R statistical software (R Core Team, 2016), to investigate the statistical significance of geochemical differences between various pairs of sub-depositional environments. Following ANOVA, Tukey's post hoc honestly significant difference (HSD) test was then employed, using R statistical software (R Core Team, 2016), to determine which individual depositional environment were statistically different from one another as a function of elemental indices. The difference between each pair, for each elemental index, is defined as being significant if the "*p*" value is less than 0.05 (R Core Team, 2016; Scheffe, 1999).

2.4.5.2 Boxplots and Classification Trees

Univariate analysis of geochemical indices, split by the sub-depositional environment, was undertaken using boxplots produced using ggplot2 in RStudio (Wickham, 2016). The Recursive Partitioning and Regression Tree (RPART) package (Therneau and Atkinson, 2019), available in R statistical software (R Core Team, 2016), was used to characterise the sediment geochemical signatures (continuous data) into sub-depositional environments (categorical data). The RPART routine allows the development of a classification tree by using one or more variable (in this case, elemental indices) to find the optimum splits of the dataset, into different categories (e.g., sub-depositional environment) (Simon et al., 2021).

2.4.6 Holocene Cores

A sediment core was drilled through the Holocene succession in the tidal bar sub-depositional environment in the Esk arm of the inner Ravenglass Estuary, under tender by Geotechnical Engineering Ltd. (GEL) (McGhee et al., 2021). The core is nearly 5 m in length and was acquired with a Geotechnical Engineering Limited lightweight "Pioneer" rig. This rig was employed due to the soft nature of the sediment surface. The drilled core was retrieved in a series of 12 cm in diameter, and 1 m in length,

semi-rigid plastic liners for protection and easy transport. Each 1 m segment of the sediment core was sliced and photographed wet and air-dried for extensive study and subsequent analysis at the University of Liverpool. The core description involved detailed sedimentary logging of each core segment, at a scale of 1:5, and lithofacies were characterised in terms grain size, colour, sedimentary structures, bed thickness, presence of roots and shell fragments, bioturbation extent and type. The core was sampled at 5 cm intervals for pXRF and LPSA analyses, using techniques described above.

2.5 Results

Here, we present details of the distributions of sub-depositional environments in the Ravenglass Estuary and the absolute and relative distribution of elements.

2.5.1 Sub-Depositional Environments Present across the Estuary

The sub-depositional environments identified (Figure 2.2) across the Ravenglass Estuary are gravel beds (De1), tidal flats (sub-divided into mud flats, De2, mixed flats, De3, and sand flats, De4), tidal bars (De5), tidal inlet (De6), backshore (De7), foreshore (De8), ebb-tidal delta (De9), and salt marsh (De10). The subdivision of tidal flats was based on laboratory-derived laser particle size analysis data, with average grain size distribution curves for the mud, mixed and sand flats illustrated in Figure 2.3.

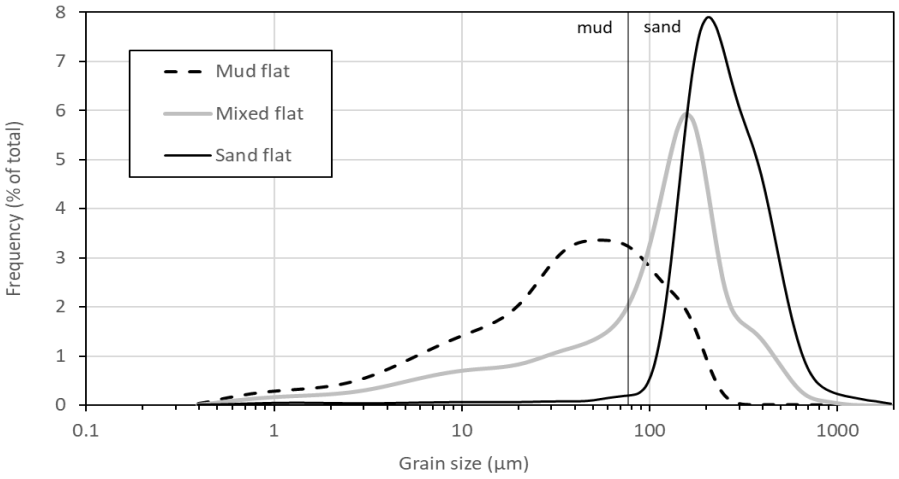

Figure 2.3; Frequency distribution curves of the mud, mixed and sand flat sub-depositional environments revealing how laser particle size analysis data were used to differentiate tidal flat sediments.

The inner estuary comprises: (a) gravel beds (De1), are locally distributed in the lower part of the Esk and Irt arms of the estuary and are dominated by a loose aggregate of rock fragments; (b) salt marsh (De10), is present in the Esk and Irt arms of the estuary and is dominated by salt-tolerant plants; (c) tidal bars (De5), are sand bars present in the intertidal zone, with a long axis oriented parallel to the direction of the main current; (d) sand flats (De4), are intertidal flats bordering the main channel; (e) mixed flats (De3), are sandwiched between sand mud flats; (f) mud flats (De2), are furthest away from the main channel (Figure 2.2).

The central estuary comprises: (a) sand flats (De4); (b) mixed flats (De3); (c) mud flats (De2); and (d) salt marsh (De10).

The outer estuary contains: (a) the main tidal inlet (De6) that cuts between the barrier spits; (b) foreshore (De8), is the part of the beach, that lies between the backshore and the mean-low-water line; and (c) backshore (De7), is situated above the mean-low-water line and can be inundated during spring tides and storm events. The foreshore has been split into north and south of the main channel (becoming NDe8 and SDe8), as these areas have texturally and geochemically distinct sediment.

2.5.2 Element Concentrations in the Ravenglass Estuary

The number of samples from each depositional environment that are above the detection limit is shown in Table 2.2. A summary of elements with their minimum reported values is presented in Table 2.3, where, for elements that have many samples below detection, the minimum reported value effectively represents the detection limit in Ravenglass surface sediments. The elements present in Ravenglass surface sediments include the major elements typically present in all samples: Al, Si, K, Ca, Fe, S and Ti. Minor elements (100 and 1000 ppm) include Cl, Mn, Rb, Zr, and Ba. These minor elements were detected in all samples. Trace elements (<100 ppm), present in Ravenglass sediments include P, Sc, V, Cr, Ni, Cu, Zn, As, Sr, Nb, Pd, Ag, Sn, Sb, Te, Cs, Hg, Pb, Bi, Th and U. These trace elements were detected in small to negligible quantities in some samples but were below detection in many samples (Tables 2.3 and 2.4).

Table 2.2; Summary of geochemical elements identified by the handheld pXRF tool and number of samples for which the element is above the limit of detection.

Sub-Environment	Samples	Al	Si	P	S	Cl	K	Ca	Sc	Ti	V	Cr	Mn
Foreshore	69	69	69	17	24	69	69	69	3	69	48	35	67
Gravel bed	28	28	28	10	18	28	28	28	4	28	17	19	26
Mixed flat	94	94	94	1	54	94	94	94	2	94	51	66	93
Mud flat	55	55	55	1	52	55	55	55	16	55	33	52	54
Ebb-tidal delta	21	21	21	9	20	21	21	21	2	21	6	7	20
Sand flat	120	120	120	0	28	120	120	120	1	120	102	40	113
Tidal bars	53	53	53	0	12	53	53	53	1	53	43	18	50
Tidal inlet	25	25	25	5	8	25	25	25	0	25	20	6	24
Salt marsh	17	17	17	17	17	17	17	17	5	17	14	11	17

Sub-environment	Samples	Fe	Ni	Cu	Zn	As	Rb	Sr	Zr	Nb	Pd	Ag
Foreshore	69	69	0	0	28	15	69	69	69	25	3	0
Gravel bed	28	27	0	1	23	13	28	28	28	14	0	0
Mixed flat	94	94	0	0	93	20	94	94	94	88	0	2
Mud flat	55	54	0	0	55	19	55	55	55	55	0	0
Ebb-tidal delta	21	21	0	0	14	2	21	21	21	4	4	0
Sand flat	120	119	0	0	76	12	120	120	120	69	0	0
Tidal bars	53	52	1	0	39	6	53	53	53	31	0	2
Tidal inlet	25	25	1	1	14	6	25	25	25	7	2	1
Salt marsh	17	17	8	1	17	16	17	17	17	13	2	3

Sub-environment	Samples	Cd	Sn	Sb	Te	Cs	Ba	Hg	Pb	Bi	Th	U
Foreshore	69	13	32	20	60	65	69	3	13	0	14	8
Gravel bed	28	11	17	10	28	28	28	0	13	1	14	3
Mixed flat	94	0	51	15	92	93	94	6	3	1	46	5
Mud flat	55	0	28	4	48	54	55	3	11	8	41	1
Ebb-tidal delta	21	17	21	19	21	21	21	0	19	0	5	1
Sand flat	120	0	64	27	106	118	120	2	2	1	7	6
Tidal bars	53	0	35	8	49	53	53	2	2	1	3	1
Tidal inlet	25	4	17	9	25	25	25	3	5	0	8	1
Salt marsh	17	16	17	17	17	17	17	1	17	3	15	7

Table 2.3; Summary of geochemical elements showing the minimum detected value of each element in the Ravenglass Estuary.

Elements.	**Al**	**Si**	**P**	**S**	**Cl**	**K**	**Ca**	**Sc**	**Ti**
Minimum value (ppm)	1246	56,322	119	90	266	2189	73	6	257
Samples above minimum value	100%	100%	12%	48%	100%	100%	100%	7%	100%
Elements	**V**	**Cr**	**Mn**	**Fe**	**Ni**	**Cu**	**Zn**	**As**	**Rb**
Minimum value (ppm)	44	20	52	2245	18	17	9	4	9
Samples above minimum value	69%	53%	96%	99%	2%	1%	74%	23%	100%
Elements	**Sr**	**Zr**	**Nb**	**Pd**	**Ag**	**Cd**	**Sn**	**Sb**	
Minimum value (ppm)	28	29	2	4	100	10	13	12	
Samples above minimum value	100%	100%	63%	2%	2%	13%	59%	27%	
Elements	**Te**	**Cs**	**Ba**	**Hg**	**Pb**	**Bi**	**Th**	**U**	
Minimum value (ppm)	30	10	93	6	5	5	3	6	
Samples above minimum value	93%	98%	100%	4%	18%	3%	32%	7%	

Table 2.4; Collation of some of the significance values resulting from the ANOVA analysis and Tukey's post hoc honestly significant difference (HSD) tests for the sand-dominated sedimentary environments. The following symbols presented here highlight the statistical significance; significant when $p < 0.05$ (*), very significant when $p < 0.01$ (**), and extremely significant when $p < 0.001$ (***). We have excluded differences that are marginally significant (when $p < 0.1$).

Sub-Environment	**Variable**	***p*-Value**	**Sub-Environment**	**Variable**	***p*-Value**
De3-De2	K/(K+Si)	0.0000000	De9-De4	K/(K+Ca)	0.0000007
De4-De2	K/(K+Si)	0.0000000	N-De8-De4	K/(K+Ca)	0.0000000
De5-De2	K/(K+Si)	0.0000000	S-De8-De4	K/(K+Ca)	0.0000000
De6-De2	K/(K+Si)	0.0000000	De6-De5	K/(K+Ca)	0.0000012
De9-De2	K/(K+Si)	0.0000000	De9-De5	K/(K+Ca)	0.0000044
N-De8-De2	K/(K+Si)	0.0000000	N-De8-De5	K/(K+Ca)	0.0000000
S-De8-De2	K/(K+Si)	0.0000000	S-De8-De5	K/(K+Ca)	0.0000000
De4-De3	K/(K+Si)	0.0000000	S-De8-De6	K/(K+Ca)	0.0041914
De5-De3	K/(K+Si)	0.0000000	S-De8-De9	K/(K+Ca)	0.0112902
De6-De3	K/(K+Si)	0.0000000	S-De8-N-De8	K/(K+Ca)	0.0001769

De9-De3	K/(K+Si)	0.0000000	De3-De2	K/(K+Ti)	0.0000007
N-De8-De3	K/(K+Si)	0.0000000	De4-De2	K/(K+Ti)	0.0000000
S-De8-De3	K/(K+Si)	0.0000000	De5-De2	K/(K+Ti)	0.0000000
De6-De4	K/(K+Si)	0.0033850	De6-De2	K/(K+Ti)	0.0000000
N-De8-De4	K/(K+Si)	0.0000060	De9-De2	K/(K+Ti)	0.0002649
N-De8-De5	K/(K+Si)	0.0000939	N-De8-De2	K/(K+Ti)	0.0000000
De4-De2	K/(K+Al)	0.0000000	S-De8-De2	K/(K+Ti)	0.0000084
De5-De2	K/(K+Al)	0.0000005	De4-De3	K/(K+Ti)	0.0000000
N-De8-De2	K/(K+Al)	0.0000000	De5-De3	K/(K+Ti)	0.0004749
De4-De3	K/(K+Al)	0.0000000	De6-De3	K/(K+Ti)	0.0018964
De5-De3	K/(K+Al)	0.0000132	N-De8-De3	K/(K+Ti)	0.0035633
De9-De3	K/(K+Al)	0.0039216	De3-De2	K/(K+Mn)	0.0000000
N-De8-De3	K/(K+Al)	0.0000000	De4-De2	K/(K+Mn)	0.0000000
De6-De4	K/(K+Al)	0.0000027	De5-De2	K/(K+Mn)	0.0000000
De9-De4	K/(K+Al)	0.0000000	De6-De2	K/(K+Mn)	0.0000000
S-De8-De4	K/(K+Al)	0.0000000	De9-De2	K/(K+Mn)	0.0000000
De9-De5	K/(K+Al)	0.0000000	N-De8-De2	K/(K+Mn)	0.0000000
S-De8-De5	K/(K+Al)	0.0000044	S-De8-De2	K/(K+Mn)	0.0000000
N-De8-De6	K/(K+Al)	0.0006158	De4-De3	K/(K+Mn)	0.0000000
N-De8-De9	K/(K+Al)	0.0000000	De5-De3	K/(K+Mn)	0.0086938
S-De8-N-De8	K/(K+Al)	0.0000001	De6-De3	K/(K+Mn)	0.0004807
De3-De2	K/(K+Ca)	0.0320513	N-De8-De3	K/(K+Mn)	0.0000001
De4-De2	K/(K+Ca)	0.0000000	De6-De2	K/(K+Sr)	0.0000000
De5-De2	K/(K+Ca)	0.0000000	De9-De2	K/(K+Sr)	0.0000000
De4-De3	K/(K+Ca)	0.0000000	N-De8-De2	K/(K+Sr)	0.0000000
De5-De3	K/(K+Ca)	0.0000000	S-De8-De2	K/(K+Sr)	0.0000000
S-De8-De3	K/(K+Ca)	0.0000884	De6-De3	K/(K+Sr)	0.0000000
De6-De4	K/(K+Ca)	0.0000001	De9-De3	K/(K+Sr)	0.0000000

Table 2.4. continued.

Sub-Environment	Variable	*p*-Value	Sub-Environment	Variable	*p*-Value
N-De8-De3	K/(K+Sr)	0.0000000	S-De8-De4	Ca/(Ca+Fe)	0.0000000
S-De8-De3	K/(K+Sr)	0.0000000	De6-De5	Ca/(Ca+Fe)	0.0002164
De6-De4	K/(K+Sr)	0.0000000	De9-De5	Ca/(Ca+Fe)	0.0000749
De9-De4	K/(K+Sr)	0.0000000	N-De8-De5	Ca/(Ca+Fe)	0.0000170
N-De8-De4	K/(K+Sr)	0.0000000	S-De8-De5	Ca/(Ca+Fe)	0.0000000
S-De8-De4	K/(K+Sr)	0.0000000	S-De8-De6	Ca/(Ca+Fe)	0.0013038
De6-De5	K/(K+Sr)	0.0000000	S-De8-De9	Ca/(Ca+Fe)	0.0116983
De9-De5	K/(K+Sr)	0.0000000	S-De8-N-De8	Ca/(Ca+Fe)	0.0000284
N-De8-De5	K/(K+Sr)	0.0000000	De3-De2	Mn/(Mn+Sr)	0.0059663
S-De8-De5	K/(K+Sr)	0.0000000	De4-De2	Mn/(Mn+Sr)	0.0000000
De6-De2	Sr/(Sr+Rb)	0.0015649	De5-De2	Mn/(Mn+Sr)	0.0000001
De9-De2	Sr/(Sr+Rb)	0.0000001	De6-De2	Mn/(Mn+Sr)	0.0000000
N-De8-De2	Sr/(Sr+Rb)	0.0000002	De9-De2	Mn/(Mn+Sr)	0.0000000
S-De8-De2	Sr/(Sr+Rb)	0.0063469	N-De8-De2	Mn/(Mn+Sr)	0.0000000
De6-De3	Sr/(Sr+Rb)	0.0002659	S-De8-De2	Mn/(Mn+Sr)	0.0000000
De9-De3	Sr/(Sr+Rb)	0.0000000	De4-De3	Mn/(Mn+Sr)	0.0000000
N-De8-De3	Sr/(Sr+Rb)	0.0000000	De5-De3	Mn/(Mn+Sr)	0.0220222
S-De8-De3	Sr/(Sr+Rb)	0.0019248	De6-De3	Mn/(Mn+Sr)	0.0000000
De6-De4	Sr/(Sr+Rb)	0.0000004	De9-De3	Mn/(Mn+Sr)	0.0000003
De9-De4	Sr/(Sr+Rb)	0.0000005	N-De8-De3	Mn/(Mn+Sr)	0.0000000
N-De8-De4	Sr/(Sr+Rb)	0.0000000	S-De8-De3	Mn/(Mn+Sr)	0.0000000
S-De8-De4	Sr/(Sr+Rb)	0.0367545	De5-De4	Mn/(Mn+Sr)	0.0105295
De6-De5	Sr/(Sr+Rb)	0.0000033	De6-De4	Mn/(Mn+Sr)	0.0009477
De9-De5	Sr/(Sr+Rb)	0.0000104	N-De8-De4	Mn/(Mn+Sr)	0.0000000
N-De8-De5	Sr/(Sr+Rb)	0.0000000	S-De8-De4	Mn/(Mn+Sr)	0.0001308
De9-De6	Sr/(Sr+Rb)	0.0000000	De6-De5	Mn/(Mn+Sr)	0.0000000
S-De8-De6	Sr/(Sr+Rb)	0.0000000	De9-De5	Mn/(Mn+Sr)	0.0238969
N-De8-De9	Sr/(Sr+Rb)	0.0000000	N-De8-De5	Mn/(Mn+Sr)	0.0000000
S-De8-N-De8	Sr/(Sr+Rb)	0.0000000	S-De8-De5	Mn/(Mn+Sr)	0.0000000

De4-De2	Ca/(Ca+Fe)	0.0000000	N-De8-De9	Mn/(Mn+Sr)	0.0161029
De5-De2	Ca/(Ca+Fe)	0.0000000	De3-De2	Ti/(Ti+Mn)	0.0135132
S-De8-De2	Ca/(Ca+Fe)	0.0041582	De4-De2	Ti/(Ti+Mn)	0.0000000
De4-De3	Ca/(Ca+Fe)	0.0000000	De5-De2	Ti/(Ti+Mn)	0.0064950
De5-De3	Ca/(Ca+Fe)	0.0000000	De6-De2	Ti/(Ti+Mn)	0.0016346
S-De8-De3	Ca/(Ca+Fe)	0.0001215	N-De8-De2	Ti/(Ti+Mn)	0.0000000
De6-De4	Ca/(Ca+Fe)	0.0002233	S-De8-De2	Ti/(Ti+Mn)	0.0473812
De9-De4	Ca/(Ca+Fe)	0.0000826	De4-De3	Ti/(Ti+Mn)	0.0085386
N-De8-De4	Ca/(Ca+Fe)	0.0000040	N-De8-De3	Ti/(Ti+Mn)	0.0076982

Maps of the distribution of elemental concentrations of major, minor and trace elements have been plotted to assess the distribution in relation to geographic location and sub-depositional environments. Maps of grain size, and the concentrations of Al, K, Ca, Ti, Fe, Mn, Sr, Rb, Zr, Ba and Cs are shown in Figure 2.4. The map showing grain size distribution across the estuary (Figure 2.4A) has had boundaries between sub-depositional environments from Figure 2.2 superimposed.

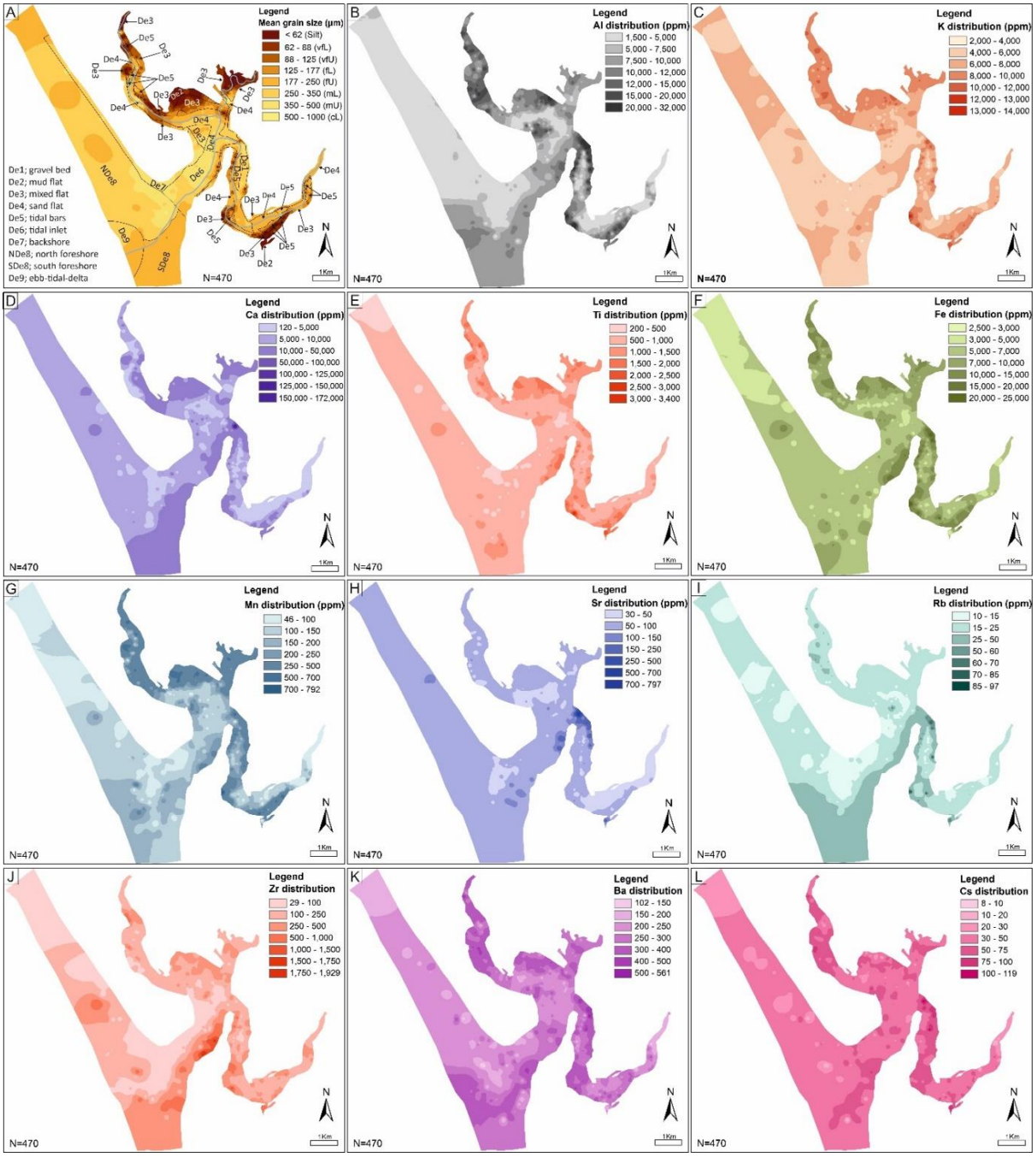

Figure 2.4; Spatial distribution of (A) grain size (mm), (B) aluminium, (C) potassium, (D) calcium, (E) titanium, (F) iron, (G) manganese, (H) strontium, (I) rubidium, (J) zirconium, (K) barium, (L) and caesium within the Ravenglass Estuary. Note that mean grain size decreases towards the margins of the inner estuary and central basin and the grain size map (**A**) has had boundaries between sub-depositional environments from Figure 2 superimposed. The similarities in spatial distribution between Al and K with finer grain size, show potential control of clay on the distribution of these elements. Aluminium, K, Fe, Ti and Mn are high across the inner estuary, upper reaches of Irt arm and tidal bars. Grain size as well as Al, Ca and Rb distribution are higher in the southern foreshore than the northern foreshore. The elements distribution pattern, as observed, vary greatly with some apparent links to sub-depositional environment and geographic location.

Grain size tends to increase down channel and decrease toward the margin of inner estuary and central basin (Figure 2.4A). The map of Al abundance (Figure 2.4B) has a marked similarity to the grain size map (Figure 2.4A). Aluminium is not homogeneously distributed between different sub-depositional environments (Figure 2.5B). Aluminium is present at elevated concentrations in the mud and mix flat environments (De2 and De3); aluminium is present at intermediate concentrations in the ebb-tidal delta and southern foreshore (De9, SDe8); aluminium is present at relatively low concentrations in the sand-dominated sand flat, tidal bar, tidal channel and northern foreshore environments (De4, De5, De6 and NDe8).

The spatial distributions of K and Fe are heterogeneous and have some similar features (Figure 2.4C,F). Potassium abundance decreases progressively toward the open sea and tends to be highest in tidal flat sediments; there is a relative increase in K abundance in the upper reaches of the northern foreshore (Figure 2.4C). Iron and Ti abundances also have some similarities as they have highest concentrations in tidal flats, tidal bars, and in <2 mm sediment from gravel beds. Overall, the relative abundance of Fe and Ti decreases progressively toward the open sea (Figure 2.4E,F). Potassium, Fe and Ti are unevenly distributed between different sub-depositional environments (Figure 2.5C,E,F). Potassium, Fe and Ti are present at elevated concentrations in the mud and mix flat environments (De2 and De3); they are present at relatively lower concentrations in all remaining sub-depositional environments (De4, De5, De6, NDe8, SDe8 and De9).

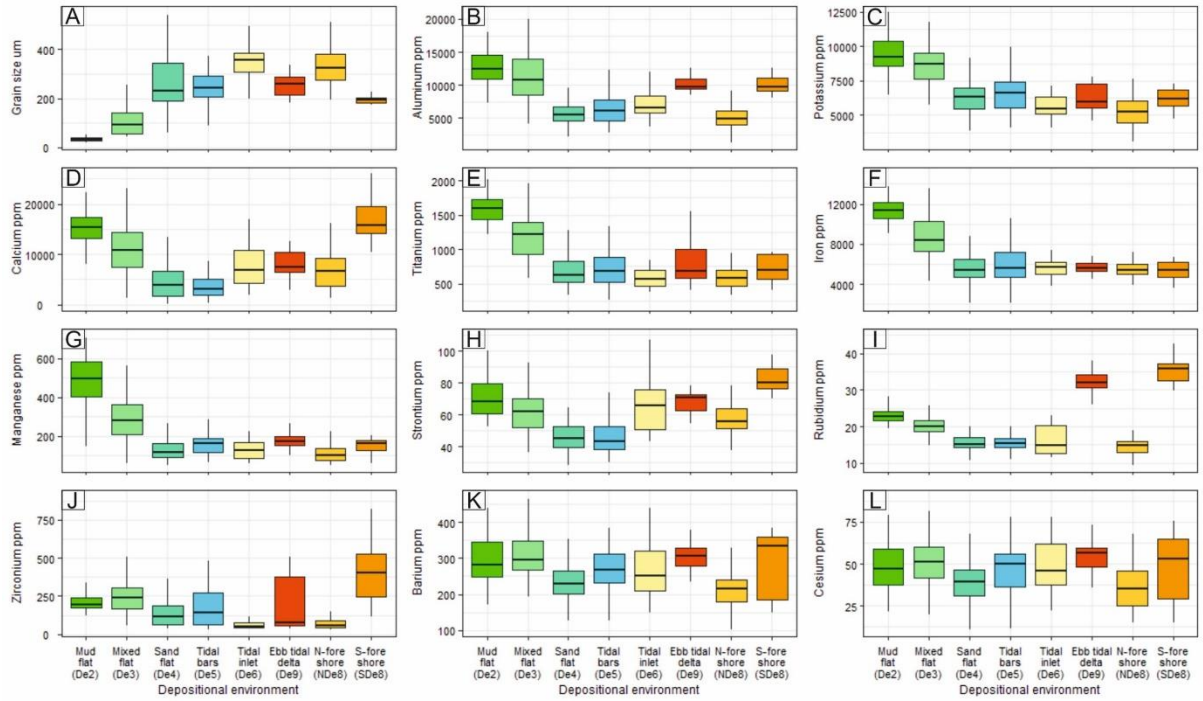

Figure 2.5; Boxplots for element concentrations as a function of the Ravenglass Estuary sub-depositional environment of (A) grain size (mm), (B) aluminium, (C) potassium, (D) calcium, (E) titanium, (F) iron, (G) manganese, (H) strontium, (I) rubidium, (J) zirconium, (**K**) barium, (**L**) caesium. Boxplots contain the median and upper and lower quartile ranges. Outliers are defined as > (or <) 1.5-fold the interquartile range, above the upper and below the lower quartiles. Element concentrations vary greatly between different sub-depositional environments; for example, Ti and Fe concentrations are highest in the mud flat, and Rb and Sr concentrations are highest in the southern foreshore. Overall, the element concentrations in the sand-dominated sub-depositional environments show weak variability, potentially because of quartz dilution.

The abundance of Ca in the Ravenglass Estuary sediment is heterogeneous; across the southern foreshore and tidal inlet and some pockets within the inner estuary and central basin, there is significant Ca enrichment (>10,000 ppm) (Figure 2.4D). Some of the highest concentrations of Ca (>100,000) are found in <2 mm sediment from gravel beds located at the boundary with the central basin and the upper Esk arm (Figure 2.4D). Boxplots show that calcium is not homogeneously distributed between different sub-depositional environments (Figure 2.5D). Calcium is present at elevated concentrations in the mud and mix flat environments and in the southern foreshore (De2, De3 and SDe8); calcium is present at intermediate concentrations in the tidal inlet, ebb-tidal delta, and northern foreshore (De6, De9, NDe8); calcium is present at relatively low concentrations in the sand-dominated sand flat and tidal bar environments (De4, De5).

The abundance of Mn is highest (200 to 700 ppm) in the upper and lower reaches of the Irt arm of the estuary, in the mud and mixed flats of the central basin and in the finer-grained parts of the upper and lower Esk arm (Figure 2.4G). Manganese is heterogeneous across the outer estuary with abundance broadly decreasing progressively toward the open sea. Manganese is unevenly distributed between different sub-depositional environments (Figure 2.5G). Manganese is present at elevated concentrations in the mud and mix flat environments (De2 and De3); manganese is present at relatively lower concentrations in all remaining sub-depositional environments (De4, De5, De6, NDe8, SDe8 and De9).

Strontium is mostly a trace element with concentrations <100 ppm across much of the estuary, but the <2 mm sediment from gravel beds has unusually high Sr concentrations (>700 ppm) (Figure 2.4H). Strontium is heterogeneously distributed between different sub-depositional environments (Figure 2.5H); the sub-environment distribution of strontium closely matches the distribution of calcium.

Rubidium is a trace element with relatively low concentration (<15 ppm) across the estuary except in the southern foreshore, part of the tidal inlet, gravel beds and margins of the upper Esk estuary, where the concentrations are highest and reach up to 70 ppm (Figure 2.4I). Rubidium is not uniformly distributed between different sub-depositional environments (Figure 2.5I). Rubidium is present at the highest concentrations in the ebb-tidal delta and southern foreshore (De9, SDe8); rubidium is present at intermediate concentrations in the mud and mixed flats (De2 and De3) and low concentrations in all other sub-depositional environments.

Zirconium varies from <100 to nearly 2000 ppm (Figure 2.4J). The most noteworthy aspects of the distribution of Zr are the high concentration along the southern part of the tidal inlet and southern foreshore and the low concentration along the northern part of the tidal inlet and northern foreshore. Like all other elements, zirconium is heterogeneously distributed between different sub-depositional environments (Figure 2.5J). Zirconium is present at the highest concentrations in the southern foreshore (SDe8).

Barium concentrations range from approximately 160 to 540 ppm (Figure 2.4K). Barium is present at the highest concentrations in parts of the Esk and Irt arms of the estuary, along the southern side of the tidal inlet and in the ebb-tidal delta. Barium concentrations do not seem to show any systematic pattern with the sub-environments of deposition (Figure 2.5K).

Caesium has a modal concentration of 35 to 50 ppm (Figure 2.4L). Caesium concentrations are slightly higher in the lower part of the Esk estuary, the upper part of the Irt estuary and along part of the southern side of the tidal inlet. Like barium, caesium concentrations (Figure 2.5L) do not seem to show any systematic pattern for the sub-environments of deposition.

We have here not mapped the distribution of Cl as it is wholly linked to halite precipitation from seawater and may reflect estuary water composition rather than sediment composition. Similarly, we have not mapped the distribution of sulphur as is it is present as a sulphate in the sediment and may be an evaporite mineral, like halite, or linked to Fe-sulphide oxidation.

2.5.3 Relative Element Concentrations

Maps displaying surface sediment characteristics, such as elemental concentration, are generally considered to be an important tool for sediment analysis (Reimann et al., 2011). However, elemental concentrations in quartz-rich sediment will be strongly influenced by the diluting effect of quartz (SiO_2) (Griffiths et al., 2019a), as this mineral is effectively pure SiO_2 and contains next to no trace elements. The element concentration maps (Figures 2.4B-H) will be strongly influenced by variable depletion and enrichment of quartz. However, the observation that not all the elemental concentration maps are identical (Figures 2.4B-H) suggests that there are meaningful differences in the sediment composition that are not due to variable depletion and enrichment of quartz.

The element index maps show that the spatial distributions of K/(K+Al) and K/(K+Mn) have some similar features (Figure 2.6A,D). The data from the index maps are summarised as a series of boxplots, displayed in Figure 2.7. K/(K+Al) and K/(K+Mn) increase progressively toward the open sea and tend

to be low in tidal flat sediments (Figures 2.6A,D; 2.7A,D). K/(K+Al) in the foreshore and tidal inlet is relatively lower in the north side than the south side. K/(K+Mn) has variable distribution in the upper reaches of both Esk and Irt arms, and in the outer estuary (Figure 2.6D).

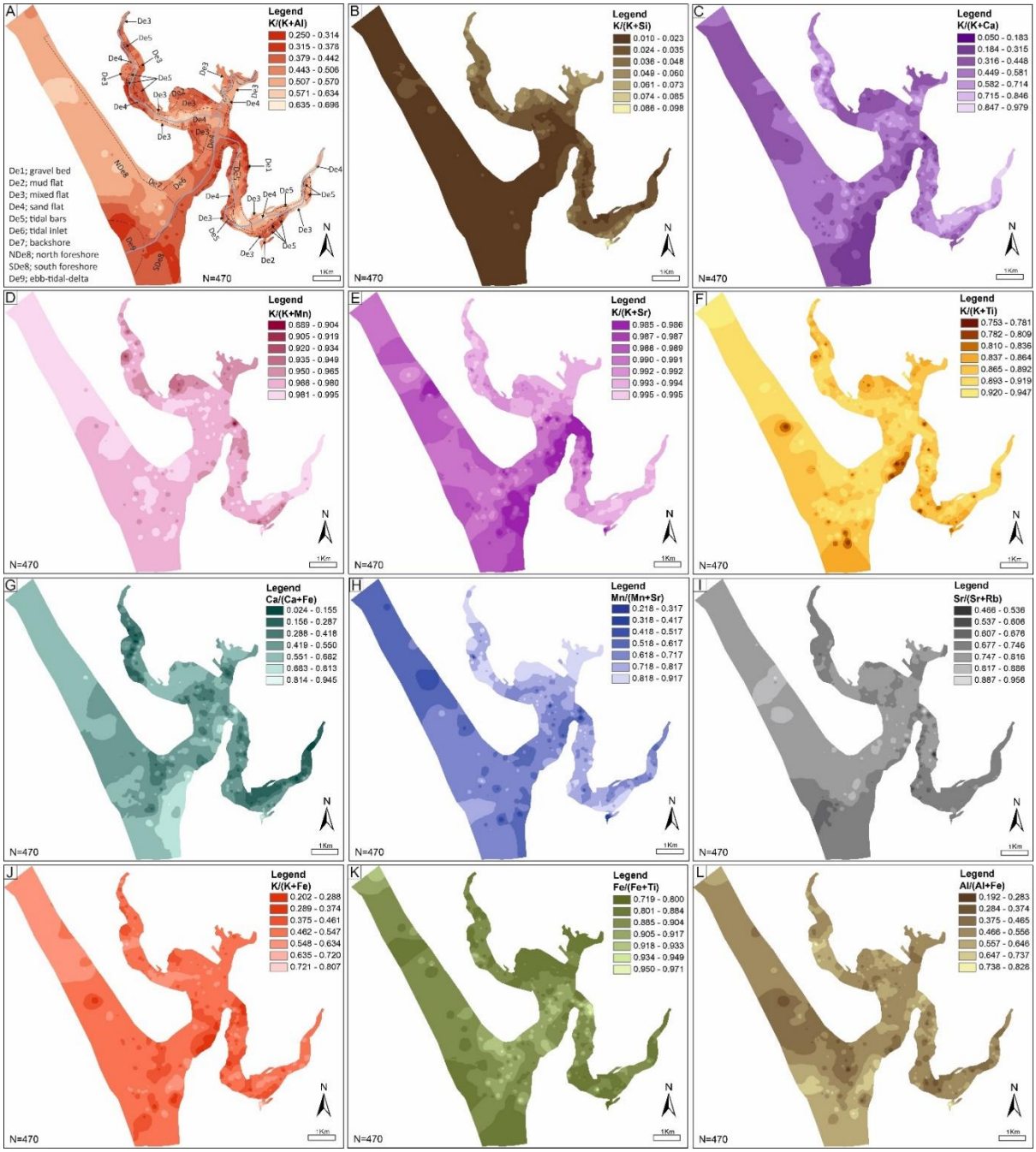

Figure 2.6; Spatial distribution of element indices (A) K/(K+Al), (B) K/(K+Si), (C) K/(K+Ca), (D) K/(K+Mn), (E) K/(K+Sr), (F) K/(K+Ti), (G) Ca/(Ca+Fe), (H) Mn/(Mn+Sr), (I) Sr/(Sr+Rb), (J) K/(K+Fe), (K) Fe/(Fe+Ti), and (L) Al/(Al+Fe) within the Ravenglass Estuary. Note that these element indices vary systematically for the Ravenglass Estuary sub-depositional environments. The combination of these elemental indices may be used to successfully discriminate mud flat, mixed flat, sand flat, tidal bars, tidal inlet, north foreshore, south foreshore and ebb-tidal delta in the Ravenglass Estuary. Maps A to I represent

the indices that RPART classification, in R Statistical Software, used to discriminate the various sub-depositional environments (see section 2.6.3.2).

K/(K+Si), K/(K+Sr), and Mn/(Mn+Sr) tend to decrease progressively toward the open sea and are highest in the inner estuary and central basin (Figures 2.6B,E,H, 2.7B,E,H). Sr/(Sr+Rb) has a narrow range of values, with most falling between 0.677 and 0.816, except along the upper reaches of both the Esk and Irt arms of the estuary, and in the ebb-tidal delta and south foreshore where it is low (Figure 2.6I).

K/(K+Ca) and K/(K+Ti) are quite variable across the study area (Figures 2.6C,G,F, 2.7C,G,F). K/(K+Ti) is low in a range of areas including the southern foreshore, ebb-tidal delta, the southern part of the main channel and the mixed and mud flats of the central basin and a few other sporadic localities (Figure 2.6F). K/(K+Ca) is highest in both the upper reaches of the Irt and Esk arms of the estuary; it is intermediate in the gravel bed, the middle part of the central basin, and the northern part of the tidal inlet and into the northern foreshore (Figure 2.6C).

Indices related to Fe concentration are variable across the estuary. The Ca/(Ca+Fe) index is lowest in both the upper reaches of the Irt and Esk arms of the estuary and it is intermediate in the mixed and mud flats of the central basin and much of the northern and southern foreshores (Figures 2.6G, 2.7G). The southern foreshore and parts of the southern side of the tidal inlet have the highest Ca/(Ca+Fe) index values (Figure 2.6G). K/(K+Fe), related to the Fe/K index used for clastic sedimentary rock geochemical classification by (Herron, 1988), shows that most values fall into an intermediate category (Figures 2.6J, 2.7J). The highest values are in the tidal bars of the Esk and Irt and at some localities within the foreshore and tidal inlet. Fe/(Fe+Ti), where both elements are mafic indicators, is highest in the middle part of the system, from the uppermost Esk arm through the northern part of the main channel (Figures 2.6K, 2.7K). This index is lowest in the southern foreshore, ebb-tidal delta, and mixed and mud flats of the Esk and Irt inner estuaries. Al/(Al+Fe) is lower in the Esk arm than the Irt arm of the estuary; it is also low in parts of the northern foreshore (Figure 2.6L). Al/(Al+Fe) is highest in the southern foreshore, the ebb-tidal delta and parts of the Irt arm of the estuary (Figure 2.6L).

2.5.4 Holocene Cores

Based on the sedimentary log of the geotechnical core (McGhee et al., 2021), mud and sand are the dominant lithologies in the tidal bar in the Esk arm of the estuary (Figure 2.8). This sand-dominated core has a narrow grain size range. The core was drilled into a vegetated tidal bar (fresh marsh) sub-depositional environment at the surface; the uppermost part down to 100 cm in depth is dominated by mud to very fine sand (Figure 2.8). Below this depth, most of the sediment is composed of different units of medium- and coarse-grained sand that may represent mixed fluvial-tidal deposits (McGhee et al., 2021). The specific sedimentary sub-depositional environments, in this core drilled into a vegetated tidal bar, could not have been automatically predicted as there is a range of grains sizes (gravel beds through to mud-dominated sediment) not typical of vegetated tidal bars. The Holocene core was analysed using the pXRF spectrometer, and the nine key indices used to classify the sediment (and see Figures 2.6 and 2.7) are shown with critical cut-off values marked by dashed lines.

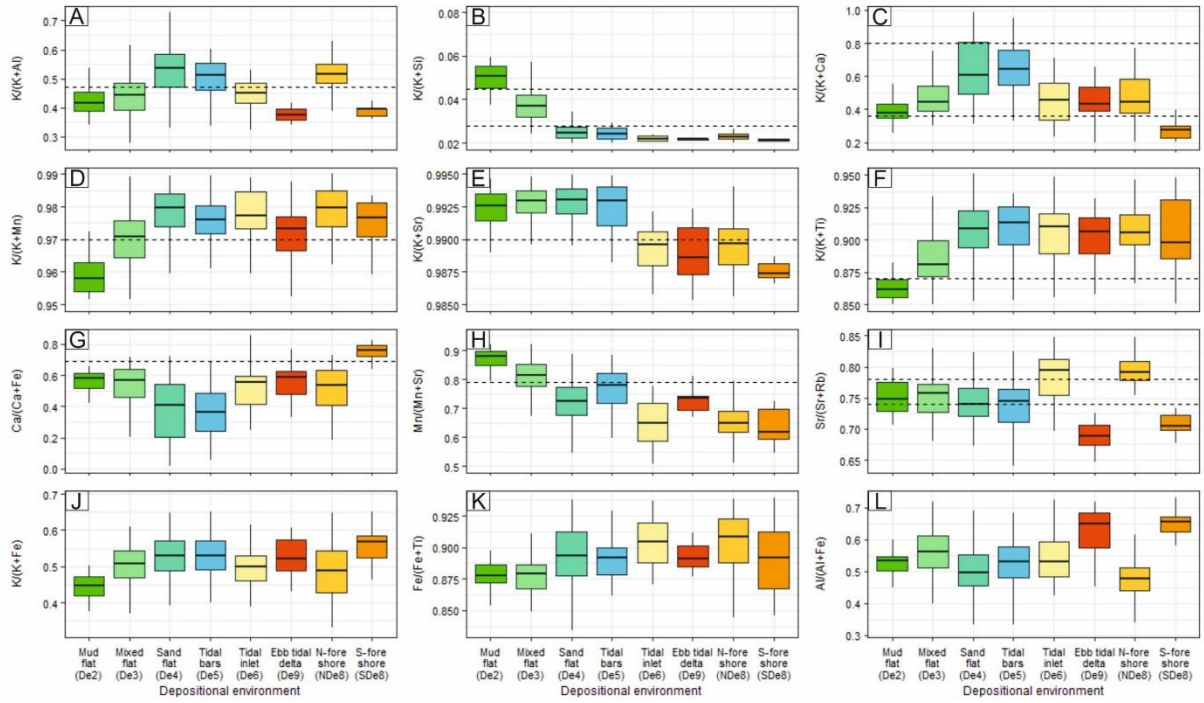

Figure 2.7; Box plots for element indices as a function of the Ravenglass Estuary depositional environment. (A) K/(K+Si), (B) K/(K+Ca), (C) Mn/(Mn+Sr), (D) K/(K+Al), (E) K/(K+Mn), (F) K/(K+Ti), (G) K/(K+Sr), (H) Sr/(Sr+Rb), (I) Ca/(Ca+Fe), (J) Ti/(Ti+Mn), (**K**) Fe/(Fe+Ti), and (**L**) Al/(Al+Fe). Boxplots contain the median and upper and lower quartile ranges. Outliers are defined as > (or <) 1.5-fold the interquartile range, above the upper and below the lower quartiles. This figure should be examined in conjunction with Table 2.4 to reveal the most important differentiators between sub-depositional

environments. The critical values for parts A to I have been taken from the machine learning-derived decision nodes (see section 2.6.3.2).

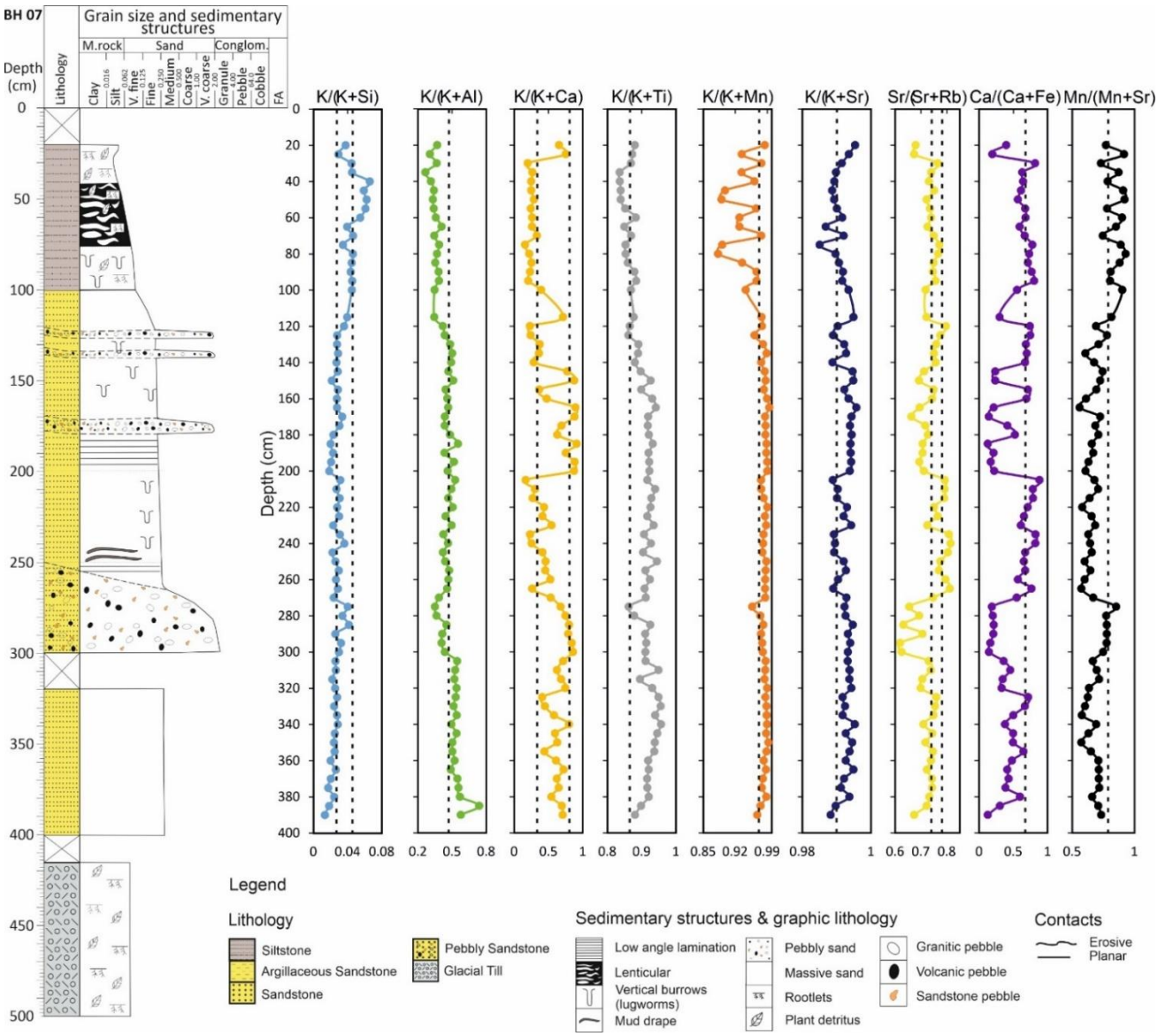

Figure 2.8; Sedimentary log of the 5 m Holocene core drilled in the tidal bars along to the Esk Arm of the Ravenglass Estuary with the geochemical data, derived from XRF analysis, illustrated. These nine indices are represented here as these are the ones that RPART classification, in R Statistical Software, used to discriminate the various sub-depositional environments (e.g., section see section 2.6.3.2and Figure 2.9). The critical values superimposed on the nine indices, were taken from machine learning-derived decision nodes in Figure 2.9.

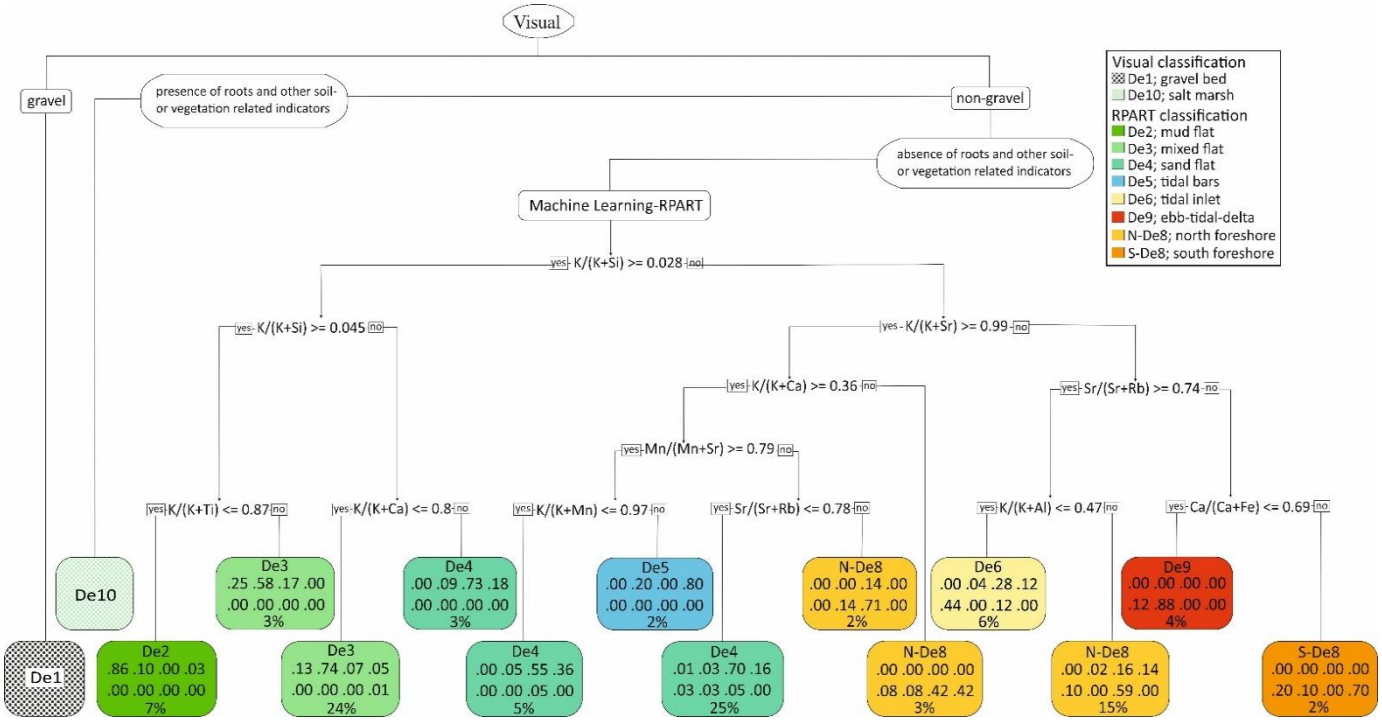

Figure 2.9; Classification tree for the discrimination of estuarine sub-depositional environments, based on surface samples collected from the Ravenglass Estuary, developed through a combination of visual analysis (Figure 2.2) and pXRF analyses, using supervised classification and the recursive partitioning package, RPART (Therneau and Atkinson, 2019), available in R studio software (R Core Team, 2016). Each machine learning-derived decision node splits the data using one data (chemical index) type. In each leaf node, the classification of depositional environment is listed first, followed by the quantity of samples in the classified depositional environment, this is presented as a fractional quantity; the higher the fractional quantities, the higher the classification certainty, the value presented at the bottom of the node is the total percentage of the whole sample set that lies in each leaf node. This RPART-supervised machine learning approach differentiated De2, De3, De4, De5, De6, NDe8, SDe8 and De9 based on multi-element analyses of K/(K+Si), K/(K+Al), K/(K+Ca), K/(K+Ti), K/(K+Mn), K/(K+Sr), Sr/(Sr+Rb), Ca/(Ca+Fe), and Mn/(Mn+Sr) index data. In each leaf node, the fraction of samples in that specific classification category are listed as fractional quantity and where these fractional values are less than 1.00, the uncertainty is because of some depositional environments having an overlapping attribute, even when nine dimensions are considered. This classification tree has a model accuracy of 72.3% (Figure 2.10).

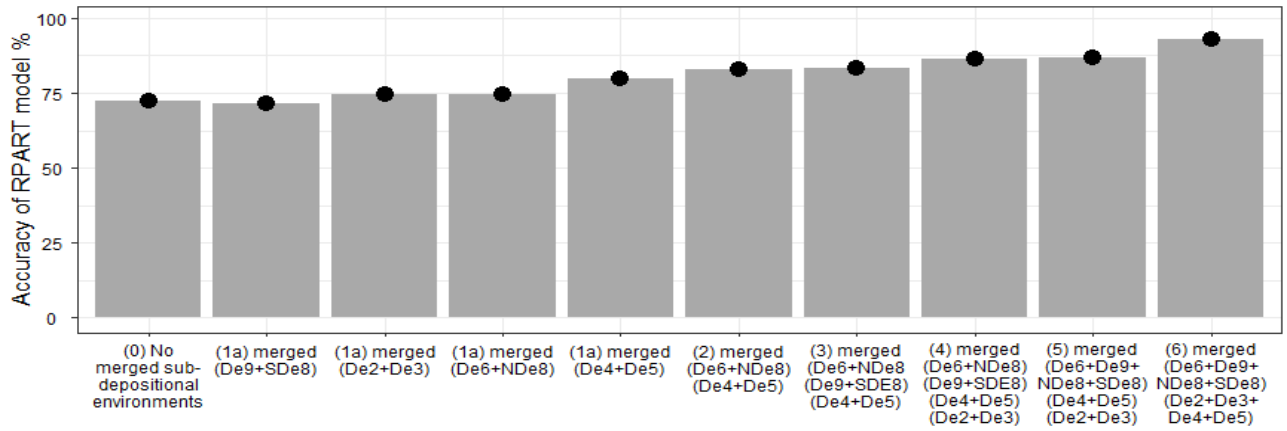

Figure 2.10; Bar chart showing model accuracy for different approach of classification trees. High model accuracy can be achieved by engineering the datasets, through selective merging of neighbouring sub-depositional environments.

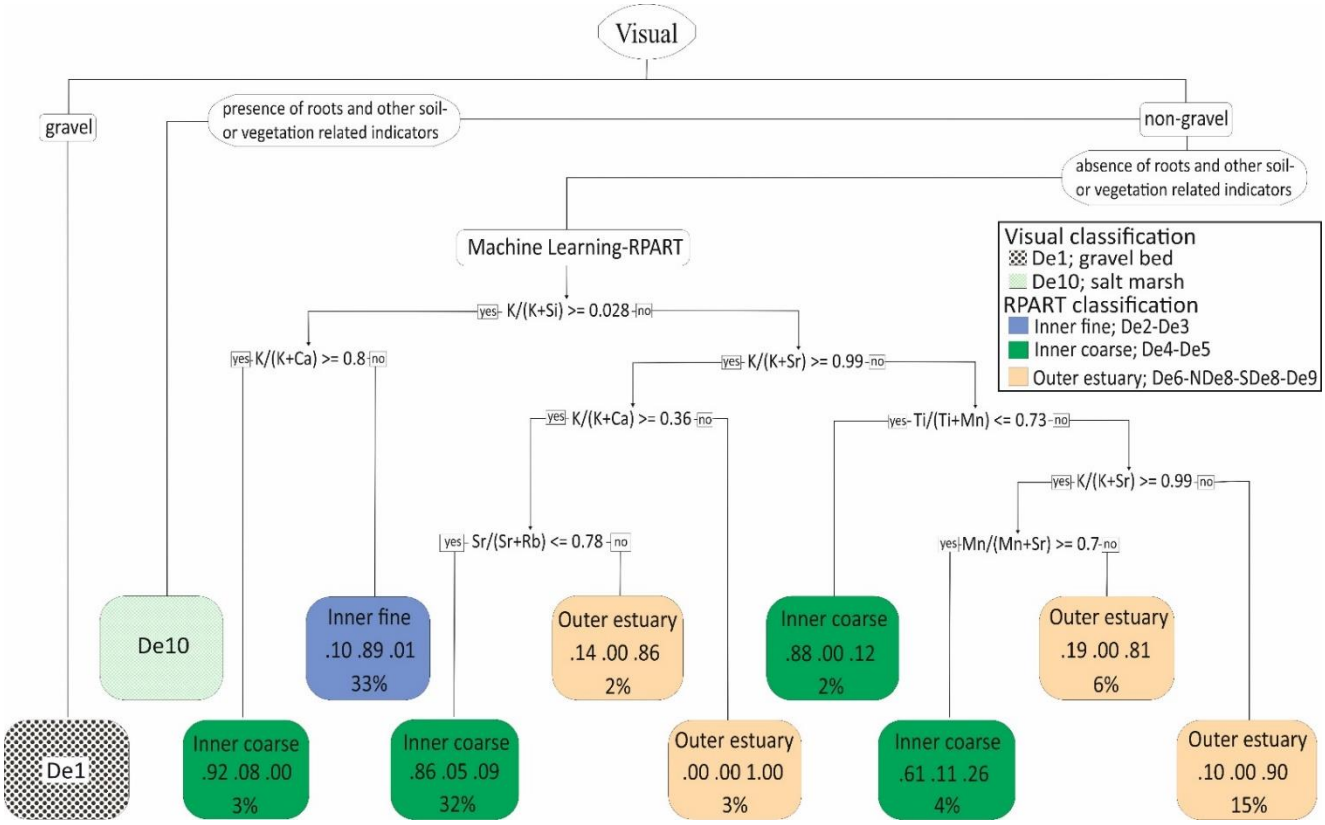

Figure 2.11; Classification tree based on partly merged data, developed using the same approach as Figure 2.10. This classification tree has a model accuracy of 87.0% (Figure 2.10) and shows how high model accuracy can be achieved with subsequent grouping of neighbouring or near neighbouring, sub-depositional environments.

2.6 Discussion

The primary aim of this study was to determine the ability of pXRF data to discriminate sedimentary environment in an estuarine setting. To ascertain how elemental data can be used to predict sub-depositional environments, parameters such as sediment source areas, and the statistical relationship between element concentrations and sub-environment, will be evaluated and discussed.

2.6.1 Elemental Distribution in the Ravenglass Estuary

One of the aims of this research was to understand the controls on the distribution of elements across an entire estuarine system. This is of interest to clastic sedimentary geologists, especially those who work with rock properties, because elemental distribution reflects, and potentially controls, mineral distribution via clay synthesis, Fe-reduction and silica precipitation (Aller and Michalopoulos, 1999;

Daneshvar and Worden, 2017; Michalopoulos and Aller, 1995; Michalopoulos et al., 2000; Nelson, 1960).

The distributions of Al, K, Ca, Ti, Fe, Mn, Sr, and Rb, as well as Zr, Ba and Cs in the sediment of the Ravenglass Estuary vary greatly with some apparent links to sub-depositional environment and geographic location (Figure 2.4). For example, Al and K display similar maps of concentration patterns (Figure 2.4B,C). Aluminium and K are present at the highest concentrations in the finest-grained sediments of the mud and mixed flat sediment (De2 and De3) and are present at the lowest concentrations in coarsest-grained sediments of the northern foreshore and parts of the tidal inlet (De6 and NDe8) (Figure 2.4A–C). Aluminium sits predominantly in the detrital minerals K-feldspar, muscovite, plagioclase, and in the dominant clay mineral, illite, with lesser quantities of detrital biotite and chlorite and weathering-related kaolinite (Griffiths et al., 2019a). Potassium sits predominantly in K-feldspar, muscovite, and illite with lesser quantities in biotite (Griffiths et al., 2019a). The distribution patterns of Al and K are almost certainly controlled by illite clay distribution as they are present at the highest concentrations in the finest-grained sediment (Figure 2.4A–C). Conversely, if Al and K were largely controlled by K-feldspar distribution, then the highest concentrations of these elements would be in the coarser sedimentary sub-depositional environments. The dominant role of weathering-related illite in controlling Al and K distribution reveals the important role of chemical weathering in the hinterland. Rubidium has similar geochemical properties to K, in terms of ionic radius and charge (Krauskopf and Bird, 1967), and the two elements seem to have broadly similar distributions in the estuary (Figure 2.4I), although the concentration of K is high in the mixed and mud flats (Figure 2.4C) whereas the concentration of Rb is relatively low, possibly indicating that Rb is partly controlled by variable K-feldspar as well as illite abundance (given that mixed and mud flats are the finest-grained sediment in the estuary (Figure 2.4A).

Iron, Mn and Ti concentrations display some similarities in terms of their mapped distributions at Ravenglass (Figure 2.4E–G). Iron, Mn and Ti are present at the highest concentrations in the finest-

grained sediments of the mud and mixed flat sediment (De2 and De3) and are present at the lowest concentrations in coarsest-grained sediments of the foreshore, tidal inlet, tidal bar (De5, De6, SDe8, NDe8, and De9) (Figures 2.4A,E–G and 2.5E–G). Iron and Mn have similar geochemical properties, as they can have a similar ionic radius and charge (when divalent) but they both have variable oxidation states and probably exist in the Ravenglass sediment in a combination of divalent ions within detrital lithic grains and minerals (e.g., chlorite and biotite) (Griffiths et al., 2019a) and in higher valence states in weathering products such as hydroxides (Daneshvar, 2015). Fe is observed to be preferentially concentrated in the upper reaches of the Ravenglass Estuary, confirming that fluvially-transported iron is trapped at the site of mixing between river water and seawater (Worden et al., 2020a). In contrast, Ti can sit in ilmenite and rutile (and other oxides) or as a trace element in mica minerals. In the Ravenglass Estuary surface sediments, the rutile concentration is approximately 0.40% in mud and mixed flats and approximately 0.10% in the sand-dominated environments (Wooldridge et al., 2019a). The increase in Ti in the finest-grained sediments is therefore likely to be due to rutile as well as mica minerals (illite, muscovite and biotite) (Figure 2.4A,E).

Calcium displays a strongly variable distribution (Figure 2.4D). The concentration of calcium closely matches the distribution of $CaCO_3$ (calcite and aragonite) (Griffiths et al., 2019a). $CaCO_3$ is largely found as bioclastic material, including as 10 cm shells in the gravel beds on the lower Esk Estuary and the southern side of the tidal inlet. Strontium has similar geochemical properties to calcium and is present in carbonate minerals, especially aragonite. However, the relationship between Ca and Sr maps is not especially strong (Figure 2.4D,H). Strontium seems to display a weak relationship with Ravenglass sub-depositional environments but there are some pockets of local enrichment, especially in gravel-rich sediment deposits, potentially due to their present in lithic fragments (Andrew-Oha et al., 2017; Brookins, 1988), and shell fragments possibly due to Sr–Ca association, as Sr can substitute for Ca in carbonates (Baker et al., 1982).

Zirconium is probably only present in the mineral zircon. The distribution of Zr reveals the distribution of zircon (Figure 2.4J). The map of Zr (Figure 2.4J) seems to follow the inverse of the grain size map, with the lowest concentrations of Zr in the coarsest-grained sands (Figure 2.4A). Barium might be present substituting for K in detrital K-feldspar or possibly in barite. Caesium may also substitute for K in micas and feldspars. Barium and Cs have similarly bland distribution maps (Figure 2.4K,L), with most values varying tightly about the modal value, with the lowest concentrations in the coarsest-grained sands (Figure 2.4A). Variable dilution by quartz may be responsible for much of the variation in Zr, Ba and Cs.

2.6.2 Relationship between Element Indices and Sub-Depositional Environment

One of the problems with element concentration maps is that they are strongly influenced by variable dilution by quartz and, perhaps to a lesser extent, calcite. Given that quartz has negligible trace elements, doubling the quantity of quartz would halve the concentration of a trace element, all other factors remaining the same. We therefore consider that relative element concentrations are more useful to understanding the relationship between sediment supply, weathering intensity, etc., and the sub-depositional environment (Rothwell and Croudace, 2015). Element indices have been analysed in terms of the sub-depositional environment as these will be useful for developing a quantitative classification tool.

K/(K+Al) is low in mud flats, ebb-tidal delta, and southern foreshore sub-environments (De2, De3, De9 and SDe8) (Figure 2.7A). It is highest in sand flat, tidal bar and northern foreshore sediment sub-environments (De4, De5 and NDe8). It has intermediate values in mixed flat and tidal inlet environments (De3 and De6). In these sediments, the K/(K+Al) index reflects the relative concentrations of K-feldspar, illite (and muscovite) and kaolinite (there is no gibbsite in these sediments); high values imply more K-feldspar, low values imply more kaolinite and illite.

K/(K+Si) simply reflects dilution, by quartz, of the collection of K-bearing minerals (K-feldspar, illite, muscovite and, to a lesser extent, biotite). This index is highest in the least quartz-rich, most fine-

grained mud flat sediments (De2) (Figure 2.7B). It has consistently low values in the sand-rich sub-depositional environments (De4–De9) and an intermediate value in mixed flats (Figure 2.7B). Every other element indexed to silicon looks like Figure 2.7B, reflecting variable dilution by quartz; we have chosen not to replicate such distributions as they all show the same pattern and do not help to further discern the sub-depositional environment. Silicon and its element indices seem to have minimal value to this study of estuarine sub-depositional environments.

K/(K+Ca) is low in mud flats and southern foreshore sub-environments (De2, De3, SDe8) (Figure 2.7C). It is highest in sand flat and tidal bar sub-environments (De4, De5). It has intermediate values in mixed flat tidal inlet, northern foreshore, and ebb-tidal delta sub-environments (De3, De6, NDe8, De9). In these sediments, the K/(K+Ca) index reflects the relative concentrations of K-bearing K-feldspar, illite (and muscovite) compared to carbonate concentrations. As K is broadly consistent in all sand-dominated sub-environments (Figure 2.5C), the variation in K/(K+Ca) in these sandy sediments is largely due to variations in Ca (Figure 2.5D) and therefore $CaCO_3$ minerals.

K/(K+Mn) is low in mud flats (De2) (Figure 2.7D). It is highest in sand flat, tidal bar, tidal inlet, and northern and southern foreshore (De4, De5, De6, NDe8, SDe8) sub-environments. It has intermediate values in mixed flat tidal inlet and ebb-tidal delta sub-environments (De3, De9). In these sediments, the K/(K+Mn) index (Figure 2.7D) reflects the subtle changes in the relative concentrations of K-bearing K-feldspar, illite (and muscovite) (Figure 2.5C) compared to mafic minerals and/or Mn oxides and hydroxides (Figure 2.5G). K/(K+Ti) resembles the boxplot distribution of K/(K+Mn) (Figure 2.7D,F), which suggests that Ti and Mn come from the same mafic sources.

K/(K+Sr) is uniformly high in inner estuary mud, mixed and sand flats and tidal bar sub-environments (De2, De3, De4, De5) (Figure 2.7E). It is lowest in mid and outer estuary tidal inlet, northern and southern foreshore, and ebb-tidal delta (De6, NDe8, SDe8, De9) sub-environments. In these sediments, the K/(K+Sr) index (Figure 2.7D) reflects the subtle changes in the relative concentrations of K-bearing K-feldspar, illite (and muscovite) (Figure 2.5C) compared to Sr-bearing carbonate minerals

(Figure 2.5H). K/(K+Sr) better differentiates inner and outer estuarine sub-environments than either K or Sr on their own (Figures 2.5C,H,E). Mn/(Mn+Sr) resembles the boxplot distribution of K/(K+Sr) (Figures 2.7E,H), which suggests that Sr dilution is an important discriminator in these sediments.

Ca/(Ca+Fe) is lowest in sand flat and tidal bar sub-environments (De4, De5) (Figure 2.6G). It is highest in southern foreshore sediment (SDe8) and intermediate in all other sub-environments (De2, De3, De6, NDe8, De9). The Ca/(Ca+Fe) index reflects subtle variations in the amount of Ca and therefore $CaCO_3$ minerals (Figure 2.5D) and iron in mafic minerals and oxides and hydroxides (Figure 2.5G).

Sr/(Sr+Rb) is lowest in ebb-tidal delta and southern foreshore (De9, SDe8) (Figure 2.7I). It is highest in tidal inlet and northern foreshore (De6 and NDe8), showing that this index is a good differentiator of the two parts of the lower estuary/marine part of the system. The inner estuary sub-environments have intermediate values (De2, De3, De4, De5).

K/(K+Fe) (Figure 2.7J), related to the K/Fe ratio used by (Herron, 1988) for log-based clastic identification, has a similar, but more muted, pattern than, K/(K+Mn). The latter will thus prove to be better at discriminating sub-environments. Fe/(Fe+Ti) (Figure 2.7K), composed of two mafic-associated elements, has a limited range of overlapping values with highest values in the tidal inlet and northern foreshore sub-environments (De6, NDe8), lowest values in the mud and mixed flat sub-environments (De2, De3) and intermediate for all other sub-environments (De4, De5, De9, SDe8).

Al/(Al+Fe) (Figure 2.7L) has high values in ebb-tidal delta and southern foreshore sub-environments (De9, SDe8) and low values in the northern foreshore sub-environments (NDe8) but similar and overlapping values in all other sub-environments (De2, De3, De4, De5, and De6).

2.6.3 Multi-Element Analyses in Discriminating Estuarine Sub-Depositional Environments

The application of compositional geochemical signatures in the classification of sediments for the interpretation of large-scale depositional environments has been widely reported (Armstrong-Altrin et al., 2015; Calvert and Pedersen, 2007; Doerner et al., 2020; Driskill et al., 2018; Hatch and Leventhal,

1992; Rübsam, 2019; Vaalgamaa and Korhola, 2007). However, the use of major and trace element compositional data has not been used to differentiate *sub*-depositional environments.

Here, we have developed a new technique for the independent classification of sedimentary sub-environment using bulk compositional data. Given that the classification scheme is intended for application to core samples, or poorly-defined depositional environment, we have elected to initially discriminate gravel beds (De1) and salt marsh (De10), as this can be achieved by inspecting any core for the obvious presence of gravel and roots. Additionally, aeolian sediment (De11) is excluded because of its poor preservation potential in estuarine sedimentary systems (Mountney and Thompson, 2002). We have used element indices (Figure 2.6) and supervised machine learning (RPART) with natural splits in the indices illustrated by the dashed lines superimposed on boxplots (Figure 2.7) to develop an automated way to determine sub-environments based on pXRF-derived compositional data (Figures 2.4 to 2.7).

2.6.3.1 ANOVA and Tukey's Post Hoc Test to Differentiate Estuarine Sub-Depositional Environments

To establish whether there are statistically significant differences in index values between pairs of sub-depositional environments, we have employed analysis of variance (ANOVA) and Tukey's post hoc honestly significant different (HSD) statistical tests using R (R Core Team, 2016). The statistical significance of a difference is defined by the derived "*p*" values: $p > 0.1$ represents an insignificant difference, $p < 0.05$ represents a significant difference, $p < 0.01$ represents a very significant difference, and $p < 0.001$ represents an extremely significant difference (R Core Team, 2016; Scheffe, 1999). Table 2.4 presents *p*-values based on elemental index values that indicate statistically significant geochemical differences between pairs of sub-depositional environments.

2.6.3.2 Development and Application of a Classification Diagram Using a Supervised Machine Learning Approach (RPART)

The results of the statistical ANOVA and HSD tests (Table 4) can also be visualised using the boxplots in Figure 2.7 (Hintze and Nelson, 1998; Hullman et al., 2015). We have here illustrated boxplots of the key indices K/(K+Si), K/(K+Ca), Mn/(Mn+Sr), K/(K+Al), K/(K+Mn), K/(K+Ti), K/(K+Sr), Sr/(Sr+Rb), and Ca/(Ca+Fe), all of which will be used to differentiate the estuarine sub-depositional environment (Figure 7).

The combination of initial visual discrimination of gravel beds and root-bearing salt marsh, followed by the use of numerous element indices via a supervised machine learning approach, in the form of recursive partitioning (RPART), has led to a new quantitative classification approach to discriminate sub-depositional environments in an estuarine setting.

The RPART package (Therneau and Atkinson, 2019), available in R statistical software (R Core Team, 2016), was employed to classify the geochemical signatures of sediments into sub-depositional environments. We employed Recursive Partitioning and Regression Tree (RPART) software in R to develop a classification tree by using elemental indices to find best splits for the data set into different surface sub-depositional environments that are present in the Ravenglass Estuary. A similar approach was employed by Simon et al. (2021) to subdivide sediment textural data from the Ravenglass Estuary. It was hoped that the geochemical data might lead to an improved classification compared to the textural data; note that the risk of closed datasets (Aitchison, 1982), has here been circumvented by using element indices.

Classification trees, derived by machine learning, create quantitative decision node split-points for a given index. The software establishes the dominant discriminators; these sit highest up the tree. At the end of each branch, there is either another decision node or a terminal leaf node. For each terminal leaf node, the software states the sub-depositional environment that has the highest probability (i.e., the “answer”), but it also lists the fractional probability of each sub-depositional

environment in the order in which they are listed in the key. The percentage of all samples in that terminal leaf node is also stated.

The RPART-supervised machine learning approach (Figure 2.9) selected decision nodes of the following elemental indices to achieve a supervised classification: K/(K+Si), K/(K+Al), K/(K+Ca), K/(K+Ti), K/(K+Mn), K/(K+Sr), Sr/(Sr+Rb), Ca/(Ca+Fe), and Mn/(Mn+Sr). Initially, we trained the model to identify all eight sub-depositional environments—De2, De3, De4, De5, De6, NDe8, SDe8 and De9. In each leaf node (Figure 2.9), the proportion of the data in each category is listed as a fractional value. The terminal node is named after the category with the highest fraction. The classification is most successful when the highest fractional values in each terminal node are close to 1.00. Values are less than 1.00 when there are overlaps in the geochemical attributes of two or more sub-depositional environments.

The decision nodes each relate to a specific question imposed on the data by the software, in terms of whether values are greater than or less than a given value for a specific index (Figure 2.8). We have transposed the critical values for the software-selected optimal indices onto the boxplots in Figure 2.7. For example, towards the left-hand side of the classification diagram, K/(K+Ti) has a critical value of 0.87, whereby if samples are less than this value, there is an 86% probability that the samples are from mud flat sub-depositional environments. We have superimposed the value of 0.87 as a dashed line on Figure 2.7F, which illustrates the previous point about discriminating De2 and De3 sediments.

The code in R can be used to evaluate the accuracy of the RPART classification. In the case of the eight sub-depositional environments, the accuracy is 72.3% (Figure 2.10). We have engineered the dataset, to try to achieve higher-accuracy models, by selectively merging neighbouring sub-depositional environments. The most accurate classification model resulted from merging all inner estuary sediments (De2, De3, De4, and De5) and all outer estuary sediments (De6, De9, NDe8, and NDe8), leading to an accuracy of 92.9% (Figure 2.10). One of the single biggest improvements is in the merging

of sand flat and tidal bar sediment (De4 and De5) sediments, as this led to a 7.5% increase in the model accuracy (Figure 2.10).

We have here displayed one of the simpler classification trees, based on partly merged sub-depositional environments (Figure 2.11). This model was developed with all outer estuary sediments grouped (De6, De9, NDe8, and NDe8) but leaving inner estuary sediments grouped into coarser (De4 and De5) and finer (De2 and De3) sediments. This classification approach led to a model accuracy of 87.0% (Figures 2.10 and 2.11).

The method proposed above, calibrated with geochemical data from the Ravenglass Estuary surface sediments from known sub-depositional environments, has been applied to the geochemical data from the Holocene core. This approach could also be used to study sediment cores from other modern estuaries with similar geomorphological architecture, to interpret the sub-depositional environment from cores. It is also conceivable that the approach could be applied to ancient and deeply buried sandstones.

2.6.4 Application of Proposed Model for Discrimination of Estuarine Sub-Environments

We have applied the fully resolved RPART model (no merging of sub-depositional environments) (Figure 9) to the geochemical data from the Holocene core (Figure 2.7). The output from the application of the model has allowed us to define palaeo-sub-depositional environments, instead of using an indirect method of describing sedimentary facies, grouping these into facies associations and then interpreting palaeo-sub-depositional environments (McGhee et al., 2021). We first applied visual identification to establish the presence of gravel beds and salt marsh in the core. Using our new approach, we were able to identify mud flat, mixed flat, sand flat, tidal bar, tidal inlet, northern foreshore, and ebb-tidal delta sub-depositional environments throughout the core interval (Figure 2.12).

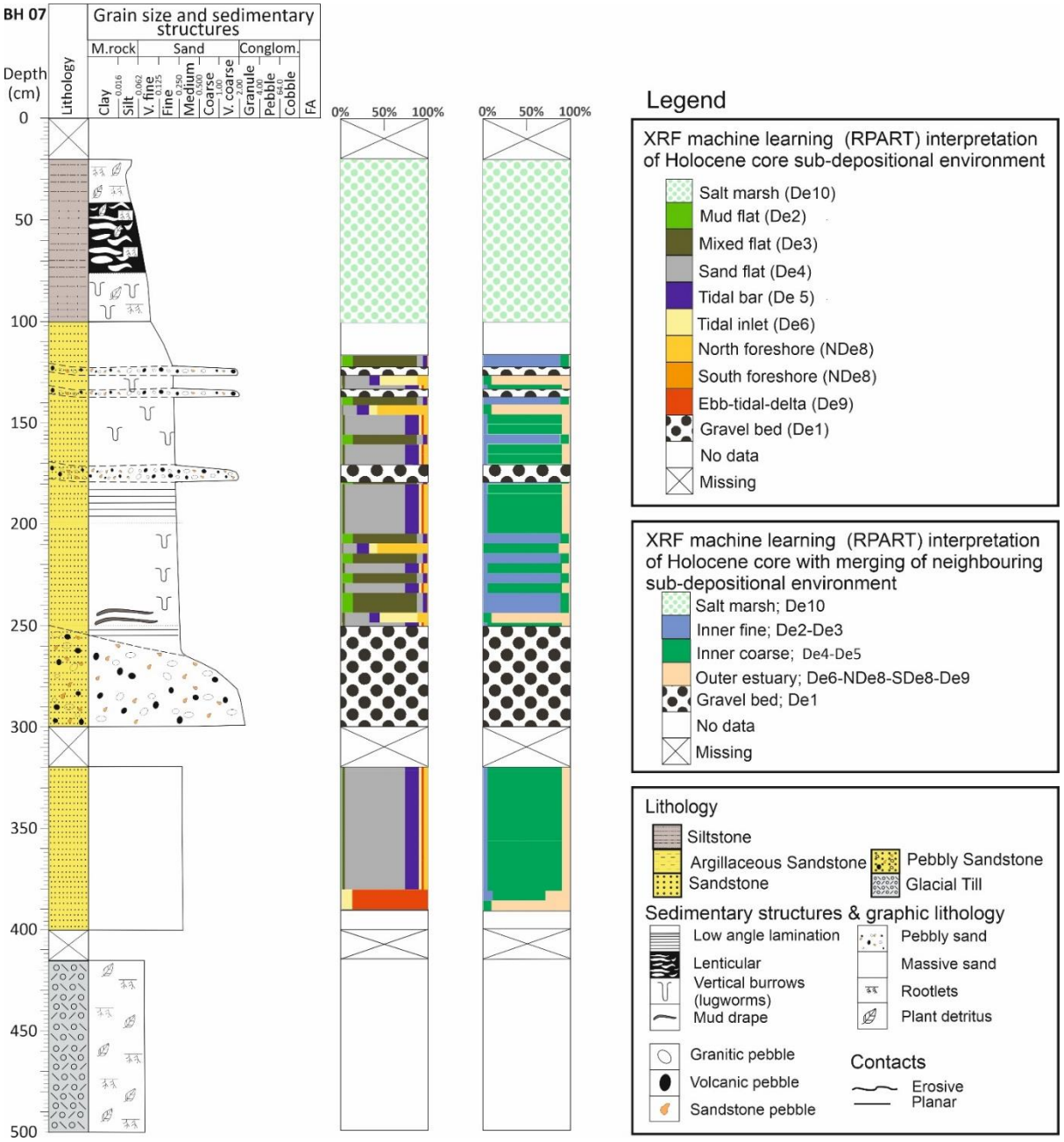

Figure 2.12; Schematic sedimentary log of the cored sediment beneath inner estuary vegetated tidal bars deposits (see Figure 2.1 for core location) with application of the classification tree in Figures 2.9 (wholly split sub-depositional environments) and 11 (partly merged sub-depositional environments) to data presented in Figure 2.7. The split and merged geochemical classification models reveal a succession of sub-depositional environments that could not easily be predicted based only on classical core description methods.

In detail, the texturally bland section between a depth of 300 and 400 cm was hard to interpret in terms of descriptive facies-based analysis. The sand between a depth of 300 and 400 cm may have been due to inner or outer estuary deposition, given the lack of diagnostic sediment structures, trace

fossils, or other features. The application of the automated classification approach has here revealed that this section was due to inner estuary deposition.

The sediment accumulation in this core started with a late glacial event and the accumulation of glacial diamicton (McGhee et al., 2021). The first sediments preserved on top of the till were apparently from a marine outer estuary environment (De9, Figure 2.12). This was succeeded by 100 cm of sand bar deposits (De4) and then approximately 200 cm of interbedded sand flat and mixed flat deposits (De3, Figure 12). The final 100 cm of deposition represents salt marsh deposits. This overall sequence could represent a time of (a) falling sea level, or (b) a greater rate of delivery of sediment to the estuary compared to net flux to the ocean. Salt marsh commonly represents the final stages of the levelling of marine coastal plains and the presence of marsh above the implies a phase of abandonment due to river migration (McGhee et al., 2021). Overall, the Holocene core shows an upward profile at the multi-metre scale and represents a highstand-into-regression sequence. The newly revised interpretation, based on the geochemical classification of sub-depositional environments, shows that the core, drilled into a present-day tidal bar sub-depositional environment, was not always the site of a tidal bar throughout the Holocene.

The interpretation of the occurrence of a few discrete samples of northern foreshore and tidal inlet sediments is probably anomalous and a consequence of the fact that the RPART models are not 100% accurate, as shown by the lead nodes in the classification diagram not having values of 1.0 in the dominant sub-depositional environment (Figure 2.10). It is probably appropriate to be led by the overall stacking pattern of the sediments rather than be driven by potentially anomalous 5 cm beds that seem to be out of sequence. Note that this interpretation is based on the concept that all environments in the core exist in the estuary at the present time; this assumption is reasonable but is difficult to unequivocally prove.

A question remains about the significance of the interpretation of the basal ebb-tidal delta sediments in Figure 2.12. This question arises as there are no intermediate sediments from foreshore, tidal inlet

or tidal bar sub-depositional environments between the ebb-tidal delta and sand flat successions, thus seeming to break Walther's law. It seems unlikely that sand flat deposits would sit directly on top of ebb-tidal delta deposits as they are not adjacent sub-depositional environments. There is no sign of erosion of intermediate sediment between ebb-tidal delta and sand flat deposits. The significance of the ebb-tidal delta sub-depositional environment in the core in Figure 2.12 is unclear, but it may be due to mis-classification due to overlapping characteristics of the ebb-tidal delta and sand flat sediments. Despite this question, the development of a ML-approach, using a surface sediment calibration dataset, has proved to be a valuable tool to better understand palaeo-environments in 10,000 years of post-Holocene deposition recorded in a core. This approach could be applied to other estuarine successions and even potentially to ancient and deeply buried estuarine sandstones.

This novel geochemical classification of sub-depositional environments has a good level of accuracy at discriminating outer estuary sediments, fine-grained inner estuary sediments and coarse-grained inner estuary sediments. It can also differentiate eight sub-depositional environments but with a lower degree of accuracy than the less refined classification scheme. This approach could be applied to any estuarine sediment and cores. The Ravenglass classification models (Figures 2.9 and 2.11) may be applicable to other estuaries but differences in provenance and in-basin geochemical processes may result in different cut-offs at decision nodes: such an approach remains to be tested. It is also possible that the geochemical indices that proved to be effective at differentiating sub-depositional environments could be effective for estuarine cores from deeply buried and ancient sandstones. As a final point, the approach laid out here could also be applied to other modern and ancient depositional environments that also have subtleties that are not easy to differentiate using classical core description and facies analysis approaches.

2.7 Conclusions

1. This work represents a detailed study of sediment, analysed for composition using pXRF analyses, from the Ravenglass Estuary, NW England, United Kingdom.

2. The depositional environments, mapped and defined across the estuary, include gravel beds, salt marsh, mud flats, mixed flats, sand flats, tidal bars, tidal inlet, foreshore, and ebb-tidal delta. The foreshore of the Ravenglass Estuary was subdivided into discrete northern and southern portions as they have distinct textural and elemental attributes.

3. Elements are heterogeneously distributed throughout the estuary, especially in terms of localised concentrations of Al, K, Ca, Fe, Mn, Zr, Rb.

4. Major, minor and trace element indices, varying between 0 and 1, were employed for the discrimination of sub-depositional environments, instead of raw concentration data, to circumvent the problem of variable dilution by quartz and closed datasets.

5. Element indices are heterogeneously distributed throughout the estuary, showing that element concentration patterns are not simply due to variable dilution by quartz.

6. There are strong relationships between specific sub-depositional environments and element indices within the estuary.

7. Provenance, sediment mineralogy and grain size, controlled by estuarine hydrodynamics, are the dominant controls on the distribution of elements (and their indices) in the Ravenglass Estuary.

8. A supervised machine learning method was developed, using the RPART routine in R Statistical Software, for the automatic discrimination of palaeo sub-depositional environments, with the model calibrated using surface sediment element indices. The model was successfully applied to a core drilled through the Holocene succession at Ravenglass to predict palaeo sub-depositional environments over the last 10,000 years.

9. This work has proved that there are strong and predictable relationships between estuarine sub-environments of deposition and sediment geochemistry.

3. Provenance and geochemistry of modern estuarine sediment

3.1 Abstract

Estuaries are sites of accumulation and deposition of Fe required for Fe-rich clay mineral development. Iron-rich clay minerals (such as chlorite) inhibit the development of porosity-filling quartz cement in deeply buried sandstone reservoir. The occurrence of well-crystallised clay coats has been reported in sandstone reservoirs deposited in marginal marine settings, such as estuaries and deltas. A novel study of the geochemistry and provenance of sediments in a modern analogue has here been employed to understand the distribution of Fe-bearing clay minerals and their precursors. We have applied a range of techniques, including XRF spectroscopy, grain size analysis and TOC analysis, to develop an understanding of the provenance and controls on the distribution of Fe in the surface sediments of the Ravenglass Estuary, NW England, UK. The Ravenglass Estuary is supplied by two main rivers; the River Esk drains a Palaeozoic granite-dominated hinterland while the River Irt drains a Palaeozoic andesite and Mesozoic red bed sandstones. The sediments of the Esk arm of the estuary are richer in Fe than those of the Irt arm. In contrast, the sediments of the Irt arm of the estuary are richer in Ti than those of the Esk arm. Estuarine mixing has overprinted the provenance signals in the outer estuary. The finest sediments in tidal flats, in the central and upper estuary, have the highest concentration of organic carbon and contain the highest concentration of Fe (and other metals). Iron, capable of producing Fe-rich grain coating minerals, was partly transported into the estuary as Fe-rich minerals, such as biotite and detrital chlorite, predominantly derived from the granite via the Esk arm of the estuary. However, Fe was also transported into the estuary as fluvially-transported complexes with organic matter, that were subsequently destabilised in the saline estuary and deposited at slack water conditions along with the finest grained sediment. Provenance has played an important role in controlling detrital mineral distribution in the Ravenglass Estuary but local geochemical processes of fluvial organic complexation, estuarine flocculation, and co-deposition in sub-depositional environment-specific locations have partly over-printed provenance signals.

3.2 Introduction

Chlorite, an Fe-Mg clay mineral, can occur as a thin coat on sand grains; chlorite grain coats typically inhibit quart cementation in a deeply buried sandstone (Worden et al., 2020a; Worden and Morad, 2003). Understanding the distribution of Fe in clastic sedimentary systems is vital, as Fe plays a key role in the occurrence and abundance of chlorite in sandstone, especially Fe-rich chlorite (Worden et al., 2020a). The factors that influence Fe distribution at the site of deposition includes provenance,

water chemistry, grain size, redox condition, bioturbation, weathering regime and hydraulic conditions (Rateev et al., 2008; Worden et al., 2020a). To enable Fe-enrichment or -accumulation in a sedimentary setting, abundant iron must be supplied from the sediment hinterland (Worden et al., 2020a). Bedrock weathering causes the chemical alteration of high-temperature, Fe-bearing igneous and metamorphic minerals such as olivine, pyroxene, and amphibole, to lower temperature Fe-bearing clay minerals and Fe oxides. Different degrees of weathering tend to give different forms of Fe-bearing minerals; for example, intense chemical weathering may yield iron oxides and hydroxides, where as weak chemical weathering may yield smectite or chlorite (Chamley, 1989; Rateev et al., 2008). Hydrodynamic sorting tends to separate coarse grains from finer grains, Fe-bearing lithic grain that contain chlorite or biotite are relatively more chemically stable and are more likely to be deposited in lithic sand grains rather than silt- or clay-grade sediment (Worden et al., 2020a). Fe-bearing heavy minerals, such as ilmenite, garnet and haematite (Walderhaug and Porten, 2007), are typically found in the sand fraction of sediment. Clay grade products of weathering, such as Fe-bearing clay minerals and iron oxides, tend to be present in the suspended sediment of estuary (Chamley, 1989; Rateev et al., 2008).

Iron typically occurs as colloidal hydroxide in fluvial water and tend to be complexed with organic materials; the adsorption of organic carbon on Fe hydroxide decreases with increasing pH (Forsgren et al., 1996). Iron in oxidised surface sediment can form Fe oxide coats on grain surfaces that is capable of strongly binding trace elements. Fe oxide can be in different forms, e.g., amorphous, or crystalline. Amorphous Fe oxides are the most reactive form of Fe as they tend to have more binding sites per unit mass (Poulton and Canfield, 2005). Organic matter plays an important role in metal distribution, by sequestering metals (Shaheen et al., 2019). The solubility of Fe and the stabilisation of Fe colloids is also influenced by the nature of organic complexes (Forsgren et al., 1996).

Iron is transported from the hinterland by rivers in both dissolved and organically-complexed (colloidal) form; the vast majority of this fluvially-transported Fe is deposited within river water-

seawater mixing zones, for example in estuaries and deltas (Boyle et al., 1977; Eckert and Sholkovitz, 1976; Sholkovitz, 1978). The concentration of total Fe in water decreases significantly down an estuary; this is a consequence of flocculation that occurs when dispersed organically-complexed Fe in fresh water is destabilised when it meets seawater, thus creating Fe-rich flocs that then settle out of suspension (Boyle et al., 1977). Fe is converted from a colloidal to a particulate phase in the low salinity part of estuaries (Boyle et al., 1977). Flocculation of Fe in estuarine systems has been explained by three possible processes; (i) oxidation of Fe(II) to Fe(III) with the precipitation of ferric hydroxide, (ii) The scavenging of iron by natural sediment particles, when they acts as negatively charged nuclei for the aggregation of iron colloids (Aston and Chester, 1973), or (iii) the coagulation of colloidal particles in suspension, during the mixing of estuarine and fresh water (Boyle et al., 1977). Dissolved or colloidal forms of Fe undergo hydrolysis, precipitation and flocculation with changing physio-chemical conditions (pH, Eh, ionic strength etc.) during transportation from river-estuary-marine environment (Aston and Chester, 1973). For example, dissolved Fe transported by rivers is precipitated and flocculated in the presence of estuarine saline waters (Mosley et al., 2003), and this is largely attributed to the increase in pH and ionic strength during the mixture of fresh water and saline water (Borgnino, 2013). Salinity-induced flocculation of dispersed fluvial Fe explains why 90% of all fluvial Fe is retained in deltas and estuaries (Martin and Meybeck, 1979). Neoformed Fe-rich minerals, i.e., those that develop during the subsequent diagenetic alteration of the primary sediment, can have significant influence on the reservoir quality of sandstone (Daneshvar, 2015), and may explain why most chlorite-bearing sandstones were deposited in estuaries and deltas (Dowey et al., 2012).

Dissolved Fe colloids, organic material and clay minerals can be transported to estuaries by rivers. Fluvially-transported clay minerals can undergo ion-exchange when in contact with solution water, while Fe from colloids be mobilised in the presence of cations, for example when freshwater mixes with seawater in an estuary (Pokrovsky and Schott, 2002). Hence estuaries are sites for potential clay mineral alteration processes (and specifically ion exchange) and Fe flocculation. The adsorption of iron hydroxide and organic matter onto clay is dependent on the pH of the water (Forsgren et al., 1996).

Estuaries have been reported to be favourable sites for the accumulation of fluvial transported clay minerals and organic materials (Roy et al., 2011). Estuaries are highly organically-productive natural environments that act as dynamic transitional habitats between the marine and terrestrial. They also serve as a bottleneck for the transit of many organisms, sediment and its major elements and trace elements from the continental to the coastal realm, thus constituting a transient or final sediment trap (Coynel et al., 2016). Investigation of the Loire estuary by Negrel in 1997 showed high spatial variability of trace elements, caused by the interplay between co-precipitation and/or flocculation of and adsorption onto clay minerals, Fe oxyhydroxides and/or humic acid complexes. Although estuaries can trap sediments, Fe and other metals, they can also act as sources due to break down of sediment-bound metals by chemical processes enhanced by water salinity, estuarine turbidity and redox boundaries (Audry et al., 2006; Dabrin et al., 2009; Elbaz-Poulichet et al., 1987b; Lanceleur et al., 2013) and sediment remobilisation due to tide or flood events (Coynel et al., 2007). At the present time, estuaries in UK tend to act as sinks rather than sources because tidal influx tends to relatively outweigh fluvial outflux (Dyer, 1997).

Sediments deposited in marginal marine to marine environments are typically complex due numerous factors acting simultaneously including water circulation, grain size, sediment mineralogy and geochemistry as well as anthropogenic factor (De Lazzari et al., 2004). Although sediment geochemistry is considered to be critically important for the understanding of mineral distribution in deeply buried sandstones, our knowledge of the relative and absolute concentration of elements in surface sediments is limited (Smith et al., 2009). The characteristics of surface sediments result from the range of biological, chemical and physical processes that occur in an estuarine environment, for example, sorption and desorption of surface-active solutes, deposition and erosion of suspended materials and the downward percolation of redox-sensitive species such as sulphate and Fe- and Mn-oxides (Thomson-Becker and Luoma, 1985). In the oxidised surface sediment, metal species (e.g., Fe) and other surface active constituents (e.g., organic carbon) are concentrated in the fine-grained (clay/silt size) sediments because (i) fine-grained sediment has large surface area per unit mass, and

(ii) fine-grained sediment provides shelter for micro-organisms that break down complex compounds (Dale, 1974). Variation in the distribution of fine sediments is commonly accompanied by changes in the concentration and distribution of different surface-active species that are surface area-dependent. Significant features in estuaries that influence the distribution of species that influence Fe-clay accumulation include organic coats on grains (Longbottom, 1970), Fe- and Mn-oxides (Santschi et al., 1983), and concentration of trace metals (Mayer and Fink, 1980).

Detrital sediment must be Fe-bearing for a sandstone to contain Fe-clay minerals; hinterland geology ultimately supplies the Fe (Worden et al., 2020a). Therefore, a geochemical understanding of the source sediment area to understand the source of Fe is paramount; geochemical provenance studies may hold a key to understand the distribution of Fe-clay minerals, e.g., chlorite, in sandstones (Armstrong-Altrin et al., 2004). The geochemical composition of clastic rocks reflects an interplay between multiple variables; source area, weathering, transportation, physical sorting, and diagenesis (Cox and Lowe, 1995; Fralick and Kronberg, 1997; McLennan et al., 1993; Meinhold et al., 2007). The application of sediment geochemical data to understand sedimentary processes has been widely employed due to the sensitivity of some trace elements that can be used to identify minor components not easily recognised with petrographic analysis (Armstrong-Altrin et al., 2004; Garver et al., 1996). The concentration of trace elements such Zr and Th have the potential to provide insight into the sedimentological origin, lithological and grain size variation, redox and depositional conditions of siliciclastic sediments (Dypvik and Harris, 2001).

The concentration of major elements has been used to classify clastic sediments (Herron, 1988), and to understand the relationship between element concentrations and the processes controlling their distribution (Vital et al., 1999). Geochemical data can also lead to understanding of sedimentary environments in relation to sedimentary provenance studies (Andersson et al., 2004), lithology delineation (Herron, 1986; Herron, 1988), understanding weathering effect and intensity (Mongelli et al., 2006), paleoclimate and paleoenvironment studies in the sediment's source area (Andersson et

al., 2004; Nesbitt and Young, 1982). Portable X-ray fluorescence spectroscopy (pXRF) is a rapid, non-destructive technique that gives element concentration with relatively little sample preparation. X-ray fluorescence spectrometry has numerous advantages in relation to other multi-element techniques, such as inductively coupled plasma mass spectrometry (ICP-MS). XRF is fast with simple optical arrangement, has low operational cost, rapid in situ analysis, versatile and allows the analysis of numerous elements simultaneously in both sediments and sedimentary rocks (Holler et al., 2009; Nagata et al., 2001). Other important techniques such as whole rock neutron activation analysis, inductively coupled plasma atomic emission spectrometry and inductively coupled plasma mass spectrometry (ICPMS), ion microprobe, atomic absorption spectrophotometry, and electron microprobe analysis have all been in used in geochemical analysis of sediments and sedimentary rocks, for important work such as provenance studies, weathering and diagenetic alterations, chemostratigraphic correlation and lithological evaluations (Aehnelt et al., 2013; Andersson et al., 2004; Herron, 1988; Kumpan et al., 2014; Nesbitt and Young, 1982). Recent developments of pXRF devices have made it possible to replicate numerous conventional analytical approaches in determining both major, minor and trace elements chemistry of sediments and sedimentary rocks.

Iron distribution in an estuary is of great significance in understanding Fe geochemical cycle, particularly its mobility, liberation, and mobilisation during diagenetic evolution of Fe-bearing aluminosilicate. This study has focused on the geochemistry and provenance of sediments in a modern estuarine environment, to understand the provenance and distribution of Fe-bearing clays and their precursors. This research was designed to address the distribution and accumulation of Fe in the Ravenglass estuary as function of sub-depositional environment, grain size, clay minerals and organic matter concentration. The study has addressed the following research questions, focusing on the Ravenglass Estuary in NW England, UK:

1. Can pXRF analysis be used to discern provenance in estuarine sediments?

2. Can pXRF analysis be used as a proxy for mineralogy in the estuarine sediments?

3. What are the different types of Fe present in the estuarine sediments?

4. What factors control the distribution and accumulation of Fe in the estuarine sediments?

3.3 Study Area: Ravenglass Estuary

3.3.1 Ravenglass sedimentary environment

The Ravenglass Estuary is located along the west coast of Cumbria, in northwest England, UK, with an area of about 5.6 km^2 (Fig. 3.1A). The Ravenglass Estuary is a macro-tidal estuary with a recorded tidal range of ~ 7.55 m and limited wave-action owing to the presence of coastal spits; about 86 % of the area of the inner estuary is exposed at low tide (Bousher, 1999; Griffiths et al., 2018; Griffiths et al., 2019a; Griffiths et al., 2019b; Lloyd et al., 2013; Wooldridge et al., 2017a; Wooldridge et al., 2017b). The estuary connects with the Irish Sea via a 500 m-wide tidal inlet that flows between two coastal spits (Drigg and Eskmeals Spits) and stretches up to the tidal reaches of the Rivers Mite, Irt and Esk. The estuary is a 'dual-funnelled', mixed-energy estuary dominated by tide and wave action; it has a longer outward ebb tidal-flow than inward flood tidal-flow (Kelly et al., 1991). Sediments are fed into the estuary via the Rivers Mite, Irt and Esk which have average flow-rates of 0.04 m^3s^{-1}, 0.34 m^3s^{-1}, and 0.42 m^3s^{-1} respectively (Bousher, 1999). The estuary has a brackish, river- and tide dominated inner basin; its central basin is mixed-energy with near-seawater salinity, dominated by Saltcoats tidal flat. The outer estuary is dominated by seawater with wave and/or tidal currents and covers the main tidal channel, estuary mouth and the foreshore (Figs. 3.2). The Ravenglass Estuary represents a complete fluvial to marine transect sediment routing system, with a well-established link between sediment sources and sinks. Much research has been conducted on this estuary, in terms of sedimentary systems and processes, detrital clay and clay coats; their origin, mineralogy and distribution (Daneshvar, 2015; Daneshvar and Worden, 2017; Griffiths et al., 2018; Griffiths et al., 2019a; Griffiths et al., 2019b; Verhagen et al., 2020; Wooldridge et al., 2017a; Wooldridge et al., 2017b). The Ravenglass Estuary represents an ideal study site to address the research questions presented in the introduction.

3.3.2 Geological setting and provenance

The Ravenglass Estuary sediments are transported from different types of bedrock and Quaternary drift-deposits. The geology of the source area comprises of Ordovician Borrowdale Volcanic Group (BVG), Devonian Eskdale Granite and Cambrian Skiddaw Group slate; Triassic Sherwood Sandstone Group at the west of the drainage area is largely covered by drift (Fig. 3.1B). Quaternary drift-deposits are mainly composed of glacial till, peat, and glacial-lacustrine deposits and dominate the lowland geology (Griffiths et al., 2018; Griffiths et al., 2019a; Griffiths et al., 2019b; Merritt and Auton, 2000).

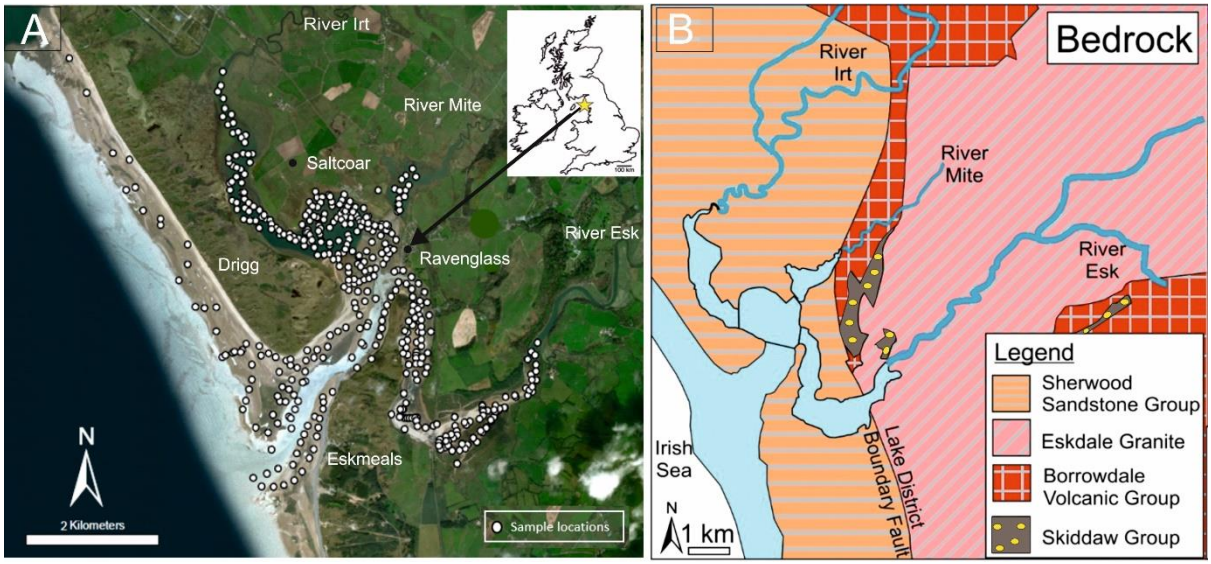

Figure 3.1; (A) Location map of the Ravenglass Estuary, north-west England (Aerial image sourced from ArcGIS) and distribution of surface-sediment samples (<2 cm) used for XRF analysis (B) Geological setting showing the bedrock geology of Ravenglass Estuary, NW England, UK.

The River Esk predominantly drains the Eskdale Granite, and the River Irt predominantly drains Borrowdale Volcanic Group andesite (Daneshvar and Worden, 2017; Griffiths et al., 2018; Griffiths et al., 2019a; Griffiths et al., 2019b). The Eskdale Granite is the largest exposed intrusion in Cumbria (Soper, 1987); it forms part of the Lake District Batholith and has resulted in the central-western part of the Lake District massif (Quirke et al., 2015). Hydrothermal mineralisation of the granite, leading to alteration of mafic silicates and plagioclase, has caused a significant localised chlorite growth (Moseley, 1978; Quirke et al., 2015; Rundle, 1979; Young et al., 1986). The feldspathic Sherwood Sandstone Group, locally known as the St Bees Sandstone Formation, is a fluviatile sandstones sequence (Strong et al., 1994). The Sherwood Sandstone is dominated by quartz, with subordinate

feldspar, muscovite and biotite, albite, and carbonate clasts (Barnes et al., 1994b; Strong et al., 1994); heavy minerals include zircon, tourmaline, apatite, anatase and rutile (Strong et al., 1994). The Ordovician Borrowdale Volcanic Group is present in the Lake District in two different outcrops; the older exposed in the north-west and the younger exposed in the south-east (Entwisle et al., 2005). These extrusive rock suites are comprised mainly of subduction-related, K-rich, calc-alkaline basalt, andesitic-rhyolitic volcanic lavas, sills and pyroclastic rocks, and constitute the central part of the Lake District massif (Millward, 2004; Quirke et al., 2015). Quirke et al. (2015) reported that, during the Caledonian Orogeny, the Borrowdale Volcanic Group was subjected to regional, sub-greenschist facies metamorphism at about 395 Ma, with multiple stages of hydrothermal activity that developed complex zones of alteration including variable amounts of vein haematite (Entwisle et al., 2005; Milodowski et al., 1998). The estuary is characterised by the presence of knolls of glacial till, exposed across the entire region. Peat is also present, mostly found sitting on top of the glacial deposits (Lloyd et al., 2013). The impact of anthropogenic activities in the Ravenglass Estuary is insignificant, owing to the sparse population of its surrounding environment. However, the effect of population on the natural environment is profound. Pretty much all of the UK, including Ravenglass, is not 'natural'. E.g. the present of sheep farms bordering the estuary along the salt coat, and that means the vegetation is partly as a result of farming practices. Additionally, the construction of railway bridge in 1868 led to the expansion of the salt marsh, thereby protecting the lower reaches of River Mite from tidal currents (Carr and Blackley, 1986).

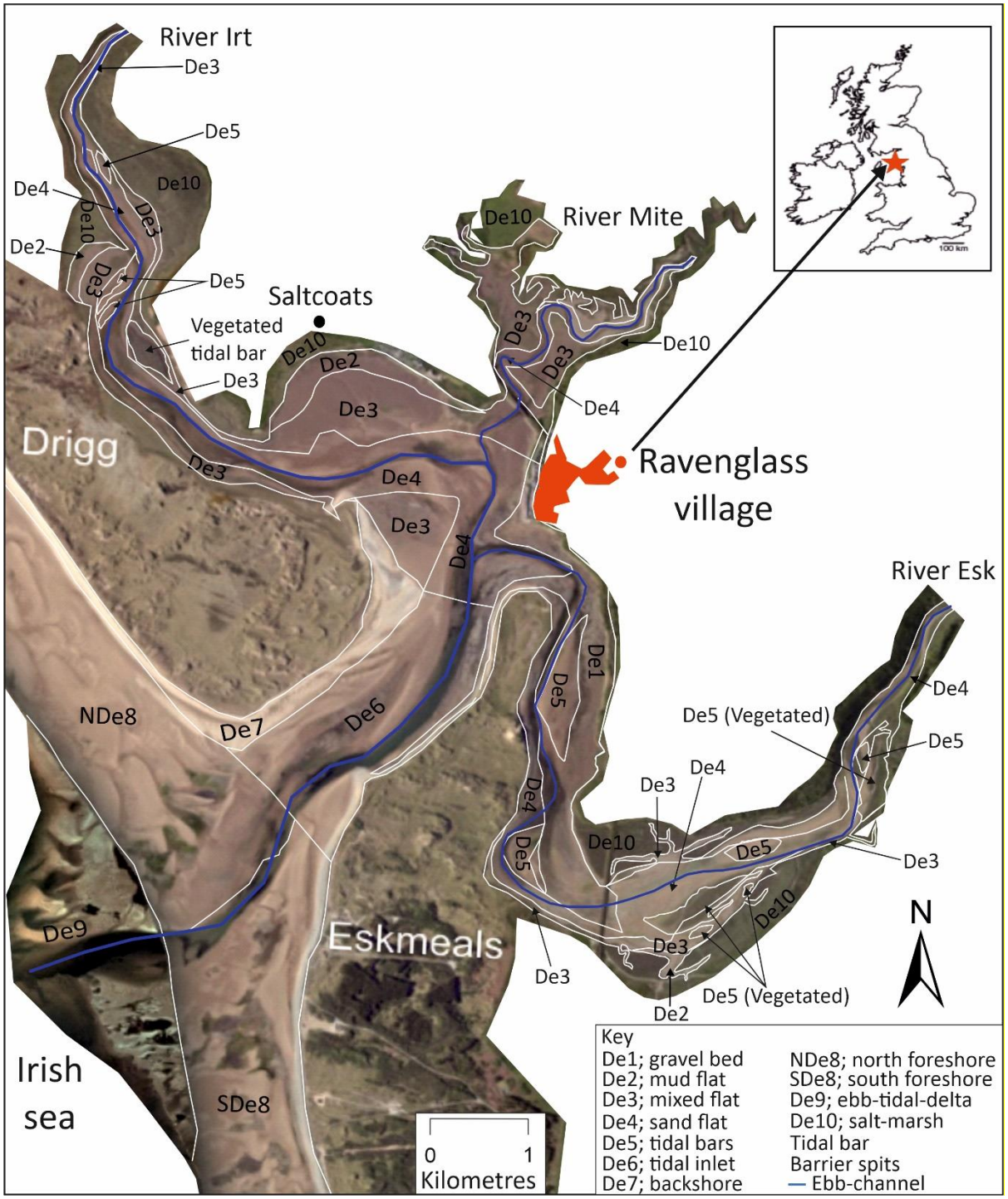

Figure 3.2; Distribution of estuarine sub-depositional environments mapped across the Ravenglass Estuary. These sub-depositional environments are labelled; De1, gravel-bed; De2, mud-flat; De3, mixed-flat; De4, sand-flat; De5, tidal bars and dunes; De6, tidal-inlet; De7, backshore; De8, foreshore (northern and southern sites); De9, ebb-tidal-delta; and De10, salt-marsh.

3.4 Samples and Methods

3.4.1 Field mapping and sample collection

Detailed mapping of sub-depositional environments was undertaken, based on geomorphological mapping criteria and supported by aerial imagery and grain size analysis to subdivide tidal flats. The sub-depositional environments identified across the estuary are gravel beds, vegetated surfaces, barrier spits, tidal flats (sub-divided into mud flat, mixed flat and sand flat), tidal bars, tidal inlet, backshore, foreshore, ebb-tidal-delta (Fig. 3.2). Tidal flat sub-depositional environments were sub-divided based laboratory-derived sand percentages, modified from a scheme that was initially proposed by Brockamp and Zuther (2004), where: 90-100% sand is sand flat, 50–90% sand is mixed flat, and 15–50% sand is mud flat.

Surface sediment samples (from < 2 cm below the surface) were collected from 497 different sites, that covers the entire estuary and the coast (Fig. 3.1A). Sediments were placed in airtight plastic bags in the field and dried in the laboratory prior to the analysis.

3.4.2 XRF analysis

All samples from the Ravenglass Estuary were analysed using a handheld Thermo Scientific Niton +XL3t GOLDD XRF spectrometer (pXRF). The pXRF is a self-contained, energy dispersive XRF spectrometer with a variable intensity energy source (6-50 kV, 0-200 µA) Ag anode X-ray tube. It is equipped with a factory-calibrated, GOLDD (Geometrically Optimised Large Area Drift Detector) detection system, optimised by the manufacturer for low detection limits, and high-precision measurements of more than 40 elements. Sediment samples were prepared by air drying whole sediment samples in a 50 mm petri dishes, which were then placed 2 mm from the pXRF detector. Problems of horizontal and vertical heterogeneity of the sample, variable moisture and surface roughness, associated with core-based, “point and shoot” pXRF studies (Carr et al., 2008; Chou et al., 2010; Gutiérrez-Ginés et al., 2013; Weindorf et al., 2012) have here been avoided (Argyraki et al., 1997).

Table 3.1; Detection limit and mean and standard deviation of multiple analyses from one given sample.

Element	Reported detection limit (ppm)	Mean of 30 repeat analyses from one sample (ppm)	Standard deviation of 30 repeat analyses from one sample (ppm)
Al	2000	64099	1685
K	250	18234	145
Ca	70	2610	46
Ti	6	2477	92
Fe	25	11837	90
Mn	30	172	19
Rb	6	70	1
Sr	8	73	2
Zr	3	352	3
Ba	50	487	18
Cs	12	85	4

The reported limit of detections of the instrument for Al, K, Ca, Ti, Fe, Mn, Rb, Sr, Zr, Ba and Cs are listed in Table 3.1. The instrument's high precision and accuracy was validated by replicating the XRF analysis, on a single sample 30 times, the average and standard deviation of Al, K, Ca, Ti, Fe, Mn, Rb, Sr, Zr, Ba and Cs are listed in Table 1. Each analysis was conducted, for 150 seconds, in "Test All GEO" mode; this combines mining and soil modes which thus permits the determination of major and trace elements. The optimum analysis time of 150 seconds was selected by repeating analysis of one sample for different replicate durations to identify when there was no significant improvement in the reported uncertainty.

Despite concentrations for 40 elements being reported by the pXRF, only 12 elements were present in all samples (Table 3.2). These elements are Al, Si, K, Ca, Ti, Fe, Mn, Rb, Sr, Zr, Ba and Cs. Other elements were variably present at concentrations above the element-specific detection limit.

3.4.3 Grain size analysis

Sieved samples (< 2 mm fraction) were analysed for grain size distribution using Laser Particle Size Analysis (LPSA) with a Beckman Coulter LS13 320 Counter. The LPSA-derived data were then analysed using GRADISTAT© to determine the statistical parameters of the sediment. Prior to grain size analysis,

organic matter present in samples was removed by sample digestion, based on established laboratory procedures. Calgon was added to the sample in order to convert the dried sediment into a paste for optimum mixing and homogenisation (Simon et al., 2021).

Table 3.2; Sample numbers from each sub-depositional environment and number of elements above detection limit for each sub-depositional environment.

Sub-environment	**Samples**	**Al**	**Si**	**P**	**S**	**Cl**	**K**	**Ca**	**Sc**	**Ti**	**V**	**Cr**	**Mn**
Foreshore	69	69	69	17	24	69	69	69	3	69	48	35	67
Gravel bed	28	28	28	10	18	28	28	28	4	28	17	19	26
Mixed flat	94	94	94	1	54	94	94	94	2	94	51	66	93
Mud flat	55	55	55	1	52	55	55	55	16	55	33	52	54
Ebb-tidal-delta	21	21	21	9	20	21	21	21	2	21	6	7	20
Sand flat	120	120	120	0	28	120	120	120	1	120	102	40	113
Tidal bars	53	53	53	0	12	53	53	53	1	53	43	18	50
Tidal inlet	25	25	25	5	8	25	25	25	0	25	20	6	24
Salt marsh	17	17	17	17	17	17	17	17	5	17	14	11	17

Sub-environment	**Samples**	**Fe**	**Ni**	**Cu**	**Zn**	**As**	**Rb**	**Sr**	**Zr**	**Nb**	**Pd**	**Ag**
Foreshore	69	69	0	0	28	15	69	69	69	25	3	0
Gravel bed	28	27	0	1	23	13	28	28	28	14	0	0
Mixed flat	94	94	0	0	93	20	94	94	94	88	0	2
Mud flat	55	54	0	0	55	19	55	55	55	55	0	0
Ebb-tidal-delta	21	21	0	0	14	2	21	21	21	4	4	0
Sand flat	120	119	0	0	76	12	120	120	120	69	0	0
Tidal bars	53	52	1	0	39	6	53	53	53	31	0	2
Tidal inlet	25	25	1	1	14	6	25	25	25	7	2	1
Salt marsh	17	17	8	1	17	16	17	17	17	13	2	3

Sub-environment	**Samples**	**Cd**	**Sn**	**Sb**	**Te**	**Cs**	**Ba**	**Hg**	**Pb**	**Bi**	**Th**	**U**
Foreshore	69	13	32	20	60	65	69	3	13	0	14	8
Gravel bed	28	11	17	10	28	28	28	0	13	1	14	3
Mixed flat	94	0	51	15	92	93	94	6	3	1	46	5
Mud flat	55	0	28	4	48	54	55	3	11	8	41	1
Ebb-tidal-delta	21	17	21	19	21	21	21	0	19	0	5	1
Sand flat	120	0	64	27	106	118	120	2	2	1	7	6
Tidal bars	53	0	35	8	49	53	53	2	2	1	3	1
Tidal inlet	25	4	17	9	25	25	25	3	5	0	8	1
Salt marsh	17	16	17	17	17	17	17	1	17	3	15	7

3.4.4 TOC analysis

Surface sediments were sampled with a screw neck vial (15-mm diameter) and immediately oven dried. The dried samples were crushed into powder with an agate mortar and pestle. Total organic carbon analysis of sediment was undertaken using a Thermo Scientific Flash Smart Organic Elemental Analyser after vapour phase de-carbonation using 12N Analar Grade HCl, following Yamamuro and Kayanne (1995). Two-point daily calibration was performed using High Organic Sediment Standard OAS (Elemental Microanalysis Ltd). Results for the standards were within uncertainty limits of certified value which are Carbon 7.17 % +/- 0.09 %, Nitrogen 0.57 % +/- 0.02 %.

3.4.5 Mineral Analysis

Sediment mineralogy was determined using automated mineralogy using SEM-EDS analysis. SEM-EDS was undertaken using a FEI WellSite QEMSCAN®, which comprises a scanning electron microscope combined with energy dispersive spectrometers. The QEMSCAN system has an electronic processing unit for integrating scanned data using a software suite (iDiscover), to provide information regarding the chemical and mineral compositions of the samples. SEM-EDS analyses were conducted on carbon-coated polished thin sections. Data were collected with user-defined step sizes of 2 µm to ensure that all the clast sizes were analysed.

3.4.6 Spatial mapping

Maps of the distribution of pXRF data, total organic carbon and grain size were generated in ArcGIS software, using an inverse distance weighted (IDW) interpolation function. IDW was selected because, it tends to have minimal mean prediction errors and high correlations between predicted and measured values (Zarco-Perello and Simões, 2017). Also, the IDW method does not generate negative concentrations, as observed when using spline-based interpolation function are used, and problems of the formation of valleys and ridges are avoided (Watson and Philip, 1985). A polyline in ArcGIS was drawn down the long axes of the Drigg and Eskmeals Spits, to separate the marine data from estuarine data when performing the interpolations (Griffiths et al., 2019a).

3.4.7 Statistical analysis

Statistical techniques were used to investigate relationships between different variables (Cheng et al., 2006; Dempster et al., 2013; Grunsky and Smee, 1999; Klovan, 1966). Pearson correlation analysis was performed on Al, Si, Ti, V, Mn, Fe, Zr, TOC and grain size data, to see how their relationships can affect Fe distribution in the Ravenglass Estuary. The correlation analysis was performed in Minitab statistical software, The statistical significance of the analysis are presented as: marginally significant when $p < 0.1$; significant when $p < 0.05$; very significant when $p < 0.01$; and extremely significant when $p < 0.001$ (Scheffe, 1999). Bivariate plot of geochemical data, total organic carbon and grain size, split by sub-depositional environment, was produced using ggplot2 in RStudio (Wickham, 2016).

3.5 Results

3.5.1 Mapped Sediment parameters

Maps of the distribution of element concentrations, total organic carbon and grain size have been plotted to assess the distribution of these sediment parameters, in relation to geographic location and sub-depositional environments (Figs. 3.3A to F, 3.4A to B). These maps have boundaries between sub-depositional environments superimposed.

Table 3.3; Average compositional data of the four main parts of the Ravenglass Estuary

Location	Stats	Mn ppm	Ti ppm	Fe ppm	Al ppm	Zr ppm	V ppm	TOC %	TiO2/Zr
Esk arm	Average	207	931	7305	7449	222	40	0.325	0.00090
	Std	***159***	***454***	***3484***	***3856***	***152***	***24***	***0.370***	***0.00053***
Irt arm	Average	311	1129	8893	12047	191	35	0.613	0.00132
	Std	***160***	***458***	***2907***	***4272***	***165***	***30***	***0.451***	***0.00061***
Central	Average	237	993	7307	8652	196	35	0.307	0.00110
	Std	***153***	***427***	***2414***	***5729***	***128***	***25***	***0.259***	***0.00056***
Outer	Average	133	675	5972	6996	178	27	0.060	0.00138
	Std	***58***	***274***	***1852***	***2766***	***244***	***18***	***0.009***	***0.00084***

3.5.1.1 Element distributions

Here we have specifically focussed on elements that relate to sediment provenance and the source of Fe in clastic sediment. Maps of Al, Ti, V, Mn, Fe, and Zr concentrations are shown in Figure 3.3. Aluminium is heterogeneously distributed across the different sub-depositional environments and geographic location (Fig. 3.3A). It has elevated concentration in the mud and mix flat environments (De2 and De3); it has intermediate concentration in the ebb tidal-delta and southern foreshore (De9, SDe8); it has relatively low concentration in the sand-dominated sand flat, tidal bar, tidal channel and northern foreshore environments (De4, De5, De6 and NDe8). Overall, Al concentration is higher in the Irt arm with average concentration value of 12047 ppm, than in the Esk arm and central basin, with average concentrations of 7449 and 8652 respectively. The outer estuary shows the lowest Al concentration with an average of 6996 ppm (Table 3.3).

Table 3.4; Pearson's Correlation Coefficient (R) matrix calculated from the Ravenglass estuary sediment parameters. R-values in plain text, p-values are in bold. For p-values <0.05, the correlation is statistically significant. P values of <0.01 and <0.001 represent very and extremely significant correlations. The positive correlation between Al and Ti, Fe, Mn suggests the significant influence of aluminous clay minerals on the distribution of those metals

	Mn	Si	Ti	Fe	Al	Zr	V	Sc	Th	Grain size
Si	-0.606									
	0.0000									
Ti	0.766	-0.592								
	0.0000	***0.0000***								
Fe	0.748	-0.501	0.811							
	0.0000	***0.0000***	***0.0000***							
Al	0.563	-0.051	0.575	0.576						
	0.0000	***0.2900***	***0.0000***	***0.0000***						
Zr	0.184	-0.1	0.507	0.399	0.252					
	0.0000	***0.0370***	***0.0000***	***0.0000***	***0.0000***					
V	-0.059	-0.131	-0.024	-0.042	-0.026	-0.121				
	0.2220	***0.0060***	***0.6180***	***0.3820***	***0.5910***	***0.0110***				
Sc	0.177	-0.326	0.23	0.171	0.041	0.058	0			
	0.0000	***0.0000***	***0.0000***	***0.0000***	***0.3920***	***0.2260***	***0.9930***			
Th	-0.069	-0.042	0.077	-0.064	0.043	0.289	-0.011	0.121		
	0.1500	***0.3770***	***0.1080***	***0.1830***	***0.3660***	***0.0000***	***0.8190***	***0.0120***		
Grain size	-0.566	0.621	-0.688	-0.498	-0.385	-0.41	-0.027	-0.205	0.019	
	0.0000	***0.0000***	***0.0000***	***0.0000***	***0.0000***	***0.0000***	***0.5800***	***0.0000***	***0.6900***	
TOC	0.702	-0.734	0.711	0.649	0.467	0.154	0.11	0.363	0.115	-0.69
	0.0000	***0.0000***	***0.0000***	***0.0000***	***0.0000***	***0.0010***	***0.0240***	***0.0000***	***0.0180***	***0.0000***

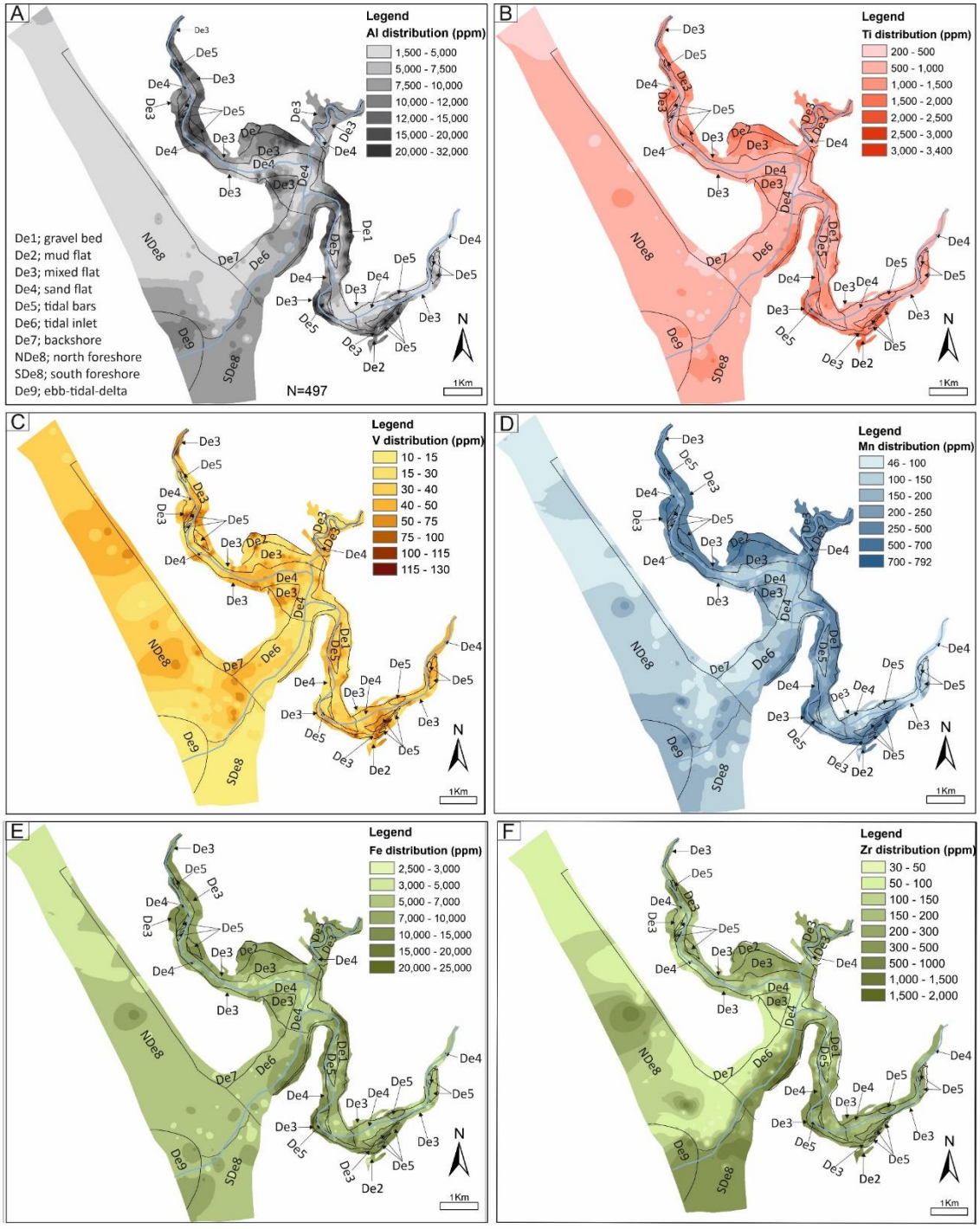

Figure 3.3; Spatial distribution of (A) Aluminium, (B) Titanium, (C) Vanadium, (D) Manganese, (E) Iron and (F) Zircon within the Ravenglass Estuary. Note, the concentration of Fe, Al, and Ti is highest in the lower and upper reaches of the estuary arms where sediment is dominated by mud and their similarities in spatial distribution in these areas is due to their presence in Fe-bearing alumino silicate for example chlorite, mica and Fe-rich illite. Vanadium is supplied via Esk river and have varying distribution in the central basin, attributed to different factors e.g., vanadium in fine grain is attached to iron oxide or vanadium sensitivity to redox. Variation in Zr and Ti distribution represent granite versus volcanic provenance signature in the Ravenglass sediments.

Titanium and Fe are heterogeneously distributed and have some similar features (Fig. 3.3B & 3.3E). Titanium and Fe concentrations decrease progressively toward the open sea and tend to be highest in tidal flat, tidal bars, and in < 2 mm sediment from gravel beds. Titanium and Fe are unevenly distributed between different sub-depositional environments (Fig. 3.3B & 3.3E). They have elevated concentrations in the mud and mix flat environments (De2 and De3); they have relatively lower concentrations in all remaining sub-depositional environments (De4, De5, De6, NDe8, SDe8 and De9). Titanium concentration is highest in the Irt arm of the inner estuary with average values of 1129 ppm. The average Ti concentrations in the Esk arm of the estuary and central basin are similar but lower than Irt arm (931 and 993 ppm). The average Ti concentration in the outer estuary is lowest at 675 ppm (Table 3.3). Iron concentration is highest in the Irt arm of the inner estuary with average values of 8893 ppm. The average Fe concentrations in the Esk arm of the estuary and central basin are nearly identical and but lower than Irt arm (7305 and 7307 ppm). The average Fe concentration in the outer estuary is lowest for the whole estuary at 5972 ppm (Table 3.3).

Manganese is heterogeneously distributed between different sub-depositional environments and geographic locations (Fig. 3.3D). The concentration of Mn is highest in the Irt arm of the estuary with an average of 311 ppm. The Esk arm of the estuary has an average Mn concentration of 207 ppm. The central basin has an average of 237 ppm. The outer estuary has the lowest Mn concentration with an average of 133 ppm (Table 3.3). Manganese has elevated concentrations in the mud and mix flat environments (De2 and De3); It has relatively low concentrations in all remaining sub-depositional environments (De4, De5, De6, NDe8, SDe8 and De9) (Fig. 3.3D).

Zirconium concentrations vary across the different sub-depositional environments and geographic locations in the estuary (Fig. 3.3F). The most noteworthy aspects of Zr distribution are the high concentration along the southern part of the tidal inlet and southern foreshore and the low concentration along the northern part of the tidal inlet and northern foreshore (Fig. 3.3F). However, Zr distribution along the estuary geographic locations show that the Esk arm of the estuary has the

highest average concentration (222 ppm); the outer estuary has the lowest average concentration (178 ppm). The central basin and Irt arm of the estuary have similar average concentrations (196 and 191 ppm) (Table 3.3).

Vanadium concentrations vary from about 10 to 130 ppm (Fig. 3.3C). Vanadium has the lowest concentrations in parts of the Esk and Irt arms of the estuary, along the southern side of the tidal inlet and in the ebb tidal delta. Vanadium average concentrations in the Esk arm, Irt arm, central basin and outer estuary are 40 ppm, 35 ppm, 35 ppm and 27 ppm, respectively (Table 3.3). Although vanadium is slightly higher concentration in the Esk arm than the rest of the geographical locations, its concentration (Fig. 3.3C) does not seem to show any systematic pattern with sub-depositional environments and geographic locations.

3.5.1.2 Grain size and TOC distribution

The mapped distributions of grain size and total organic carbon (TOC) for the Ravenglass Estuary are presented in Figure 3.4. Grain size tend to increase down channel and decrease toward the margin of inner estuary and central basin (Fig. 3.4A). TOC increases in areas with decreasing grain size (Fig. 3.4A & B). Overall, the tidal flat sediments, in the inner and central estuary, show a gradational change in TOC and grain size distribution from very fine- to fine-grained with TOC up to 1.8 % in the mud- and mixed-flats (De2 and De3). Sand flat sub-depositional environments (De4) are fine- to medium-grained with TOC of about 0.2 % in the. Tidal bar sediments (De5) are fine- to medium-grained and with low TOC concentration, except along the vegetated tidal bar sediments, where TOC concentration reaches up to 1.2 % (Fig. 3.4A & 3.4B). In the outer estuary, TOC is uniformly low (< 0.2 %) but grain size is variable. Tidal inlet (De6) and the northern foreshore (NDe8) sediments tend to be medium grained. Sediments in the southern foreshore (SDe8) and in ebb-tidal-delta (De9) are finer-grained than tidal inlet and northern foreshore sediment. Although the Esk and Irt arms and the central basin are dominated fine-grained sediments, their TOC concentration varies significantly; the average TOC

concentration in the Irt arm (0.61 %) is twice the average TOC concentration in the Esk arm (0.32 %) and the central basin. The outer estuary has an average TOC concentration of 0.060 % (Table 3.3).

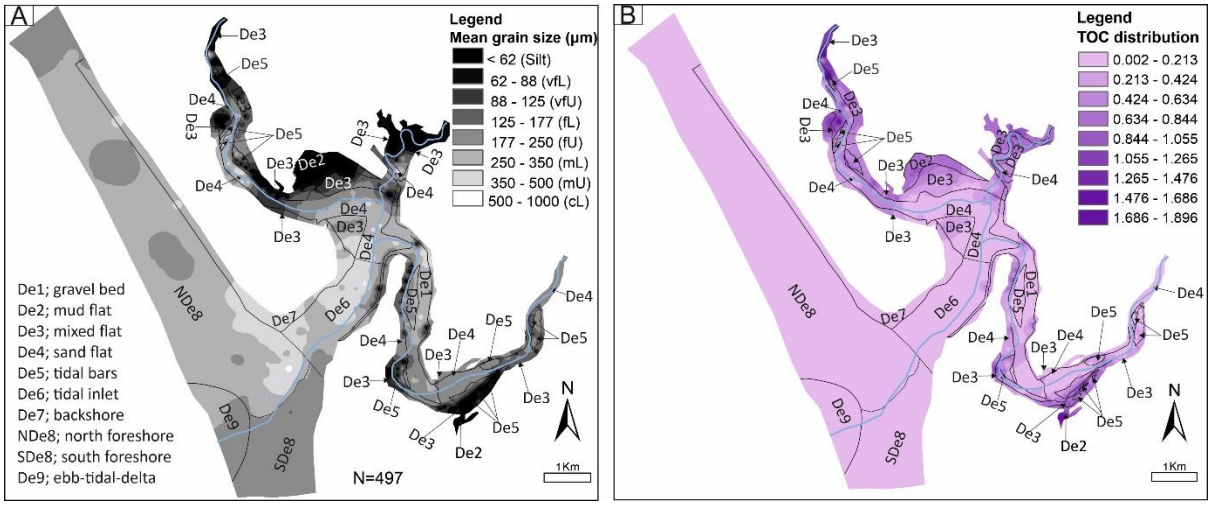

Figure 3.4; Grain size and TOC distribution in the Ravenglass Estuary. (A) mean grain size, and (B) TOC. Note that mean grain size and TOC decrease toward the margins of the inner estuary and central basin, large proportion of TOC is locked in the clay and silt size sediment due their surface area dependency, as exhibited by fine sediments. Fine sediments in the lower and upper estuary are a major sink for TOC and non-detrital or fluvial transported metals such as Fe and V.

3.5.1.3 Element ratio distributions

The ratio TiO_2/Zr has been used to help identify relative importance of mafic and felsic sources of clastic sediment (Hayashi et al., 1997). The distribution map of TiO_2/Zr shows that the upper reaches of the Irt arm, the northern tidal inlet and foreshore, ebb-tidal-delta and the gravel bed along the Esk arm, have the highest TiO_2/Zr concentrations (Fig. 3.5). The lowest TiO_2/Zr concentrations are found along the parts of mixed and sand flat in the central basin, and the southern tidal inlet and foreshore. The distribution of TiO_2/Zr varies greatly with different geographical locations; it has the highest average concentrations in the Irt arm and outer estuary (0.00132 and 0.00138), the central basin has a slightly lower value (0.00110), the lowest average concentrations are in the Esk arm (0.00090) (Table 3.3).

The ratio V/Fe has been used to help link Fe accumulation in sediment to organically-enhanced Fe transport processes. The distribution of V/Fe varies significantly across the various sub-depositional environments and geographical locations (Fig. 3.6). In terms of geographic location, V/Fe

concentration is highest in the Esk arm, intermediate in the central basin and lowest in the Irt arm and outer estuary (Table 3.3). Overall, the V/Fe ratio ranges from 0.0035 to 0.0100 in most sub-depositional environments, except in the mud and mixed flat sub-environments of the central basin where it is 0.0034 and the ebb-tidal-delta and the southern foreshore and tidal inlet where it is 0.0033. V/Fe is high along the upper reaches of northern foreshore and some pockets along the lower reaches of northern foreshore and tidal inlet. V/Fe is also high along the tidal bars of Esk arm and sand flat in the central basin.

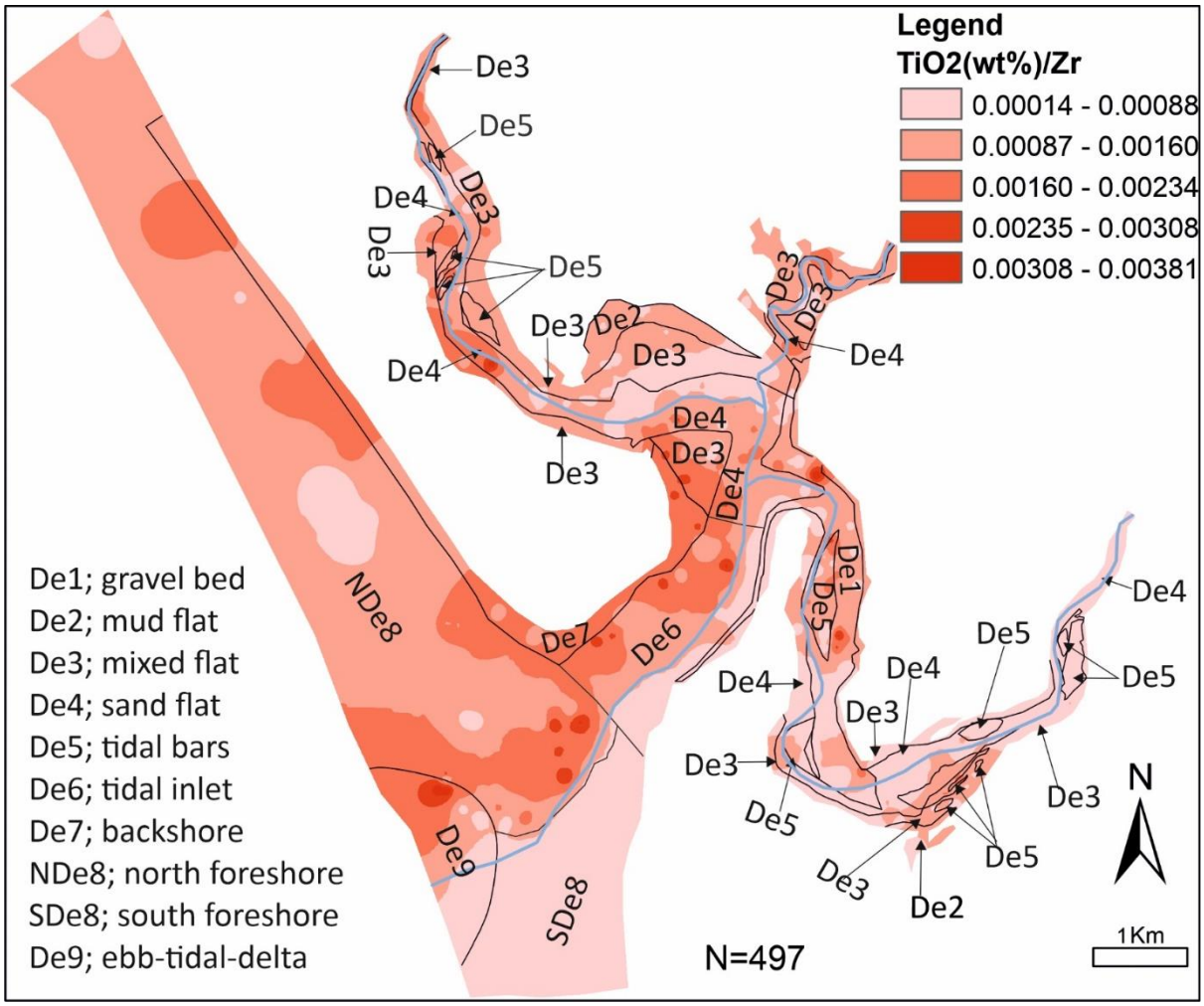

Figure 3.5; Spatial distribution map of TiO2/Zr within the Ravenglass estuary. Note sediments are transported into the estuary from Sherwood sandstone, Eskdale granite and Borrowdale volcanic via river Esk and Irt. TiO2/Zr ratios from the BVG (0.0025), SBS (0.0008) and EG (0.0016) (Quirke et al., 2015)

3.5.2 Elements, grain size, TOC and mineral relationships

The relationship between TOC and grain size and sub-depositional environment with varying Ti, Mn, Fe, V concentrations, is shown in Figures 3.7A to 3.7D. Overall, the finest grained sediments have the highest TOC concentration, and the lowest TOC concentrations are found in the medium to coarse grained sediments. The highest concentrations of Ti, Mn, Fe, V, shown by symbol size, are found in the mud-and mixed flat sediments that have the finest grain sizes and the highest TOC contents (Figs. 3.7A to 3.7D).

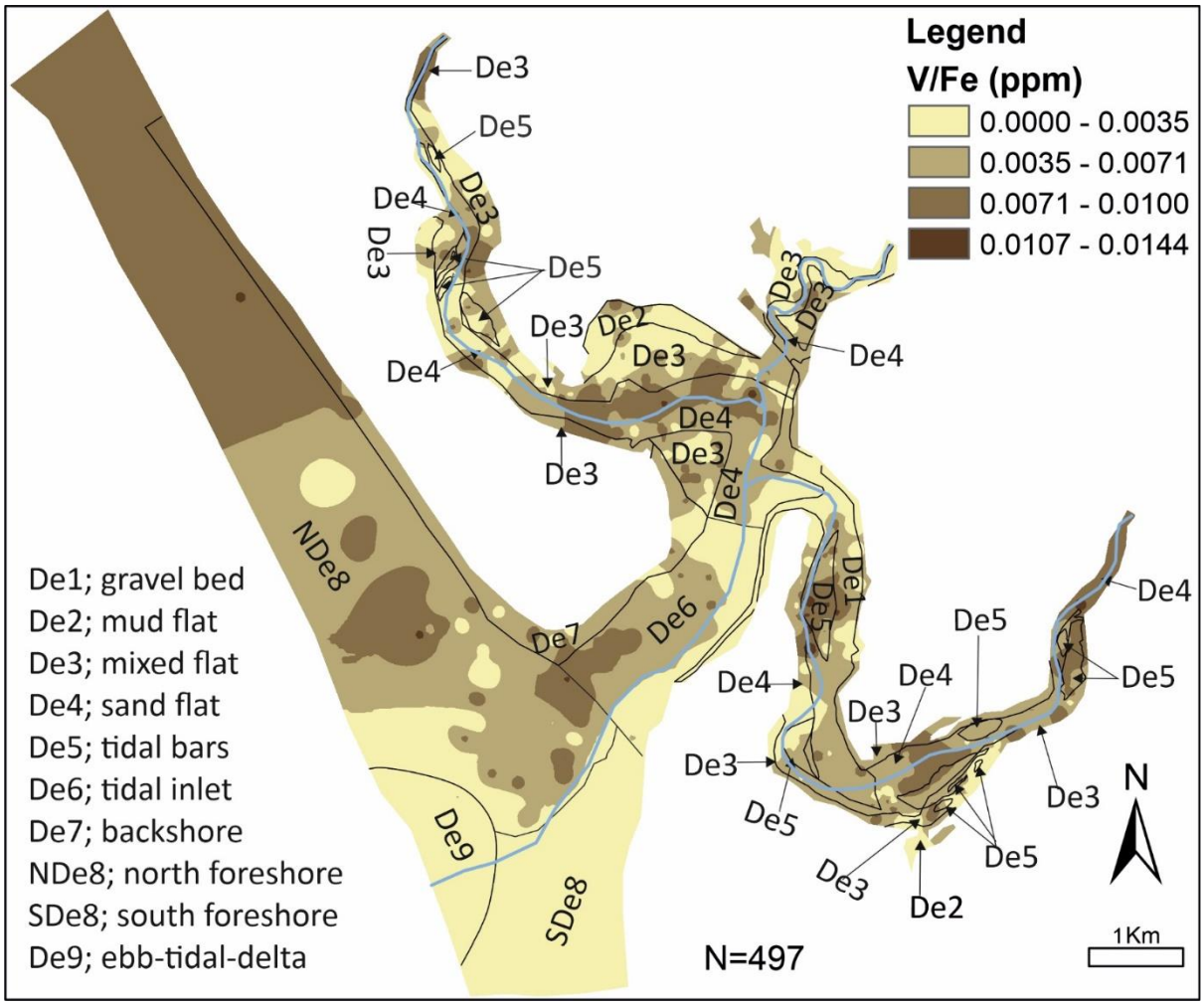

Figure 3.6; Spatial distribution of V/Fe (ppm) across the Ravenglass Estuary surface sediment. Note, Fe and V depletion in the part of inner and central estuary is caused by biological activities and redox condition. Vanadium is affected both by organic matter (through complexation and reduction) and by the effects of oxygen depletion, hence the V/Fe ratio is controlled by source rock geology, redox condition, biological activities and local estuary hydrodynamics. The V/Fe ratio in the hinterland geology ranges from 0.001-0.003 (Quirke et al., 2015) and vanadium has been reported to occur in hydrous mica and chlorite (Weeks, 1961) which are common minerals in Ravenglass Estuary.

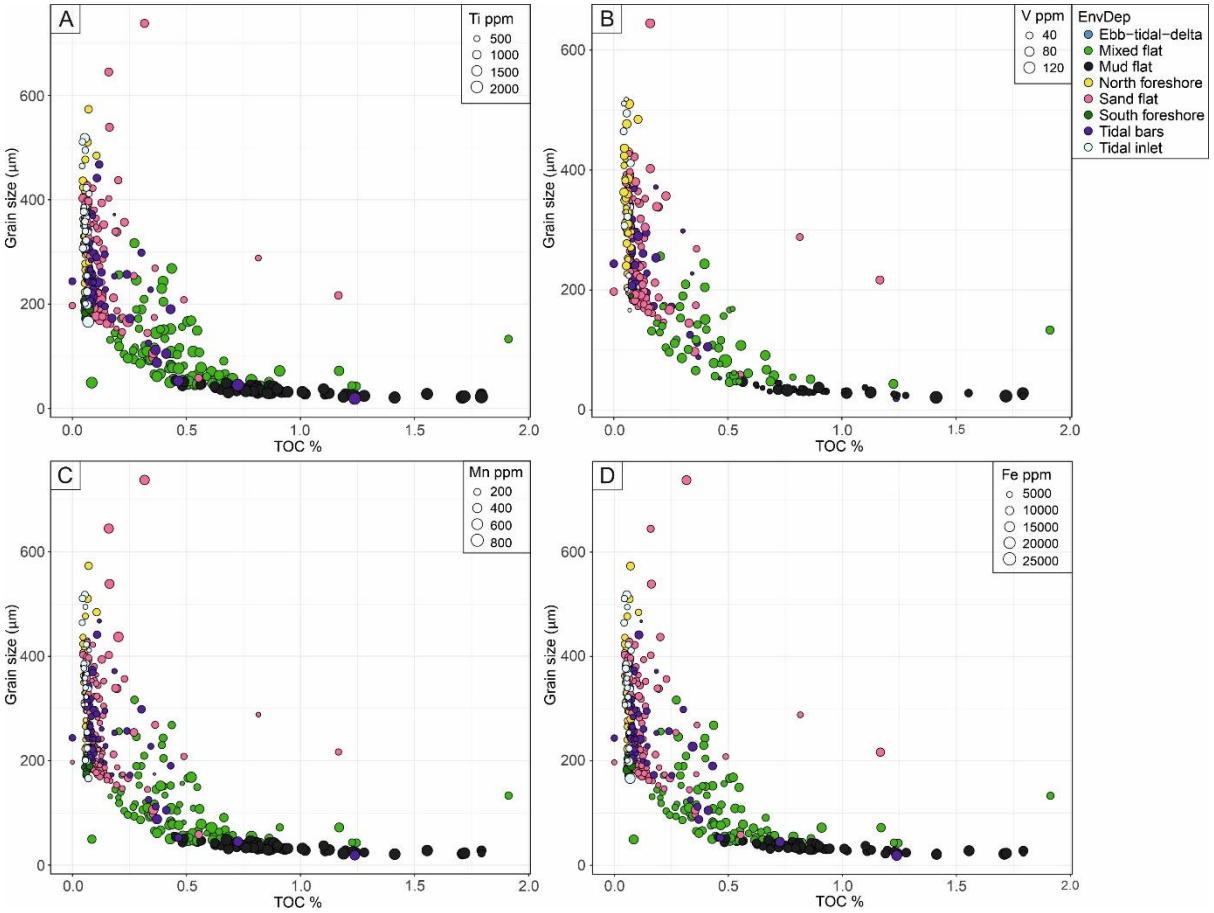

Figure 3.7; Bivariate plot of mean grain size vs TOC, (A) point size representing Ti, (B) point size representing V, (C) point size representing Mn, (D) point size representing Fe. Note Ti, V, Mn, Fe and TOC enrichment in the mud dominated sediments while sand dominated sediments have a uniformly low TOC. Ti, V, Mn and Fe distribution is somewhat uniform in the medium grain sediments but increase with decreasing grain size in the fine to clay size sediments.

The relationships between sub-depositional environment and Fe with TOC and Fe with grain size are shown in Figure 3.8. The highest Fe concentrations are found in the finest grained sediments that are also those with the highest TOC concentrations (Fig. 3.8). Fe and TOC concentrations are highest in the mud-and mixed flat sediments, revealed by symbol colour in Figure 3.8. Conversely, tidal inlet sediments tend to have the coarsest grain size, the lowest TOC and the lowest Fe concentrations.

The relationships between sub-depositional environment, Fe and V, with varying TOC and grain size, are shown in Figure 3.9. There appears to be two parts to the Fe-V relationship. Some samples show a good linear correlation with greatest enrichment of Fe (> 5,000 ppm) and V (> 60 ppm) in the mud flat and mixed flat sediments that have TOC > 1.0% and grains sizes < 200 µm. A few sand flat and tidal bar samples also seem to have elevated Fe, V and TOC and relatively fine grain size. There is a second

area to the spread of data that seems to show increasing Fe but no enrichment of V even though these samples have TOC > 1.0% and grains sizes < 200 µm. Most of these samples "high-Fe, low V" also are mud flat and mixed flat sediments but a few are also sand flat and tidal bar sediments.

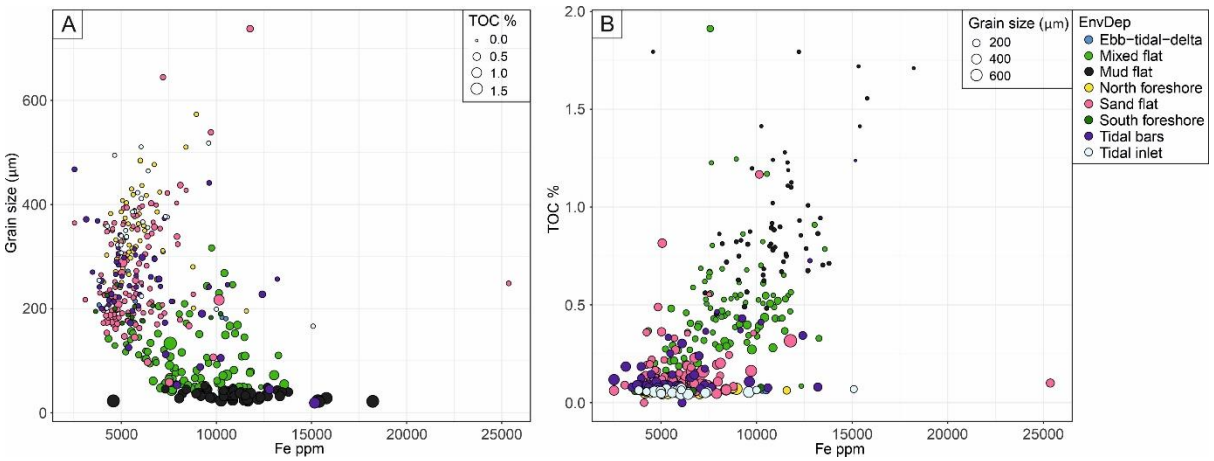

Figure 3.8; (A) Bivariate plot of mean grain size vs iron with point size representing TOC. (B) Bivariate plot of total organic carbon versus iron with point size representing mean grain size. Note, Fe increases with increasing TOC concentration, Fe enrichment in the organic rich mud dominated sediments, Fe and TOC distribution is somewhat uniform in the medium grain sediments but increase with decreasing grain size in the fine to clay size sediments. There is TOC enrichment in the mud dominated sediment. TOC and Fe distribution are controlled by grain size (surface area dependent) and hydrodynamic sorting effect.

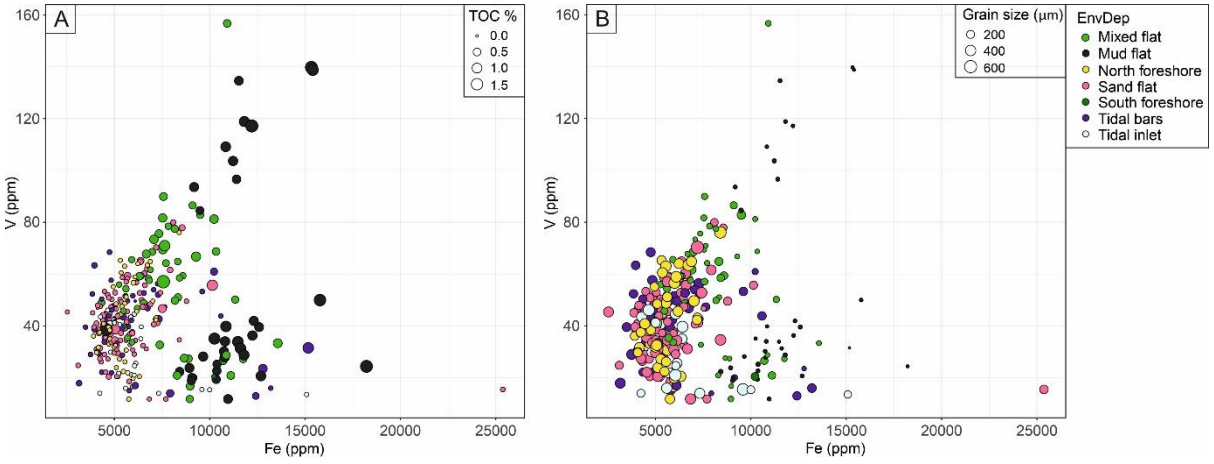

Figure 3.9; (A) Bivariate plot of vanadium vs iron with point size representing TOC. (B) Bivariate plot of vanadium versus iron with point size representing mean grain size. Note, the formation of flocculates and organo-metallic complexes in the clay rich sediments through the combination of Fe, V, TOC and fine sediments. V in the fine grain can be attached to iron oxide and weakly attached to TOC. Fe oxide grain coatings can act as metal carrier such as V. Fluvial vanadium is potentially affected both by organic matter (through complexation and reduction) and oxygen depletion. Fine sediments in the lower and upper estuary trapped significant concentration of TOC and non-detrital metals. V depletion as observed in the part of inner and central estuary is associated with localised biological activities and redox condition.

The relationships between sub-depositional environment, Fe and Ti, with varying TOC and grain size, are shown in Figure 3.10. The relationships between sub-depositional environment, Fe and Mn, with varying TOC and grain size, are shown in Figure 3.11. There is a good correlation between Fe and Ti in the different estuarine sub-depositional environments with both increasing with decreasing mean grain size and increasing TOC (Fig. 3.10). There is also a good correlation between Fe and Mn in the different estuarine sub-depositional environments with both increasing with decreasing mean grain size and increasing TOC (Fig. 3.11).

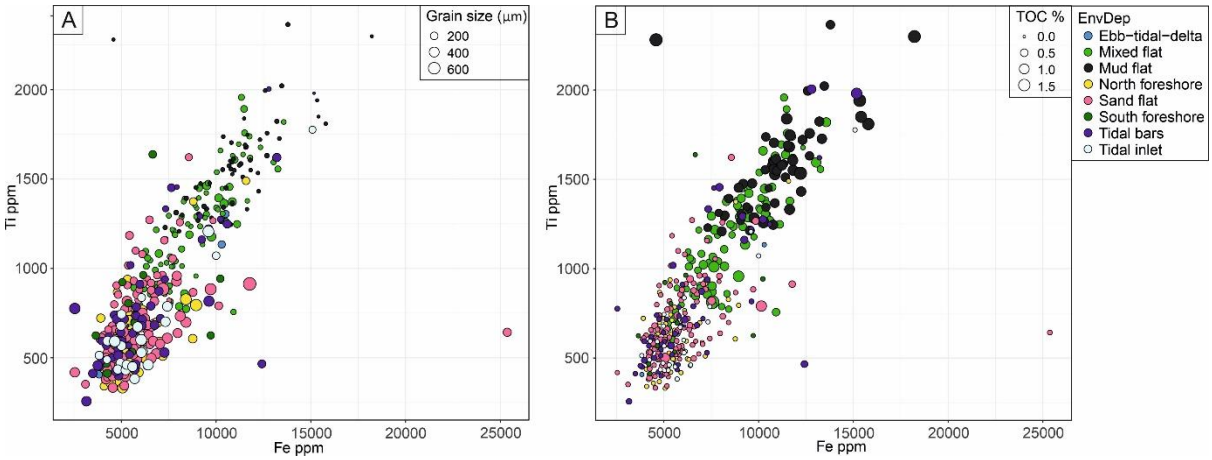

Figure 3.10; (A) Bivariate plot of titanium vs iron with point size representing mean grain size. (B) Bivariate plot of titanium versus iron with point size representing total organic carbon. Note, the distribution of Fe and Ti changes with varying grain size and TOC distribution. There is a correlation between Fe and Ti and this relationship could reveal the occurrence of Fe-Ti bearing aluminosilicates such as micas, in the coarser sediment or lithic fragment. There is significant enrichment of Fe and Ti in the mud dominated sediments and formation of organo-metallic complex with organic carbon, as fine sediments in the estuary are a major sink for TOC and non-detrital metals. Grain size and organic matter content play a significant role in Fe accumulation and distribution in the Ravenglass Estuary.

Mineral abundances, revealed by a relatively small number of SEM-EDS analyses, have been compared to total Fe concentration derived from the bulk pXRF analyses (Figure 3.12). Detrital chlorite is relatively iron-rich in Ravenglass sediment (Fig. 3.12A) (Worden et al., 2020b). Detrital illite occurs in two main types at Ravenglass: an Al-rich type and a relatively Fe-Mg-rich type and is relatively abundant and so may convey substantial Fe into the estuary (Fig. 3.12B) (Griffiths et al., 2019b). Detrital biotite is less abundant than chlorite and illite and yet is relatively Fe-rich and so may be important for the Fe budget (Fig. 3.12C). Fe-oxides are the least abundant Fe-phase identified by SEM-

EDS at Ravenglass (Fig 12D). Note that the spatial resolution of SEM-EDS is > 1 or 2 µm so that ultra-fine-grained materials cannot be identified or quantified.

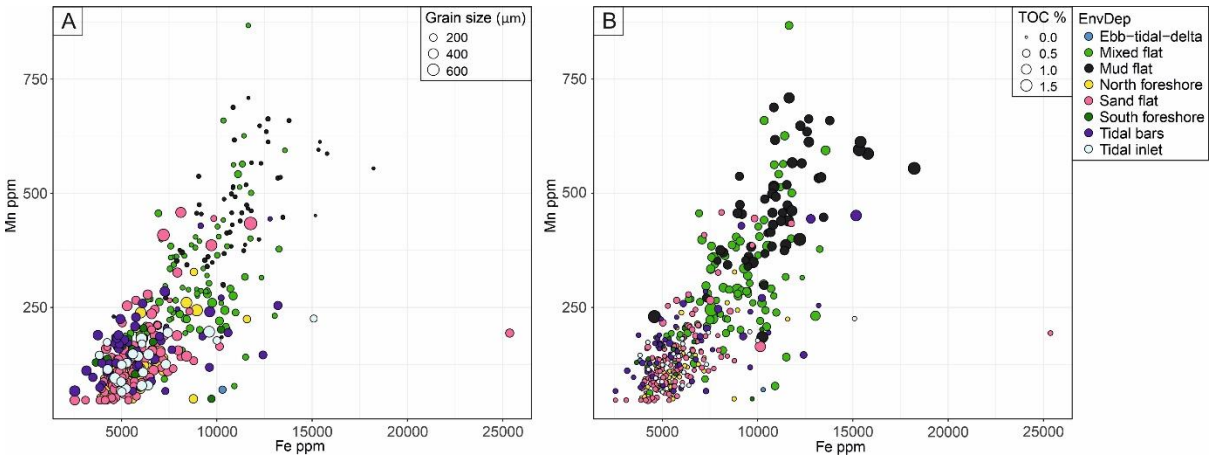

Figure 3.11; Bivariate plot of manganese vs iron with point size representing mean grain size. (B) Bivariate plot of manganese versus iron with point size representing total organic carbon. Note, the distribution of Fe and Mn changes with varying grain size and TOC distribution. There is enrichment of both Fe and Mn in the finer sediments due to formation of oxyhydroxide.

3.5.3 Geochemical indicators of provenance and mineralogy

Two useful diagrams that have been previously used to reveal primary provenance are Th/Sc versus Zr/Sc plot and TiO_2 versus Zr (Hayashi et al., 1997; McLennan et al., 1993). Zr plotted versus TiO_2 reveals that there were both mafic and felsic sources of Ravenglass sediment (Figs. 3.13A and C). Th/Sc versus Zr/Sc reveals relative inputs of basic-, intermediate- and acidic-igneous sourced material plus modifications from sediment recycling and hydraulic concentration of zircon relative to Ti-phases. Ravenglass Estuary sediment seems to have two primary sources (Figs. 3.13B and D).

The atomic fraction of Al has been plotted versus the atomic fraction of Fe to reveal what types of clay minerals are dominant in the Ravenglass sediment (Fig. 3.14). This diagram has mineral-specific atomic Fe/Al ratios superimposed. The distance along each mineral vector is dictated by the degree of dilution by other dominant elements such as Si and Ca present in quartz and calcite. Samples to the lower left of Figure 3.14 are predominantly enriched in quartz (or calcite), samples away from the lower left corner are enriched in one or more of the named mineral vectors marked on the plot.

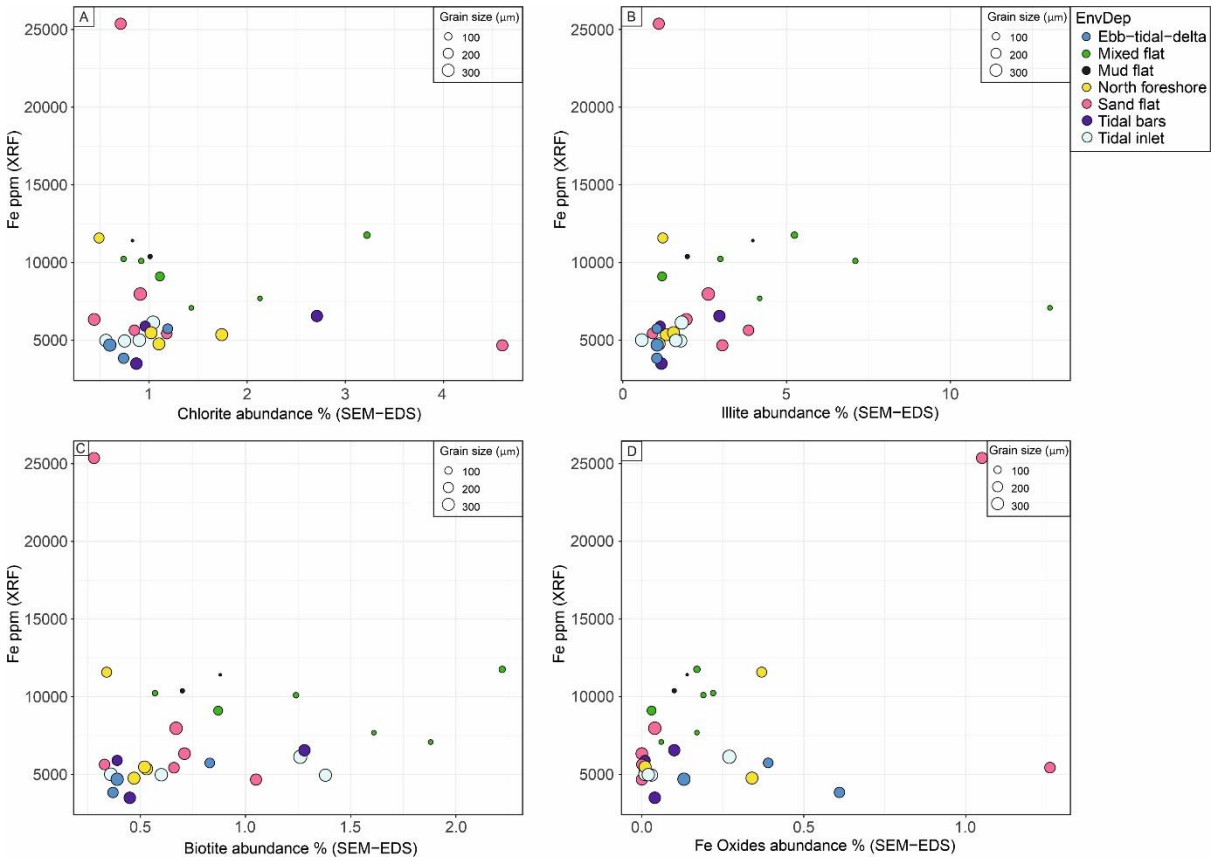

Figure 3.12; Bivariate plot of iron vs Fe-bearing minerals with point size representing mean grain size (A) chlorite, (B) illite, (C) biotite, (D) Fe-oxide. The correlation between Fe and Fe-bearing minerals signifies their coexistence and potentially source of Fe in the estuary, however, the samples independent of Fe-bearing minerals abundance, indicate that there is other form of Fe in the estuary, Fe flocculant that forms the organo-metallic complexes.

3.5.4 Pearson correlation analysis of sediment parameters

Pearson correlation values between major and trace elements, TOC and grain size are presented in Table 3.4. Iron shows strong positive correlations with Mn, Ti, Al and TOC, and a strong negative correlation with Si and grain size. Total organic carbon shows a strong positive correlation with Mn and Ti, and strong negative correlation with Si and grain size, it also shows moderate positive correlation with Al and Sc, and a weak positive correlation with Zr. Grain size shows a strong positive correlation with Si and strong negative correlation with Mn, it also shows a moderate negative correlation with Al, Zr and Sc.

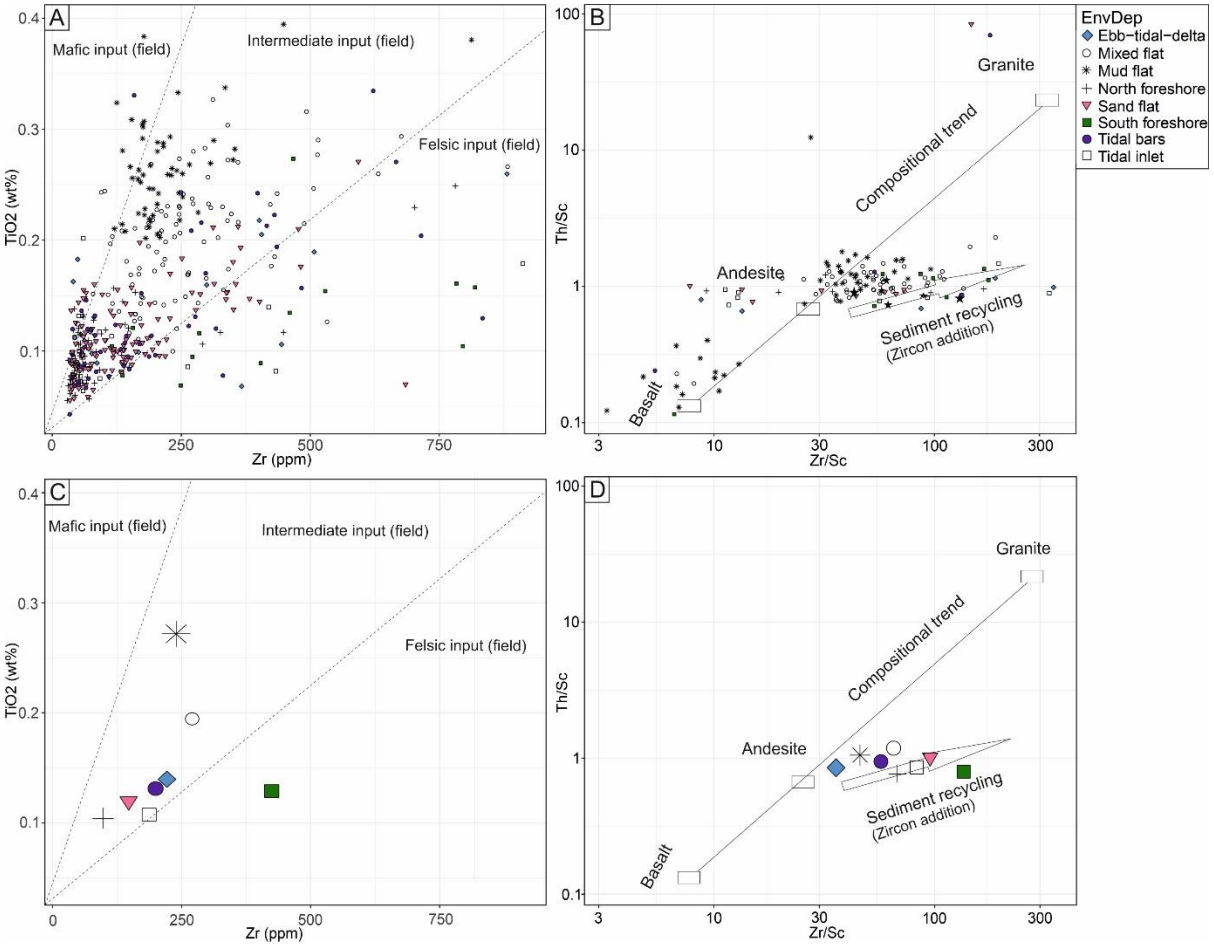

Figure 3.13; Elemental ratio for provenance (A) TiO2 (wt%) vs. Zr (ppm) (after Hayashi et al. (1997), and (B) Th/Sc vs. Zr/Sc plot (McLennan et al., 1993)for Ravenglass surface sediments. (A) The sediment compositions reveal mixed felsic and mafic sources with high degrees of dilution by quartz shown by the dense cluster of data near the origin of the graph. (B) The data reveal that much of the sediment has an intermediate igneous composition (andesitic, halfway between felsic and mafic) with zircon enrichment revealing an input of recycled sediment probably from the S-type Eskdale granite.

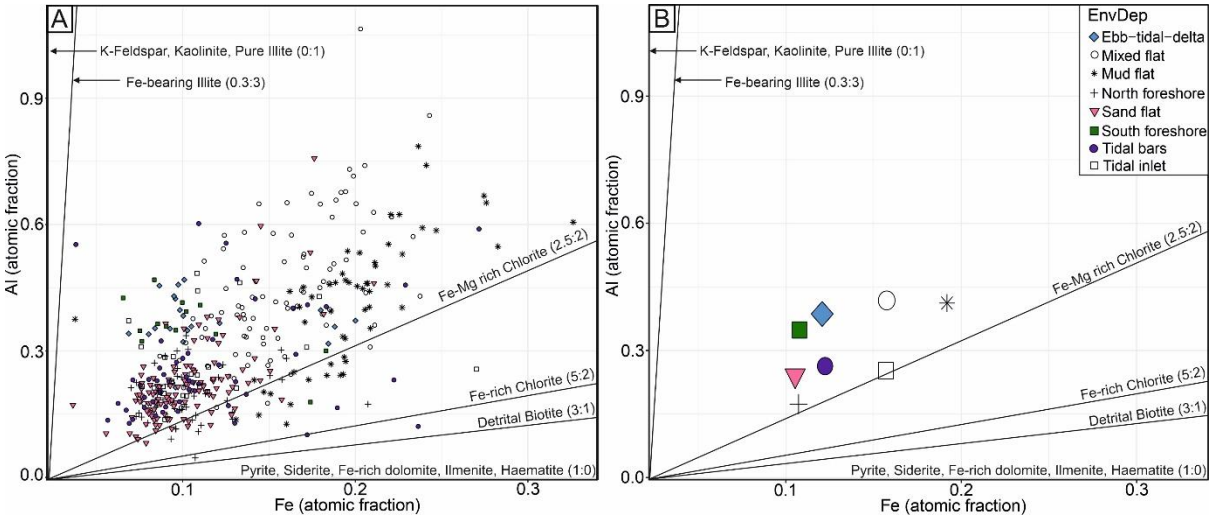

Figure 3.14; (A) Al and Fe pXRF data converted into atomic fractions, with data subdivided by sub-depositional environment and different theoretical mineral trajectories defined. Values falling close to the origin of the graph are enriched in quartz, and possibly calcite. The data do not necessarily

prove that a given mineral is dominant in the sediment at the present, but they do show what minerals might develop as the sediment samples undergo heating and gradually attain equilibrium conditions during diagenesis. (B) Same data as Fig. 3.14A, but with average values for each sub-depositional environment plotted.

3.6 Discussion

Understanding the distribution and accumulation of Fe in sedimentary deposits is a positive step towards predicting the concentration and distribution of Fe-bearing clays and their precursors. This can be achieved by identifying and establishing a link between numerous factors such as provenance, sediment mineralogy, grain size, weathering regime, redox conditions, and organic matter. These factors have been reported to exert strong controls on the distribution of Fe (Aston and Chester, 1973; Boyle et al., 1977; Forsgren et al., 1996; Mosley et al., 2003; Poulton and Canfield, 2005; Rateev et al., 2008; Roy et al., 2011; Walderhaug and Porten, 2007; Worden et al., 2020a; Zhu et al., 2012).

3.6.1 Provenance

Zircon and the high-field-strength elements (HFSE) are enriched in felsic rather than mafic rocks but in contrast Ti is enriched in mafic minerals (e.g., olivine, pyroxene, hornblende, biotite, ilmenite); these elements have been reported to reflect provenance compositions due to their generally immobile behaviour (Hayashi et al., 1997; Taylor and McLennan, 1985). In addition, geochemically relatively immobile Th and Sc can be used to infer provenance classification (Das and Haake, 2003), as their distributions are not affected by weathering or post-depositional process (McLennan, 2001). Th concentration is higher in felsic than in mafic igneous rocks, whereas Sc is higher in mafic than in felsic igneous rocks. Furthermore, ratios such as Th/Sc are significantly different in mafic and felsic source rocks. Hence, they are commonly employed in the provenance analysis of sedimentary rocks (Condie and Wronkiewicz, 1990; Cullers, 1994).

The Ravenglass sediments were sourced from both felsic and intermediate-mafic igneous rocks (Fig. 3.13A) (Daneshvar and Worden, 2017; Griffiths et al., 2018; Griffiths et al., 2019a; Griffiths et al., 2019b; Merritt and Auton, 2000). The source area drained is mostly andesitic with minor basaltic input

that was probably derived from the andesite-dominated Borrowdale Volcanic Group; the other source has a major recycled sediment input, probably derived from the S-type Eskdale granite (Fig. 3.13B) (Millward, 2002). The Esk arm drains mainly felsic sourced sediments, while the intermediate-mafic-sourced sediments were transported via the Irt arm (Daneshvar and Worden, 2017; Griffiths et al., 2018; Griffiths et al., 2019a; Griffiths et al., 2019b). Table 3.3 provides average TiO_2/Zr ratios for the four parts of the Ravenglass system. The Esk part of the estuary has the lowest ratio (0.0090) seeming to support a dominant Eskdale Granite source. The Irt part of the estuary has a high ratio (0.0132) supporting a dominant Borrowdale Volcanic Group source. On this basis the Central Basin (0.0110) has a mixed provenance with a slight predominance of an Eskdale Granite source and the outer estuary, with the highest TiO_2/Zr ratio (0.0138) seems to have a dominant Borrowdale Volcanic Group. The TiO_2 vs. Zr summary diagram (Fig. 3.13C) shows that mud flat sediment falls mostly in the mafic igneous rock field, and the southern foreshore sediments fall mostly in the felsic igneous rock field, the sand flat, tidal bars, tidal inlet, northern foreshore and ebb-tidal-delta sediments fall close to the boundary between intermediate, mafic and felsic igneous rock fields. The southern foreshore being fed by Eskdale Granite sourced sediment accords with Simon et al. (2021), who interpreted sediment movement patterns on the basis of the spatial distribution of grain size classes at Ravenglass.

Zr/Sc and Th/Sc values from Ravenglass sediment samples confirm that the sediment has an andesitic source mixed with a S-type granite (recycled sediment) source (Fig. 3.13B and D) (McLennan et al., 1993). The andesite source is the Borrowdale Volcanic Group to the north of the sediment source area, drained by the upper River Irt (Fig. 3.1B). The recycled sediment source is the S-type Eskdale Granite drained by the upper River Esk (Fig. 3.1B).

Surface sediments from the Irt arm are marked by the highest Mn, Ti, and Fe concentrations (Table 3.3), revealing a predominance of intermediate-mafic igneous source material. The relatively higher Zr concentration and lower Mn, Ti, and Fe concentrations in the Esk arm than the Irt arm of the estuary

confirms that provenance signals remain in the estuarine sediments and that the Esk had a less mafic, more felsic, supply of sediment than the Irt.

The felsic and intermediate-mafic igneous rock source areas for Ravenglass sediment contains Fe-bearing minerals such as chlorite, ilmenite, haematite, Fe-rich micas (phengite) (Moseley, 1978; Quirke et al., 2015; Rundle, 1979; Simpson, 1934; Young et al., 1986). The intermediate-mafic source area that was predominantly drained by the Irt arm, has abundant chlorite and this probably explains why the Irt sediments are relatively more Fe-enriched than the Esk sediments.

3.6.2 Sediment metal geochemistry, TOC content and sub-depositional environments

Iron distribution has been reported to be controlled by grain size and TOC (Figs. 3.4, 3.8) (Poulton and Canfield, 2005; Zhu et al., 2012). Grain size is an important parameter in determining sediment composition (Jones and Bowser, 1978), as further demonstrated, by Poulton and Canfield (2005), that river-borne Fe (mainly amorphous and crystalline iron oxide) is concentrated in finer sediments and closely associated with the concentration of clay-grade sediment and organic carbon. Grain size in the Ravenglass Estuary, decreases toward the margins of the inner estuary and central basin, mirroring the distribution of Ti, Fe, Mn and TOC (Fig. 3.3).

The finer grained sediments from tidal flat sub-depositional environments have higher concentration of Ti, Fe and Mn than sand-dominated sediments (Fig. 3.7, 3.8, 3.10 & 3.11). Similar types of patterns have been explained previously as being the result of metal-scavenging phases such as Fe- and Mn-hydroxides, organic carbon (via metal-organic complexes), and clay minerals are more abundant in silt and clay fractions than in sand (Padmalal et al., 1997; Padmalal and Seralathan, 1995). Transported-in clay minerals in estuary brackish waters exacerbate the occurrence of Fe sedimentation by the creation of Fe-rich floccules and sorption of Fe (Forsgren et al., 1996). Clay grade sediment, owing to its large surface area, acts as a mechanical substrate upon which some constituents (e.g., Fe and Mn oxides/hydroxides, organic matter) can become attached (Horowitz and Elrick, 1987). The complexation of the Fe (and Mn) and TOC, in the mud and mixed flat sub-depositional environments,

provide materials required for the subsequent formation of Fe-bearing minerals in the estuary (Berner, 1970; Lalonde et al., 2012). This explains the enrichment of Fe in fine grained sediments in the estuary (Fig. 3.15).

In contrast to the pattern of Fe-enrichment in the finest sediments, the correlation between Fe and Ti in coarser sediments of sand dominated sub-depositional environments (Fig. 3.10 & 3.12C), is probably a result of the occurrence of different Fe- and Ti-bearing detrital aluminosilicates minerals such as micas and chlorite, in sand-grade lithics, owing to the hydrodynamic concentration of coarser sediments (Fig. 3.15) (Griffiths et al., 2019a; Worden et al., 2020a). Coarser sand-grade sediment is typically richer in lithic grains than fine sand (Kairo et al., 1993) so that elevated Fe from lithics in the coarser sand is not unexpected. This interpretation is in agreement with the reported occurrence of chlorite-bearing lithic grains in the coarser sands from foreshore, tidal inlet, and tidal bar sub-depositional environments in Ravenglass Estuary (Griffiths et al., 2019b). These chlorite- and biotite-bearing lithics have survived initial weathering and transport and then been deposited with sand because of their relatively high resistance to chemical weathering, compared to lithic grains composed of high temperature minerals such as olivine, pyroxene and amphibole (Worden et al., 2020a).

Vanadium, an element potentially related to organic carbon via porphyrins and other complex organic compounds (Breit and Wanty, 1991; Premović et al., 1986), shows a complex pattern with Fe, TOC and grain size (Fig. 3.9). Some Fe-rich, fine-grained sediment has elevated V concentration; other Fe-rich, fine-grained sediment has low V concentration. We suggest that this difference is caused by biologically-induced changes in redox conditions, whereby V depletion is due to localised chemical reduction linked to the presence of organic material i.e., algae or vegetation (Shiller and Boyle, 1987; Shiller and Mao, 1999). Particulate V concentration in estuary waters rapidly decreases with increasing salinity (Bauer et al., 2017), closely matching Fe concentration behaviour (Bauer et al., 2017; Boyle et al., 1977). This suggests that V and Fe behaviour may be genetically linked. However, V behaviour also varies as a function of redox state in the sediment with locally elevated V in the dissolved form

occurring in the Mn and Fe redox zone that lies beneath the sediment's oxic zone before decreasing again in the bacterial sulphide reduction zone (Bauer et al., 2017).

It is possible that the map of the ratio of V/Fe (Fig. 3.6) represents localised metal (Fe and Mn) reduction, associated with V mobilisation, and thus V loss from the local sediment. Both Fe and V are affected by the presence of organic matter (through complexation, providing ingredients needed for microbial activity and chemical oxidation and reduction), hence their distribution is influenced by redox condition and biological activities (Fig. 3.6 & 3.9). The mud flats (De2), on the northern side of the central basin, have high TOC (Fig. 3.4B) and high Fe (Fig. 3.3E) and yet are locally enriched and locally depleted in V (with two distinct V/Fe patterns, Fig. 3.6) suggesting that the mud flats are geochemically heterogeneous in terms of the processes controlling V. Based on the data available, it is not yet clear what has caused this trace element heterogeneity.

3.6.3 Types of Fe present

Iron in sediment is mainly present as either reactive amorphous and semi-crystalline iron oxide or less reactive Fe that primarily sits in aluminosilicate minerals (such as clay minerals or detrital chlorite or biotite), haematite or siderite (Li et al., 2017; Poulton and Raiswell, 2005). The reactive amorphous and semi-crystalline iron oxide phases are usually found within the oxic, near-surface sediment layer (Canfield, 1997; Poulton and Raiswell, 2005), which, over time and during eodiagenesis, becomes more crystalline. Organic matter hinders this crystallisation process (Schwertmann, 1966).

Iron in estuarine sediment, measured here by pXRF, seems to show no obvious relationship to the concentration any of the Fe-minerals identified by SEM-EDS (Fig. 3.12). However, it is noteworthy that the greatest Fe mineral concentrations are not associated with the two sub-depositional environments that have the highest Fe-concentration (mud flat or mixed flat sediments; Figs. 3.7-3.11). This anomaly suggests that SEM-EDS has not been able to identify the Fe-phase present in these sub-depositional environments, probably as it is too fine grained to be resolved by this technique (Fig. 3.12). To be clear, this suggests that SEM-EDS, with its spatial resolution of 2 µm, has not managed to

analyse or identify the dominant Fe-phase present in these sub-depositional environments, probably as the Fe-phase is too fine grained to be resolved by this technique. This leads us to conclude that much of the Fe in the sediment in the Ravenglass Estuary is composed of sub-2 µm sized, reactive amorphous and semi-crystalline iron oxide. Note that the highest concentrations of Fe are associated with the highest organic carbon concentrations (Figs. 3.7D, 3.8B) and the finest grained sediment (Figs. 3.7D, 3.8A) in tidal flat sub-depositional environments (Fig. 3.8, 3.12 & 3.15). This further suggests that the Fe may have been transported by rivers into the estuary, in an Fe-organic-complex form, that was flocculated when the river water met elevated salinity in the estuary. The resulting flocs were deposited along with first sediment fraction (clay) with the highest concentration occurring in the most clay-rich sediment (Figs. 3.3E, 3.4A, 3.4B).

3.6.4 Occurrence of Fe-clay

The use of geochemical data to discriminate lithology, which may reflect mineral composition of sediment, has been well documented (Herron, 1986; Herron, 1988). The potential presence and relative abundance of chlorite can be determined from the relationship between Fe-Al (Fig. 3.14). Samples furthest from the origin on Figure 3.14, are most enriched in the minerals linked to the vectors and least enriched in the dominant diluting minerals of quartz and calcite. Mixed flat and mud flat sediments are least enriched in quartz. The main mineral responsible for Fe enrichment seem to be Fe-Mg rich chlorite but enrichment with minerals such as Fe-oxide or biotite cannot be ruled out (as Figure 3.14 does not represent the minerals that are present so much as the minerals that could be present based on the chemical ingredients. Fe-Mg rich chlorite also brings Al into the sediment but much of the Al will be carried by illite, kaolinite and K-feldspar as illustrated by the deviation of the data points from the Fe-Mg rich chlorite line towards the Y-axis.

Figure 3.14 shows what minerals might develop during subsequent diagenetic modification of the sediment during eodiagenesis and mesodiagenesis. Samples closest to the Y-axis will develop Al-rich clay minerals such as illite and kaolinite, whereas samples in the middle and towards the X-axis will

develop Fe-rich clay minerals, such as chlorite and its precursors (Fig. 3.14). On this basis, northern foreshore (NDe8), tidal inlet (De6), sand flat (De4), tidal bar (De4) and mud flat (De2) sub-depositional environments would be more likely to be Fe clay enriched than southern foreshore (SDe8), ebb-tidal delta (De9) and mixed flat (De3) sub-depositional environments (Fig. 3.14B), once the sediments have undergone eodiagenesis and mesodiagenesis. This at least partly reinforces the results of mineralogical studies of Ravenglass Estuary sediment (Griffiths et al., 2019b).

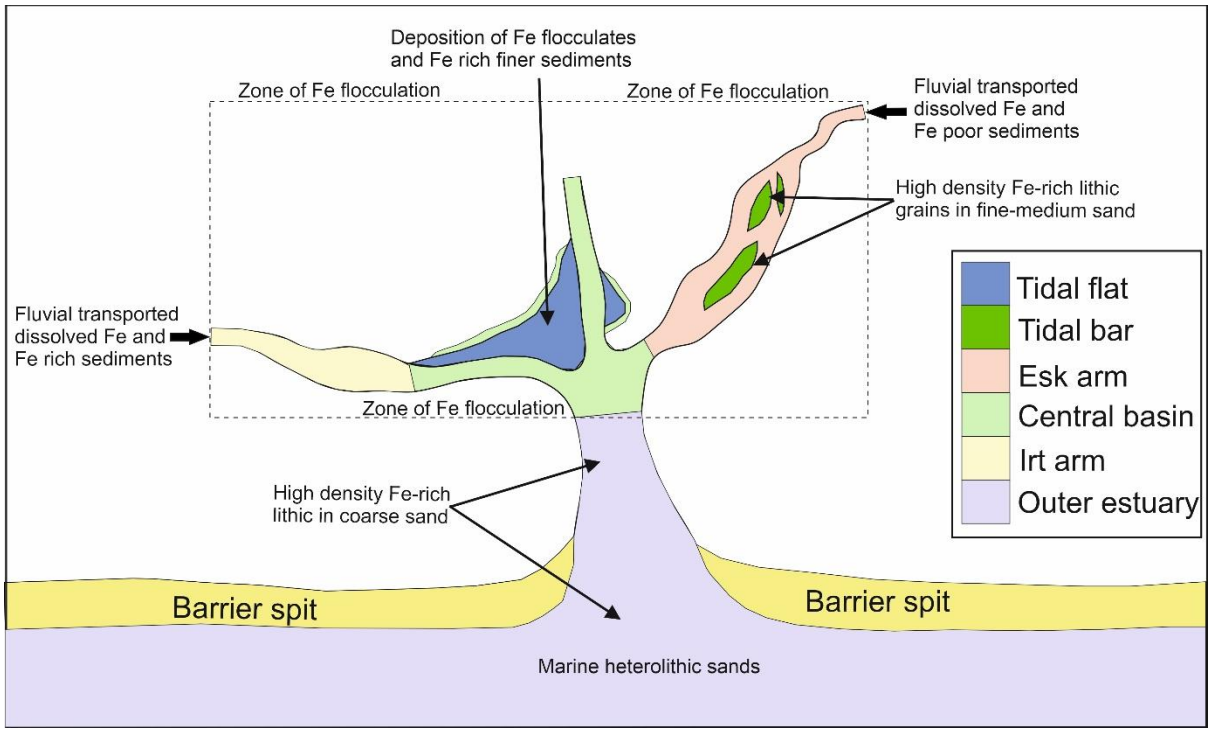

Figure 3.15; Conceptual model showing the distribution of Fe in the Ravenglass Estuary.

However, enrichment of Fe in sediment does not guarantee that Fe-clay minerals such as chlorite, or its precursors, will develop. If sediment has pore-waters dominated by sulphate-rich seawater, if the sediment is enriched in organic matter and if the sediment is buried sufficiently slowly, then bacterial sulphate reduction can occur creating H_2S that reacts with available Fe-phases to create eodiagenetic Fe-sulphides (e.g., pyrite) (Berner, 1970; Berner, 1980). The phenomenon of pyrite growth in Fe-rich sediment therefore inhibits the formation of eogenetic Fe-clay minerals and subsequent mesogenetic chlorite due to sequestration of Fe (Worden et al., 2020a). Similarly, in the absence of sulphate-rich marine pore-waters, oxidation of organic-enriched sediment can lead to elevated aqueous

bicarbonate concentrations due to a wide range of bacterial oxidation processes. If bicarbonate-enriched pore waters encounter sediment that is enriched in Fe, then siderite can develop (Worden and Burley, 2003).

Like the situation for pyrite growth, siderite growth in Fe-rich sediment inhibits the formation of eogenetic Fe-clay minerals and subsequent mesogenetic chlorite due to sequestration of Fe (Worden et al., 2020a). Pyrite is not present in the surface sediments at Ravenglass but it has been reported in 1-m cores, especially in the inner portion of the estuary (Griffiths et al., 2018) where we now know there is relative enrichment of organic matter in the estuary (Figs. 3.4B, 3.7, 3.8). This suggests that some of the most Fe-enriched sediments, that are also TOC-enriched, may result in pyrite development instead of Fe clay mineral development, if the pore waters are enriched in marine sulphate. Estuary waters have the lowest sulphate concentrations in the upper estuary (Daneshvar, 2015), so that Fe-enriched sites highest up the estuary may be most likely to leave Fe capable of creating Fe clay minerals rather than pyrite. In contrast, it is noteworthy that little or no siderite has been reported from the surface sediments from Ravenglass distribution (Daneshvar, 2015; Daneshvar and Worden, 2017; Griffiths et al., 2018; Griffiths et al., 2019a; Griffiths et al., 2019b), suggesting that siderite has not developed at the expense of Fe-clay minerals in this type of environmental setting, despite the local abundance of organic matter (Figs. 3.4B, 3.7, 3.8).

3.7 Conclusions

1. Portable XRF analysis can be used to help identify the provenance of sediment in estuaries. The trace and major element compositions of the different arms of the Ravenglass Estuary, can be used to help discern the different hinterland lithologies.

2. Portable XRF analysis can be used as a proxy for what minerals might develop in estuarine sediment, i.e., during eo- or meso-diagenesis, but it cannot be employed to unequivocally reveal present-day mineralogy.

3. Iron increases from the river to the estuary with some local variations and then gradually decrease seaward, the Fe concentration is highest in tidal flat. Iron is present in detrital Fe minerals including chlorite, biotite, Fe-bearing white mica, and minor Fe-oxides that are mainly present within lithic grains. Iron is also present as a fine-grained material, probably an oxide or hydroxide, that is below the spatial resolution of SEM-EDS (therefore < 2 μm), that is associated with elevated organic carbon concentrations. The fine-grained Fe may be brought into the estuary as fluvially-derived metal-organic complexes that are destabilised in the saline waters of the estuary and settle out as floccules or coats on sand grains.

4. The distribution and accumulation of Fe in the estuarine sediments are controlled by hinterland lithology and degree of weathering, sediment grain size, organic enrichment of the supplied sediment, and local estuary hydrodynamic conditions.

4. Understanding the distribution of clay minerals in modern estuarine sediment based on geochemical classification of environments and petrographic analysis.

4.1 Abstract

Sandstones deposited in marginal marine settings, such as estuaries and deltas, can contain chlorite-coated sand grains; in deeply buried (> 3000 m) sandstone reservoirs, these grain coats can have a positive impact on reservoir quality by inhibiting quartz overgrowths. There is limited understanding of the controls on the distribution of clay minerals thus hindering the prediction of chlorite grain-coats. This study focused on Holocene sediment mineralogy and sub-depositional environments in an estuarine environment from Ravenglass, NW England, UK. A geochemical-based classification scheme was employed to define palaeo-sub-depositional environments from cores using bulk element geochemistry. SEM-EDS-, grain size-, and image-analysis were used to understand the distribution of different clay mineral types and clay coats. Results show that the dominant minerals of the inner estuary sediments are quartz, K-feldspar, plagioclase, muscovite, biotite, illite, chlorite, kaolinite, and smectite. Clay mineral distributions vary greatly between the different sub-depositional environments; chlorite is relatively most abundant in the sand flat and tidal inlet and is likely to occur as clay forming grain coats or as lithic grains in coarser sediment, kaolinite is relatively most abundant in the mixed flat, smectite is relatively most abundant in the ebb-tidal-delta, north foreshore and tidal inlet, illite is relatively most abundant in the salt-marsh and mud flat. Clay occur as either pore-filling or grain-coating material in the salt-marsh and mud flat, with over 40% coat coverage. In the mixed flat, sand flat and tidal bar sediment, clay is mostly present as grain coat with coat coverage of as much as 40%. The tidal inlet, foreshore and ebb-tidal-delta have a coat coverage of as much as 5%. Clay coat coverage increases with increasing clay fraction abundance. Sand flat and tidal bar sediments have >10% detrital coat coverage, and that contain chlorite-bearing lithic grains, can form diagenetic chlorite coats that can preserve anomalously high porosity in inhibiting quarts cementation, in deeply buried sandstones. The distribution patterns of sediment mineralogy and different clay mineral types in the Ravenglass Estuary Holocene core, are primarily controlled by the grain size and estuarine hydrodynamics. Post-depositional processes, particularly early-diagenetic mineral alteration appeared to have influenced clay-mineral distribution patterns, in the coarser sediment of Ravenglass Holocene cores, via mineral alteration of feldspar grains.

4.2 Introduction

Sandstones in marginal marine systems, such as estuaries and deltas, have the potential to develop clay coated sand grains (Dowey et al., 2012; Dowey et al., 2017; Pittman et al., 1992; Worden and Morad, 2003). Chlorite grain coats can have a positive impact on reservoir quality in deeply buried sandstone reservoirs (> 3000 m), by inhibiting quartz overgrowths (Ajdukiewicz and Lander, 2010; Ajdukiewicz and Larese, 2012; Bloch and Helmold, 1995; Bloch et al., 2002; Ehrenberg, 1993; Worden et al., 2020a; Worden and Morad, 2003). Sediment mineralogy and coat coverage therefore exert a strong control on the ability of clay coats on sand grains to preserve reservoir quality (Ajdukiewicz and Larese, 2012; Billault et al., 2003; Bloch et al., 2002; Lander et al., 2008). Consequently, there is a need to understand the controls on clay mineral distribution patterns at a scale relevant to oil and gas reservoirs. There is, however, a paucity of research, knowledge and understanding about the relationships between environment of deposition and post-depositional processes, in terms of the origin and distribution of reservoir quality controlling clay minerals.

The composition of sedimentary deposits is typically heterogenous in terms of total clay content, sediment mineralogy, grain size and grain sorting. The distribution of sediment mineralogy, especially clay minerals, has been studied in modern marginal marine environments (Dalrymple et al., 1992; Dowey et al., 2017; Griffiths et al., 2018; Griffiths et al., 2019a; Griffiths et al., 2019b; Wooldridge et al., 2017a; Wooldridge et al., 2017b; Wooldridge et al., 2019a); this modern analogue work has made it possible to link geographic locations and depositional environments to the abundance of clay minerals, and especially that of chlorite. The most common origin of clay minerals in marginal marine (estuarine) environments as summarised (Aagaard et al., 2000; Bokuniewicz, 1995; Daneshvar and Worden, 2017; Sionneau et al., 2008; Tucker, 2001; Worden and Morad, 2003) are;

- Inherited clay minerals that originated from either weathering profiles or soil and drift deposits in a fluvial hinterland,

- Neo-formed clay minerals that originated from other pre-existing aluminosilicate minerals such as feldspars, and
- Transformed clay minerals that originated from precursor clay minerals.

Clay minerals which originate in hinterlands (inherited clay minerals) can be transported as suspended load into the estuarine environment through fluvial system (Fan et al., 2008; Zhang et al., 1990). In modern sedimentary systems, clay mineral distribution has been reported to reflect weathering patterns (Thiry, 2000; Tucker, 2001), whereas neo-formed clay minerals have been interpreted to derive from alteration of pre-existing aluminosilicates during diagenesis (Bjorlykke, 1998; Worden and Morad, 2003). Chlorite can originate from the transformation of specific clay precursors or pre-existing clays (Beaufort et al., 2015; Haile et al., 2015; Storvoll et al., 2002; Worden and Morad, 2003), or in a low-temperature brines (<220^{o}C), through a range of chloritisation processes (Ajdukiewicz and Lander, 2010).

Estuaries are influenced by both fluvial and marine processes that collectively control mineral distribution patterns (Berner and Berner, 2012). Estuaries serve as efficient sediment traps which have a high preservation potential during marine transgression (Boyle et al., 1974; Boyle et al., 1977; Dalrymple et al., 1992). The formation of minerals *in situ* in mixed fluvial-marine pore waters through direct growth (neoformation), and transformation of detrital minerals (Aller and Aller, 1998; Berner, 1980; Feininger, 2013), may occur in an estuarine environment. These processes usually take place soon after deposition, within the depositional environment (Berner, 1980; McIlroy et al., 2003; Worden and Burley, 2003; Worden and Morad, 2003). Climatic conditions, which in turn define weathering intensity and degree of alteration of hinterland geology, is a major factor controlling the type and relative abundance of clay minerals found in modern coastal settings (Chamley, 1989; Eberl et al., 1984; Rateev et al., 2008). Under cold climatic conditions, where mechanical weathering is dominant, chlorite and illite are reported to be the most abundant types of clay (Chamley, 1989; Eberl et al., 1984; Rateev et al., 2008; Windom, 1976). In contrast, in warm and humid climatic conditions,

with intense chemical weathering, kaolinite is reported to be the most abundant type of clay (Chamley, 1989; Eberl et al., 1984; Rateev et al., 2008; Windom, 1976). Smectite generally represents an early stage of chemical weathering, typical of semi-arid climatic conditions (Salem et al., 2000). In an estuarine setting, the redistribution of deposited sediment is controlled primarily by hydrodynamic processes; the physical forces of river flow, wave energy and twice-daily tidal actions combine to distribute the deposited sediment into corresponding sub-depositional environments, such as salt marshes, mud flats, tidal bars, tidal inlet, foreshore and ebb-tidal-delta (Dalrymple et al., 1992).

Early diagenesis can alter the mineralogy of sediment within the environment of deposition through different processes; it may represent a continuation of physical and chemical processes that started at the initial weathering site (hinterland). However, sediment deposited in estuaries is likely to be in a state of thermodynamic disequilibrium and, therefore, remains geochemically active, especially in the presence of organic matter, and a range of micro- and macro-biological communities (Berner and Berner, 2012). There are numerous reports on early-diagenetic mineral alteration in an estuarine setting, attributed to both physicochemical processes (Daneshvar and Worden, 2017; Griffin and Ingram, 1955; Grim and Johns, 1954; Nelson, 1960; Powers, 1957) and biologically-mediated processes (McIlroy et al., 2003; Needham et al., 2004; Worden et al., 2006). Deltaic sediment at Amazon River mouth undergoes rapid alteration of clay minerals and the accumulation of biogenic silica (Aller and Michalopoulos, 1999; Michalopoulos and Aller, 1995; Michalopoulos and Aller, 2004; Michalopoulos et al., 2000). Diagenetic processes in estuarine depositional environments include the formation of kaolinite and/or illite from feldspar alteration, the transformation of mixed-layer chlorite to Fe-rich chlorite and the precipitation of gibbsite at the expense of kaolinite (Daneshvar and Worden, 2017; Drever and Zobrist, 1992; Huang, 1993; Velde and Church, 1999; Worden and Morad, 2003).

Understanding the primary depositional conditions in a modern sedimentary system may serve to better constrain controls on sediment mineralogy and its impact on the distribution of clay mineral

types and abundance, clay coat and clay precursors (Ehrenberg, 1993; Saïag et al., 2016). Detrital clays have been reported to form clay coats on sand grains in tidal flat environment location (Dowey et al., 2017; Wooldridge et al., 2017b; Wooldridge et al., 2019a). However, an extensive understanding regarding the formation and distribution of detrital clay grain coats in marginal marine sands, has not been established (Dowey et al., 2017; Griffiths et al., 2018; Wooldridge et al., 2017b; Wooldridge et al., 2019a; Worden and Morad, 2003).

During depositional processes, clay-sized and sand-sized fractions tend to separate by hydrodynamic processes (Virolle et al., 2019a). The incorporation of clay minerals into sand has not been fully explained; several reports have linked this phenomenon to the infiltration of clay, or the influence of bioturbation (Matlack et al., 1989; Needham et al., 2006; Needham et al., 2004; Needham et al., 2005; Saïag et al., 2016; Wilson, 1992; Worden and Morad, 2003; Worden et al., 2006). The origin and distribution of clay coats in sandstones are also not well known. There are few studies of modern clastic deposits, such as tidal bars; this has made the prediction of clay coats during reservoir quality studies relatively difficult (Ehrenberg, 1993; Wooldridge et al., 2017b; Worden and Morad, 2003). The origin and distribution of clay minerals and clay coats in the depositional environments of the Ravenglass Estuary, have been previously investigated (Daneshvar, 2015; Daneshvar and Worden, 2017; Griffiths et al., 2018; Griffiths et al., 2019a; Griffiths et al., 2019b; Wooldridge et al., 2017a; Wooldridge et al., 2017b; Wooldridge et al., 2019a; Worden et al., 2020a) This present research was designed to advance the study of sediment mineralogy and Holocene palaeoenvironments in an estuarine environment, and to investigate the relationship between clay abundance, clay coat occurrence, mineral alteration and early diagenetic processes. In this study, the main research questions are:

1. What Holocene sub-depositional environments are represented beneath a present-day vegetated tidal bar in the Ravenglass Estuary? how do they relate to the lithostratigraphic correlation of Ravenglass Holocene sediment?

2. What is the dominant mineral assemblage within the Holocene sub-depositional environment?

3. How are clay minerals distributed and what controls clay-mineral distribution patterns?

4. Is it possible to predict the distribution of clay minerals, and specifically clay coat minerals as a function of sub-depositional environments in the Ravenglass Estuary?

4.3 Study area: Ravenglass Estuary

The Ravenglass Estuary covers about 5.6 km^2; the estuary is situated on the west coast of Cumbria in northwest England, UK (Fig. 4.1A). It is a macro-tidal estuary, with a maximum recorded tidal range of ~ 7.55 m; up to about 86 % of the area of the estuary is exposed at low tide (Bousher, 1999; Griffiths et al., 2018; Griffiths et al., 2019a; Griffiths et al., 2019b; Lloyd et al., 2013; Wooldridge et al., 2017a; Wooldridge et al., 2017b). The estuary stretches east (i.e., landward) up to the tidal reaches of the Rivers Mite, Irt and Esk, and to the west (i.e., seaward), it is connected to the Irish Sea through a 500 m-wide tidal inlet that flows between two, dune-topped coastal spits (Drigg and Eskmeals Spits). These barrier-coastal spits shelter the estuary from wave-action but the estuary is exposed to periodic tidal currents as result of the macro-tidal regime.

Sediments are fed into the estuary via the Rivers Mite, Irt and Esk with reported average flow-rates of 0.04 m^3s^{-1} , 0.34 m^3s^{-1} , and 0.42 m^3s^{-1}, respectively (Bousher, 1999). According to Kelly et al. (1991), the Ravenglass Estuary is tide- and wave-dominated. The estuary's shallow bathymetry causes frictional effects and, thus, promotes strong tidal-asymmetry, with a longer outward ebb tidal-flow than inward flood tidal-flow. The estuary is brackish in the river- and tide dominated Irt, Mite, and Esk inner parts of the estuary. The estuary's central region, dominated by Saltcoats tidal flats, has mixed-energy with near-seawater salinity. The outer estuary, including the main tidal channel, estuary mouth and the foreshore, is dominated by seawater with wave and/or tidal currents.

The impact of anthropogenic activities in the Ravenglass Estuary is insignificant, because of the sparse population of its surrounding environment. However, the effect of population on the natural

environment is profound. Pretty much all of the UK, including Ravenglass, is not 'natural'. E.g. the present of sheep farms bordering the estuary along the salt coat, and that means the vegetation is partly as a result of farming practices. Additionally, the construction of railway bridge in 1868 led to the expansion of the salt marsh, thereby protecting the lower reaches of River Mite from tidal currents (Carr and Blackley, 1986). Numerous research studies have been conducted on this estuary, in terms of sedimentary processes, stratigraphic evolution, and the origin and distribution of detrital clay mineralogy and clay coats (Daneshvar, 2015; Daneshvar and Worden, 2017; Griffiths et al., 2018; Griffiths et al., 2019a; Griffiths et al., 2019b; McGhee et al., 2021; Simon et al., 2021; Wooldridge et al., 2017a; Wooldridge et al., 2017b). Ravenglass thus represents an ideal field site to answer the research questions set out in the introduction.

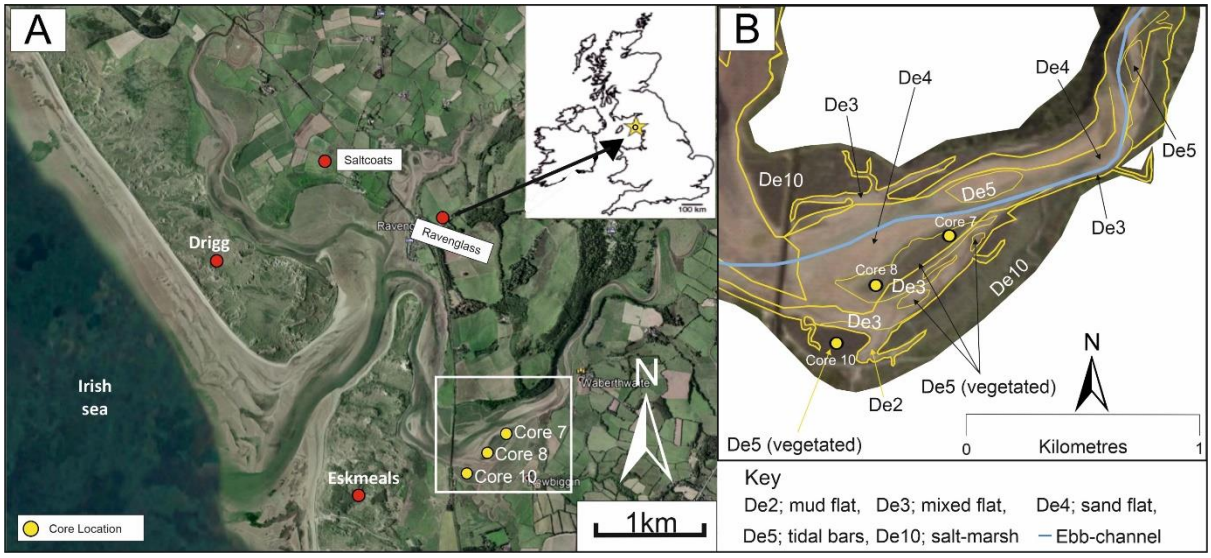

Figure 4.1; Location map of the Ravenglass Estuary, north-west England with an inset map showing the location of the estuary in the UK, the yellow dot shows the location of core. (B) Sub-depositional environment map with boundary superimposed showing the tidal bar core sites.

4.3.1 Geological setting and provenance

Ravenglass Estuary sediments are sourced from a range of different bedrock types and Quaternary drift-deposits (Daneshvar and Worden, 2017; Griffiths et al., 2018; Griffiths et al., 2019a; Griffiths et al., 2019b). The source area is composed of the Devonian Eskdale Granite, the Ordovician Borrowdale Volcanic Group (BVG), the Triassic Sherwood Sandstone Group and the Cambrian Skiddaw Group slate.

The Devonian Eskdale Granite is reported to be largest exposed intrusion in Cumbria (Soper, 1987) and forms part of the Lake District Batholith, along the western-margin of the Lake District massif (Quirke et al., 2015). Hydrothermal mineralisation of some part of granite components, the mafic silicates and plagioclase has caused a significant chlorite alteration (Moseley, 1978; Quirke et al., 2015; Rundle, 1979; Young et al., 1986). The Skiddaw Group is a fine-grained (metapelitic) sedimentary rocks that has been weakly metamorphosed (Merritt and Auton, 2000).

The Ordovician Borrowdale Volcanic Group is present in the Lake District in two different outcrops; the older exposed in the north-west and the younger exposed in the south-east (Entwisle et al., 2005). These extrusive rock suites are comprised mainly of subduction-related, K-rich, calc-alkaline basalt, andesitic-rhyolitic volcanic lavas, sills and pyroclastic rocks, and constitute the central part of the Lake District massif (Millward, 2004; Quirke et al., 2015). Quirke et al. (2015) reported that, during the Caledonian Orogeny, the Borrowdale Volcanic Group was subjected to regional, sub-greenschist facies metamorphism at about 395 Ma, and nine stages of hydrothermal activity that developed a complex zones of alteration with some variable amounts of vein haematite (Entwisle et al., 2005; Milodowski et al., 1998). A small area of Triassic Sherwood Sandstone Group, to the west of the drainage area, is largely covered by drift. The Sherwood Sandstone Group locally known as the St Bees Sandstone Formation is a dominantly fluviatile sandstones sequence. It is a feldspathic sandstone (Strong et al., 1994), and the dominated mineral assemblages are detrital quartz, subordinate feldspar, muscovite and biotite, albite, and carbonate clasts (Barnes et al., 1994a; Strong et al., 1994), heavy minerals reported include zircon, tourmaline, apatite, anatase and rutile (Strong et al., 1994).

Quaternary drift-deposits are composed of glacial till, peat, and glacial-lacustrine deposits (Griffiths et al., 2018; Griffiths et al., 2019a; Griffiths et al., 2019b; Merritt and Auton, 2000). The post-glacial record records nearly 10,000 years of Holocene deposition (McGhee et al., 2021). The estuary is characterised by the present of knolls of glacial till, exposed across the entire region, peat is also present with most found sitting on top of glacial deposits (Lloyd et al., 2013).

4.4 Samples and Methods

4.4.1 Ravenglass Holocene Cores

Sediment cores were drilled by subcontractors Geotechnical Engineering Ltd (GEL) through the Holocene succession in the inner-estuary, partly vegetated, tidal bar depositional environment in the Esk arm of the Ravenglass Estuary (Fig. 4.1A) (McGhee et al., 2021). The lengths of the three different cores are 5 m, 7 m and 10 m, for BH07, BH08 and BH10, respectively. The drilled cores were retrieved in a series of 12 cm diameter, and 1 m long, semi-rigid plastic liners for protection and easy transport. Each 1-m segment of the sediment core was sliced and photographed, wet and air-dried, for sedimentary logging and subsequent analysis at the University of Liverpool. Detailed sedimentary logs were prepared with different sediment types identified, based on grain size, colour, sedimentary structures, bed thickness, presence of roots and shell fragments, extent and type of bioturbation. All the cores were sampled at every 5 cm for pXRF and LPSA analyses.

4.4.2 XRF analysis

X-ray florescence (XRF) analysis was performed using a portable Thermo Scientific Niton +XL3t GOLDD XRF spectrometer, to measure the abundance of geochemical elements. The portable XRF spectrometer (pXRF) is a self-contained energy dispersive X-ray instrument, built with a variable intensity energy source (6-50 kV, 0-200 µA Ag anode) X-ray tube and the equipment has a factory-calibrated GOLDD (Geometrically Optimised Large Area Drift Detector) detection system. The pXRF has relatively low detection limits and high-precision measurements of > 40 elements. Accuracy and precision were tested by replicating the analysis on a single sample 30 times, the average element concentration and standard deviation (in bracket), in ppm, of Al, Si, K, Ca, Ti, Fe, Mn, Rb, Sr, Zr, Ba and Cs are 64099 (1685), 376925 (4191), 18234 (145), 2610 (46), 2477 (92), 11837 (90), 172 (19), 70 (1), 73 (2), 352 (3), 487 (18) and 85 (4), respectively. The duration for the analysis of each sample was 150 seconds, with the analysis performed in “Test All GEO” mode. The 150 seconds duration (optimum

analysis duration) was determined, by subjecting a single sample to a repeat analysis, under increasing durations until no detectable improvement in uncertainty was recorded.

4.4.3 Interpretation of palaeo-sub-depositional environment

A classification tree (Fig. 4.2) for the discrimination of Holocene sub-depositional environments from cores from the Ravenglass Estuary has been developed (Muhammed et al., 2022) through a combination of visual analysis and multi-element XRF analyses, using supervised classification and the recursive partitioning package, RPART (Therneau and Atkinson, 2019), available in R studio software (R Core Team, 2016).

The first step in defining a sample palaeo-sub-depositional environment, is visual identification of gravel beds (De1) and vegetated salt marsh (De10), by screening the sample for the presence of pebbles and roots and plant detritus, respectively (Fig. 4.2). The next stage involves the use of supervised machine learning classification tree RPART-model on the geochemical data. Each machine-learning-derived decision node splits the data using one data type. In each leaf node, the classification of depositional environment is listed first, followed by the fractional quantity of samples in all the classified depositional environment; the higher the fractional quantity of the "decision", the higher the classification certainty. The value presented at the bottom of the node is the total percentage of the whole sample set that lies in each leaf node. This RPART supervised machine learning approach differentiates De2, De3, De4, De5, De6, NDe8, SDe8 and De9 based on pXRF data: K/(K+Si), K/(K+Al), K/(K+Ca), K/(K+Ti), K/(K+Mn), K/(K+Sr), Sr/(Sr+Rb), Ca/(Ca+Fe), and Mn/(Mn+Sr).

4.4.4 Grain size analysis

Laser particle size analysis was performed using methods previously defined (Simon et al., 2021), using sieved samples (< 2 mm fraction) for grain size distribution using a Beckman Coulter counter. The LPSA output data were analysed using GRADISTAT© to determine the sediment statistical parameters. Organic matter present in the sample was removed by sample digestion before grain size analysis.

Calgon was then added to the sample in order to convert the dried sediment into a paste for optimum mixing and homogenisation.

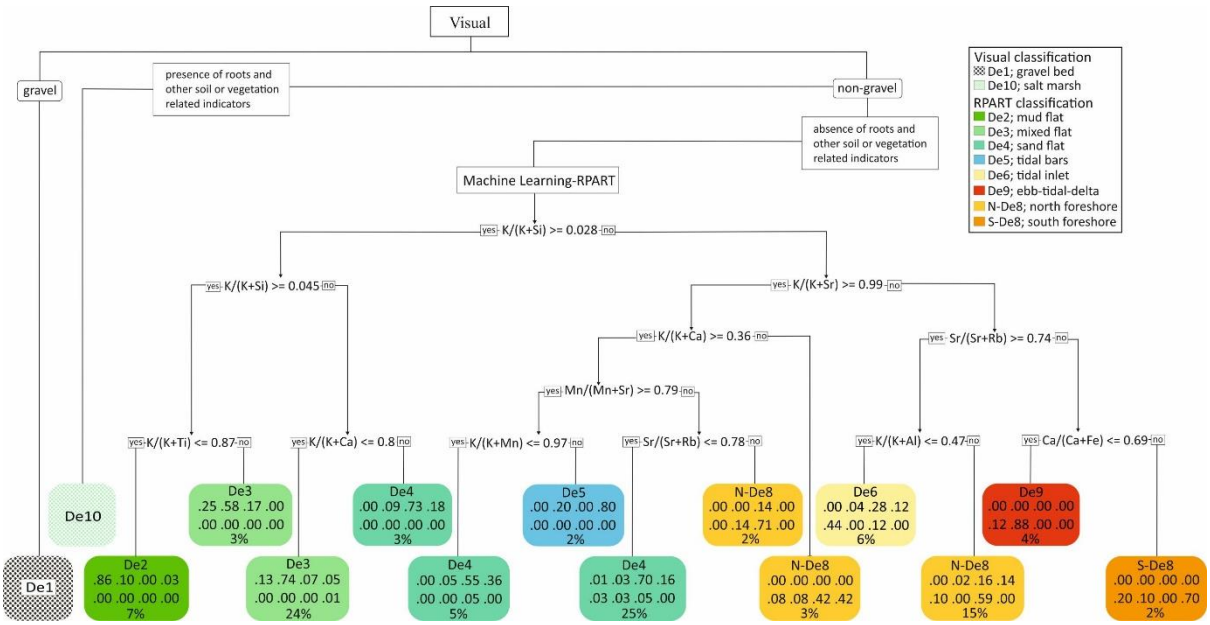

Figure 4.2; Classification tree for the discrimination of estuarine paleo-sub-depositional environments, developed through a combination of visual analysis and multi-element XRF analyses, using supervised classification and the recursive partitioning package, RPART (Therneau and Atkinson, 2019), available in R studio software(R Core Team, 2016). Each machine-learning-derived decision node splits the data using one data type. In each leaf node, the classification of depositional environment is listed first, followed by the quantity of samples in the classified depositional environment, this is presented as a fractional quantity; the higher the fractional quantities, the higher the classification certainty, the value presented at the bottom of the node is the total percentage of the whole sample set that lies in each leaf node. This RPART supervised machine learning approach differentiated De2, De3, De4, De5, De6, NDe8, SDe8 and De9 based on multi-element analyses of K/(K+Si), K/(K+Al), K/(K+Ca), K/(K+Ti), K/(K+Mn), K/(K+Sr), Sr/(Sr+Rb), Ca/(Ca+Fe), and Mn/(Mn+Sr) indices data. In each leaf node, the fraction of samples in that specific classification category are listed as fractional quantity and where these fractional values are less than 1.00, the uncertainty is as a result of some depositional environments having an overlapping attribute, even when nine dimensions are considered. This classification tree has a model accuracy of 72.3 % (Muhammed et al., 2022).

4.4.5 Mineral analysis

Sediment mineralogy was determined with automated mineralogy using SEM-EDS analysis. SEM-EDS was undertaken using a FEI WellSite QEMSCAN®, which comprises a scanning electron microscope combined with energy dispersive spectrometers. The QEMSCAN machine operates with a 15-kV electron beam and two Bruker EDS detectors, to measure primary and secondary backscatter electrons, with the brightness indicating the sample density while the surface signal defines atomic weight. The QEMSCAN system has an electronic processing unit for integrating scanned data using a

software suite (iDiscover) that constitute a Species Identification Protocol (SIP) which uses a mineral chemical database, stored in the system library, to provide information regarding the chemical and mineral compositions of the samples. The SEM-EDS analysis defined sediment mineralogy in a fully quantitative term, it divides each sample into a series of 2 mm ×2 mm fields and analyse each field individually. SEM-EDS analyses were conducted on carbon-coated polished thin sections. Data were collected with user-defined step sizes of 2 μm to ensure that all the clast sizes were analysed, the resolution of the output is dependent upon the step size selected at the time of data collection. The output is a mineral map that contain the summary of the fully quantitative mineralogical content of the analysed sample, in addition to textural information.

4.4.6 Measuring clay-coat coverage: Petrog

Clay coat coverage was quantified using a new perimeter tool developed in Petrog software by Wooldridge et al. (2019b). The new tool allows the quantification of clay-coat grain coverage on SEM petrographic images. To quantify clay coats coverage, 2,160 backscattered electron microscope images, with approximately 60 sand grains per sample. The perimeter tool was used to define the total outer length of a grain and then to identify the length that is covered by attached clay-coat material manually, in order to calculate the percentage of the perimeter of a grain covered by clay-coat material. Any form of web or lump of clays, surrounding a sand grain without any single or continuous contact, will not be regarded as attached clay-coat.

4.5 Results

4.5.1 Ravenglass Holocene cores

Cores 7 was drilled to the east of the tidal bar (Figs. 4.1 and 4.3). Core 8 was drilled to the west of the tidal bar (Figs. 4.1 and 4.4). Core 10 was drilled in a westward (seaward) direction compared to cores 7 and 8 (Figs. 4.1 and 4.5).

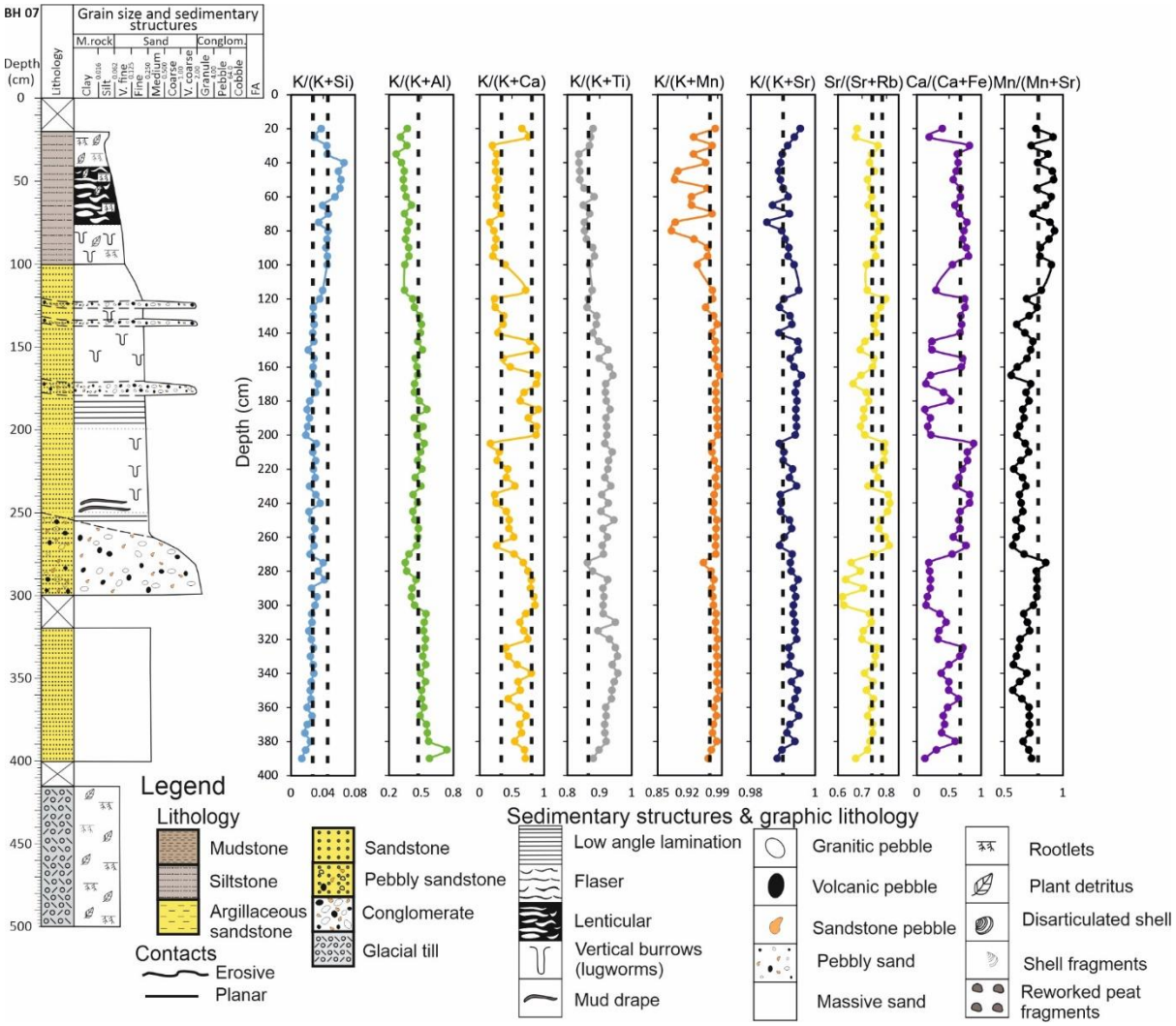

Figure 4.3; Sedimentary log of the 5 m core drilled in the tidal bars along to the Esk Arm of the Ravenglass Estuary with the geochemical data, derived from XRF analysis, illustrated. These nine indices are represented here as these are the ones that RPART classification, in R Statistical Software, used to discriminate the various sub-depositional environments. The critical values superimposed on the nine indices, are taken from the machine learning-derived decision nodes in Figure 4.2.

The sedimentary logs of all cores show that sand, with a narrow grain size range, is the dominant lithology present. All three cores were drilled into vegetated tidal bar sub-depositional environment at the surface and the uppermost part of each core, down to between 90 cm (cores 7 and 8) and 230 cm (core 10) grain size is dominated by mud and very fine sand (Fig. 4.3). Below this depth, most of the sediment in each core is composed of different units of medium- and coarse-grained sand that may represent mixed fluvial-tidal deposits (McGhee et al., 2021).

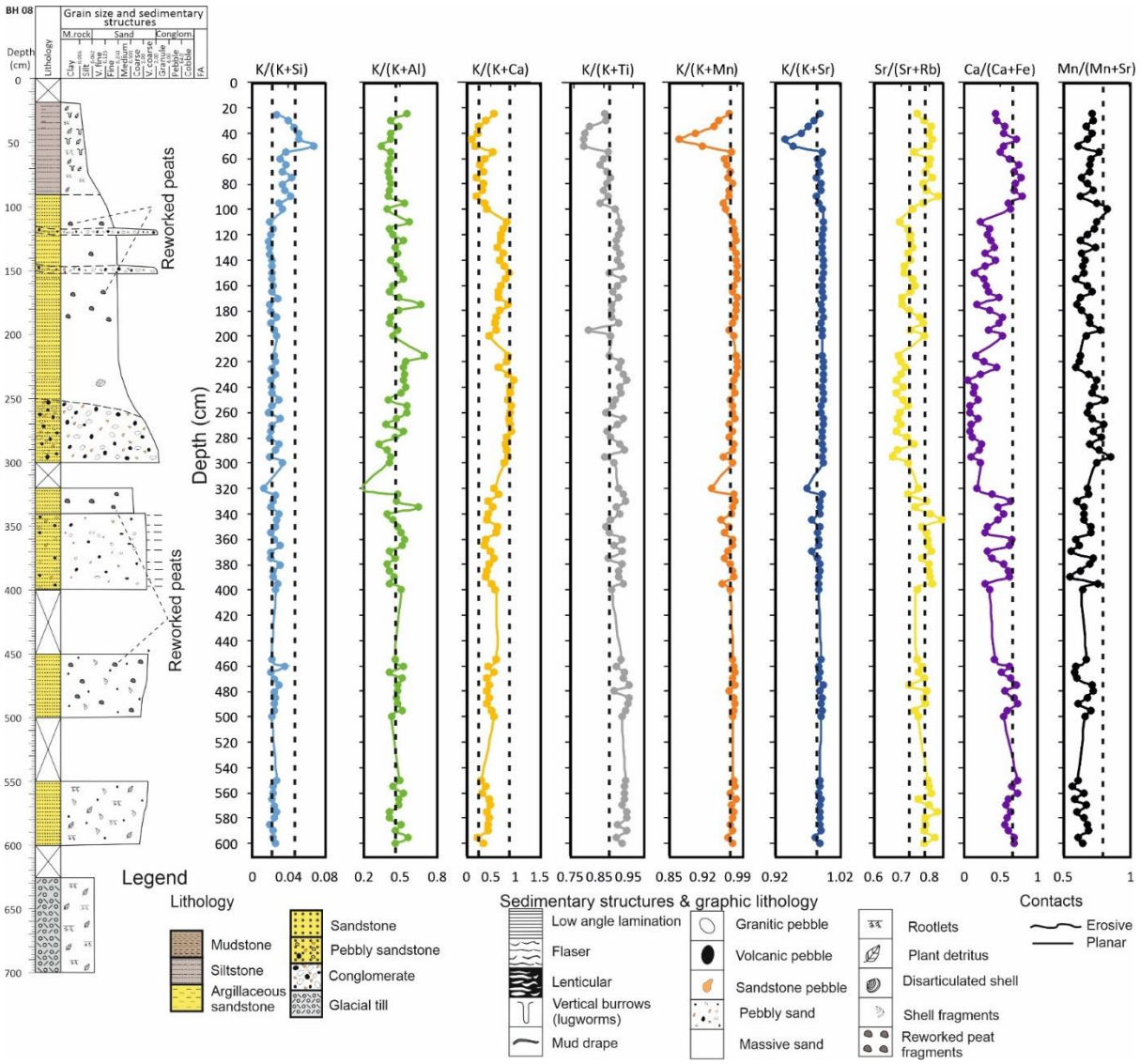

Figure 4.4; Sedimentary log of the 7 m core drilled in the tidal bars along to the Esk Arm of the Ravenglass Estuary with the geochemical data, derived from XRF analysis, illustrated. These nine indices are represented here as these are the ones that RPART classification, in R Statistical Software, used to discriminate the various sub-depositional environments. The critical values superimposed on the nine indices, are taken from the machine learning-derived decision nodes in Figure 4.2.

The specific palaeo-sub-depositional environments could not have been automatically predicted in the deeper parts of these cores, as there is a range of grains sizes that varies lithologically (gravel beds through to mud-dominated sediment) not typical of vegetated tidal bars. The Holocene cores were analysed using pXRF, the nine key indices used to classify the sediment (Fig. 2) are displayed with critical cut-off values, defined by the machine-learning routine, marked by dashed lines (Fig. 4.3, 4.4, and 4.5).

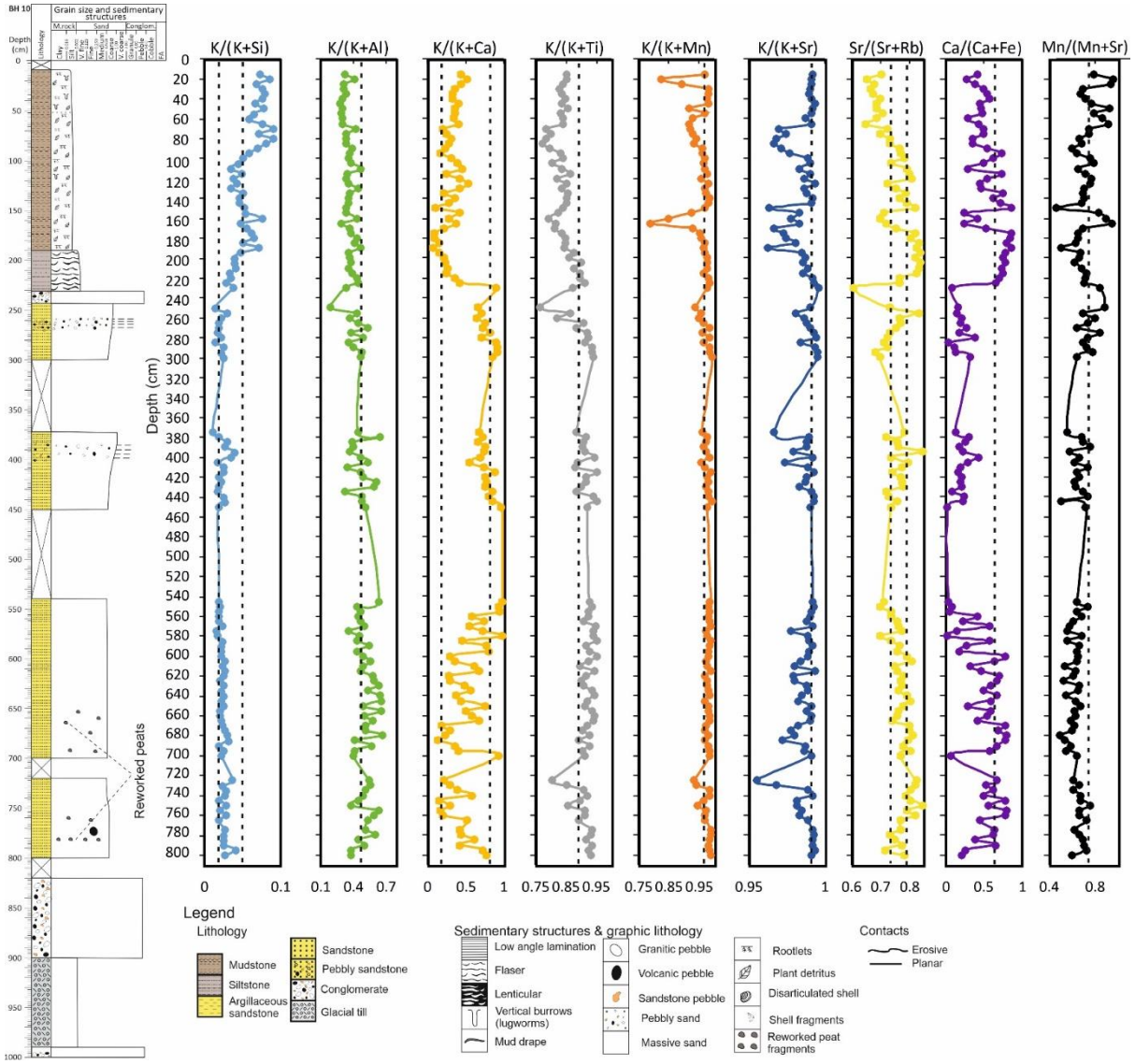

Figure 4.5; Sedimentary log of the 10 m core drilled in the tidal bars along to the Esk Arm of the Ravenglass Estuary with the geochemical data, derived from XRF analysis, illustrated. These nine indices are represented here as these are the ones that RPART classification, in R Statistical Software, used to discriminate the various sub-depositional environments. The critical values superimposed on the nine indices, are taken from the machine learning-derived decision nodes in Figure 4.2.

The absolute abundance of the total clay fraction, clay coat coverage, the relative clay mineral proportions and the quantities of other Fe minerals are presented in Figure 4.6. Clay coat coverage and clay fraction abundance, decrease with increasing depth of burial. The relative proportion of smectite shows a progressive increase with increasing burial depth, while that of the illite decrease progressively with increasing burial depth. The relative proportion of chlorite and kaolinite, and the absolute proportion of biotite, pyrite and iron oxide, were not affected by depth variation. Their abundance is affected by different sediment intervals (Fig. 4.6).

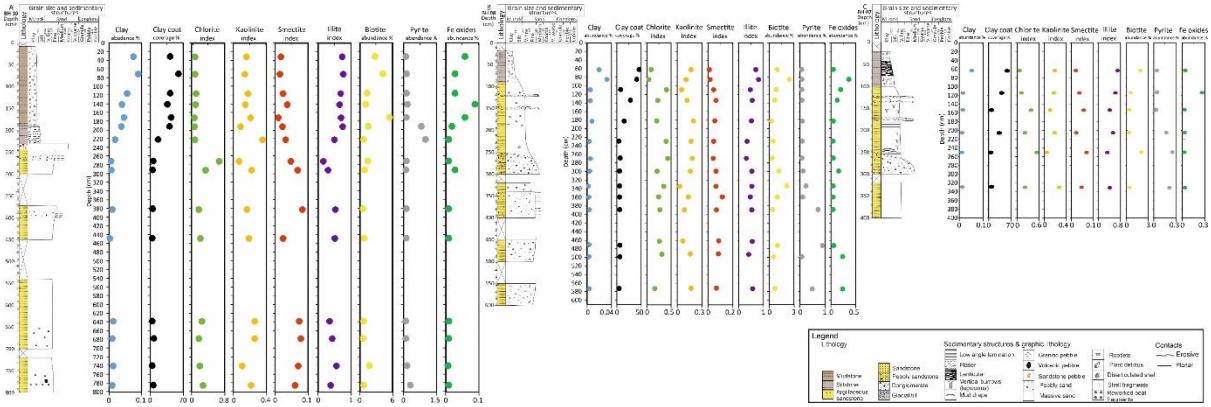

Figure 4.6; Distribution of clay fraction, clay coat coverage, clay mineral types and Fe-bearing minerals with depth, along the Ravenglass Holocene core sediments.

4.5.2 Interpreted palaeo-sub-depositional environment

The sub-depositional environments in each core were interpreted using the decision tree classification scheme (Fig. 4.2) based on geochemical data (Fig. 4.3, 4.4, and 4.5). Interpreted palaeo-sub-depositional environments present in the cores include salt marsh (De10), mud flat (De2), mixed flat (De3), sand flat (De4), tidal bar (De5), tidal inlet (De6), northern foreshore (NDe8), southern foreshore (SDe9), ebb tidal delta (De9), and gravel bed (De1).

Table 4.1; Mineralogical composition of Ravenglass Holocene sediment from SEM-EDS analysis

Depth cm	Depositional environments	Coat coverage	Mean grain size	Clay fraction	Quartz	Plagioclase	K-Feldspar	Muscovite	Biotite	Carbonates	Chlorite	Kaolinite	Smectite	Illite	Pyrite	Fe Oxides
64	Saltmarsh	58	29	0.0548	44	6	6	2.68	1.95	4.53	1.45	5.86	0.66	20.26	0.05	0.03
115	Mixed flat	41	140	0.0161	79	4	5	0.72	0.61	0.51	0.79	1.11	0.24	3.82	0.00	0.27
154	Sand flat	10	114	0.0174	75	8	8	0.33	0.45	0.04	1.39	0.42	0.21	1.54	0.02	0.00
206	Sand flat	33	180	0.0105	82	6	3	1.02	0.27	0.52	0.89	0.81	0.10	2.24	0.18	0.00
251	Sand flat	7	170	0.0115	60	16	7	2.82	2.13	0.01	5.13	0.46	0.68	3.27	0.26	0.01
306	Sand flat	7	230	0.0075	82	4	6	1.07	0.51	0.53	0.68	0.87	0.15	1.34	0.22	0.01
63	Saltmarsh	46	114	0.0204	68	6	8	0.87	1.03	2.51	0.97	1.68	0.13	6.80	0.01	0.04
86	Saltmarsh	41	103	0.0333	56	6	5	1.62	2.48	3.69	1.11	2.26	0.40	16.69	0.03	0.37
300	Mixed flat	5	420	0.0027	70	12	6	2.84	1.24	0.67	1.17	0.87	0.36	2.83	0.15	0.16
110	Sand flat	9	188	0.0065	83	5	6	0.63	0.94	0.43	1.06	0.15	0.12	1.21	0.01	0.20
135	Sand flat	29	190	0.0063	80	3	8	1.91	0.72	0.37	0.84	0.43	0.23	1.91	0.03	0.13
183	Sand flat	16	198	0.0089	82	5	6	0.59	0.35	1.02	0.50	0.46	0.13	1.20	0.02	0.00
230	Sand flat	5	269	0.0028	77	7	4	2.23	0.53	0.02	2.46	1.03	0.28	2.14	0.02	0.00
270	Sand flat	8	281	0.0038	75	6	12	0.71	0.44	0.31	1.51	0.65	0.15	1.10	0.01	0.00
390	Tidal inlet	3	474	0.0030	80	5	7	1.02	0.49	1.37	0.73	0.23	0.18	1.40	0.76	0.00
335	North foreshore	6	413	0.0025	71	12	5	0.70	2.19	1.61	1.85	0.14	0.34	2.79	0.26	0.02
360	North foreshore	5	491	0.0026	80	7	5	0.44	1.05	0.88	0.86	0.48	0.40	1.63	0.14	0.00
450	North foreshore	3	296	0.0041	76	8	9	0.81	1.07	0.19	0.94	0.24	0.30	1.91	0.94	0.00
480	North foreshore	7	296	0.0044	83	4	6	0.46	0.58	1.08	0.72	0.36	0.19	0.93	0.02	0.24
560	North foreshore	5	314	0.0042	80	6	6	0.99	0.79	1.64	0.45	0.45	0.18	1.47	0.52	0.24
33	Saltmarsh	44	16	0.0776	36	7	3	3.30	2.84	1.84	2.16	6.29	0.72	28.59	0.05	0.06
73	Saltmarsh	61	12	0.0964	27	8	3	3.25	4.26	1.95	2.29	6.09	0.69	32.32	0.17	0.03
118	Saltmarsh	45	24	0.0577	49	8	5	2.25	1.42	4.06	1.66	3.89	0.53	14.81	0.01	0.03
143	Saltmarsh	39	32	0.0422	61	10	6	1.72	1.14	3.36	1.48	1.82	0.45	8.04	0.01	0.09
173	Saltmarsh	47	25	0.0492	28	6	3	3.82	5.60	2.39	2.09	9.06	0.46	29.54	0.03	0.06
193	Mud flat	43	27	0.0406	55	9	6	2.11	1.58	2.19	1.87	1.95	0.46	14.87	0.84	0.02
223	Mixed flat	19	75	0.0204	70	7	8	1.23	0.71	3.61	0.42	1.86	0.17	2.64	1.03	0.01
273	Sand flat	5	440	0.0016	55	13	4	2.48	1.53	0.00	13.96	1.59	0.99	3.51	0.00	0.01
293	Sand flat	3	330	0.0027	80	6	6	0.63	0.96	0.02	1.46	0.91	0.28	1.30	0.00	0.03
450	Sand flat	6	333	0.0043	82	6	5	0.63	0.86	0.02	0.73	0.64	0.08	1.68	0.00	0.01
787	Sand flat	8	334	0.0040	84	5	2	0.76	0.43	0.01	1.27	0.95	0.26	1.73	0.35	0.01
383	Ebb-tidal-delta	3	530	0.0017	85	6	3	0.99	0.52	0.01	0.57	0.51	0.25	1.61	0.01	0.00
640	North foreshore	6	297	0.0059	80	5	5	1.15	0.76	0.03	1.24	1.23	0.34	1.68	0.01	0.00
680	North foreshore	10	288	0.0071	71	12	8	1.10	0.68	0.02	0.78	1.05	0.31	1.75	0.01	0.01
742	North foreshore	6	345	0.0050	74	9	5	1.09	1.76	0.02	1.36	0.70	0.43	3.53	0.02	0.00

4.5.3 Sediment mineralogical composition

The SEM-EDS analysis revealed a range of minerals in the cores (Table 4.1). In absolute terms, quartz is the most abundant mineral with its abundance varying between 27.4 and 85.4%. Both plagioclase and k-feldspar abundance vary between 2.1 and 15.7%. Carbonates, biotite and muscovite are the least abundant minerals, with their abundance ranging from 0.1 to 5.6%. Chlorite abundance ranges from 0.4 to 14.0%, illite abundance ranges from 0.9 to 32.2% kaolinite abundance ranges from 0.1 to 9.1%, and smectite ranges between 0.1 to 1.0%.

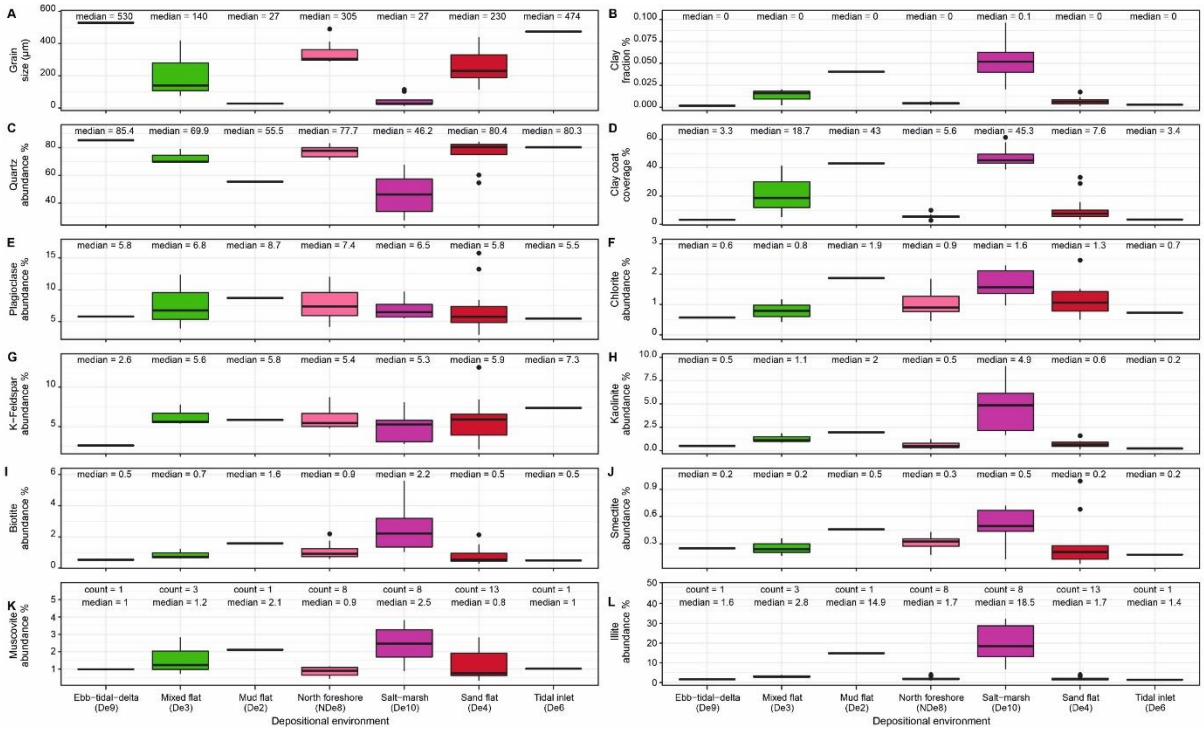

Figure 4.7; Figure 4.7; Box plots for sediment parameters as a function of Ravenglass Estuary interpreted paleo-sub-depositional environment of; (A) Grain size (mm), (B) clay fraction (C) quartz abundance, (D) clay coat coverage, (E) plagioclase abundance, (F) chlorite abundance, (G) k-feldspar abundance, (H) kaolinite abundance, (I) biotite abundance, (J) smectite abundance, (K) muscovite abundance, (L) illite abundance. Boxplots contain the median and upper and lower quartile ranges. Outliers are defined as > (or <) 1.5 times the interquartile range, above the upper and below the lower quartiles. Median value defined in each plot. Feldspar abundance is independent of grain size distribution but varies across the sub-depositional environment; plagioclase is most abundant in the mixed flat, mud flat and north foreshore while K-feldspar is most abundant in the mixed flat, mud flat, sand flat, tidal inlet and north foreshore. Micas abundance is highest in the finer sediment and varies greatly across the sub-depositional environments; biotite is most abundant in mud flat and saltmarsh and muscovite is most abundant in mud flat, mixed flat and saltmarsh. Clay coat coverage increase with increasing clay fraction abundance and is most abundant in the mud flat, mixed flat and saltmarsh; chlorite abundance is somewhat uniform and is independent of clay fraction abundance and clay coat coverage, kaolinite abundance is highest in saltmarsh and relatively higher in the mud and mixed flat, smectite abundance in mixed flat, mud flat, sand flat and saltmarsh, tends to reflect

clay coat coverage and illite is most abundant in mud flat and saltmarsh, and is uniformly low in the remaining depositional environment. Clay minerals abundance and clay coat coverage vary greatly between the different depositional environment.

4.5.4 Mineral abundance versus mean grain size and sub-depositional environment

The distribution of minerals in relation to grain size and clay fraction, as a function of sub-depositional environment are presented in Figures 4.7. Quartz is most abundant in coarser sediment (>200 µm) deposited in ebb-tidal-delta, north foreshore, tidal inlet, sand flat, and mixed flat and has a least abundance in salt marsh and mud flat, that have highest clay abundance (>0.035%, Fig. 4.7C). K-feldspar and plagioclase are most abundant in sediment with low clay abundance (< 0.02%); they are most abundant in the mixed flat, mud flat and north foreshore, while K-feldspar is also abundant in the sand flat, and tidal inlet, both are lowest in ebb-tidal-delta (Fig. 4.7E and 4.7G). Biotite and muscovite show variable concentration with different grain size distribution and they increase with increasing clay fraction abundance in sediment with clay fraction above 0.02% (Fig. 4.7B, 4.7I and 4.7K); they are most abundant in mud flat and saltmarsh, while muscovite is also abundant in mixed flat, both are least abundant in ebb-tidal-delta, north foreshore and tidal inlet (Fig. 4.7I and 4.7K). Chlorite is uniformly low (< 3%) among the different grain size distribution, it shows a slight increase in sediment with clay abundance above 0.02% (Fig. 4.7A, 4.7B and 4.7F). Kaolinite is most abundant in finer sediments (<62 µm), it shows a significant increase in sediment with clay abundance above 0.02% (Fig. 4.7A, 4.7B and 4.7H). Smectite shows a variable distribution in finer sediments but shows a slight increase in sediment with grain size above 200 µm, and clay abundance above 0.02% (Fig. 4.7A, 4.7B and 4.7J). Illite is most abundant in finer sediment, but shows a slight decrease with decreasing grain size in sediment with grain size below 70 µm, it tends to increase significantly in sediment with clay abundance above 0.02% (Fig. 4.7A, 4.7B and 4.7L)

4.5.5 Relative abundance of clay minerals versus sub-depositional environments

The relative abundance of chlorite, illite, smectite and kaolinite, as a function of sub-depositional environment, is presented in Figure 4.8, where they vary between different depositional environment (Fig. 4.8A, 4.8B, 4.8C, and 4.8D). Chlorite relative abundance is highest in the sand flat and tidal inlet,

intermediate in north foreshore and ebb-tidal-delta, and uniformly low in mud flat, mixed flat and salt-marsh (Fig. 4.8A). The relative abundance of kaolinite is slightly higher in the mixed flat and uniformly intermediate in north foreshore, ebb-tidal-delta, tidal inlet, sand flat, mud flat and salt-marsh (Fig. 4.8B). Smectite relative abundance is highest in the ebb-tidal-delta, north foreshore and tidal inlet, intermediate in sand flat and mixed flat, and low in mud flat and salt-marsh (Fig. 4.8C). The relative abundance of illite is high in salt-marsh and mud flat, and uniformly intermediate in north foreshore, ebb-tidal-delta, tidal inlet, sand flat, and mixed flat (Fig. 4.8D).

Figure 4.8; Clay minerals relative abundance as a function of estuarine sub-depositional environments (A) Chlorite index. (B) Kaolinite index. (C) Smectite index. (D) illite index. Note that outliers are defined as an observation that is numerically distant from the rest of the data (i.e. a value that is 15times the interquartile range below the lower quartile and above the upper quartile). The relative abundance of clay minerals varies greatly between the different depositional environment.

4.5.6 Clay coat coverage

Clay coat coverage increases with increasing clay fraction abundance. It is most abundant in the mud flat, mixed flat and saltmarsh (up to 40%). Sand flat sediments have an average clay coat coverage above 7%, whereas tidal inlet, north foreshore and ebb-tidal-delta have an average clay coat coverage

of less than 5% (Fig. 4.7D and 4.12). Overall, clay coat coverage varies greatly between the different sub-depositional environment.

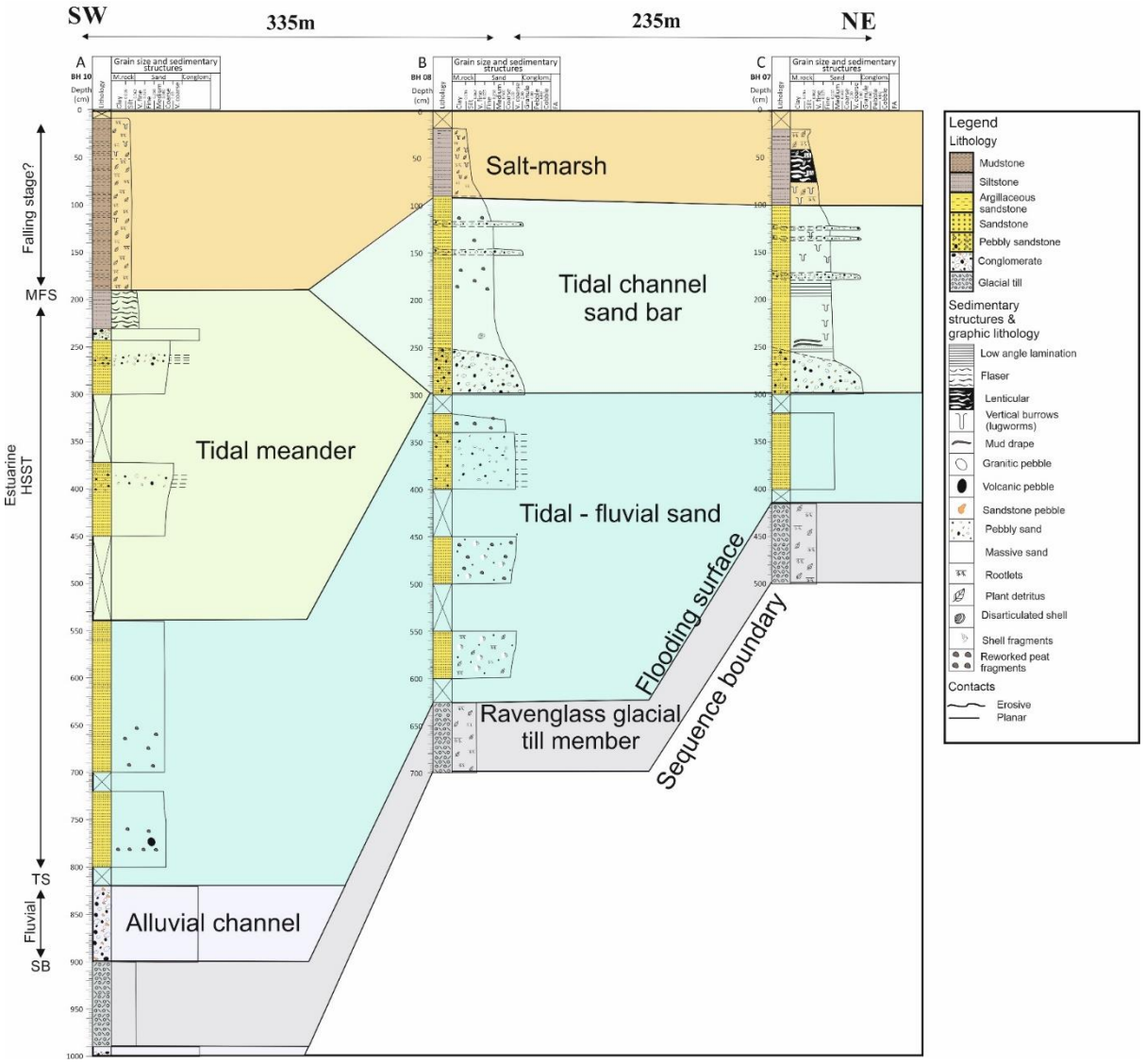

Figure 4.9; Inner estuary vegetated tidal bars deposits correlation panel from the Devensian to present-day highlighting the facies and sequence stratigraphic boundaries, presented in McGhee et al. (2021).

4.6 Discussion

4.6.1 Interpretation and correlation of sub-depositional environments

A lithostratigraphic correlation of the three cores has been published previously by McGhee et al. (2021), and it is here presented in Figure 4.9. This approach was based on description of the cores, sediment facies analysis, sediment distribution and high-resolution ^{14}C ages. Indirect method of describing sedimentary facies by grouping the sediments into facies associations and then interpreting

palaeo-sub-depositional environments, was employed. The lithostratigraphic correlation of the sedimentary infill of Ravenglass Estuary, has identified and correlated nine sedimentary facies namely; Ravenglass Glacial Till Member (RGTM), fluvial gravel and coarse sands, transgressive brown-black peat, tidal–fluvial sands, tidal bar sands, tidal-meander sands, outer estuary–shoreface sands, dune sands and salt marsh sediments (Fig. 4.9) (McGhee et al., 2021).

In this study, we have applied the decision tree of the classification scheme (RPART model, Fig. 4.2) to the geochemical data of the Holocene cores and defined palaeo-sub-depositional environments from all three cores (Fig. 4.10). The interpreted palaeo-sub-depositional environments are gravel bed (De1) salt-marsh (De10), mud flat (De2), mixed flat (De3), sand flat (De4), tidal bar (De5), tidal inlet (De6), northern foreshore (NDe8), southern foreshore (SDe8) and ebb-tidal-delta (De9). The mud flat (De2), mixed flat (De3), sand flat (De4), and tidal bar (De5) represent the tidal flat and tidal bar sediment. The tidal inlet (De6), northern foreshore (NDe8), southern foreshore (SDe8) and ebb-tidal-delta (De9) represent the outer estuary sediment. The interpreted palaeo-sub-depositional environments were correlated based on this geochemical classification approach, in order to establish an understanding of sediment's evolution and how it is been distributed laterally and vertically. The new geochemically based correlation was then compared with the lithostratigraphic based correlation by McGhee et al. (2021), as presented in Figure 4.11. The Ravenglass Glacial Till Member (RGTM) has been adopted as a the base of the succession as it occurs throughout the three inner estuary cores (Figs. 4.9, 4.10 and 4.11).

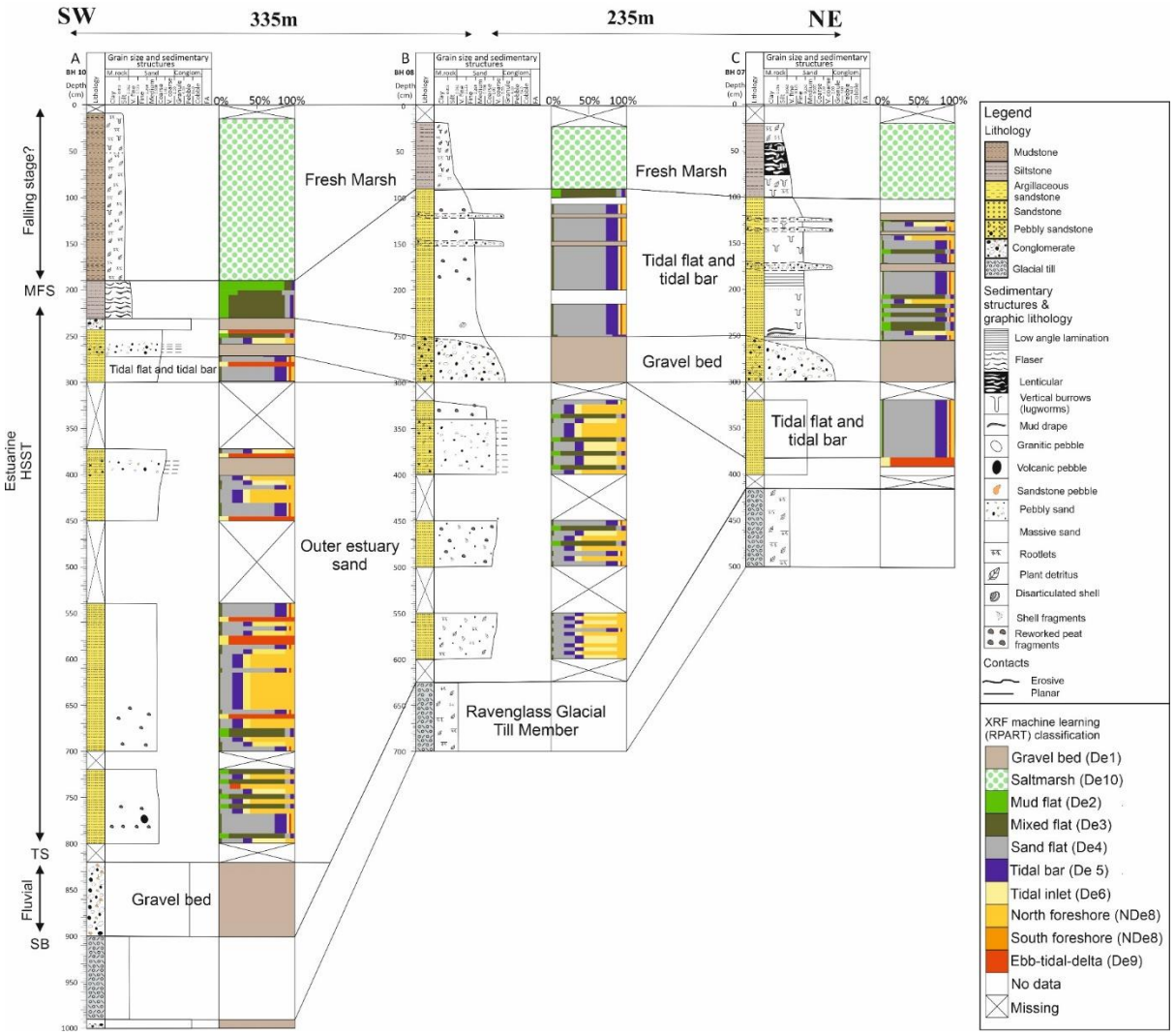

Figure 4.10; Schematic sedimentary log of inner estuary vegetated tidal bars deposits (see Figure 4.1 for core location) with application of the classification tree in Figure 4.2 to data presented in Figure 4.3, 4.4 and 4.5. Showing the graphic log of a core from a tidal bar in the inner estuary, with the paleo-sub-depositional-environments defined in the column to the right of the graphic log following application of the classification diagram (Figure 4.2). A correlation boundary was superimposed to show the stratigraphic evolution of the different group of estuarine deposit; RGTM, Gravel deposits, Outer estuary sand, Tidal bar and tidal flat, and salt-marsh.

Sediments in Ravenglass Holocene cores are underlain by the RGTM (Fig. 4.10), overlying the RGTM is the Alluvial channel gravel deposits. The gravel bed was interpreted visually, based on the presence of pebble deposits. They are poorly sorted, sub-angular and angular, and lack shell fragments, hence represent fluvial–alluvial origin. The first set of gravel beds sit directly above the Ravenglass Glacial Till Member (RGTM) and is only restricted to core 10 (Fig. 4.10A), the lack of gravel beds in cores 7 and 8, directly above the RGTM, is due the absent of channel thalweg in those locations during the lowstand incision phase (McGhee et al., 2021). According to Merritt and Auton (2000), the deposition of this

gravel bed is associated with the relative sea-level fall of -30 m below ordnance datum at *ca* 7,200 years BP. The second set of gravel beds sit between the inner estuary sediment and the outer estuary sediment, and was correlated across the three Holocene cores (Fig. 4.10).

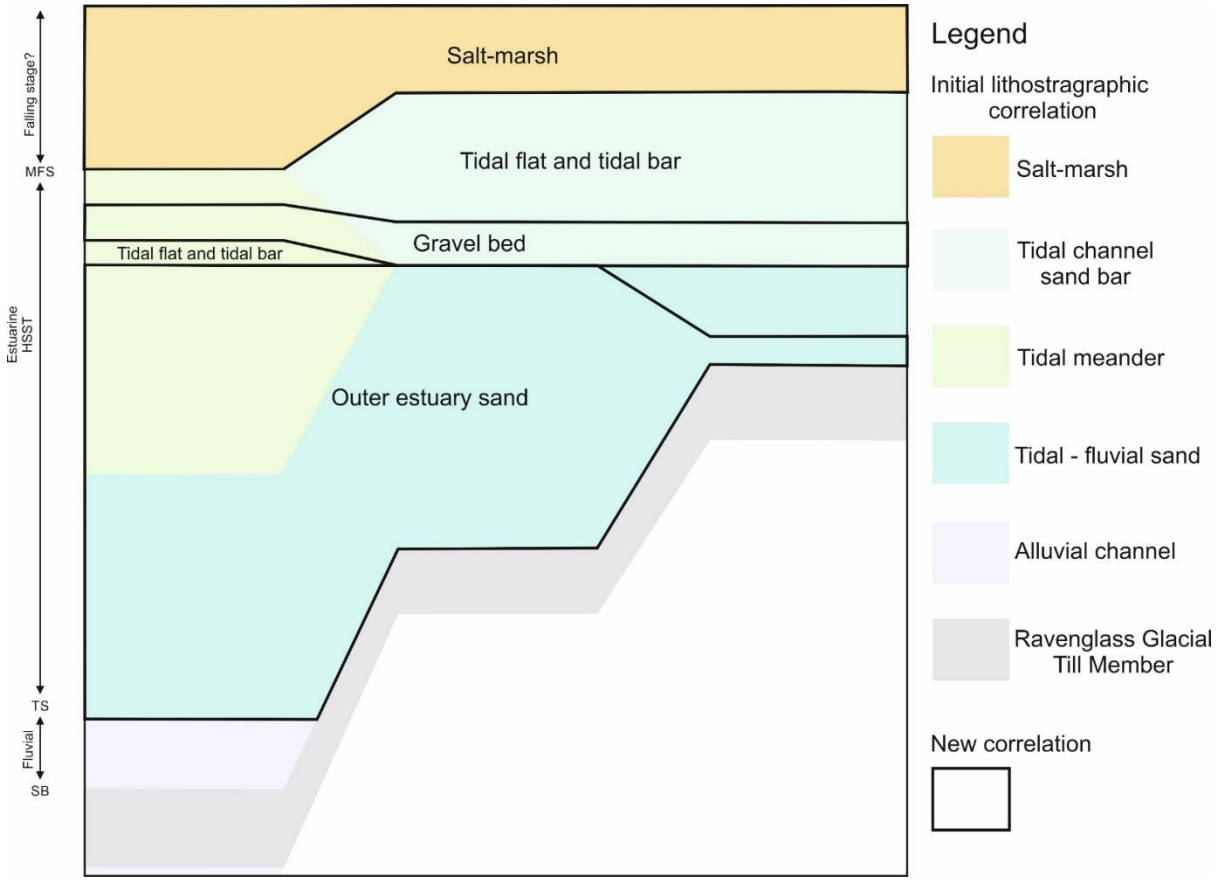

Figure 4.11; A correlation showing the comparisons between lithostratigraphic based correlation and geochemical data-based classification.

The Salt-marsh was interpreted visually, based on the present of rootlets and plant detritus. They are composed of mottled clay, silt, and very fine-grained sand sediment. The very fine-grained sand formed a lenticular bedding, while the clay and silt sediments are bioturbated with roots from salt tolerant vegetation. The trace fossils identified are lugworm burrows, plant detritus and rootlets. The salt marsh is distributed throughout the top few cm of the inner estuary cores, with a variable thickness that ranges between 85 to 190 cm, the thickest deposits is in core 10 (Fig. 4.10). The deposits accumulated within the saltmarsh sub-depositional environment, represent a degree of sediment stability, and their present on top of the inner estuary cores, may suggest a period of abandonment, as a result of estuarine channel migration (Allen and Posamentier, 1994; McGhee et al., 2021).

The Tidal flat and Tidal bar deposits are interpreted automatically by the machine learning RPART, based on the combination of multiple indices of geochemical data. The mud flat (De2) sediments are composed of mottled, clay- and silt-grade deposit, forming a flaser bedding. The mixed flat (De3) sediments are composed of very fine-grained heterolithics sand, that formed a flaser bedding and low angle lamination, there are localised clay drapes, peat fragments and lugworm burrows present. The sand flat (De4) and tidal bar (De5) sediments are composed of fine to medium-grained sand, with mud drapes and low angle lamination. There are pebbles, fragments of peat and shell, and lugworm burrows present. The present of peat and shell fragments together with pebble surface is likely due to internal erosion and migration surfaces within the bar. The mud and mixed flat sub-depositional environments underlying directly the saltmarsh deposits, likely represent the development of floodplain in a meandering river system. The accumulation of massive sand deposits forming sand bar, represent a period of sea-level stability that eventually led to the development of channel bank. The tidal flat and tidal bar sediments are correlated across the three cores, they present a heterogeneous sediment deposits with huge thickness variability, developed within a short distance of less than 1 km (Fig. 4.10).

The outer estuary deposits are interpreted automatically by the machine learning RPART, based on the combination of multiple indices of geochemical data**.** They are composed of fine to medium grained sand, pebbles and shell deposits. Sediment deposited in tidal inlet and north foreshore are relatively richer in pebbles and shell lag deposits, than those deposited in south foreshore and ebb-tidal delta. Although all the outer estuary sub-depositional environments are correlated across the three cores (core 7, 8 and 7), the marine influence is more dominant in the distal cores (core 8 & 10) (Fig. 4.10). The marine influence is been interpreted as tide-dominated condition, at the time when the River Esk is directly feeding the sea (McGhee et al., 2021). The outer estuary deposits are segregated in such a way that foreshore deposits are dominated by wave processes, while tidal inlet deposits are dominated by tidal processes, that developed in a transgressive-highstand-regression conditions (McGhee et al., 2021). This massive sand deposits are present above the RGTM, suggesting

that they are the first estuarine sand to accumulate within the deeper part of the palaeo-valley during marine transgression, and represent the tidal influenced coastal sands (Fig. 4.10).

According to McGhee et al. (2021) this huge variability within the inner estuary deposits indicates that the palaeo-channel (Esk Arm) has been subjected to different phases of abandonment and reactivation. Overall the sediment deposits represent an aggrading, transgressive to highstand system onlapping a lowstand fluvial deposits, that were developed during landward migration of the shoreline. The newly revised interpretation, based on the geochemical classification of sub-depositional environments, shows that core 7, 8, & 10, drilled into a vegetated tidal bar sub-depositional environment (at the present time) were not always the site of a tidal bar throughout the Holocene period. Furthermore, the cores show a valley filling fining upward sequence, at the multi-metre scale, that could represent a time of (a) falling sea-level, or (b) greater rate of delivery of sediment to the estuary compared to net flux to the ocean.

In comparisons, the lithostratigraphic based and the geochemical data-based correlations present a well-established understanding of the lateral and vertical stacking patterns of the Ravenglass sedimentary valley fill. However, the lithostratigraphic based correlation has matched all basal sands above the RGTM, as inner straight tidal-fluvial sands (Fig. 4.9 and 4.11) (McGhee et al., 2021), whereas the geochemical data based correlation subdivided basal sands into outer estuary sand and inner estuary tidal flat and tidal bar sand (Fig. 4.10 and 4.11). It is noteworthy that the basal sands show an evidence of marine inputs, similar to what has been reported by McGhee et al. (2021) (Fig. 4.9 and 4.10). The geochemical data-based interpretation and the subsequent correlation, has allowed the discerning at even a greater resolution and also presenting a more detailed understanding of the evolution of the valley fill estuarine sediments.

4.6.1.1 Significance of new correlation

The novel geochemical data-based classification of Holocene sub-depositional environments has provided a well-established understanding of estuarine sediment evolution. The texturally bland sand

intervals of the Holocene cores were hard to interpret in terms of descriptive facies-based analysis. The sand may have been due to inner or out estuary deposition, given the general lack of sedimentary structures, trace fossils, or other features. With the application of the automated classification approach, these deposits were revealed to be due to a combination of outer and inner estuary depositional processes, dominated by meandering river system, wave and tidal processes. Furthermore, the geochemical data-based correlation (Fig. 4.10) has presented more detailed understanding of the lateral and vertical distribution of estuarine sedimentary fills and their corresponding palaeo-sub-depositional environments in the inner Ravenglass Estuary. The presence of outer estuarine marine influenced sand deposit, typically in the mid- to bottom section of core 8 and 10, suggests that the cores drilled into the inner estuary tidal bar sub-depositional environment (at the present time) were not always the site of a tidal bar throughout the Holocene, it shows an earlier period when the sediment were deposited under strong coastal-tidal influenced than it is at the present time, most likely when the River Esk Ravenglass was more open to the Irish Sea (McGhee et al., 2021).

4.6.2 Sediment mineral composition

The mineral composition of clastic sediments is controlled by the geology of source area, weathering, vigour and distance of the fluvial transport system, and the redox conditions at the site of deposition (Fralick and Kronberg, 1997). Post-depositional processes in a form of in-situ weathering and mineral–biological interaction such as bioturbation, microbial activity and soil-forming processes, can alter the mineralogical composition of clastic sediments (Daneshvar and Worden, 2017). The Ravenglass Holocene sediments are predominantly quartz rich with quartz been the most abundant mineral (≈69%) (Table 4.1 and Fig. 4.7). The sediment composition of the Ravenglass Estuary is reported as been arkosic to subarkosic and thus, reflect the drainage of Eskdale granite, Sherwood Sandstone and andesite Borrowdale Volcanic in the hinterland (Daneshvar and Worden, 2017; Griffiths et al., 2019a). Feldspar distribution is independent of grain size but varies across the sub-depositional environment, while micas abundance is highest in the finer sediment and varies greatly across the sub-depositional

environments. The occurrence of iron-bearing lithics such chlorite and biotite have been reported in both the Borrowdale Volcanic Group (Quirke et al., 2015) and the Eskdale Intrusions (Moseley, 1978; Quirke et al., 2015; Young et al., 1986). Therefore, iron-bearing lithics in the Ravenglass Estuary (Fig. 4.12C) are likely to have been sourced from the Borrowdale Volcanic Group and the Eskdale Intrusions and the chlorite present in the sediment is likely a detrital mineral. The carbonate is likely to have been primarily derived from the shell rich gravel beds, as there are no reported carbonate rocks in the hinterland of the Ravenglass Estuary.

4.6.3 Clay minerals distribution

The distribution of clay minerals in the palaeo-sub-depositional environments of Ravenglass Estuary, is presented in Figure 4.8; Illite is the most abundant clay mineral, chlorite and kaolinite abundance is relatively lower and smectite is the lowest abundant clay minerals. The proportion of illite, chlorite and kaolinite in the estuary, seemingly match the global oceanic clay-mineral trend (Rateev et al., 2008). The high relative abundance of illite and kaolinite in the mud dominated sub-depositional environment of Ravenglass estuary, indicate that these clay minerals are predominantly present in a clay grade form (Fig. 4.8B and 4.8D). The high relative abundance of chlorite and smectite in the sand dominated sub-depositional environment, coupled with their present in lithic grain (SEM image), can be interpreted as chlorite and smectite are predominantly present in coarser sediment fraction, potentially lithic grain (Fig. 4.8B, 4.8D, 4.12B, and 4.12C). The abundance of chlorite in the inner estuarine sand dominated sub-depositional environment of Ravenglass, has been reported (Griffiths et al., 2018; Griffiths et al., 2019b), also chlorite in sand and lithic grade are typically present along the estuary head (Worden et al., 2020a). In addition, the influence of sub-depositional environment on the distribution of clay minerals, in Ravenglass surface and near surface sediments has been reported (Griffiths et al., 2018; Griffiths et al., 2019b).

4.6.4 Controls on clay distribution

As observed in the previous section, clay minerals distribution varies significantly across the different sub-depositional environment in the Ravenglass Estuary (Fig. 4.7 and 4.8). The heterogenous distribution of clay minerals in modern sedimentary deposits is affected by the interplay between multiple factors (Brockamp and Zuther, 2004; Daneshvar and Worden, 2017; Edzwald and O'Mella, 1975; McIlroy et al., 2003; Needham et al., 2004; Worden and Morad, 2003); composition of the provenance, degree of chemical weathering in the hinterland, grain size and shape of the clay mineral type, effect of flocculation when exposed to saline water typically in mixed fresh-marine settings, in-situ alteration of detrital minerals, biological activity, physical form of the clay minerals and how they have been transported to the depositional site (e.g., grain coat or suspended particles). Recent studies on the Ravenglass Estuary Holocene sediments, reported that provenance, depositional environment, estuarine hydrodynamics, sediment supply and resident time, are the main controls on the distribution of clay minerals (Daneshvar and Worden, 2017; Griffiths et al., 2018; Griffiths et al., 2019a; Griffiths et al., 2019b).

Clay minerals in the Ravenglass estuary originate from the following geological processes; the weathering of Palaeozoic and Triassic bedrock and Quaternary drift, the internal erosion of Ravenglass Glacial Till Members, and the landward displacement of sediment along the intertidal zone (Griffiths et al., 2018). The most abundant clay mineral in the estuary (Illite) is been reported to originate from two different sources; the Fe-Mg-rich illite originated from Ravenglass Glacial Till Members (Griffiths et al., 2018), while the Al-rich illite came from feldspars alteration within bedrock geology; Eskdale granite (Quirke et al., 2015; Simpson, 1934; Young et al., 1986), Borrowdale Volcanic Group (Quirke et al., 2015). The origin of kaolinite is attributed to the chemical weathering of any silicate minerals within the estuary or at the hinterland, the glaciofluvial and glaciolacustrine sediments of the Fishgarth Wood Till Member also serve as another source of kaolinite into the estuary (Griffiths et al., 2019b). Smectite typically originate at the initial stage of chemical weathering (Salem et al., 2000), the alteration of plagioclase to smectite has been observed in the coarser sediment of Ravenglass (Fig

4.12B). Chlorite is most abundant in high-energy and coarser-grained depositional environment (Fig. 4.8A) and occurs in lithic grain (Fig. 4.12C), and according to (Griffiths et al., 2018; Griffiths et al., 2019b) chlorite distribution reflects the fluvial deposition of chlorite-enriched sediment, sourced from the chloritised Eskdale Granite.

Diagenetic influence on clay minerals distribution pattern is been exerted by both physicochemical processes (Grim and Johns, 1954; Nelson, 1960; Powers, 1957) and biological processes (McKinley et al., 2003; Needham et al., 2006; Needham et al., 2004; Needham et al., 2005; Worden et al., 2006). Previous work on Ravenglass Holocene sediment showed the neoformation of kaolinite and illite from alteration of detrital plagioclase and k-feldspar respectively, as K-feldspar grains are preferentially rimmed by illite and plagioclase grains are preferentially rimmed by kaolinite (Daneshvar and Worden, 2017), although Griffiths et al. (2018) on the effect of eodiagenesis on the distribution of clay minerals in Ravenglass Holocene sediment, have agreed that there is a possibility, they strongly argued that kaolinite is formed due to intense alteration of feldspars in the hinterland as reported by (Moseley, 1978; Quirke et al., 2015; Young et al., 1986). In this study, we have observed that, plagioclase detrital mineral has undergone relatively rapid alteration, to smectite clay minerals (Fig. 4.12B). The development of clay minerals from the alteration and dissolution of phyllosilicate minerals has been widely reported, notably the meteoric water flushing that led to the leaching of feldspars and mica occurring at shallow depths (<20m) (Barshep and Worden, 2021; Bjorlykke, 1998; Ehrenberg and Nadeau, 1989; Scotchman et al., 1989). It is noteworthy that the mineral alteration is strongly influenced by the sediment grain size, as most of the alteration is associated with coarser sediment (Fig. 4.12), suggesting the alteration of feldspar lithic grade in sand dominated sub-depositional environments.

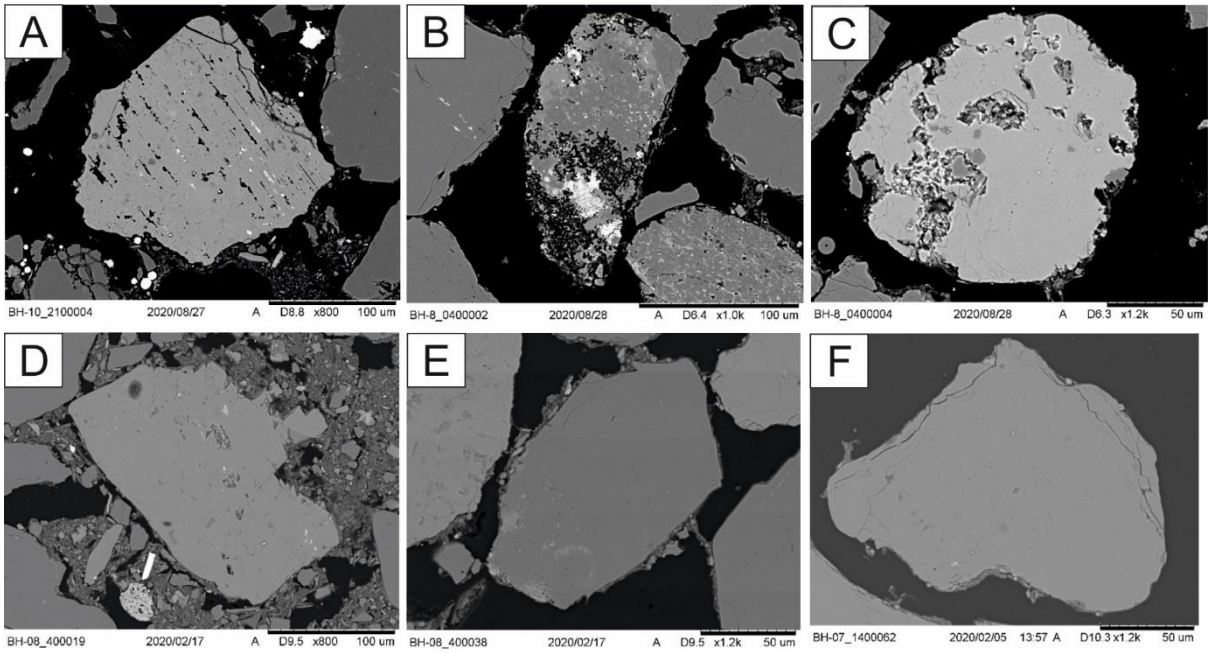

Figure 4.12; Scanning-electron-microscopy (SEM) images of (A) Muscovite alteration. (B) Plagioclase alteration. (C) Chlorite-biotite lithic grain. (D) clay-coated sand grains with coverage > 40%. (E) clay-coated sand grains with coverage < 40%. (F) clay-coated sand grains with coverage < 10%. Chlorite may occur as clay forming grain coat or as lithic grain in coarser sediment. The mineral alteration is dominantly observed in the coarser sediment and mostly associated with micas or feldspar lithic grains. In the salt marsh and mud flat sediment, clay occur as either pore filling or grain coating, with over 40% coat coverage. In the mixed flat and sand flat sediment, clay is mostly present as grain coat with reported coat coverage of less than 40%. The tidal inlet, foreshore and ebb-tidal-delta have a reported coat coverage of less than 10%.

As widely reported, hydrodynamic forces have a significant influence on the textural characteristics of estuarine sediment (Dalrymple et al., 1992), for example the physical sorting of clay minerals due to grain size variation during transport (Gibbs, 1977). Furthermore, previous studies on this estuary showed that the distribution patterns of clay minerals in the Ravenglass Estuary sediment are governed by estuarine hydrodynamics (Griffiths et al., 2018; Griffiths et al., 2019b). This study also shows that hydrodynamic processes have a significant control on the distribution of specific clay minerals in the Ravenglass Estuary; the highest relative abundance of chlorite is observed in predominantly coarse sediment (Fig. 4.7A, 4.7F and 4.8A), because chlorite is relatively concentrated in the high-energy and coarser-grained sub-depositional environment, and are partly deposited as sand grade lithic (Fig. 4.12C). Illite is most abundant in the finer sediment dominated sub-depositional environments of the estuary (mud flat and salt marsh) (Fig. 4.7A, 4.7L and 4.8D), therefore, illite enrichment in these finer sediments reflects deposition under relatively quiescent conditions, typically

along the margin of the inner estuary and the central basin of the estuary. Kaolinite flocculates at a lower salinity (Whitehouse et al., 1960) and has a faster aggregation rate (Edzwald and O'Mella, 1975), which led to early deposition of kaolinite upstream at the fluvial-marine interface. However, kaolinite abundance is relatively homogeneous throughout the Ravenglass Estuary (Fig. 4.8B), because the effect of differential settling has been dissipated due to the intense estuarine mixing, caused by combined action of strong tidal currents, wind, and a short-estuarine length. This interpretation with agrees with what has been earlier reported by Griffiths et al. (2018). Although smectite is present in negligible abundance in Ravenglass Estuary sediments, it is relatively abundant in the high energy sub-depositional environments of the estuary (Fig. 4.8C), where it is mostly associated with coarser plagioclase lithic alterations (Fig. 4.12B). However, other reports have linked the negligible abundance of smectite in coastal settings, to tidal flushing and subsequent deposition offshore (Edzwald and O'Mella, 1975; McKinley et al., 2003; Worden and Burley, 2003).

Experiments undertaken by Matlack et al. (1989) showed that mechanical infiltration of clay-laden waters has led to a stratification of specific clay minerals within sand packages; illite and smectite passing (percolate in suspension) through sediment deposits but chlorite is preferentially trapped as clay coats. Although, this study shows that, smectite slightly increase with increasing depth, but overall there is no systematic changes in specific clay minerals with depth (Fig. 4.6) along the Ravenglass Holocene sediments. The interpretation made here, is in agreement with the previous work in Ravenglass Estuary (Griffiths et al., 2018) and Gironde Estuary (Virolle et al., 2019a). Furthermore, the reason why clay minerals distribution in Ravenglass Holocene sediments, does not fit into the Matlack et al. (1989) experiment of mechanical infiltration has been extensively explained by Griffiths et al. (2018).

4.6.5 Detrital clay grain coats in estuary sub-depositional environment

The distribution of clay coat coverage, clay fraction and clay minerals in the different sub-depositional environment, are broadly similar (Fig. 4.7), hence the clay coats are potentially detrital. This

relationship has been previously reported in Ravenglass sediments (Griffiths et al., 2018). The distribution patterns of clay coat coverage in both the Holocene cores (this study), the surface and the near-surface sediment of Ravenglass Estuary, are broadly similar (Fig. 4.7 and 4.12) (Griffiths et al., 2018; Wooldridge et al., 2017a; Wooldridge et al., 2017b). This is because the depositional patterns are preserved in the Holocene cores indicating that there is no post-depositional addition or loss of clay coats (or clay). In addition, clay fraction (including clay coats) abundance is controlled by estuarine hydrodynamics and thus predictable as a function of sub-depositional environments. The high-energy outer-estuary sub-depositional environments; tidal inlet, foreshore and ebb-tidal-delta, have no or negligible clay coat coverage due to lack of clay fraction deposit (low suspended load) (Fig. 4.7D and 4.12F), whereas low energy, inner estuary and central basin sub-depositional environments have extensive clay coat coverage (Fig. 4.7D, 4.12D and 4.12E), due to abundance of clay fraction material deposited under slack-water condition.

The distribution patterns of clay-coat coverage in the Ravenglass palaeo-sub-depositional environments, reflects the clay-coat coverage in Ravenglass Estuary surface sediments (Wooldridge et al., 2017a; Wooldridge et al., 2017b). However, the Holocene cores of Ravenglass Estuary are capped by a clay rich saltmarsh and mud flats (Fig. 4.3, 4.4, 4.5 and 4.6), that tend to act as an impermeable layer of sediment, thus blocking the downward movement of porewaters laden with clay and clogging pore throats (Griffiths et al., 2018b). This resulted in no or negligible mechanical infiltration during post-depositional processes (Fig. 4.3, 4.4, 4.5 and 4.6). The broad similarities in the extent of clay-coat coverage, between surface and Holocene sediment, may likely suggests the lack of significant mechanical infiltration, tidal pumping, lateral flow of water along sand layers or bioturbation, during post depositional processes, that may overprint the primary depositional processes in the Holocene sediment (Griffiths et al., 2018; Wooldridge et al., 2017b; Wooldridge et al., 2019a). In addition, infiltration-derived penetration of clay material into coarse sediment can be hindered by flocculation of clays and suspended clay- to silt-sized material, since the pore space of the near surface sediment will got clogged by the clay flocs (Buurman et al., 1998).

The observed relationship between clay fraction and clay coat coverage (Fig. 4.7B and 4.7D), is in agreement with published work, on the distribution of clay coats in marginal marine settings, for example distribution of detrital clay coats in near-surface estuarine sediments (Griffiths et al., 2018), controls on modern sand grain coat formation (Dowey et al., 2017), detrital clay grain coats in tidal bars (Virolle et al., 2020), clay-coated sand grains of estuarine surface sediment (Wooldridge et al., 2017b) and detrital clay coats in estuarine clastic deposits (Virolle et al., 2019a). Furthermore, the extent of coat coverage in the sand flat and tidal bar sediments (Fig. 4.7D and 4.12E), is within the reported optimum range of grain coats coverage, to preserve porosity (Bloch and Helmold, 1995; Bloch et al., 2002; Heald and Baker, 1977; Pittman et al., 1992; Wooldridge et al., 2017b), thus making the sand flat and tidal bar sediments in Ravenglass Holocene cores, a potential site for clay coat that would preserve porosity, by inhibiting quartz overgrowth in deeply buried sandstone. Clay coats present in ancient and deeply buried sandstone reservoirs, are composed of two different layers; a densely packed inner layer with a tangentially orientation, which constitute the root layer, and is overlain by an outer coat layer, that is made up of a perpendicular euhedral flake that tends to grow into grain pore spaces (Ajdukiewicz and Larese, 2012; Wise et al., 2001; Worden et al., 2020a). To this regard, the clay coats in the Ravenglass Holocene sediments as presented in this study and numerous studies in Ravenglass Estuary (Griffiths et al., 2018; Griffiths et al., 2019a; Wooldridge et al., 2017b; Wooldridge et al., 2019a; Wooldridge et al., 2018), are analogues for the inner layer of clay coats in deeply buried reservoirs, formed as a result of thermally driven recrystallisation of precursor detrital-clay coats (Aagaard et al., 2000; Billault et al., 2003; Bloch et al., 1997). Therefore, the study of clay coats distribution in Ravenglass Estuary Holocene sediments, will be helpfull in developing a predictive model, that will aid in understanding the distribution of clay-coat in deeply buried sandstone reservoirs. Furthermore, knowledge of the distribution of minerals and elements (and chlorite) is helpful in petroleum exploration and reservoir development in both deep and shallow reservoirs as clays (chlorite) can be good or bad, depending on the amount and the diagenetic setting. It is also of interest in carbon capture and storage and geothermal applications.

4.7 Conclusions

1. This work involves the application of classification scheme based on geochemical data, developed using supervised machine RPART routine in R Statistical Software, to automatically discriminate palaeo-sub-depositional environments of an inner estuary Holocene core sediments of Ravenglass Estuary, NW England, United Kingdom.

2. The interpreted palaeo-sub-depositional environments are salt marsh, mud flat, mixed flat, sand flat, tidal bar, tidal inlet, northern foreshore, southern foreshore, ebb tidal delta, and gravel bed, these environments of deposition were successfully correlated to revealed the stratigraphic organisation of the valley infills.

3. The dominant mineral assemblages of the inner estuary Holocene sediments of the Ravenglass Estuary, as revealed by BSE and QEMSCAN analyses, are: quartz, K-feldspar, plagioclase, muscovite, biotite, illite, chlorite, kaolinite, smectite.

4. Both plagioclase and k-feldspar distribution are independent of grain size distribution but varies across the sub-depositional environment, whereas biotite and muscovite are highest in the finer sediment and varies greatly across the sub-depositional environments.

5. Clay minerals distribution varies greatly between the sub-depositional environments; chlorite is relatively most abundant in the sand flat and tidal inlet, and uniformly low in mud flat, mixed flat and salt-marsh, chlorite is likely to occur as clay forming grain coat or as lithic grain in coarser sediment, kaolinite is relatively most abundant in the mixed flat and uniformly distributed in north foreshore, ebb-tidal-delta, tidal inlet, sand flat, mud flat and salt-marsh, smectite is relatively most abundant in the ebb-tidal-delta, north foreshore and tidal inlet and low in mud flat and salt-marsh, illite is relatively most abundant in salt-marsh and mud flat, and uniformly distributed in north foreshore, ebb-tidal-delta, tidal inlet, sand flat, and mixed flat.

6. Clay coat coverage increases with increasing clay fraction abundance; in the salt marsh and mud flat sediment, clay occur as either pore-filling or grain-coating, with over 40% coat coverage, in the mixed flat and sand flat sediment, clay is mostly present as grain coat with reported coat coverage of as much as 40%. The tidal inlet, foreshore and ebb-tidal-delta have a coat coverage of as much as 7%.

7. Sand flat and tidal bars sediments, that in Ravenglass have >10% detrital coat coverage (within optimum range), and that contain chlorite-bearing lithic grains, can form diagenetic chlorite coats that can preserve anomalously high porosity in inhibiting quartz cementation, in deeply buried sandstones.

8. The distribution patterns of sediment mineralogy and different clay mineral types in the Ravenglass Estuary Holocene core, are primarily controlled by the grain size and estuarine hydrodynamics. Post-depositional processes, particularly early-diagenetic mineral alteration appeared to have influenced clay-mineral distribution patterns, in the coarser sediment of Ravenglass Holocene cores, via mineral alteration of feldspar grains.

9. This work has proved that there are strong and predictable relationships between sediment geochemistry and mineralogy with specific sub-depositional environments within the Ravenglass Estuary.

5. Synthesis Discussion and Synopsis

5.1 Estuarine sediment geochemical signatures

5.1.1 What is the geochemical composition of the surface sediment and how are they distributed, in the Ravenglass Estuary sediment?

The elements present in all samples are; Al, Si, K, Ca, Ti, Fe, Mn, Rb, Sr, Zr, Ba and Cs (Table 2.2). The distribution of elements in the sediment of Ravenglass Estuary vary greatly with some apparent links to sub-depositional environment and geographic location.

Aluminium and K have the highest concentration in the finest grained sediments of the mud and mixed flat sediment and are lowest in coarsest grained sediments of the northern foreshore and tidal inlet (Fig. 2.4 and 2.5). The distribution of Al and K is controlled by illite clay distribution. Rubidium has similar geochemical properties to K, in terms of ionic radius and charge (Krauskopf and Bird, 1967), and the two elements show similar distributions in the estuary, although the concentration of K is highest in the mixed and mud flats whereas Rb is relatively low possibly indicating that Rb is controlled by K-feldspar rather than illite abundance.

Iron, Mn and Ti have their highest concentrations in the finest grained sediments of the mud and mixed flat sediment and have their lowest concentrations in coarsest grained sediments of the foreshore, tidal inlet, tidal bar (Fig. 2.4 and 2.5). Iron and Mn probably exist within detrital lithic grains and minerals (e.g., chlorite, biotite) (Griffiths et al., 2019a) and in weathering products such as hydroxides (Daneshvar, 2015). Fe is observed to be preferentially concentrated in the upper reaches of the Ravenglass estuary confirming that fluvially-transported iron is trapped at the site of mixing between river water and seawater (Worden et al., 2020a). The increase in Ti in the finest grained sediments is likely to be due to mica minerals (illite, muscovite and biotite) as rutile is likely to be concentrated in the sand fraction. Gibbs (1977) reported that particle size has a significant role in the accumulation and exchange processes of metals between sediments water interface and the heaviest enrichment of metals occurs in the finer particles.

The concentration of calcium closely matches the distribution of calcite (Griffiths et al., 2019a). Calcite is largely found as bioclastic material, in the gravel beds on the lower Esk Estuary and the southern side of the tidal inlet (Fig. 2.4 and 2.5). Strontium show some pockets of local enrichment (Fig. 2.4), especially in gravel-rich sediment deposits, potentially due to their present in lithic fragments (Andrew-Oha et al., 2017; Brookins, 1988), and shell fragments, possibly due to an Sr-Ca association, as Sr can isomorphously substitute for Ca in carbonates (Baker et al., 1982).

Barium concentration is highest in parts of the Esk and Irt arms of the estuary, along the southern side of the tidal inlet and in the ebb-tidal delta (Fig. 2.4). Caesium concentrations are slightly higher in the lower part of the Esk estuary, the upper part of the Irt estuary and along part of the southern side of the tidal inlet (Fig. 2.4). Like barium, caesium concentrations do not seem to show any systematic pattern for the sub-environments of deposition (Fig. 2.5), they have similarly bland distribution maps, with lowest concentrations in the coarsest grained sands. Barium might be present substituting for K in detrital K-feldspar or possibly in barite. Caesium may also substitute for K in micas and feldspars.

Zirconium has high concentration along the southern part of the tidal inlet and southern foreshore and the low concentration along the northern part of the tidal inlet and northern foreshore (Fig. 2.4 and 2.5) The distribution of Zr in the sand fraction is related to abundance of heavy mineral contents (Padmalal et al., 1997; Padmalal and Seralathan, 1995).

The sporadic high concentrations of elements in several sites across the Ravenglass Estuary and the great deal heterogeneity in a given sub-depositional environment (Fig. 2.4 and 2.5), is caused by the local-specific condition of the estuary (for example different source area, hydrodynamics and wave-direction). Sediment geochemical data is heterogeneously distributed, thus reflecting different sediment sources and interplay between multiple factors; supply type (provenance), hydrodynamics (transport and deposition); and early diagenesis (post depositional processes) (Daneshvar and Worden, 2017; Griffiths et al., 2018; Griffiths et al., 2019a; Griffiths et al., 2019b).

5.1.2 What is the relationship between the distribution of geochemical data and estuary sub-depositional environments, in the Ravenglass Estuary?

In Ravenglass estuary, there is a strong relationship between specific sub-depositional environments and element indices within the estuary (Fig. 2.6 and 2.7). K/(K+Al) is low in mud flats, ebb-tidal delta and southern foreshore sub-environments, it is highest in sand flat, tidal bar and northern foreshore sediment sub-environments; K/(K+Si) is highest in the least quartz-rich, most fine-grained mud flat sediments. It has consistently low values in the sand-rich sub-depositional environments; K/(K+Ca) is low in mud flats and southern foreshore sub-environments. It is highest in sand flat and tidal bar sub-environments; K/(K+Mn) is low in mud flats. It is highest in sand flat, tidal bar, tidal inlet, and northern and southern foreshore sub-environments; K/(K+Sr) is uniformly high in inner estuary mud, mixed and sand flats and tidal bar sub-environments. It is lowest in mid and outer estuary tidal inlet, northern and southern foreshore and ebb-tidal delta sub-environments, it differentiates the inner and outer estuarine sub-environments; Ca/(Ca+Fe) is lowest in sand flat and tidal bar sub-environments. It is highest in southern foreshore sediment and intermediate in all other sub-environments; Sr/(Sr+Rb) is lowest in ebb-tidal delta and southern foreshore. It is highest in tidal inlet and northern foreshore showing that this index is a good differentiator of the two parts of the lower estuary/marine part of the system.

The relationship between element indices and sub-depositional environment is controlled by estuarine hydrodynamics. However, the distribution pattern could be heterogenous within a given subenvironment (Fig. 2.6). The estuary central basin shows no significant variations in chemical composition and this is due intense sediment mixing by estuarine hydrodynamics and also dilution from different sediment sources, as the estuary sediments sources and their respective pathways are grouped as granite; Esk River, andesite and red bed sandstone; Irt River and glacial till (Daneshvar and Worden, 2017; Griffiths et al., 2018; Griffiths et al., 2019a)

5.2 Distribution of iron in the estuary

5.2.1 What are the fundamental controls on the distribution of Fe in the estuary?

The Ravenglass sediments were sourced from the andesite-dominated Borrowdale Volcanic Group and the Eskdale granite suite (Daneshvar and Worden, 2017; Griffiths et al., 2018; Griffiths et al., 2019a; Griffiths et al., 2019b; Merritt and Auton, 2000; Millward, 2002). Surface sediments from the Irt arm are marked by the highest Mn, Ti, and Fe concentrations, revealing a predominance of intermediate-mafic igneous source material (Fig. 3.3). The relatively higher Zr concentration and lower Mn, Ti, and Fe concentrations in the Esk arm than the Irt arm of the estuary confirms that the Esk had a less mafic, more felsic, supply of sediment than the Irt (Fig. 3.3). The felsic and intermediate-mafic igneous rock source areas for Ravenglass sediment contains Fe-bearing minerals such as chlorite, ilmenite, haematite, Fe-rich micas (phengite) (Moseley, 1978; Quirke et al., 2015; Rundle, 1979; Simpson, 1934; Young et al., 1986). The intermediate-mafic source area that was predominantly drained by the Irt arm, has abundant chlorite and this probably explains why the Irt sediments are relatively more Fe-enriched than the Esk sediments. Thus, geochemical data prove that provenance signals are present in the estuary despite estuarine mixing and the influence of glacial till.

Iron distribution in estuaries is influenced by grain size and TOC distribution (Poulton and Canfield, 2005; Zhu et al., 2012). Grain size in the Ravenglass Estuary decreases toward the margins of the inner estuary and central basin, mirroring the distribution of Fe. The finer grained sediments from tidal flat sub-depositional environments have higher concentration of Fe than sand-dominated sediments. Similar types of patterns have been explained previously as being the result of metal-scavenging phases such as Fe- and Mn-hydroxides, organic carbon (via metal-organic complexes), and clay minerals, being more abundant in silt and clay fractions than in sand (Padmalal et al., 1997; Padmalal and Seralathan, 1995). The transported-in clay minerals in estuary brackish waters increase the concentration of Fe in sediment by the creation of Fe-rich floccules and sorption of Fe (Forsgren et al., 1996); this is because clay grade sediment, owing to its large surface area, acts as a mechanical

substrate upon which Fe oxides/hydroxides can become attached (Horowitz and Elrick, 1987). However, Fe was also transported into the estuary as fluvially-transported complexes with organic matter, that were subsequently destabilised in the saline estuary and deposited at slack water conditions along with the finest grained sediment. Iron, capable of producing Fe-rich grain coating minerals, was also transported into the estuary as Fe-rich minerals, such as biotite and detrital chlorite, predominantly derived from the granite via the Esk arm of the estuary. This was interpreted from the Fe and Ti similar distributions in coarser sediments of sand dominated sub-depositional environments (Fig. 3.10), resulting from the occurrence of Fe- and Ti-bearing detrital aluminosilicates minerals in sand-grade lithics, owing to the hydrodynamic concentration of coarser sediments (Griffiths et al., 2019a; Worden et al., 2020a). Coarser sand-grade sediment is typically richer in lithic grains than fine sand (Fig. 3.15) (Kairo et al., 1993) and this interpretation is in agreement with the reported occurrence of chlorite-bearing lithic grains in the coarser sands from foreshore, tidal inlet, and tidal bar sub-depositional environments in Ravenglass Estuary (Griffiths et al., 2019a).

5.2.2 How does different type of Fe present in the estuary, affect Fe-minerals distribution?

Iron in the surface sediment is mainly present as either reactive amorphous and semi-crystalline iron oxide or less reactive Fe that primarily sits in aluminosilicate minerals, haematite or siderite (Li et al., 2017; Poulton and Raiswell, 2005). SEM-EDS analysis linked to geochemical data showed that much of the Fe in the Ravenglass sediment is present in the sub-2 µm sized, reactive amorphous and semi-crystalline iron oxide (Fig. 3.12). This type of Fe is associated with the highest organic carbon concentrations and finest grained sediment in tidal flat sub-depositional environments (Fig. 3.8). This type of Fe tends to form Fe-organic complexes in fluvial systems that then flocculate when they meet saline water in an estuary. The resulting flocs are deposited along with first sediment fraction (clay), with the highest concentration occurring in the most clay-rich sediment, and provide materials required for the subsequent formation of Fe-bearing minerals in the estuary (Berner, 1970; Lalonde et al., 2012).

The use of geochemical data, which may reflect mineral composition of sediment, has been used to discriminate lithology (Herron, 1986; Herron, 1988). The potential presence and relative abundance of Fe bearing clay minerals in surface sediment, has been determined from the relationship between Fe-Al. The high Fe-Al relationship shows that Fe-rich clay minerals, such as chlorite and its precursors might develop during subsequent diagenetic modification of the sediment during eodiagenesis and mesodiagenesis. Northern foreshore (NDe8), tidal inlet (De6), sand flat (De4), tidal bar (De4) and mud flat (De2) sub-depositional environments would be more likely to be Fe clay-enriched than southern foreshore (SDe8), ebb-tidal delta (De9) and mixed flat (De3) sub-depositional environments (Fig. 3.14), if the sediments underwent eodiagenesis and mesodiagenesis. This reinforces the results of mineralogical studies of Ravenglass Estuary sediment (Griffiths et al., 2019b).

However, enrichment of Fe in sediment does not guarantee that Fe-clay minerals such as chlorite, or its precursors, would develop. If sediment had pore-waters dominated by sulphate-rich seawater, if the sediment is enriched in organic matter and if the sediment was buried sufficiently slowly, then bacterial sulphate reduction would occur, creating H_2S that reacts with available Fe-phases to create eodiagenetic Fe-sulphides (e.g., pyrite) (Berner, 1970; Berner, 1980). The phenomenon of pyrite growth in Fe-rich sediment therefore inhibits the formation of eogenetic Fe-clay minerals and subsequent mesogenetic chlorite due to sequestration of Fe (Worden et al., 2020a). Similarly, in the absence of sulphate-rich marine pore-waters, oxidation of organic-enriched sediment can lead to elevated aqueous bicarbonate concentrations, due to a wide range of bacterial oxidation processes. If bicarbonate-enriched pore waters encounter sediment that is enriched in Fe, then siderite can develop (Worden and Burley, 2003). Pyrite is not present in the surface sediments at Ravenglass, but it has been reported in 1-m cores, especially in the inner portion of the estuary (Griffiths et al., 2018) where we now know there is relative enrichment of organic matter in the estuary. This suggests that some of the most Fe-enriched sediments, that are also TOC-enriched, may result in pyrite development instead of Fe clay mineral development, if the pore waters are enriched in marine sulphate. Estuary waters have the lowest sulphate concentrations in the upper estuary (Daneshvar,

2015), so that Fe-enriched sites highest up the estuary may be most likely to leave Fe capable of creating Fe clay minerals rather than pyrite. In contrast, it is noteworthy that little or no siderite has been reported from the surface sediments from Ravenglass distribution (Daneshvar, 2015; Daneshvar and Worden, 2017; Griffiths et al., 2018; Griffiths et al., 2019a; Griffiths et al., 2019b), suggesting that siderite has not developed at the expense of Fe-clay minerals in this type of environmental setting, despite the local abundance of organic matter.

5.3 Distribution of clay minerals in Holocene Ravenglass sediments

5.3.1 What are the clay minerals present and how are they distributed in the Ravenglass Estuary Holocene sediments?

The dominant clay minerals present in the Ravenglass Holocene sediment are chlorite, illite, kaolinite and smectite; chlorite ranges between 0.4 to 14.0%, illite ranges between 0.9 to 32.2%, kaolinite ranges between 0.1 to 9.1%, and smectite ranges between 0.1 to 1.0% (Table 4.1 and Fig. 4.7). The proportion of illite, chlorite and kaolinite in the estuary, seemingly match the global oceanic clay-mineral trend (Rateev et al., 2008). The relative abundance of chlorite is highest in the sand flat and tidal inlet, and low in mud flat, mixed flat and salt-marsh, kaolinite is high in the mixed flat and uniformly distributed in north foreshore, ebb-tidal-delta, tidal inlet, sand flat, mud flat and salt-marsh, smectite is highest in the ebb-tidal-delta, north foreshore and tidal inlet and low in mud flat and salt-marsh, illite is high in salt-marsh and mud flat, and uniformly distributed in north foreshore, ebb-tidal-delta, tidal inlet, sand flat, and mixed flat (Fig. 4.8 and 5.1). Chlorite is likely to occur as clay forming grain coat or as lithic grain in coarser sediment, while illite closely followed the distribution of clay fraction, because illite is predominantly present in a clay grade form. The influence of sub-depositional environment on the distribution of clay minerals in Ravenglass surface and near surface sediments has been reported (Griffiths et al., 2018; Griffiths et al., 2019b). The high relative abundance of chlorite in the sand flat and tidal inlet, this is expected, as the abundance of chlorite in sandy sediment deposited along inner estuarine sub-depositional environment of Ravenglass, has been reported

(Griffiths et al., 2018; Griffiths et al., 2019b), also chlorite widely occurs in sand and lithic grade sediment, deposited along estuary head (Worden et al., 2020a).

5.3.2 What controls clay-mineral distribution patterns and detrital clay coat in the Ravenglass Estuary?

Recent study on the Ravenglass Estuary Holocene sediments, reported that provenance, depositional environment, estuarine hydrodynamics, sediment supply and resident time, are the main controls on the distribution of clay minerals (Daneshvar and Worden, 2017; Griffiths et al., 2018; Griffiths et al., 2019a; Griffiths et al., 2019b).

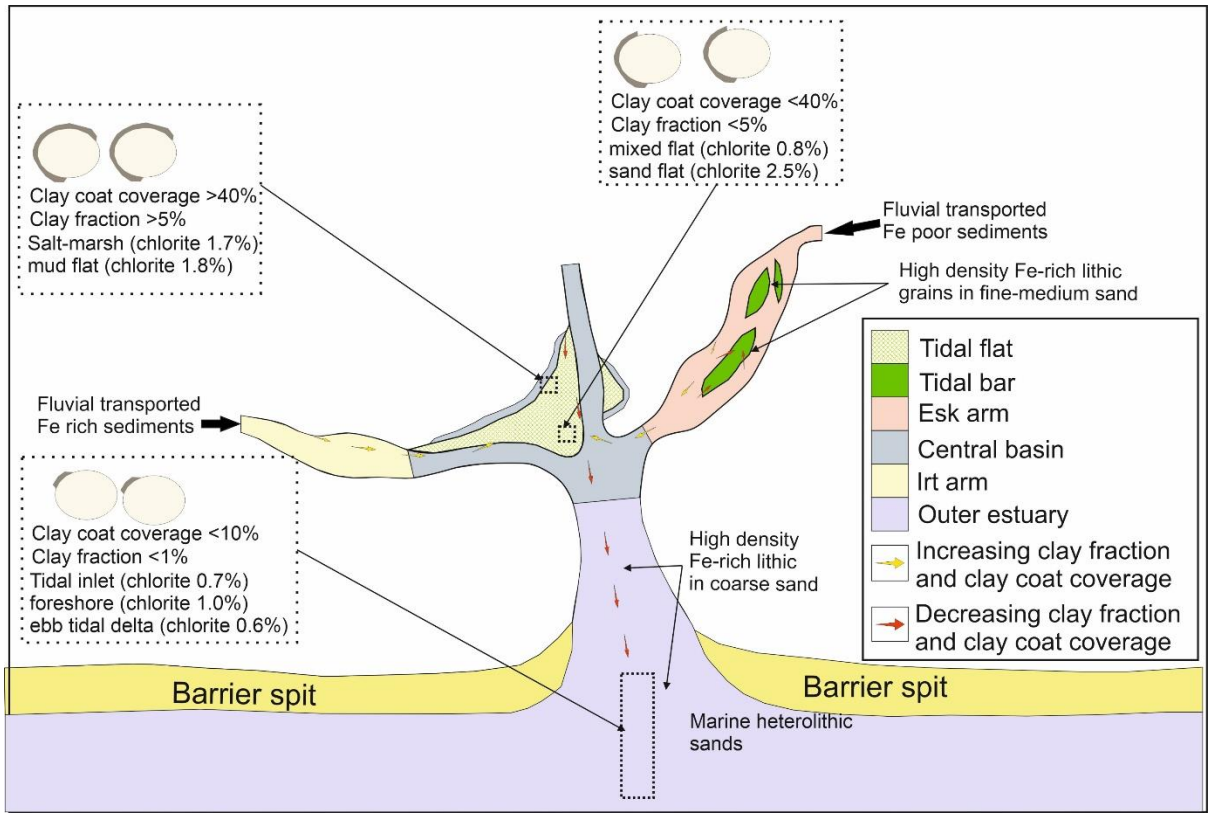

Figure 5.1; Conceptual model showing the distribution of clay fraction, clay coat coverage and chlorite across the different sub-depositional environments of Ravenglass Estuary.

Clay minerals in Ravenglass estuary originate from the following geological processes; the weathering of Palaeozoic and Triassic bedrock and Quaternary drift, the internal erosion of Ravenglass Glacial Till Members, and the landward displacement of sediment along the intertidal zone (Griffiths et al., 2018). Illite is reported to originate from Ravenglass Glacial Till Members (Griffiths et al., 2018), Eskdale granite (Quirke et al., 2015; Simpson, 1934; Young et al., 1986), and Borrowdale Volcanic Group

(Quirke et al., 2015). The origin of kaolinite is attributed to the chemical weathering of glaciofluvial and glaciolacustrine sediments of the Fishgarth Wood Till Member (Griffiths et al., 2019b). Smectite typically originate at the initial stage of chemical weathering (Salem et al., 2000), the alteration of plagioclase to smectite has been observed in the coarser sediment of Ravenglass. Chlorite distribution reflects the fluvial deposition of chlorite-enriched sediment, sourced from chloritised Eskdale Granite.(Griffiths et al., 2018; Griffiths et al., 2019b).

Diagenetic influence on clay minerals distribution across different depositional sites, is been exerted by both physicochemical processes (Grim and Johns, 1954; Nelson, 1960; Powers, 1957) and biological processes (McKinley et al., 2003; Needham et al., 2006; Needham et al., 2004; Needham et al., 2005; Worden et al., 2006). Plagioclase detrital mineral has undergone relatively rapid alteration, to smectite. The neoformation of clay minerals in Ravenglass Holocene sediment has been recently reported (Daneshvar and Worden, 2017), although Griffiths et al. (2018) have strongly argued that kaolinite origin is detrital (Moseley, 1978; Quirke et al., 2015; Young et al., 1986), rather than diagenetic.

As widely reported, hydrodynamic forces have a significant influence on the textural characteristics of estuarine sediment (Dalrymple et al., 1992), for example the physical sorting of clay minerals due to grain size variation during transport (Gibbs, 1977). Furthermore, previous studies on this estuary showed that the distribution patterns of clay minerals in the Ravenglass Estuary sediment are governed by estuarine hydrodynamics (Griffiths et al., 2018; Griffiths et al., 2019b). This study also shows that hydrodynamic processes appear to have a significant control on the distribution of specific clay minerals in the Ravenglass Estuary; the highest relative abundance of chlorite is observed in predominantly coarse sediment (Fig. 4.7, 4.8 and 5.1), because chlorite is relatively concentrated in the high-energy and coarser-grained sub-depositional environment and deposited as sand grade lithic (Fig. 4.12 and 5.1). Illite is most abundant in the finer sediment dominated sub-depositional environments of the estuary (mud flat and salt marsh) (Fig. 4.7 and 4.8), therefore, illite enrichment

in these finer sediments reflects deposition under relatively quiescent conditions, typically along the margin of the inner estuary and the central basin of the estuary. Kaolinite flocculates at a lower salinity (Whitehouse et al., 1960) and has a faster aggregation rate (Edzwald and O'Mella, 1975), which led to early deposition of kaolinite upstream at the fluvial-marine interface. However, kaolinite abundance is relatively homogeneous throughout the Ravenglass Estuary (Fig. 4.8B), because effect differential settling has been dissipated due to the intense estuarine mixing, caused by combined action of strong tidal currents, wind, and a short-estuarine length. This interpretation with regards to distribution of kaolinite, agrees with what has been earlier reported by Griffiths et al. (2018). Although smectite is present in negligible abundance in Ravenglass Estuary sediments, it is relatively abundant in the high energy sub-depositional environments of the estuary (Fig. 4.8), where it is mostly associated with coarser plagioclase lithic alterations (Fig. 4.12). However, other reports have linked the negligible abundance of smectite in coastal settings, to tidal flushing and subsequent deposition offshore (Edzwald and O'Mella, 1975; McKinley et al., 2003; Worden and Morad, 2003).

The distribution of clay coat coverage, clay fraction and clay minerals in the different sub-depositional environment, are broadly similar (Fig. 4.7 and 5.1), hence the clay coats are potential detrital. This relationship has been previously reported in Ravenglass sediments (Griffiths et al., 2018). The distribution patterns of clay coat coverage in both the Holocene cores (this study), the surface and the near-surface sediment of Ravenglass Estuary, are broadly similar (Fig. 4.7, 4.12 and 5.1) (Griffiths et al., 2018; Wooldridge et al., 2017a; Wooldridge et al., 2017b). This is because the depositional patterns are preserved in the Holocene cores proving that there is no post-depositional addition or loss of clay coats (or clay). In addition, clay fraction (including clay coats) abundance is controlled by estuarine hydrodynamics and thus predictable as a function of sub-depositional environments. The high-energy outer-estuary sub-depositional environments; tidal inlet, foreshore and ebb-tidal-delta, have no or negligible clay coat coverage due to lack of clay fraction deposit (low suspended load) (Fig. 4.12 and 5.1), whereas low energy, inner estuary and central basin sub-depositional environments; salt marsh, mud flat, have extensive clay coat coverage (Fig. 4.12 and 5.1), due to abundance of clay fraction

material deposited under lack-water condition. The depositional condition has significance influence on the extent of clay coat coverage (Matlack et al., 1989; Wooldridge et al., 2017a; Wooldridge et al., 2017b). The observed relationship between clay fraction and clay coat coverage as modified by estuarine hydrodynamics and depositional environments, is in agreement with numerous published work, on the distribution of clay coats patterns in marginal marine settings, for example distribution of detrital clay coats in near-surface sediments of Ravenglass Estuary (Griffiths et al., 2018), sedimentary controls on modern sand grain coat formation (Dowey et al., 2017), detrital clay grain coats in estuary tidal bars (Virolle et al., 2020), clay-coated sand grains of Ravenglass surface sediment (Wooldridge et al., 2017b) and Detrital clay grain coats in estuarine clastic deposits (Virolle et al., 2019a).

5.4 Synopsis

1. This work represents a detailed study of Holocene sediment, analysed for geochemistry and mineralogy using pXRF, QEMSCAN, LPSA, TOC analyses and statistical techniques, from the Ravenglass Estuary, NW England, United Kingdom.

2. The depositional environments defined across the estuary, include gravel beds, salt marsh, mud flats, mixed flats, sand flats, tidal bars, tidal inlet, foreshore, and ebb-tidal-delta. The foreshore of Ravenglass Estuary was subdivided into discrete northern and southern portions as they have distinct textural and elemental attributes.

3. Portable XRF analysis helped in identifying the provenance of sediment and sub-depositional environment; it can also be used as a proxy for what minerals might develop in estuarine sediment, i.e., during eo- or meso-diagenesis, but it cannot be employed to unequivocally reveal present-day mineralogy.

4. Elements are heterogeneously distributed in the estuary, especially in terms of localised concentrations of Al, K, Ca, Fe, Mn, Zr, Rb. However, element indices, varying between 0 and 1,

were employed for the discrimination of sub-depositional environments, instead of raw concentration data, to circumvent the problem of variable dilution by quartz and closed datasets. These indices are heterogeneously distributed throughout the estuary, showing that element concentration patterns are not simply due to variable dilution by quartz

5. Iron increases from the fluvial sediment to the estuarine sediment, with some local variations and then gradually decreases seaward. The Fe concentration is highest in tidal flat sediments. Iron is present in detrital Fe minerals including chlorite, biotite, Fe-bearing white mica, and minor Fe-oxides that are present within lithic grains. Iron is also present as a fine-grained material, probably as an oxide or hydroxide, that is below the spatial resolution of SEM-EDS (therefore < 2 μm). This iron is associated with elevated organic carbon concentrations. The fine-grained Fe may be brought into the estuary as fluvially-derived metal-organic complexes that are destabilised in the saline waters of the estuary and that settle out as floccules in fine sediment or as coats on sand grains. The distribution and accumulation of Fe in the estuarine sediments are controlled by hinterland lithology, sediment grain size, organic enrichment, and hydrodynamic conditions.

6. The application of classification scheme based on geochemical data, developed using supervised machine RPART routine in R Statistical Software, was used to discriminate paleo-sub-depositional environments from Holocene core of Ravenglass. A supervised machine learning method was developed for the automatic discrimination of paleo-sub-depositional environments, with the model calibrated using element indices from surface sediment. The model was successfully applied to cores drilled through the Holocene succession at Ravenglass to predict sub-depositional environments.

7. The interpreted paleo-sub-depositional environments from Holocene core are salt marsh, mud flat, mixed flat, sand flat, tidal bar, tidal inlet, northern foreshore, southern foreshore, ebb tidal delta, and gravel bed. These environments of deposition were successfully correlated to reveal

the stratigraphic organisation of the valley infills and to show that there was a much greater marine influence at the core sites during the Holocene than at the present time.

8. The dominant minerals of the Ravenglass Holocene sediments, as revealed by BSE and QEMSCAN analyses, are: quartz, K-feldspar, plagioclase, muscovite, biotite, illite, chlorite, kaolinite, smectite. Both plagioclase and K-feldspar distributions are independent of grain size distribution but they vary across the sub-depositional environments, whereas biotite and muscovite are at highest concentrations in the finer sediment.

9. Clay minerals distribution varies greatly between the different sub-depositional environment; chlorite is relatively most abundant in the sand flat and tidal inlet and chlorite is likely to occur as clay forming grain coat or as lithic grain in coarser sediment, kaolinite is relatively most abundant in the mixed flat, smectite is relatively most abundant in the ebb-tidal-delta, north foreshore and tidal inlet, illite is relatively most abundant in salt-marsh and mud flat.

10. Clay coat coverage increase with increasing clay fraction abundance; in the salt marsh and mud flat sediment, clay occur as either pore filling or grain coating, with over 40% coat coverage, in the mixed flat and sand flat sediment, clay is mostly present as grain coat with reported coat coverage of less than 40%. The tidal inlet, foreshore and ebb-tidal-delta have a coat coverage of less than 10%. Sand flat and tidal bars sediments, that in Ravenglass have >10% detrital coat coverage (within optimum range), and that contain chlorite-bearing lithic grains, can form diagenetic chlorite coats that can preserve anomalously high porosity in inhibiting quarts cementation, in deeply buried sandstone.

11. The distribution patterns of minerals in the Ravenglass Estuary Holocene core, are primarily controlled by the grain size and estuarine hydrodynamics. Post-depositional processes, particularly early-diagenetic mineral alteration appeared to have influenced clay-mineral

distribution patterns, in the coarser sediment of Ravenglass Holocene cores, via mineral alteration of feldspar grains.

12. Provenance, sediment mineralogy and grain size, controlled by estuarine hydrodynamics, are the dominant controls on the distribution of sediment geochemical data and mineralogy in the Ravenglass Estuary. This work has proved that there are strong and predictable relationships between sediment geochemistry and mineralogy with specific sub-depositional environments within the Ravenglass Estuary Holocene sediment.

6. Suggestion for future work

6.1 Sediment Geochemistry

1. Considering that the majority of Fe is present in the < 2µm fraction, QEMSCAN struggle to identify this form of Fe. The different Fe form can be identify with chemical extraction reagent using a simplified three stage extraction procedure developed by Poulton and Raiswell (2005). Followed by the determining the amount of organic carbon associated with reactive Fe phase, the extraction of Fe oxide bound organic carbon can be carried out through reductive dissolution of Fe oxides and associated release of sorbed/incorporated OC by bicarbonate-citrate buffered dithionite as developed by Mehra and Jackson (2013).
2. pXRF analysis of different grain sizes and types; clay size, silt size and different sand grades, as well as sand grain and lithic grain, where each size separate should be analysed, to determine whether Fe is preferentially concentrated with different grades of sediment.
3. The analysis of pore-water chemistry, for trace metals, major elements isotopes, could potentially provide better understanding, with regards to the mineral alteration and/or neoformation, related to eogenetic processes in the Ravenglass Holocene core sediments. Pore-water chemical analysis may also provide a critical insight into the role detrital clay coat formation during mechanical infiltration, for example, the enrichment of clays in sediment pore-water overlying an impermeable glacial layers, and thus lead to the post-depositional formation of detrital clay coats (Morad et al., 2010).
4. Different sources of organic matter into the Ravenglass Estuary. Although the population is sparse, the effect on the natural environment is profound. Pretty much all of the UK, including Ravenglass, is not ‘natural’. E.g. the present of sheep farms bordering the estuary along the salt coat, and that means the vegetation is partly as a result of farming practices. The composition of organic matter in the Ravenglass Estuary is the result of mixing between external inputs such as atmospheric deposition, riverine transport, and anthropogenic input (including farming activities), sediment bound biological activities. Bulk parameters, e.g.

$\delta^{13}C_{org}$ and OC/N ratio have been widely used to estimate relative contributions of terrestrial and marine organic matter in marine environments (Hedges et al., 1997).

6.2 Clay minerals and Clay coat distribution

5. The modern analogue study of clay minerals and clay coat distribution has been extensively carried out in the surface sediment (< 2 cm) and near surface core (< 1 m) of Ravenglass Estuary (Griffiths et al., 2018; Griffiths et al., 2019a; Griffiths et al., 2019b; Wooldridge et al., 2017a; Wooldridge et al., 2017b; Wooldridge et al., 2019a; Wooldridge et al., 2019b; Wooldridge et al., 2018). To better understand clay minerals and clay-coat coverage in marginal-marine sandstone reservoirs, there is a need to extend this study across the entire Holocene succession, through core studies (< 15 m) of 20 geotechnical drilled cores, so that a detailed understanding of the control on clay minerals and clay coat distribution, can be established. Therefore, the future work suggests that this core studies should be replicated across the entire Ravenglass Estuary sub-depositional environment. The work should involve the application of geochemical data based automatic classification scheme developed by (Muhammed et al., 2022), to define the pekoe-sub-depositional environment of the core samples, then followed by petrographic analyses and statistical techniques for clay minerals and clay coat studies.
6. It is theoretically possible that mechanical-infiltration could lead to the formation of clay coats within estuarine sediment (Buurman et al., 1998; Matlack et al., 1989; Pittman et al., 1992; Wilson, 1992). However, results presented in this study suggest that mechanical-infiltration, does not affect the distribution patterns of clay minerals or detrital clay coat in Holocene (< 15 m) sediments. Furthermore, the reason why clay minerals distribution in Ravenglass Holocene sediments does not fit into the Matlack et al. (1989) experiment of mechanical infiltration has been extensively explained by Griffiths et al. (2018), and to address this challenges, and to better understand how clay size material are been distributed within sand

packages in tidally-influenced depositional environments through mechanical infiltration, following experiments are envisaged; (1) Set up an experiment for mechanical infiltration, where clay-laden pore-waters are flushed through clean sand, over different tidal-cycles (e.g. simulation of both rising and falling water levels). (2) Matlack et al. (1989) conducted the experiment (mechanical infiltration) with fresh water instead of saline water, and saline waters typically lead to flocculation of clay minerals (Forsgren et al., 1996). Therefore, an experiment for mechanical infiltration with saline water can simulate a condition similar to marine settings and subsequently lead to a better understanding on how infiltration affects the distribution of specific clay minerals in sands.

7. References

Aagaard, P., Jahren, J.S., Harstad, A.O., Nilsen, O. and Ramm, M. (2000) Formation of grain-coating chlorite in sandstones. Laboratory synthesized vs. natural occurrences. *Clay Minerals*, **35,** 261-269.

Aase, N.E., Bjorkum, P.A. and Nadeau, P.H. (1996) The effect of grain-coating microquartz on preservation of reservoir porosity. *American Association of Petroleum Geologists Bulletin*, **80,** 1654-1673.

Aehnelt, M., Worden, R.H., Canham, A.C., Hill, S.J., Hodgson, D.M. and Flint, S.S. (2013) Geochemical Correlation in an Exhumed Submarine Channel Complex (Tabernas Basin, SE Spain): Comparison to Sedimentological Correlation at Various Length Scales. *Journal of Sedimentary Research*, **83,** 669-690.

Ainsworth, R.B. (2005) Sequence stratigraphic-based analysis of reservoir connectivity: influence of depositional architecture – a case study from a marginal marine depositional setting. *Petroleum Geoscience*, **11,** 257-276.

Aitchison, J. (1982) The Statistical Analysis of Compositional Data. *Journal of the Royal Statistical Society: Series B (Methodological)*, **44,** 139-160.

Ajdukiewicz, J., Nicholson, P. and Esch, W. (2010) Prediction of deep reservoir quality using early diagenetic process models in the Jurassic Norphlet Formation, Gulf of Mexico. *AAPG bulletin*, **94,** 1189-1227.

Ajdukiewicz, J.M. and Lander, R.H. (2010) Sandstone reservoir quality prediction: The state of the art. *American Association of Petroleum Geologists Bulletin*, **94,** 1083-1091.

Ajdukiewicz, J.M. and Larese, R.E. (2012) How clay grain coats inhibit quartz cement and preserve porosity in deeply buried sandstones: Observations and experiments. *American Association of Petroleum Geologists Bulletin*, **96,** 2091-2119.

Al-Ramadan, K.A., Hussain, M., Imam, B. and Saner, S. (2004) Lithologic characteristics and diagenesis of the Devonian Jauf sandstone at Ghawar Field, eastern Saudi Arabia. *Marine and Petroleum Geology*, **21,** 1221-1234.

Allen, G.P. (1972) Etude des processus sédimentaires dans l'estuaire de la Gironde. *These Doctorat des Sciences, Universite Bordeaux I*.

Allen, G.P. and Posamentier, H.W. (1994) Transgressive facies and sequence architecture in mixed tide-and wave-dominated incised valleys: example from the Gironde Estuary, France.

Aller, R.C. and Aller, J.Y. (1998) The effect of biogenic irrigation intensity and solute exchange on diagenetic reaction rates in marine sediments. *Journal of Marine Research*, **56,** 905-936.

Aller, R.C. and Michalopoulos, P. (1999) *Invited lecture: Tropical, mobile mud belts as global diagenetic reactors*. Balkema, Rotterdam, 289-292 pp.
Andersson, P.O.D., Worden, R.H., Hodgson, D.M. and Flint, S. (2004) Provenance evolution and chemostratigraphy of a palaeozoic submarine fan-complex: Tanqua Karoo Basin, South Africa. *Marine and Petroleum Geology*, **21,** 555-577.
Anderton, R. (1985) Clastic facies models and facies analysis. *Geological Society, London, Special Publications*, **18,** 31-47.
Andrew-Oha, I., Mosto-Onuoha, K. and Sunday-Dada, S. (2017) Contrasting styles of lead-zinc-barium mineralization in the Lower Benue Trough, Southeastern Nigeria. *Earth Sciences Research Journal*, **21,** 7-16.
Anjos, S.M.C., De Ros, L.F. and Silva, C.M.A. (1999) Chlorite Authigenesis and Porosity Preservation in the Upper Cretaceous Marine Sandstones of the Santos Basin, Offshore Eastern Brazil. In: *Clay Mineral Cements in Sandstones*, pp. 289-316.
Argyraki, A., Ramsey, M.H. and Potts, P.J. (1997) Evaluation of portable X-ray fluorescence instrumentation for in situ measurements of lead on contaminated land. *Analyst*, **122,** 743-749.
Armitage, P.J., Worden, R.H., Faulkner, D.R., Aplin, A.C., Butcher, A.R. and Iliffe, J. (2010) Diagenetic and sedimentary controls on porosity in Lower Carboniferous fine-grained lithologies, Krechba field, Algeria: A petrological study of a caprock to a carbon capture site. *Marine and Petroleum Geology*, **27,** 1395-1410.
Armstrong-Altrin, J.S., Lee, Y.I.l., Verma, S.P. and Ramasamy, S. (2004) Geochemistry of sandstones from the upper Miocene Kudankulam Formation, southern India: Implications for provenance, weathering, and tectonic setting. *Journal of Sedimentary Research*, **74,** 285-297.
Armstrong-Altrin, J.S., Machain-Castillo, M.L., Rosales-Hoz, L., Carranza-Edwards, A., Sanchez-Cabeza, J.-A. and Ruíz-Fernández, A.C. (2015) Provenance and depositional history of continental slope sediments in the Southwestern Gulf of Mexico unraveled by geochemical analysis. *Continental Shelf Research*, **95,** 15-26.
Aston, S.R. and Chester, R. (1973) The influence of suspended particles on the precipitation of iron in natural waters. *Estuarine and Coastal Marine Science*, **1,** 225-231.
Audry, S., Blanc, G., Schäfer, J., Chaillou, G. and Robert, S. (2006) Early diagenesis of trace metals (Cd, Cu, Co, Ni, U, Mo, and V) in the freshwater reaches of a macrotidal estuary. *Geochimica et Cosmochimica Acta*, **70,** 2264-2282.
Bahlis, A.B. and De Ros, L.F. (2013) Origin and impact of authigenic chlorite in the Upper Cretaceous sandstone reservoirs of the Santos Basin, eastern Brazil. *Petroleum Geoscience*, **19,** 185-199.
Baker, J.C., Havord, P.J., Martin, K.R. and Ghori, K.A.R. (2000) Diagenesis and Petrophysics of the Early Permian Moogooloo Sandstone, Southern Carnarvon Basin, Western Australia. *AAPG Bulletin*, **84,** 250-265.
Baker, P.A., Gieskes, J.M. and Elderfield, H. (1982) Diagenesis of carbonates in deep-sea sediments; evidence from Sr/Ca ratios and interstitial dissolved Sr (super 2+) data. *Journal of Sedimentary Research*, **52,** 71-82.
Barnes, R., Ambrose, K., Holliday, D. and Jones, N. (1994a) Lithostratigraphical subdivision of the Triassic Sherwood sandstone group in west Cumbria. *Proceedings of the Yorkshire Geological Society*, **50,** 51-60.
Barnes, R.P., Ambrose, K., Holliday, D.W. and Jones, N.S. (1994b) Lithostratigraphical subdivision of the Triassic Sherwood sandstone group in west Cumbria. *Proceedings of the Yorkshire Geological Society*, **50,** 51-60.
Barrie, G.M., Worden, R.H., Barrie, C.D. and Boyce, A.J. (2015) Extensive evaporation in a modern temperate estuary: stable isotopic and compositional evidence. *Limnology and Oceanography*, **60,** 1241-1250.
Barshep, D.V. and Worden, R.H. (2021) Reservoir Quality of Upper Jurassic Corallian Sandstones, Weald Basin, UK. *Geosciences*, **11,** 446.

Bauer, S., Blomqvist, S. and Ingri, J. (2017) Distribution of dissolved and suspended particulate molybdenum, vanadium, and tungsten in the Baltic Sea. *Marine Chemistry*, **196,** 135-147.
Beaufort, D., Rigault, C., Billon, S., Billault, V., Inoue, A., Inoue, S. and Patrier, P. (2015) Chlorite and chloritization processes through mixed-layer mineral series in low-temperature geological systems – a review. *Clay Minerals*, **50,** 497-523.
Benn, C. (2012) Lithological discrimination in deeply weathered terrains using multielemental geochemistry–an example from the Yanfolila gold project, Mali. *Explore*, **156,** 1-8.
Berger, A., Gier, S. and Krois, P. (2009) Porosity-preserving chlorite cements in shallow-marine volcaniclastic sandstones: Evidence from Cretaceous sandstones of the Sawan gas field, Pakistan. *American Association of Petroleum Geologists Bulletin*, **93,** 595-615.
Berner, E.K. and Berner, R.A. (2012) *Global environment: water, air and geochemical cycles. Second edition*. Princeton University Press, Princeton, 444 pp.
Berner, R.A. (1970) Sedimentary pyrite formation. *American journal of science*, **268,** 1-23.
Berner, R.A. (1980) *Early diagenesis: a theoretical approach*. Princeton University Press.
Billault, V., Beaufort, D., Baronnet, A. and Lacharpagne, J.C. (2003) A nanopetrographic and textural study of grain-coating chlorites in sandstone reservoirs. *Clay Minerals*, **38,** 315-328.
Bjorkum, P.A., Mjos, R., Walderhaug, O. and Hurst, A. (1990) The role of the late Cimmerian unconformity for the distribution of kaolinite in the Gullfaks field, northern North Sea. *Sedimentology*, **37,** 395-406.
Bjorlykke, K. (1998) Clay mineral diagenesis in sedimentary basins - a key to the prediction of rock properties. Examples from the North Sea Basin. *Clay Minerals*, **33,** 15-34.
Bjorlykke, K. (2010) *Petroleum geoscience- from sedimentary environments to rock physics*. Springer, Heidelberg, 508 pp.
Bloch, S., Gjelberg, J. and Dreyer, T. (1997) Preservation of anomalously high reservoir quality in deeply-buried, chlorite-coated, shallow marine sandstones (abs.): AAPG Annual Convention, Program with Abstracts, v. 6, p. *A12*.
Bloch, S. and Helmold, K.P. (1995) Approaches to predicting reservoir quality in sandstones. *American Association of Petroleum Geologists Bulletin*, **79,** 97-115.
Bloch, S., Lander, R.H. and Bonnell, L. (2002) Anomalously high porosity and permeability in deeply buried sandstone reservoirs: Origin and predictability. *American Association of Petroleum Geologists Bulletin*, **86,** 301-328.
Blott, S.J. and Pye, K. (2001) GRADISTAT: a grain size distribution and statistics package for the analysis of unconsolidated sediments. *Earth Surface Processes and Landforms*, **26,** 1237-1248.
Bokuniewicz, H. (1995) Chapter 3 Sedimentary Systems of Coastal-Plain Estuaries. In: *Developments in Sedimentology* (Ed G.M.E. Perillo), **53**, pp. 49-67. Elsevier.
Boles, J.R. and Franks, S.G. (1979) Clay diagenesis in Wilcox Sandstones of southwest Texas - implications of smectite diagenesis on sandstone cementation. *Journal of Sedimentary Petrology*, **49,** 55-70.
Borgnino, L. (2013) Experimental determination of the colloidal stability of Fe(III)-montmorillonite: Effects of organic matter, ionic strength and pH conditions. *Colloids and Surfaces A: Physicochemical and Engineering Aspects*, **423,** 178-187.
Bousher, A. 1999. Ravenglass Estuary: Basic characteristics and evaluation of restoration options, Whitehaven, United Kingdom, Westlakes Scientific Consulting.
Bowles, J., Howie, R., Vaughan, D. and Zussman, J. (2011) Rock-forming minerals. *Volume 5A Non-Silicates: Oxides, Hydroxides and Sulphides, 2nd edition. The Geological Society, London***,** 237-239.
Bowles, J.F.W. (2021) Oxides. In: *Encyclopedia of Geology (Second Edition)* (Eds D. Alderton and S.A. Elias), pp. 428-441. Academic Press, Oxford.
Boyle, E., Collier, R., Dengler, A.T., Edmond, J.M., Ng, A.C. and Stallard, R.F. (1974) Chemical mass balance in estuaries. *Geochimica et Cosmochimica Acta*, **38,** 1719-1728.
Boyle, E.A., Edmond, J.M. and Sholkovitz, E.R. (1977) Mechanism of iron removal in estuaries. *Geochimica et Cosmochimica Acta*, **41,** 1313-1324.

Breit, G.N. and Wanty, R.B. (1991) Vanadium accumulation in carbonaceous rocks: A review of geochemical controls during deposition and diagenesis. *Chemical Geology*, **91,** 83-97.
Brigatti, M.F., Galán, E. and Theng, B.K.G. (2013) Chapter 2 - Structure and Mineralogy of Clay Minerals. In: *Developments in Clay Science* (Eds F. Bergaya and G. Lagaly), **5**, pp. 21-81. Elsevier.
Brockamp, O. and Zuther, M. (2004) Changes in clay mineral content of tidal flat sediments resulting from dike construction along the Lower Saxony coast of the North Sea, Germany. *Sedimentology*, **51,** 591-600.
Brookins, D.G. (1988) Strontium. In: *Eh-pH Diagrams for Geochemistry*, pp. 166-167. Springer, Berlin/Heidelberg, Germany.
Buatois, L.A., Gingras, M.K., MacEachern, J., Mángano, M.G., Zonneveld, J.-P., Pemberton, S.G., Netto, R.G. and Martin, A. (2005) Colonization of brackish-water systems through time: evidence from the trace-fossil record. *Palaios*, **20,** 321-347.
Burley, S.D. (1986) The development and destruction of porosity within Upper Jurassic reservoir sandstones of the Piper and Tartan fields, Outer Moray Firth, North Sea. *Clay Minerals*, **21,** 649-694.
Burley, S.D. and Macquaker, J.H. (1992) Authigenic Clays Diagenetic Sequences and Conceptual Diagenetic Models in Contrasting Basin-Margin and Basin-Center North Sea Jurassic Sandstones and Mudstones.
Buurman, P., Jongmans, A.G. and PiPujol, M.D. (1998) Clay illuviation and mechanical clay infiltration — Is there a difference? *Quaternary International*, **51-52,** 66-69.
Caliani, J.C.F., Munoz, F.R. and Galan, E. (1997) Clay mineral and heavy metal distributions in the lower estuary of Huelva and adjacent Atlantic shelf, SW Spain. *Science of the Total Environment*, **198,** 181-200.
Calvert, S. and Pedersen, T. (2007) Chapter fourteen elemental proxies for palaeoclimatic and palaeoceanographic variability in marine sediments: interpretation and application. *Developments in Marine Geology*, **1,** 567-644.
Canfield, D.E. (1997) The geochemistry of river particulates from the continental USA: Major elements. *Geochimica et Cosmochimica Acta*, **61,** 3349-3365.
Cao, Z., Liu, G., Meng, W., Wang, P. and Yang, C. (2018) Origin of different chlorite occurrences and their effects on tight clastic reservoir porosity. *Journal of Petroleum Science and Engineering*, **160,** 384-392.
Carr, A.P. and Blackley, M.W.L. (1986) Implications of sedimentological and hydrological processes on the distribution of radionuclides: the example of a salt marsh near Ravenglass, Cumbria. *Estuarine, Coastal and Shelf Science*, **22,** 529-543.
Carr, R., Zhang, C., Moles, N. and Harder, M. (2008) Identification and mapping of heavy metal pollution in soils of a sports ground in Galway City, Ireland, using a portable XRF analyser and GIS. *Environmental Geochemistry and Health*, **30,** 45-52.
Castaing, P. (1970) *Contribution à l'étude sédimentologique des terrasses fluviatiles du Bordelais: relations avec le sable des Landes*, Éditeur inconnu.
Castaing, P. and Allen, G.P. (1981) Mechanisms controlling seaward escape of suspended sediment from the Gironde: a macrotidal estuary in France. *Marine Geology*, **40,** 101-118.
Cerda, C.M. (1987) Mobilization of kaolinite fines in porous media. *Colloids and surfaces*, **27,** 219-241.
Chamley, H. (1989) *Clay Sedimentology*. Springer-Verlag.
Chamley, H. (2013) *Clay sedimentology*. Springer Science & Business Media.
Chan, M.A. (1985) Correlations of diagenesis with sedimentary facies in Eocene sandstones, western Oregon. *Journal of Sedimentary Petrology*, **55,** 322-333.
Chang, H.K., Mackenzie, F.T. and Schoonmaker, J. (1986) Comparisons Between the Diagenesis of Dioctahedral and Trioctahedral Smectite, Brazilian Offshore Basins. *Clays and Clay Minerals*, **34,** 407-423.
Cheng, Q., Jing, L. and Panahi, A. (2006) Principal component analysis with optimum order sample correlation coefficient for image enhancement. *International Journal of Remote Sensing*, **27,** 3387-3401.

Chou, J., Clement, G., Bursavich, B., Elbers, D., Cao, B. and Zhou, W. (2010) Rapid detection of toxic metals in non-crushed oyster shells by portable X-ray fluorescence spectrometry. *Environmental pollution*, **158,** 2230-2234.
Chuhan, F.A., Bjorlykke, K. and Lowrey, C.J. (2001) Closed-system burial diagenesis in reservoir sandstones: Examples from the Garn Formation at Haltenbanken area, offshore mid-Norway. *Journal of Sedimentary Research*, **71,** 15-26.
Churchill, J.M., Poole, M.T., Skarpeid, S.S. and Wakefield, M.I. (2017) Stratigraphic architecture of the Knarr Field, Norwegian North Sea: sedimentology and biostratigraphy of an evolving tide- to wave-dominated shoreline system. *Geological Society, London, Special Publications*, **444,** 35.
Condie, K.C. and Wronkiewicz, D.J. (1990) The Cr/Th ratio in Precambrian pelites from the Kaapvaal Craton as an index of craton evolution. *Earth and Planetary Science Letters*, **97,** 256-267.
Cox, R. and Lowe, D.R. (1995) A conceptual review of regional-scale controls on the composition of clastic sediment and the co-evolution of continental blocks and their sedimentary cover. *Journal of Sedimentary Research*, **65,** 1-12.
Coynel, A., Gorse, L., Curti, C., Schafer, J., Grosbois, C., Morelli, G., Ducassou, E., Blanc, G., Maillet, G. and Mojtahid, M. (2016) Spatial distribution of trace elements in the surface sediments of a major European estuary (Loire Estuary, France): Source identification and evaluation of anthropogenic contribution. *Journal of Sea Research*, **118,** 77-91.
Coynel, A., Schäfer, J., Blanc, G. and Bossy, C. (2007) Scenario of particulate trace metal and metalloid transport during a major flood event inferred from transient geochemical signals. *Applied Geochemistry*, **22,** 821-836.
Craigie, N.W. (2015a) Applications of chemostratigraphy in Cretaceous sediments encountered in the North Central Rub' al-Khali Basin, Saudi Arabia. *Journal of African Earth Sciences*, **104,** 27-42.
Craigie, N.W. (2015b) Applications of chemostratigraphy in Middle Jurassic unconventional reservoirs in eastern Saudi Arabia. *GeoArabia*, **20,** 79-110.
Craigie, N.W. (2016) Chemostratigraphy of the Silurian Qusaiba Member, Eastern Saudi Arabia. *Journal of African Earth Sciences*, **113,** 12-34.
Craigie, N.W., Breuer, P. and Khidir, A. (2016a) Chemostratigraphy and biostratigraphy of Devonian, Carboniferous and Permian sediments encountered in eastern Saudi Arabia: An integrated approach to reservoir correlation. *Marine and Petroleum Geology*, **72,** 156-178.
Craigie, N.W., Rees, A., MacPherson, K. and Berman, S. (2016b) Chemostratigraphy of the Ordovician Sarah Formation, North West Saudi Arabia: An integrated approach to reservoir correlation. *Marine and Petroleum Geology*, **77,** 1056-1080.
Craigie, N.W. and Rees, A.J. (2016) Chemostratigraphy of glaciomarine sediments in the Sarah Formation, northwest Saudi Arabia. *Journal of African Earth Sciences*, **117,** 263-284.
Cullers, R.L. (1994) The controls on the major and trace element variation of shales, siltstones, and sandstones of Pennsylvanian-Permian age from uplifted continental blocks in Colorado to platform sediment in Kansas, USA. *Geochimica et Cosmochimica Acta*, **58,** 4955-4972.
Curtis, C.D., Hughes, C.R., Whiteman, J.A. and Whittle, C.K. (1985) Compositional variation within some sedimentary chlorites and some comments on their origin. *Mineralogical Magazine*, **49,** 375-386.
Dabrin, A., Schäfer, J., Blanc, G., Strady, E., Masson, M., Bossy, C., Castelle, S., Girardot, N. and Coynel, A. (2009) Improving estuarine net flux estimates for dissolved cadmium export at the annual timescale: application to the Gironde Estuary. *Estuarine, Coastal and Shelf Science*, **84,** 429-439.
Dahl, T.W., Ruhl, M., Hammarlund, E.U., Canfield, D.E., Rosing, M.T. and Bjerrum, C.J. (2013) Tracing euxinia by molybdenum concentrations in sediments using handheld X-ray fluorescence spectroscopy (HHXRF). *Chemical Geology*, **360–361,** 241-251.
Dale, N.G. (1974) Bacteria in intertidal sediments: Factors related to their distribution1. *Limnology and Oceanography*, **19,** 509-518.

Dalrymple, R.W. and Choi, K. (2007) Morphologic and facies trends through the fluvial–marine transition in tide-dominated depositional systems: a schematic framework for environmental and sequence-stratigraphic interpretation. *Earth-Science Reviews*, **81,** 135-174.
Dalrymple, R.W., Zaitlin, B.A. and Boyd, R. (1992) Estuarine facies models - conceptual models and stratigraphic implications. *Journal of Sedimentary Petrology*, **62,** 1130-1146.
Daneshvar, E. (2015) Dissolved iron behavior in the Ravenglass Estuary waters, an implication on the early diagenesis. *Universal Journal of Geoscience*, **3,** 1-12.
Daneshvar, E. and Worden, R.H. (2017) Feldspar alteration and Fe minerals: origin, distribution and implications for sandstone reservoir quality in estuarine sediments. *Geological Society, London, Special Publications*, **435,** SP435. 17.
Dare, S.A., Barnes, S.-J., Beaudoin, G., Méric, J., Boutroy, E. and Potvin-Doucet, C. (2014) Trace elements in magnetite as petrogenetic indicators. *Mineralium Deposita*, **49,** 785-796.
Das, B.K. and Haake, B.-G. (2003) Geochemistry of Rewalsar Lake sediment, Lesser Himalaya, India: implications for source-area weathering, provenance and tectonic setting. *Geosciences Journal*, **7,** 299-312.
De Kamp, P.C.V. (2008) Smectite-illite-muscovite transformations, quartz dissolution, and silica release in shales. *Clays and Clay Minerals*, **56,** 66-81.
De Lazzari, A., Rampazzo, G. and Pavoni, B. (2004) Geochemistry of sediments in the Northern and Central Adriatic Sea. *Estuarine, Coastal and Shelf Science*, **59,** 429-440.
De Ros, L.F., Anjos, S.M.C. and Morad, S. (1994) Authigenesis of amphibole and its relationship to the diagenetic evolution of lower cretaceous sandstones of the Potiguar rift basin, northeastern Brazil. *Sedimentary Geology*, **88,** 253-266.
De Segonzac, G.D. (1970) The transformation of clay minerals during diagenesis and low-grade metamorphism: a review. *Sedimentology*, **15,** 281-346.
Deer, W.A. (1978) Rock-forming minerals. Geological Society of London.
Delvigne, J. (1998) Atlas of micromorphology of mineral alteration and weathering.
Dempster, M., Dunlop, P., Scheib, A. and Cooper, M. (2013) Principal component analysis of the geochemistry of soil developed on till in Northern Ireland. *Journal of Maps*, **9,** 373-389.
Dixon, S.A., Summers, D.M. and Surdam, R.C. (1989) Diagenesis and Preservation of Porosity in Norphlet Formation (Upper Jurassic), Southern Alabama. *AAPG Bulletin*, **73,** 707-728.
Doerner, M., Berner, U., Erdmann, M. and Barth, T. (2020) Geochemical characterization of the depositional environment of Paleocene and Eocene sediments of the Tertiary Central Basin of Svalbard. *Chemical Geology***,** 119587.
Dogan, A.U., Dogan, M., Onal, M., Sarikaya, Y., Aburub, A. and Wurster, D.E. (2006) Baseline studies of the clay minerals society source clays: specific surface area by the Brunauer Emmett Teller (BET) method. *Clays and Clay Minerals*, **54,** 62-66.
Dou, Y.G., Yang, S.Y., Liu, Z.X., Clift, P.D., Yu, H., Berne, S. and Shi, X.F. (2010) Clay mineral evolution in the central Okinawa Trough since 28 ka: Implications for sediment provenance and paleoenvironmental change. *Palaeogeography Palaeoclimatology Palaeoecology*, **288,** 108-117.
Dowey, P.J., Hodgson, D.M. and Worden, R.H. (2012) Pre-requisites, processes, and prediction of chlorite grain coatings in petroleum reservoirs: A review of subsurface examples. *Marine and Petroleum Geology*, **32,** 63-75.
Dowey, P.J., Worden, R.H., Utley, J. and Hodgson, D.M. (2017) Sedimentary controls on modern sand grain coat formation. *Sedimentary Geology*, **353,** 46-63.
Drever, J.I. and Zobrist, J. (1992) Chemical weathering of silicate rocks as a function of elevation in the southern Swiss Alps. *Geochimica et Cosmochimica Acta*, **56,** 3209-3216.
Driskill, B., Pickering, J. and Rowe, H. (2018) Interpretation of high resolution XRF data from the Bone Spring and Upper Wolfcamp, Delaware Basin, USA. In: *Unconventional Resources Technology Conference, Houston, Texas, 23-25 July 2018*, pp. 2861-2888. Society of Exploration Geophysicists, American Association of Petroleum ….

Dupuis, C. and Beaudoin, G. (2011) Discriminant diagrams for iron oxide trace element fingerprinting of mineral deposit types. *Mineralium Deposita*, **46,** 319-335.
Duteil, T., Bourillot, R., Grégoire, B., Virolle, M., Brigaud, B., Nouet, J., Braissant, O., Portier, E., Féniès, H. and Patrier, P. (2020) Experimental formation of clay-coated sand grains using diatom biofilm exopolymers. *Geology*, **48,** 1012-1017.
Dutton, S., Hutton, M., Ambrose, W., Childers, A. and Loucks, R. (2018) Preservation of reservoir quality by chlorite coats in deep Tuscaloosa sandstones, Centrl Louisiana, USA. . *Gulf Coast Association of Geological Societies,*, **7,** 46-58.
Dutton, S.P. and Land, L.S. (1985) Meteoric Burial Diagenesis of Pennsylvanian Arkosic Sandstones, Southwestern Anadarko Basin, Texas1. *AAPG Bulletin*, **69,** 22-38.
Dutton, S.P. and Loucks, R.G. (2010) Diagenetic controls on evolution of porosity and permeability in lower Tertiary Wilcox sandstones from shallow to ultradeep (200-6700 m) burial, Gulf of Mexico Basin, USA. *Marine and Petroleum Geology*, **27,** 69-81.
Dyar, M.D., Gunter, M.E. and Tasa, D. (2008) *Mineralogy and optical mineralogy*. Mineralogical Society of America Chantilly, VA.
Dyer, K.R. (1997) *Estuaries: A physical introduction*. Wiley & Sons Ltd, Chichester, 195 pp.
Dypvik, H. and Harris, N.B. (2001) Geochemical facies analysis of fine-grained siliciclastics using Th/U, Zr/Rb and (Zr+ Rb)/Sr ratios. *Chemical Geology*, **181,** 131-146.
Eberl, D.D., Farmer, V.C. and Barrer, R.M. (1984) Clay Mineral Formation and Transformation in Rocks and Soils [and Discussion]. *Philosophical Transactions of the Royal Society of London A: Mathematical, Physical and Engineering Sciences*, **311,** 241-257.
Eckert, J.M. and Sholkovitz, E.R. (1976) The flocculation of iron, aluminium and humates from river water by electrolytes. *Geochimica et Cosmochimica Acta*, **40,** 847-848.
Edzwald, J.K. and O'Mella, C.R. (1975) Clay distributions in recent estuarine sediments. *Clays and Clay Minerals*, **23,** 39-44.
Ehrenberg, S.N. (1993) Preservation of anomalously high-porosity in deeply buried sandstones by grain coating chlorite - examples from the Norwegian continental shelf. *American Association of Petroleum Geologists Bulletin*, **77,** 1260-1286.
Ehrenberg, S.N. and Boassen, T. (1993) Factors controlling permeability variation in sandstones of the Garn Formation in Trestakk Field, Norwegian continental shelf. *Journal of Sedimentary Research*, **63,** 929-944.
Ehrenberg, S.N. and Jakobsen, K.G. (2001) Plagioclase dissolution related to biodegradation of oil in Brent Group sandstones (Middle Jurassic) of Gullfaks Field, northern North Sea. *Sedimentology*, **48,** 703-721.
Ehrenberg, S.N. and Nadeau, P.H. (1989) Formation of diagenetic illite in sandstones of the Garn Formation, Haltenbanken area, mid-Norwegian continental shelf. *Clay Minerals*, **24,** 233-253.
Ehrenberga, S.N., Dalland, A., Nadeau, P.H., Mearns, E.W. and Amundsen, E.F. (1998) Origin of chlorite enrichment and neodymium isotopic anomalies in Haltenbanken sandstonesfn1Deceased. *Marine and Petroleum Geology*, **15,** 403-425.
Elbaz-Poulichet, F., Martin, J., Huang, W. and Zhu, J. (1987a) Dissolved Cd behaviour in some selected French and Chinese estuaries. Consequences on Cd supply to the ocean. *Marine Chemistry*, **22,** 125-136.
Elbaz-Poulichet, F., Martin, J.M., Huang, W.W. and Zhu, J.X. (1987b) Dissolved Cd behaviour in some selected French and Chinese estuaries. Consequences on Cd supply to the ocean. *Marine Chemistry*, **22,** 125-136.
Emery, D., Myers, K.J. and Young, R. (1990) Ancient subaerial exposure and freshwater leaching in sandstones. *Geology*, **18,** 1178-1181.
Emmerson, R., O'Reilly-Wiese, S., Macleod, C. and Lester, J. (1997) A multivariate assessment of metal distribution in inter-tidal sediments of the Blackwater Estuary, UK. *Marine Pollution Bulletin*, **34,** 960-968.

Entwisle, D., Hobbs, P., Jones, L., Gunn, D. and Raines, M. (2005) The relationships between effective porosity, uniaxial compressive strength and sonic velocity of intact Borrowdale Volcanic Group core samples from Sellafield. *Geotechnical & Geological Engineering*, **23,** 793-809.
Fan, A., Yang, R., LI, J., Zhao, Z. and Van Loon, A.J. (2017) Siliceous Cementation of Chlorite-Coated Grains in the Permian Sandstone Gas Reservoirs, Ordos Basin. *Acta Geologica Sinica - English Edition*, **91,** 1147-1148.
Fan, D.J., Neuser, R.D., Sun, X.G., Yang, Z.S., Guo, Z.G. and Zhai, S.K. (2008) Authigenic iron oxide formation in the estuarine mixing zone of the Yangtze River. *Geo-Marine Letters*, **28,** 7-14.
Feininger, T. (2013) An Introduction to the Rock-Forming Minerals (third edition). *The Canadian Mineralogist*, **51,** 663-664.
Flood, R.P., Bloemsma, M.R., Weltje, G.J., Barr, I.D., O'Rourke, S.M., Turner, J.N. and Orford, J.D. (2016) Compositional data analysis of Holocene sediments from the West Bengal Sundarbans, India: Geochemical proxies for grain-size variability in a delta environment. *Applied Geochemistry*, **75,** 222-235.
Folk, R.L. (1966) A review of grain-size parameters. *Sedimentology*, **6,** 73-93.
Folk, R.L. (1968) Petrology of sedimentary rocks: Hemphill's. *Austin, Texas*, **170,** 85.
Forsgren, G., Jansson, M. and Nilsson, P. (1996) Aggregation and Sedimentation of Iron, Phosphorus and Organic Carbon in Experimental Mixtures of Freshwater and Estuarine Water. *Estuarine, Coastal and Shelf Science*, **43,** 259-268.
Förstner, U. and Wittmann, G.T. (2012) *Metal pollution in the aquatic environment*. Springer Science & Business Media.
Fralick, P.W. and Kronberg, B.I. (1997) Geochemical discrimination of clastic sedimentary rock sources. *Sedimentary Geology*, **113,** 111-124.
French, M.W. and Worden, R.H. (2013) Orientation of microcrystalline quartz in the Fontainebleau Formation, Paris Basin and why it preserves porosity. *Sedimentary Geology*, **284-285,** 149-158.
French, M.W., Worden, R.H., Mariani, E., Larese, R.E., Mueller, R.R. and Kliewer, C.E. (2012) Microcrystalline quartz generation and the preservation of porosity in sandstones: Evidence from the upper cretaceous of the Subhercynian Basin, Germany. *Journal of Sedimentary Research*, **82,** 422-434.
Garver, J.I., Royce, P.R. and Smick, T.A. (1996) Chromium and nickel in shale of the Taconic foreland; a case study for the provenance of fine-grained sediments with an ultramafic source. *Journal of Sedimentary Research*, **66,** 100-106.
Gazley, M.F., Vry, J.K., du Plessis, E. and Handler, M.R. (2011) Application of portable X-ray fluorescence analyses to metabasalt stratigraphy, Plutonic Gold Mine, Western Australia. *Journal of Geochemical Exploration*, **110,** 74-80.
Gibbs, R.J. (1977) Transport phases of transition metals in the Amazon and Yukon Rivers. *Geological Society of America Bulletin*, **88,** 829-843.
Gould, K., Pe-Piper, G. and Piper, D.J.W. (2010) Relationship of diagenetic chlorite rims to depositional facies in Lower Cretaceous reservoir sandstones of the Scotian Basin. *Sedimentology*, **57,** 587-610.
Griffin, G.M. and Ingram, R.L. (1955) Clay minerals of the Neuse River Estuary [North Carolina]. *Journal of Sedimentary Research*, **25,** 194-200.
Griffiths, J., Faulkner, D.R., Edwards, A.P. and Worden, R.H. (2016) Deformation band development as a function of intrinsic host-rock properties in Triassic Sherwood Sandstone. *Geological Society, London, Special Publications*, **435,** SP435. 11.
Griffiths, J., Worden, R.H., Utley, J.E., Brostrøm, C., Martinius, A.W., Lawan, A.Y. and Al-Hajri, A.I. (2021) Origin and distribution of grain-coating and pore-filling chlorite in deltaic sandstones for reservoir quality assessment. *Marine and Petroleum Geology*, **134,** 105326.
Griffiths, J., Worden, R.H., Wooldridge, L.J., Utley, J.E. and Duller, R.A. (2018) Detrital clay coats, clay minerals, and pyrite: a modern shallow-core analogue for ancient and deeply buried estuarine sandstones. *Journal of Sedimentary Research*, **88,** 1205-1237.

Griffiths, J., Worden, R.H., Wooldridge, L.J., Utley, J.E.P. and Duller, R.A. (2019a) Compositional variation in modern estuarine sands: predicting major controls on sandstone reservoir quality. *AAPG Bulletin*, **103,** 797-833.
Griffiths, J., Worden, R.H., Wooldridge, L.J., Utley, J.E.P., Duller, R.A. and Edge, R.L. (2019b) Estuarine clay mineral distribution: Modern analogue for ancient sandstone reservoir quality prediction. *Sedimentology*, **66,** 2011-2047.
Grigsby, J.D. (2001) Origin and growth mechanism of authigenic chlorite in sandstones of the lower Vicksburg Formation, south Texas. *Journal of Sedimentary Research*, **71,** 27-36.
Grigsby, J.D. and Langford, R.P. (1996) Effects of Diagenesis on Enhanced-Resolution Bulk Density Logs in Tertiary Gulf Coast Sandstones: An Example from the Lower Vicksburg Formation, McAllen Ranch Field, South Texas1. *AAPG Bulletin*, **80,** 1801-1819.
Grim, R.E. and Johns, W.D. (1954) Clay mineral investigations of sediments in the northern Gulf of Mexico. *Clays and Clay Minerals*, **2nd National Conference Pergamon, New York,** 81-103.
Grunsky, E.C. and Smee, B.W. (1999) The differentiation of soil types and mineralization from multi-element geochemistry using multivariate methods and digital topography. *Journal of Geochemical Exploration*, **67,** 287-299.
Gutiérrez-Ginés, M.J., Pastor, J. and Hernández, A.J. (2013) Assessment of field portable X-ray fluorescence spectrometry for the in situ determination of heavy metals in soils and plants. *Environmental Science: Processes & Impacts*, **15,** 1545-1552.
Haile, B.G., Hellevang, H., Aagaard, P. and Jahren, J. (2015) Experimental nucleation and growth of smectite and chlorite coatings on clean feldspar and quartz grain surfaces. *Marine and Petroleum Geology*, **68,** 664-674.
Haile, B.G., Klausen, T.G., Czarniecka, U., Xi, K., Jahren, J. and Hellevang, H. (2018) How are diagenesis and reservoir quality linked to depositional facies? A deltaic succession, Edgeoya, Svalbard. *Marine and Petroleum Geology*, **92,** 519-546.
Hansel, C.M., Benner, S.G., Nico, P. and Fendorf, S. (2004) Structural constraints of ferric (hydr)oxides on dissimilatory iron reduction and the fate of Fe(II)3 3Associate editor: J. B. Fein. *Geochimica et Cosmochimica Acta*, **68,** 3217-3229.
Hatch, J. and Leventhal, J. (1992) Relationship between inferred redox potential of the depositional environment and geochemistry of the Upper Pennsylvanian (Missourian) Stark Shale Member of the Dennis Limestone, Wabaunsee County, Kansas, USA. *Chemical Geology*, **99,** 65-82.
Hayashi, K.-I., Fujisawa, H., Holland, H.D. and Ohmoto, H. (1997) Geochemistry of ~1.9 Ga sedimentary rocks from northeastern Labrador, Canada. *Geochimica et Cosmochimica Acta*, **61,** 4115-4137.
Heald, M.T. and Baker, G.F. (1977) Diagenesis of the Mt. Simon and Rose Run sandstones in western West Virginia and southern Ohio. *Journal of Sedimentary Research*, **47,** 66-77.
Hedges, J.I., Keil, R.G. and Benner, R. (1997) What happens to terrestrial organic matter in the ocean? *Organic Geochemistry*, **27,** 195-212.
Hendry, J.P., Trewin, N.H. and Fallick, A.E. (1996) Low-Mg calcite marine cement in Cretaceous turbidites: Origin, spatial distribution and relationship to seawater chemistry. *Sedimentology*, **43,** 877-900.
Herron, M.M. (1986) Mineralogy from geochemical well logging. *Clays and Clay Minerals*, **34,** 204-213.
Herron, M.M. (1988) Geochemical classification of terrigenous sands and shales from core or log data. *Journal of Sedimentary Research*, **58,** 820-829.
Hillier, S., Fallick, A.E. and Matter, A. (1996) Origin of pore-lining chlorite in the aeolian Rotliegend of northern Germany. *Clay Minerals*, **31,** 153-171.
Hillier, S. and Velde, B. (1992) Chlorite interstratified with a 7-A mineral - and example from offshore Norway and possible implications for the interpretation of diagenetic chlorites. *Clay Minerals*, **27,** 475-486.
Hintze, J.L. and Nelson, R.D. (1998) Violin plots: a box plot-density trace synergism. *The American Statistician*, **52,** 181-184.

Holler, F.J., Skoog, D.A. and Crouch, S.R. (2009) *Princípios de análise instrumental*. Bookman.
Hornibrook, E.R.C. and Longstaffe, F.J. (1996) Berthierine from the Lower Cretaceous Clearwater Formation, Alberta, Canada. *Clays and Clay Minerals*, **44,** 1-21.
Horowitz, A.J. and Elrick, K.A. (1987) The relation of stream sediment surface area, grain size and composition to trace element chemistry. *Applied Geochemistry*, **2,** 437-451.
Huang, S.-j., Wu, W.-h., Liu, J., Shen, L.-c. and Huang, C.-g. (2003) Generation of secondary porosity by meteoric water during time of subaerial exposure: an example from Yanchang Formation sandstone of Triassic of Ordos Basin. *Earth Science/Diqiu Kexue*, **28,** 419-424.
Huang, W.-L. (1993) Stability and kinetics of kaolinite to boehmite conversion under hydrothermal conditions. *Chemical Geology*, **105,** 197-214.
Huggett, J.M., Burley, S.D., Longstaffe, F.J., Saha, S. and Oates, M.J. (2015) The nature and origin of authigenic chlorite and related cements in oligo–miocene reservoir sandstones, tapti gas fields, surat depression, offshore western india. *Journal of Petroleum Geology*, **38,** 383-409.
Hullman, J., Resnick, P. and Adar, E. (2015) Hypothetical outcome plots outperform error bars and violin plots for inferences about reliability of variable ordering. *PloS one*, **10,** e0142444.
Humphreys, B., Kemp, S.J., Lott, G.K., Bermanto, u., Dharmayanti, D.A. and Samsori, I. (1994) Origin of grain-coating chlorite by smectite transformation: an example from Miocene sandstones, North Sumatra back-arc basin, Indonesia. *Clay Minerals*, **29,** 681-692.
Hurst, A. and Nadeau, P.H. (1995) Clay microporosity in reservoir sandstones: an application of quantitative electron microscopy in petrophysical evaluation. *AAPG bulletin*, **79,** 563-573.
Hylander, L.D., Meili, M., Oliveira, L.J., de Castro e Silva, E., Guimarães, J.R.D., Araujo, D.M., Neves, R.P., Stachiw, R., Barros, A.J.P. and Silva, G.D. (2000) Relationship of mercury with aluminum, iron and manganese oxy-hydroxides in sediments from the Alto Pantanal, Brazil. *Science of The Total Environment*, **260,** 97-107.
Iljima, A. and Matsumoto, R. (1982) Berthierine and Chamosite in Coal Measures of Japan. *Clays and Clay Minerals*, **30,** 264-274.
Inoue, A. and Kitagawa, R. (1994) Morphological characteristics of illitic clay minerals from a hydrothermal system. *American Mineralogist*, **79,** 700-711.
Islam, M.A. (2009) Diagenesis and reservoir quality of Bhuban sandstones (Neogene), Titas Gas Field, Bengal Basin, Bangladesh. *Journal of Asian Earth Sciences*, **35,** 89-100.
Jahn, F., Cook, M. and Graham, M. (2008) *Hydrocarbon exploration and production*. Elsevier.
Jahren, J., Olsen, E., Bjørlykke, K., Arehart, G. and Hulston, J. (1998) Chlorite coatings in deeply buried sandstones: examples from the Norwegian shelf. *Water–rock interaction***,** 321-324.
Jahren, J.S. and Aagaard, P. (1992) Diagenetic illite-chlorite assemblages in arenites .1. Chemical evolution. *Clays and Clay Minerals*, **40,** 540-546.
Johnsson, M.J. and Meade, R.H. (1990) Chemical weathering of fluvial sediments during alluvial storage: The Macuapanim Island point bar, Solimoes River, Brazil. *Journal of Sedimentary Research*, **60**.
Jones, B.F. and Bowser, C.J. (1978) The Mineralogy and Related Chemistry of Lake Sediments. In: *Lakes: Chemistry, Geology, Physics* (Ed A. Lerman), pp. 179-235. Springer New York, New York, NY.
Kabata-Pendias, A. (2004) Soil–plant transfer of trace elements—an environmental issue. *Geoderma*, **122,** 143-149.
Kairo, S., Suttner, L.J. and Dutta, P.K. (1993) Variabilltiy of sandstone composition as a function of depositional environment in coarse-grained delta systems. In: *Processes controlling the composition of clastic sediments. GSA Special Paper 284* (Eds M.J. Johnson and A. Basu), pp. 263-284. Geological Society of America.
Kantorowicz, J.D. (1984) The nature, origin and distribution of authigenic clay minerals from Middle Jurassic Ravenscar and Brent Group sandstones. *Clay Minerals*, **19,** 359-375.
Katti, K.S. and Katti, D.R. (2006) Relationship of swelling and swelling pressure on silica− water interactions in montmorillonite. *Langmuir*, **22,** 532-537.

Kelly, M., Emptage, M., Mudge, S., Bradshaw, K. and Hamilton-Taylor, J. (1991) The relationship between sediment and plutonium budgets in a small macrotidal estuary - Esk Estuary, Cumbria, UK. *Journal of Environmental Radioactivity*, **13,** 55-74.

Kenna, T.C., Nitsche, F.O., Herron, M.M., Mailloux, B.J., Peteet, D., Sritrairat, S., Sands, E. and Baumgarten, J. (2011) Evaluation and calibration of a Field Portable X-Ray Fluorescence spectrometer for quantitative analysis of siliciclastic soils and sediments. *Journal of Analytical Atomic Spectrometry*, **26,** 395-405.

Ketzer, J.M., Morad, S. and Amorosi, A. (1999) Predictive Diagenetic Clay-Mineral Distribution in Siliciclastic Rocks within a Sequence Stratigraphic Framework. In: *Clay Mineral Cements in Sandstones*, pp. 43-61.

Ketzer, J.M., Morad, S. and Amorosi, A. (2003) Predictive Diagenetic Clay-Mineral Distribution in Siliciclastic Rocks within a Sequence Stratigraphic Framework. In: *Clay Mineral Cements in Sandstones* (Eds R.H. Worden and S. Morad), **34**, pp. 43-61. International Association of Sedimentologists.

Klovan, J. (1966) The use of factor analysis in determining depositional environments from grain-size distributions. *Journal of Sedimentary Research*, **36,** 115-125.

Knipping, J.L., Bilenker, L.D., Simon, A.C., Reich, M., Barra, F., Deditius, A.P., Wälle, M., Heinrich, C.A., Holtz, F. and Munizaga, R. (2015) Trace elements in magnetite from massive iron oxide-apatite deposits indicate a combined formation by igneous and magmatic-hydrothermal processes. *Geochimica et Cosmochimica Acta*, **171,** 15-38.

Krauskopf, K.B. and Bird, D.K. (1967) *Introduction to geochemistry*. McGraw-Hill New York.

Kumpan, T., Bábek, O., Kalvoda, J., Grygar, T.M. and Frýda, J. (2014) Sea-level and environmental changes around the Devonian–Carboniferous boundary in the Namur–Dinant Basin (S Belgium, NE France): A multi-proxy stratigraphic analysis of carbonate ramp archives and its use in regional and interregional correlations. *Sedimentary Geology*, **311,** 43-59.

Lalonde, K., Mucci, A., Ouellet, A. and Gélinas, Y. (2012) Preservation of organic matter in sediments promoted by iron. *Nature*, **483,** 198-200.

Lanceleur, L., Schäfer, J., Blanc, G., Coynel, A., Bossy, C., Baudrimont, M., Glé, C., Larrose, A., Renault, S. and Strady, E. (2013) Silver behaviour along the salinity gradient of the Gironde Estuary. *Environmental Science and Pollution Research*, **20,** 1352-1366.

Lander, R.H. and Bonnell, L.M. (2010) A model for fibrous illite nucleation and growth in sandstones. *American Association of Petroleum Geologists Bulletin*, **94,** 1161-1187.

Lander, R.H., Larese, R.E. and Bonnell, L.M. (2008) Toward more accurate quartz cement models: The importance of euhedral versus noneuhedral growth rates. *American Association of Petroleum Geologists Bulletin*, **92,** 1537-1563.

Le Vaillant, M., Barnes, S.J., Fiorentini, M.L., Santaguida, F. and Törmänen, T. (2016) Effects of hydrous alteration on the distribution of base metals and platinum group elements within the Kevitsa magmatic nickel sulphide deposit. *Ore Geology Reviews*, **72,** 128-148.

Lee, C.-T. (2018) Geochemical Classification of Elements. In: *Encyclopedia of Geochemistry: A Comprehensive Reference Source on the Chemistry of the Earth* (Ed W.M. White), pp. 545-549. Springer International Publishing, Cham.

Li, C., Yang, S., Lian, E., Wang, Q., Fan, D. and Huang, X. (2017) Chemical speciation of iron in sediments from the Changjiang Estuary and East China Sea: Iron cycle and paleoenvironmental implications. *Quaternary International*, **452,** 116-128.

Lindsley, D.H. (2018) *Oxide minerals: petrologic and magnetic significance*. Walter de Gruyter GmbH & Co KG.

Line, L.H., Jahren, J. and Hellevang, H. (2018) Mechanical compaction in chlorite-coated sandstone reservoirs – Examples from Middle – Late Triassic channels in the southwestern Barents Sea. *Marine and Petroleum Geology*, **96,** 348-370.

Liu, Z., Zhao, Y., Colin, C., Siringan, F.P. and Wu, Q. (2009) Chemical weathering in Luzon, Philippines from clay mineralogy and major-element geochemistry of river sediments. *Applied Geochemistry*, **24,** 2195-2205.

Lloyd, J.M., Zong, Y., Fish, P. and Innes, J.B. (2013) Holocene and Late-glacial relative sea-level change in north-west England: implications for glacial isostatic adjustment models. *Journal of Quaternary Science*, **28,** 59-70.
Longbottom, M.R. (1970) The distribution of Arenicola marina (L.) with particular reference to the effects of particle size and organic matter of the sediments. *Journal of Experimental Marine Biology and Ecology*, **5,** 138-157.
Longstaffe, F.J. (1993) Meteoric water and sandstone diagenesis in the Western Canada Sedimentary Basin: Chapter 5: Diagenesis and Basin hydrodynamics.
Luo, J., Morad, S., Zhang, X., Yan, S., Wu, F., Li, Y. and Xue, J. (2002) Reconstruction of the diagenesis of the fluvial-lacustrinedeltaic sandstones and its influence on the reservoir quality evolution. *Science in China Series D: Earth Sciences*, **45,** 616-634.
Ma, P.J., Lin, C.Y., Zhang, S.Q., Dong, C.M. and Xu, Y.F. (2017) Formation of chlorite rims and the impact of pore-lining chlorite on reservoir quality: a case study from Shiqianfeng sandstones in upper Permian of Dongpu Depression, Bohai Bay Basin, eastern China. *Australian Journal of Earth Sciences*, **64,** 825-839.
Macchi, L. (1987) A review of sandstone illite cements and aspects of their significance to hydrocarbon exploration and development. *Geological Journal*, **22,** 333-345.
MacKenzie, W.S. and Adams, A.E. (1994) *A Colour Atlas of Rocks and Minerals in Thin Section*. Halsted Press.
Madejova, J. (2003) FTIR techniques in clay mineral studies. *Vibrational Spectroscopy*, **31,** 1-10.
Marchand, A.M.E., Haszeldine, R.S., Macaulay, C.I., Swennen, R. and Fallick, A.E. (2000) Quartz cementation inhibited by crestal oil charge: Miller deep water sandstone, UK North Sea. *Clay Minerals*, **35,** 201-210.
Marsala, A., Loermans, T., Shen, S., Scheibe, C. and Zereik, R. (2012) Portable energy-dispersive X-ray fluorescence integrates mineralogy and chemostratigraphy into real-time formation evaluation. *Petrophysics*, **53,** 102-109.
Martin, J.-M. and Meybeck, M. (1979) Elemental mass-balance of material carried by major world rivers. *Marine Chemistry*, **7,** 173-206.
Martinius, A.W., Kaas, I., Naess, A., Helgesen, G. and Kjaerefjord, J.M. (2001) Sedimentology of the heterolithic and tide-dominated Tilje Formation. *Sedimentary Environments Offshore Norway-Palaeozoic to Recent*, 103.
Martinius, A.W., Ringrose, P.S., Brostrom, C., Elfenbein, C., Naess, A. and Ringas, J.E. (2005) Reservoir challenges of heterolithic tidal sandstone reservoirs in the Halten Terrace, mid-Norway. *Petroleum Geoscience*, **11,** 3-16.
Martins, R., Azevedo, M., Mamede, R., Sousa, B., Freitas, R., Rocha, F., Quintino, V. and Rodrigues, A. (2012) Sedimentary and geochemical characterization and provenance of the Portuguese continental shelf soft-bottom sediments. *Journal of Marine Systems*, **91,** 41-52.
Matlack, K.S., Houseknecht, D.W. and Applin, K.R. (1989) Emplacement of clay into sand by infiltration. *Journal of Sedimentary Petrology*, **59,** 77-87.
Mayer, L.M. and Fink, K.L. (1980) Granulometric dependence of chromium accumulation in estuarine sediments in Maine. *Estuarine and Coastal Marine Science*, **11,** 491-503.
McGhee, C.A., Muhammed, D.D., Simon, N., Acikalin, S., Utley, J.E.P., Griffiths, J., Wooldridge, L.M., Verhagen, I.T.E., van der Land, C. and Worden, R.H. (2021) Stratigraphy and sedimentary evolution of a modern macro-tidal incised valley– an analogue for reservoir facies and architecture. . *Sedimentology*.
McIlroy, D., Worden, R.H. and Needham, S.J. (2003) Faeces, clay minerals and reservoir potential. *Journal of the Geological Society*, **160,** 489-493.
McKinley, J., Worden, R. and Ruffell, A. (1999) Smectite in sandstones: a review of the controls on occurrence and behaviour during diagenesis. *Clay mineral cements in sandstones*, 109-128.

McKinley, J.M., Worden, R.H. and Ruffell, A.H. (2003) Smectite in sandstones: A review of the controls on occurrence and behaviour during diagenesis. *In: Clay mineral cements in sandstones (eds. Worden, R.H. and Morad, S.) International Association of Sedimentologists Special Publications*, **34,** 109-128.
McLaren, T.I., Guppy, C.N., Tighe, M.K., Forster, N., Grave, P., Lisle, L.M. and Bennett, J.W. (2012) Rapid, nondestructive total elemental analysis of vertisol soils using portable X-ray fluorescence. *Soil Science Society of America Journal*, **76,** 1436-1445.
McLennan, S.M. (2001) Relationships between the trace element composition of sedimentary rocks and upper continental crust. *Geochemistry, Geophysics, Geosystems*, **2**.
McLennan, S.M., Hemming, S., McDaniel, D.K., Hanson, G.N., Johnsson, M.J. and Basu, A. (1993) Geochemical approaches to sedimentation, provenance, and tectonics. In: *Processes Controlling the Composition of Clastic Sediments*, **284**, pp. 0. Geological Society of America.
Mehra, O.P. and Jackson, M.L. (2013) Iron oxide removal from soils and clays by a dithionite-citrate system buffered with sodium bicarbonate I. In: *Clays and Clay Minerals* (Ed E. Ingerson), pp. 317-327. Pergamon.
Meinhold, G., Kostopoulos, D. and Reischmann, T. (2007) Geochemical constraints on the provenance and depositional setting of sedimentary rocks from the islands of Chios, Inousses and Psara, Aegean Sea, Greece: implications for the evolution of Palaeotethys. *Journal of the Geological Society*, **164,** 1145-1163.
Merritt, J.W. and Auton, C.A. (2000) An outline of the lithostratigraphy and depositional history of Quaternary deposits in the Sellafield district, west Cumbria. *Proceedings of the Yorkshire Geological Society*, **53,** 129-154.
Michael, D., Paul, D., Andreas, S. and Mark, C. (2013) Principal component analysis of the geochemistry of soil developed on till in Northern Ireland. *Journal of Maps***,** 373.
Michalopoulos, P. and Aller, R.C. (1995) Rapid clay mineral transformation in Amazon Delta sediments - reverse weathering and oceanic element cycles. *Science*, **270,** 614-617.
Michalopoulos, P. and Aller, R.C. (2004) Early diagenesis of biogenic silica in the Amazon delta: Alteration, authigenic clay formation, and storage. *Geochimica et Cosmochimica Acta*, **68,** 1061-1085.
Michalopoulos, P., Aller, R.C. and Reeder, R.J. (2000) Conversion of diatoms to clays during early diagenesis in tropical, continental shelf muds. *Geology*, **28,** 1095-1098.
Millward, D. (2002) Early Palaeozoic magmatism in the English Lake District. *Proceedings of the Yorkshire Geological Society*, **54,** 65.
Millward, D. 2004. A stratigraphical framework for the upper Ordovician and Lower Devonian volcanic and intrusive rocks in the English Lake District and adjacent areas. 0852724004, British Geological Survey Research Report.
Milodowski, A., Gillespie, M., Naden, J., Fortey, N., Shepherd, T., Pearce, J. and Metcalfe, R. (1998) The petrology and paragenesis of fracture mineralization in the Sellafield area, west Cumbria. *Proceedings of the Yorkshire Geological Society*, **52,** 215-241.
Mongelli, G., Critelli, S., Perri, F., Sonnino, M. and Perrone, V. (2006) Sedimentary recycling, provenance and paleoweathering from chemistry and mineralogy of Mesozoic continental redbed mudrocks, Peloritani Mountains, Southern Italy. *Geochemical Journal*, **40,** 197-209.
Moore, D.M. and Reynolds, R.C. (1997) *X-ray Diffraction and the Identification and Analysis of Clay Minerals*. Oxford University Press.
Morad, S., Al-Ramadan, K., Ketzer, J.M. and De Ros, L.F. (2010) The impact of diagenesis on the heterogeneity of sandstone reservoirs: A review of the role of depositional facies and sequence stratigraphy. *American Association of Petroleum Geologists Bulletin*, **94,** 1267-1309.
Morad, S. and Aldahan, A.A. (1986) Diagenetic alteration of detrital biotite in Proterozoic sedimentary rocks from Sweden. *Sedimentary Geology*, **47,** 95-107.
Morris, J.E., Hampson, G.J. and Johnson, H.D. (2006) A sequence stratigraphic model for an intensely bioturbated shallow-marine sandstone: the Bridport Sand Formation, Wessex Basin, UK. *Sedimentology*, **53,** 1229-1263.

Morris, K.A. and Shepperd, C.M. (1982) The role of clay minerals in influencing porosity and permeability characteristics in the Bridport Sands of Wytch Farm, Dorset. *Clay Minerals*, **17,** 41-54.
Morris, P.A. (2009) *Field-portable X-ray fluorescence analysis and its application in GSWA*. Geological Survey of Western Australia.
Morton, A.C., Meinhold, G., Howard, J.P., Phillips, R.J., Strogen, D., Abutarruma, Y., Elgadry, M., Thusu, B. and Whitham, A.G. (2011) A heavy mineral study of sandstones from the eastern Murzuq Basin, Libya: Constraints on provenance and stratigraphic correlation. *Journal of African Earth Sciences*, **61,** 308-330.
Moseley, F. (1978) *The geology of the Lake District*. Yorkshire Geological Society.
Mosley, L.M., Hunter, K.A. and Ducker, W.A. (2003) Forces between Colloid Particles in Natural Waters. *Environmental Science & Technology*, **37,** 3303-3308.
Mountney, N.P. and Thompson, D.B. (2002) Stratigraphic evolution and preservation of aeolian dune and damp/wet interdune strata: an example from the Triassic Helsby Sandstone Formation, Cheshire Basin, UK. *Sedimentology*, **49,** 805-833.
Mu, N., Schulz, H.-M., Fu, Y., Schovsbo, N.H., Wirth, R., Rhede, D. and van Berk, W. (2015) Berthierine formation in reservoir rocks from the Siri oilfield (Danish North Sea) as result of fluid–rock interactions: Part I. Characterization. *Marine and Petroleum Geology*, **65,** 302-316.
Muhammed, D.D., Worden, R.H., Simon, N., Utley, J.E.P., Verhagen, I.T.E., Duller, R.A., Griffiths, J. and Wooldridge, L.M. (2022) Prediction of palaeo-sub-depositional environments in estua-rine surface and Holocene sands using bulk elemental compositions. *Geosciences*, **12,** 23.
Musial, G., Reynaud, J.-Y., Gingras, M.K., Féniès, H., Labourdette, R. and Parize, O. (2012) Subsurface and outcrop characterization of large tidally influenced point bars of the Cretaceous McMurray Formation (Alberta, Canada). *Sedimentary Geology*, **279,** 156-172.
Nadeau, P., Wilson, M., McHardy, W. and Tait, J. (1985) The conversion of smectite to illite during diagenesis: evidence from some illitic clays from bentonites and sandstones. *Mineralogical Magazine*, **49,** 393-400.
Nadoll, P., Angerer, T., Mauk, J.L., French, D. and Walshe, J. (2014) The chemistry of hydrothermal magnetite: A review. *Ore Geology Reviews*, **61,** 1-32.
Nagata, N., Bueno, M.I. and Peralta-Zamora, P.G. (2001) Métodos matemáticos para correção de interferências espectrais e efeitos interelementos na análise quantitativa por fluorescência de raios-X. *Química Nova*.
Needham, S.J., Worden, R.H. and Cuadros, J. (2006) Sediment ingestion by worms and the production of bio-clays: a study of macrobiologically enhanced weathering and early diagenetic processes. *Sedimentology*, **53,** 567-579.
Needham, S.J., Worden, R.H. and McIlroy, D. (2004) Animal-sediment interactions: the effect of ingestion and excretion by worms on mineralogy. *Biogeosciences*, **1,** 113-121.
Needham, S.J., Worden, R.H. and McIlroy, D. (2005) Experimental production of clay rims by macrobiotic sediment ingestion and excretion processes. *Journal of Sedimentary Research*, **75,** 1028-1037.
Nelson, B.W. (1960) Clay mineralogy of the bottom sediments, Rappahannock River, Virginia. In: *Clays and Clay Minerals: Proceedings of the Seventh National Conference on Clays and Clay Minerals Washington, DC, USA, 20–23 Octorber 1958; Elsevier: Amsterdam*, pp. 135-148. Elsevier, Washington, DC, USA.
Nesbitt, H.W. and Young, G.M. (1982) Early Proterozoic climates and plate motions inferred from major element chemistry of lutites. *Nature*, **299,** 715.
Nesbitt, H.W. and Young, G.M. (1989) Formation and Diagenesis of Weathering Profiles. *The Journal of Geology*, **97,** 129-147.
Oelkers, E.H., Bjorkum, P.A. and Murphy, W.M. (1996) A petrographic and computational investigation of quartz cementation and porosity reduction in North Sea sandstones. *American Journal of Science*, **296,** 420-452.

Osborne, M.J. and Swarbrick, R.E. (1999) Diagenesis in North Sea HPHT clastic reservoirs-consequences for porosity and overpressure prediction. *Marine and Petroleum Geology*, **16,** 337-353.
Padmalal, D., Maya, K. and Seralathan, P. (1997) Geochemistry of Cu, Co, Ni, Zn, Cd and Cr in the surficial sediments of a tropical estuary, southwest coast of India: a granulometric approach. *Environmental Geology*, **31,** 85-93.
Padmalal, D. and Seralathan, P. (1995) Geochemistry of Fe and Mn in surficial sediments of a tropical river and estuary, India—a granulometric approach. *Environmental Geology*, **25,** 270-276.
Pauling, L. (1960) *The Nature of the Chemical Bond (3rd Edition)*. Cornell University Press., Ithaca, NY.
Pay, M.D., Astin, T.R. and Parker, A. (2000) Clay mineral distribution in the Devonian-Carboniferous sandstones of the Clair Field, west of Shetland, and its significance for reservoir quality. *Clay Minerals*, **35,** 151-162.
Pe-Piper, G. and Weir-Murphy, S. (2008) Early diagenesis of inner-shelf phosphorite and iron-silicate minerals, Lower Cretaceous of the Orpheus graben, southeastern Canada: Implications for the origin of chlorite rims. *AAPG Bulletin*, **92,** 1153-1168.
Pemberton, S.G. (2001) Ichnology & sedimentology of shallow to marginal marine systems. *Geol. Assoc. Can., Short Course*, **15,** 343.
Peng, J., Liu, J., Wang, Y. and Liu, J. (2009) Origin and controlling factors of chlorite coatings—an example from the reservoir of T3x Group of the Baojie area, Sichuan Basin, China. *Petroleum Science*, **6,** 376-382.
Pevear, D.R. (1999) Illite and hydrocarbon exploration. *Proceedings of the National Academy of Sciences of the United States of America*, **96,** 3440-3446.
Pirajno, F. (2005) Hydrothermal processes associated with meteorite impact structures: evidence from three Australian examples and implications for economic resources. *Australian Journal of Earth Sciences*, **52,** 587-605.
Pirrie, D., Ditchfield, P.W. and Marshall, J.D. (1994) Burial diagenesis and pore-fluid evolution in a Mesozoic back-arc basin; the Marambio Group, Vega Island, Antarctica. *Journal of Sedimentary Research*, **64,** 541-552.
Pittman, E.D., Larese, R.E. and Heald, M.T. (1992) Clay coats: occurrence and relevance to preservation of porosity in sandstones. *In: Origin, diagenesis and petrophysics of clay minerals in sandstones (eds. Houseknecht, D.W. and Pittman, E.D.) SEPM Special Publication*, **47,** 241-255.
Pittman, E.D. and Lumsden, D.N. (1968) Relationship between chlorite coatings on quartz grains and porosity, Spiro Sand, Oklahoma. *Journal of Sedimentary Research*, **38,** 668-670.
Plourde, A., Knight, R., Kjarsgaard, B., Sharpe, D. and Lesemann, J. (2013) Portable XRF spectrometry of surficial sediments, NTS 75-I, 75-J, 75-O, 75-P (Mary Frances Lake–Whitefish Lake–Thelon River area), Northwest Territories. *Geological Survey of Canada, Open File*, **7408**.
Pokrovsky, O.S. and Schott, J. (2002) Iron colloids/organic matter associated transport of major and trace elements in small boreal rivers and their estuaries (NW Russia). *Chemical Geology*, **190,** 141-179.
Posamentier, H.W. and Walker, R.G. (Eds)(2006) *Facies models revisited*. SEPM Special Publication, Oklahoma.
Potts, P.J. (2008) Introduction, analytical instrumentation and application overview. In Portable X-ray fluorescence spectrometry: Capabilities for in situ analysis. *The Royal Society of Chemistry London, UK*, 1-12.
Poulton, S.W. and Canfield, D.E. (2005) Development of a sequential extraction procedure for iron: implications for iron partitioning in continentally derived particulates. *Chemical Geology*, **214,** 209-221.
Poulton, S.W. and Raiswell, R. (2005) Chemical and physical characteristics of iron oxides in riverine and glacial meltwater sediments. *Chemical Geology*, **218,** 203-221.
Powers, M.C. (1957) Adjustment of land derived clays to the marine environment. *Journal of Sedimentary Research*, **27**.
Premović, P.I., Pavlović, M.S. and Pavlović, N.a.Z. (1986) Vanadium in ancient sedimentary rocks of marine origin. *Geochimica et Cosmochimica Acta*, **50,** 1923-1931.

Primmer, T.J., Cade, C.A., Evans, J., Gluyas, J., Hopkins, M.S., Oxtoby, N., Smalley, P.C., Warren, E.A. and Worden, R.H. (1997) Global patterns in sandstone diagenesis: their application to reservoir quality prediction for petroleum exploration In: *Reservoir quality prediction in sandstones and carbonates. AAPG Memoir* (Eds J.A. Kupecz, J. Gluyas and S. Bloch), **69**, pp. 61-78. American Association of Petroleum Geologists, Tulsa.

Quirke, J., Henderson, C., Pattrick, R., Rosso, K., Dent, A., Sharples, J. and Pearce, C. (2015) Characterizing mineralogy and redox reactivity in potential host rocks for a UK geological disposal facility. *Mineralogical Magazine*, **79,** 1353-1367.

R Core Team (2016) R: A language and environment for statistical computing. R Foundation for Statistical Computing, Vienna, Austria.

Rao, V.P. and Rao, B.R. (1995) PROVENANCE AND DISTRIBUTION OF CLAY-MINERALS IN THE SEDIMENTS OF THE WESTERN CONTINENTAL-SHELF AND SLOPE OF INDIA. *Continental Shelf Research*, **15,** 1757-1771.

Rateev, M.A., Sadchikova, T.A. and Shabrova, V.P. (2008) Clay minerals in recent sediments of the World Ocean and their relation to types of lithogenesis. *Lithology and Mineral Resources*, **43,** 125-135.

Reimann, C., Filzmoser, P., Garrett, R. and Dutter, R. (2011) *Statistical data analysis explained: applied environmental statistics with R*. John Wiley & Sons, Hoboken, NJ, USA.

Remy, R.R. (1994) Porosity reduction and major controls on diagenesis of Cretaceous-Paleocene volcaniclastic and arkosic sandstone, Middle Park Basin, Colorado. *Journal of Sedimentary Research*, **64,** 797-806.

Rider, M. and Kennedy, M.J. (2011) *The Geological Interpretation of Well Logs*. Rider-French Consulting, Cambridge.

Rollinson, H.R. (2014) *Using geochemical data: evaluation, presentation, interpretation*. Routledge: Oxfordshire, UK.

Ross, P.-S., Bourke, A. and Fresia, B. (2014) Improving lithological discrimination in exploration drill-cores using portable X-ray fluorescence measurements:(1) testing three Olympus Innov-X analysers on unprepared cores. *Geochemistry: Exploration, Environment, Analysis*, **14,** 171-185.

Rothwell, R.G. and Croudace, I.W. (2015) Twenty years of XRF core scanning marine sediments: what do geochemical proxies tell us? In: *Developments in paleoenvironmental research, volume 17. Micro-XRF studies of sediment cores: applications of a non-destructive tool foe the environmental sciences* (Eds I.W. Croudace and R.R. G.), pp. 25-102. Springer, Dordrecht.

Rowe, H., Hughes, N. and Robinson, K. (2012) The quantification and application of handheld energy-dispersive x-ray fluorescence (ED-XRF) in mudrock chemostratigraphy and geochemistry. *Chemical Geology*, **324,** 122-131.

Roy, M., Martin, J.B., Smith, C.G. and Cable, J.E. (2011) Reactive-transport modeling of iron diagenesis and associated organic carbon remineralization in a Florida (USA) subterranean estuary. *Earth and Planetary Science Letters*, **304,** 191-201.

Rübsam, W. (2019) *The Early Toarcian environmental crisis: mechanisms and consequences of an Icehouse-Greenhouse Transition*, Universitätsbibliothek Kiel: Kiel, Germany, Germany.

Rui, Z., Lu, J., Zhang, Z., Guo, R., Ling, K., Zhang, R. and Patil, S. (2017) A quantitative oil and gas reservoir evaluation system for development. *Journal of Natural Gas Science and Engineering*, **42,** 31-39.

Rundle, C. (1979) Ordovician intrusions in the English Lake District. *Journal of the Geological Society*, **136,** 29-38.

Ryan, P. and Reynolds, R. (1997) The chemical composition of serpentine/chlorite in the Tuscaloosa Formation, United States Gulf Coast: EDX vs. XRD determinations, implications for mineralogic reactions and the origin of anatase. *Clays and Clay Minerals*, **45,** 339-352.

Ryan, P.C. and Hillier, S. (2002) Berthierine/chamosite, corrensite, and discrete chlorite from evolved verdine and evaporite-associated facies in the Jurassic Sundance Formation, Wyoming. *American Mineralogist*, **87,** 1607-1615.

Ryan, P.C. and Reynolds, R.C. (1996) The origin and diagenesis of grain-coating serpentine-chlorite in Tuscaloosa Formation sandstones, U.S. Gulf Coast. *American Mineralogist*, **81,** 213-225.
Saïag, J., Brigaud, B., Portier, E., Desaubliaux, G., Bucherie, A., Miska, S. and Pagel, M. (2016) Sedimentological control on the diagenesis and reservoir quality of tidal sandstones of the Upper Cape Hay Formation (Permian, Bonaparte Basin, Australia). *Marine and Petroleum Geology*, **77,** 597-624.
Salem, A.M., Morad, S., Mato, L.F. and Al-Aasm, I.S. (2000) Diagenesis and reservoir-quality evolution of fluvial sandstones during progressive burial and uplift: Evidence from the Upper Jurassic Boipeba Member, Reconcavo basin, northeastern Brazil. *American Association of Petroleum Geologists Bulletin*, **84,** 1015-1040.
Saner, S., Hassan, H.M., Al-Ramadan, K.A. and Abdulghani, W.M. (2006) Mineralogical, pore and petrophysical characteristics of the devonian jauf sandstone reservoir, hawiyah field, eastern saudi arabia. *Journal of Petroleum Geology*, **29,** 257-272.
Santschi, P.H., Bower, P., Nyffeler, U.P., Azevedo, A. and Broecker, W.S. (1983) Estimates of the resistance to chemical transport posed by the deep-sea boundary layer1,2. *Limnology and Oceanography*, **28,** 899-912.
Sathar, S., Worden, R.H., Faulkner, D.R. and Smalley, P.C. (2012) The Effect of Oil Saturation On the Mechanism of Compaction In Granular Materials: Higher Oil Saturations Lead To More Grain Fracturing and Less Pressure Solution. *Journal of Sedimentary Research*, **82,** 571-584.
Scheffe, H. (1999) *The analysis of variance*. John Wiley & Sons, INC., Hoboken, NJ, USA, 477 pp.
Scheinost, A.C. (2005) METAL OXIDES. In: *Encyclopedia of Soils in the Environment* (Ed D. Hillel), pp. 428-438. Elsevier, Oxford.
Schmidt, V. and McDonald, D.A. (1979) The role of secondary porosity in the course of sandstone diagenesis. In: *Aspects of Diagenesis* (Eds P.A. Scholle and P.R. Schluger), **26**. SEPM Special Publication.
Schwertmann, U. (1966) Inhibitory Effect of Soil Organic Matter on the Crystallization of Amorphous Ferric Hydroxide. *Nature*, **212,** 645-646.
Scotchman, I.C., Johnes, L.H. and Miller, R.S. (1989) Clay diagenesis and oil migration in Brent Group sandstones of NW Hutton Field, UK North Sea. *Clay Minerals*, **24,** 339-374.
Shaheen, S.M., Alessi, D.S., Tack, P.M.G., Ok, Y.S., Kim, K.-H., Gustafsson, J.P., Sparks, D.L. and Rinklebe, J. (2019) Redox chemistry of vanadium in soils and sediments: Interactions with colloidal materials, mobilization, speciation, and relevant environmental implications-A review. *Advances in Colloid and Interface Science*, **265,** 1-13.
Shannon, R.D. (1976) Revised effective ionic radii and systematic studies of interatomic distances in halides and chalcogenides. *Acta Crystallographica*, **32,** 751-767.
Sheldon, H.A., Wheeler, J., Worden, R.H. and Cheadle, M.J. (2003) An Analysis of the Roles of Stress, Temperature, and pH in Chemical Compaction of Sandstones. *Journal of Sedimentary Research*, **73,** 64-71.
Shiller, A.M. and Boyle, E.A. (1987) Dissolved vanadium in rivers and estuaries. *Earth and Planetary Science Letters*, **86,** 214-224.
Shiller, A.M. and Mao, L. (1999) Dissolved vanadium on the Louisiana Shelf: effect of oxygen depletion. *Continental Shelf Research*, **19,** 1007-1020.
Sholkovitz, E.R. (1978) The flocculation of dissolved Fe, Mn, Al, Cu, Ni, Co and Cd during estuarine mixing. *Earth and Planetary Science Letters*, **41,** 77-86.
Simon, N., Worden, R.H., Muhammed, D.D., Utley, J.E.P., Verhagen, I.T.E., Griffiths, J. and Wooldridge, L.J. (2021) Sediment textural characteristics of the Ravenglass Estuary; Development of a method to predict palaeo sub-depositional environments from estuary core samples. *Sedimentary Geology*, **418,** 105906.
Simpson, B. (1934) The petrology of the Eskdale (Cumberland) granite. *Proceedings of the Geologists' Association*, **45,** 17-34.
Sionneau, T., Bout-Roumazeilles, V., Biscaye, P.E., Van Vliet-Lanoe, B. and Bory, A. (2008) Clay mineral distributions in and around the Mississippi River watershed and Northern Gulf of Mexico: sources and transport patterns. *Quaternary Science Reviews*, **27,** 1740-1751.

Skarpeid, S.S., Churchill, J.M., Hilton, J.P.J., Izatt, C.N. and Poole, M.T. (2017) The Knarr Field: a new development at the northern edge of the North Sea. In: *Geological Society, London, Petroleum Geology Conference series*, **8**, pp. PGC8. 23. Geological Society of London.

Smith, D.B., Woodruff, L.G., O'Leary, R.M., Cannon, W.F., Garrett, R.G., Kilburn, J.E. and Goldhaber, M.B. (2009) Pilot studies for the North American Soil Geochemical Landscapes Project–site selection, sampling protocols, analytical methods, and quality control protocols. *Applied Geochemistry*, **24,** 1357-1368.

Soper, N. (1987) The Ordovician batholith of the English Lake District: Correspondence and Notes. *Geological Magazine*, **124,** 481-482.

Spoetl, C., Houseknecht, D.W. and Longstaffe, F.J. (1994) Authigenic chlorites in sandstones as indicators of high-temperature diagenesis, Arkoma foreland basin, USA. *Journal of Sedimentary Research*, **64,** 553-566.

Srodon, J. (1999) Nature of mixed-layer clays and mechanisms of their formation and alteration. *Annual Review of Earth and Planetary Sciences*, **27,** 19-53.

Środoń, J., Eberl, D. and Drits, V. (2000) Evolution of fundamental-particle size during illitization of smectite and implications for reaction mechanism. *Clays and Clay Minerals*, **48,** 446-458.

Stoessell, R.K. and Pittman, E.D. (1990) Secondary Porosity Revisited: The Chemistry of Feldspar Dissolution by Carboxylic Acids and Anions (1). *AAPG bulletin*, **74,** 1795-1805.

Storvoll, V., Bjorlykke, K., Karlsen, D. and Saigal, G. (2002) Porosity preservation in reservoir sandstones due to grain-coating illite: a study of the Jurassic Garn Formation from the Kristin and Lavrans fields, offshore Mid-Norway. *Marine and Petroleum Geology*, **19,** 767-781.

Stricker, S. and Jones, S.J. (2016) Enhanced porosity preservation by pore fluid overpressure and chlorite grain coatings in the Triassic Skagerrak, Central Graben, North Sea, UK. *Geological Society, London, Special Publications*, **435,** SP435. 4.

Stricker, S. and Jones, S.J. (2018) Enhanced porosity preservation by pore fluid overpressure and chlorite grain coatings in the Triassic Skagerrak, Central Graben, North Sea, UK. *Geological Society, London, Special Publications*, **435,** 321-341.

Stricker, S., Jones, S.J., Sathar, S., Bowen, L. and Oxtoby, N. (2016) Exceptional reservoir quality in HPHT reservoir settings: Examples from the Skagerrak Formation of the Heron Cluster, North Sea, UK. *Marine and Petroleum Geology*, **77,** 198-215.

Strong, G.E., Milodowski, A.E., Pearce, J.M., Kemp, S.J., Prior, S.V. and Morton, A.C. (1994) The petrology and diagenesis of Permo-Triassic rocks of the Sellafield area, Cumbria. In: *Proceedings of the Yorkshire Geological and Polytechnic Society*, **50**, pp. 77-89. Geological Society of London.

Sun, Z.-X., Sun, Z.-L., Yao, J., Wu, M.-L., Liu, J.-R., Dou, Z. and Pei, C.-r. (2014) Porosity preservation due to authigenic chlorite coatings in deeply buried upper triassic xujiahe formation sandstones, sichuan basin, western china. *Journal of Petroleum Geology*, **37,** 251-267.

Surdam, R., Dunn, T., Heasler, H., MacGowan, D. and Hutcheon, I. (1989) Porosity evolution in sandstone/shale systems. *Short Course on Burial Diagenesis***,** 61-133.

Surdam, R.C., Boese, S.W. and Crossey, L.J. (1984) The chemistry of secondary porosity. In: *Clastic diagenesis. American Association of Petroleum Geologists Memoir* (Eds D.A. McDonald and R.C. Surdam), **37**, pp. 127-149.

Swanson, V.E. (1961) *Geology and geochemistry of uranium in marine black shales: a review*. US Government Printing Office Washington, DC.

Taylor, K.G. and Konhauser, K.O. (2011) Iron in Earth Surface Systems: A Major Player in Chemical and Biological Processes. *Elements*, **7,** 83-88.

Taylor, S.R. and McLennan, S.M. (1985) *The Continental Crust: Its Composition and Evolution* Blackwell London.

Tebo, B.M., Bargar, J.R., Clement, B.G., Dick, G.J., Murray, K.J., Parker, D., Verity, R. and Webb, S.M. (2004) Biogenic manganese oxides: properties and mechanisms of formation. *Annu. Rev. Earth Planet. Sci.*, **32,** 287-328.

Therneau, T. and Atkinson, E. (2019) An introduction to recursive partitioning using rpart routines: The Comprehensive R Archive Network. CRAN.
Thiry, M. (2000) Palaeoclimatic interpretation of clay minerals in marine deposits: an outlook from the continental origin. *Earth-Science Reviews*, **49,** 201-221.
Thomson-Becker, E.A. and Luoma, S.N. (1985) Temporal fluctuations in grain size, organic materials and iron concentrations in intertidal surface sediment of San Francisco Bay. *Hydrobiologia*, **129,** 91-107.
Thomson, A. (1979) Preservation of porosity in the deep Woodbine/Tuscaloosa trend, Louisiana. *Transactions of the Gulf Coast Association of Geological Societies*, **29,** 396-403.
Thomson, A. (1982) Preservation of Porosity in the Deep Woodbine/Tuscaloosa Trend, Louisiana. *Journal of Petroleum Technology*, **34,** 1156-1162.
Thyne, G., Boudreau, B.P., Ramm, M. and Midtbø, R.E. (2001) Simulation of Potassium Feldspar Dissolution and Illitization in the Statfjord Formation, North Sea. *AAPG Bulletin*, **85,** 621-635.
Tucker, M.E. (2001) *Sedimentary petrology: an introduction to the origin of sedimentary rocks*. John Wiley & Sons.
Tucker, M.E. (2009) *Sedimentary Petrology: An Introduction to the Origin of Sedimentary Rocks*. John Wiley & Sons.
Tudge, J., Lovell, M., Davies, S. and Millar, M. (2014) A novel integrated approach to estimating hydrocarbon saturation in the presence of pore-lining chlorites. *Petroleum Geoscience*, **20,** 201-209.
Turner, J.N., Jones, A.F., Brewer, P.A., Macklin, M.G. and Rassner, S.M. (2015) Micro-XRF applications in fluvial sedimentary environments of Britain and Ireland: progress and prospects. In: *Micro-XRF Studies of Sediment Cores*, pp. 227-265. Springer, Berlin/Heidelberg, Germany.
Ure, A.M. and Berrow, M.L. (1982) The elemental constituents of soils. In: *Environmental Chemistry: Volume 2* (Ed H.J.M. Bowen), **2**, pp. 94-204. The Royal Society of Chemistry.
Vaalgamaa, S. and Korhola, A. (2007) Geochemical signatures of two different coastal depositional environments within the same catchment. *Journal of Paleolimnology*, **38,** 241-260.
Velde, B. (1985) *Clay Minerals. A Physico-Chemical Explanation of Their Occurrence*. Elsevier, Amsterdam.
Velde, B. and Church, T. (1999) Rapid clay transformations in Delaware salt marshes. *Applied Geochemistry*, **14,** 559-568.
Venkatramanan, S., Ramkumar, T. and Anithamary, I. (2013) Distribution of grain size, clay mineralogy and organic matter of surface sediments from Tirumalairajanar Estuary, Tamilnadu, east coast of India. *Arabian Journal of Geosciences*, **6,** 1371-1380.
Verhaegen, J. (2020) Stratigraphic discriminatory potential of heavy mineral analysis for the Neogene sediments of Belgium. *Geologica Belgica*.
Verhagen, I.T.E., Crisóstomo-Figueroa, A., Utley, J.E.P. and Worden, R.H. (2020) Abrasion of detrital grain-coating clays during sediment transport: Implications for diagenetic clay coats. *Sedimentary Geology*, **403,** 105653.
Virolle, M., Brigaud, B., Beaufort, D., Patrier, P., Abdelrahman, E., Thomas, H., Portier, E., Samson, Y., Bourillot, R. and Féniès, H. (2021) Authigenic berthierine and incipient chloritization in shallowly buried sandstone reservoirs: Key role of the source-to-sink context. *GSA Bulletin*.
Virolle, M., Brigaud, B., Bourillot, R., Féniès, H., Portier, E., Duteil, T., Nouet, J., Patrier, P. and Beaufort, D. (2019a) Detrital clay grain coats in estuarine clastic deposits: origin and spatial distribution within a modern sedimentary system, the Gironde Estuary (south-west France). *Sedimentology*, **66,** 859-894.
Virolle, M., Brigaud, B., Luby, S., Portier, E., Féniès, H., Bourillot, R., Patrier, P. and Beaufort, D. (2019b) Influence of sedimentation and detrital clay grain coats on chloritized sandstone reservoir qualities: Insights from comparisons between ancient tidal heterolithic sandstones and a modern estuarine system. *Marine and Petroleum Geology*, **107,** 163-184.
Virolle, M., Féniès, H., Brigaud, B., Bourillot, R., Portier, E., Patrier, P., Beaufort, D., Jalon-Rojas, I., Derriennic, H. and Miska, S. (2020) Facies associations, detrital clay grain coats and mineralogical

characterization of the Gironde estuary tidal bars: A modern analogue for deeply buried estuarine sandstone reservoirs. *Marine and Petroleum Geology*, **114,** 104225.
Vital, H., Stattegger, K. and Garbe-Schoenberg, C.-D. (1999) Composition and trace-element geochemistry of detrital clay and heavy-mineral suites of the lowermost Amazon River; a provenance study. *Journal of Sedimentary Research*, **69,** 563-575.
Walderhaug, O. and Porten, K.W. (2007) Stability of Detrital Heavy Minerals on the Norwegian Continental Shelf as a Function of Depth and Temperature. *Journal of Sedimentary Research*, **77,** 992-1002.
Warren, E. and Smalley, P. (1994) *North Sea formation waters atlas*. Geological Society Publishing House.
Watson, D.F. and Philip, G.M. (1985) Comment on "a nonlinear empirical prescription for simultaneously interpolating and smoothing contours over an irregular grid" by F. Duggan. *Computer Methods in Applied Mechanics and eEngineering*, **50,** 195-198.
Weaver, C.E. (1989) *Clays, muds, and shales*. Elsevier.
Wedepohl, K.H. (1995) The composition of the continental crust. *Geochimica et cosmochimica Acta*, **59,** 1217-1232.
Weeks, A.D. (1961) Mineralogy and geochemistry of vanadium in the Colorado Plateau. *Journal of the Less Common Metals*, **3,** 443-450.
Weibel, R. (1999) Effects of burial on the clay assemblages in the Triassic Skagerrak Formation, Denmark. *Clay Minerals*, **34,** 619-635.
Weindorf, D.C., Zhu, Y., Chakraborty, S., Bakr, N. and Huang, B. (2012) Use of portable X-ray fluorescence spectrometry for environmental quality assessment of peri-urban agriculture. *Environmental Monitoring and Assessment*, **184,** 217-227.
Wenk, H.-R. and Bulakh, A. (2016) *Minerals: their constitution and origin*. Cambridge University Press.
Whitehouse, U.G., Jeffrey, L.M. and Debbrecht, J.D. (1960) Differential settling tendencies of clay minerals in saline waters. *Clays and Clay Minerals*, **7,** 1-79.
Wickham, H. (2016) *ggplot2: Elegant graphics for data analysis*. springer, Berlin/Heidelberg, Germany.
Wilkinson, M. (1991) The concretions of the Bearreraig Sandstone Formation - geometry and geochemistry. *Sedimentology*, **38,** 899-912.
Wilkinson, M., Darby, D., Haszeldine, R.S. and Couples, G.D. (1997) Secondary porosity generation during deep burial associated with overpressure leak-off: Fulmar Formation, United Kingdom Central Graben. *American Association of Petroleum Geologists Bulletin*, **81,** 803-813.
Wilkinson, M., Milliken, K.L. and Haszeldine, R.S. (2001) Systematic destruction of K-feldspar in deeply buried rift and passive margin sandstones. *Journal of the Geological Society*, **158,** 675-683.
Wilson, J. (1987) The chemistry of clays and clay-minerals - NEWMAN,ACD. *Nature*, **328,** 585-585.
Wilson, M.D. (1992) Inherited grain-rimming clays in sandstones from eolian and shelf environments: their origin and control on reservoir properties. *In: Origin, diagenesis and petrophysics of clay minerals in sandstones (eds. Houseknecht, D.W. and Pittman, E.D.) SEPM Special Publication*, **47,** 209-225.
Wilson, M.D. and Pittman, E.D. (1977) Authigenic clays in sandstones; recognition and influence on reservoir properties and paleoenvironmental analysis. *Journal of Sedimentary Research*, **47,** 3-31.
Wilson, M.J. (2004) Weathering of the primary rock-forming minerals: processes, products and rates. *Clay Minerals*, **39,** 233-266.
Wilson, M.J., Wilson, L. and Patey, I. (2014) The influence of individual clay minerals on formation damage of reservoir sandstones: a critical review with some new insights. *Clay Minerals*, **49,** 147-164.
Windom, H.L. (1976) Lithogenous material in marine sediments. *Chemical Oceanography*, **5,** 103-135.
Wise, S., Smellie, J., Aghib, F., Jarrard, R. and Krissek, L. (2001) Authigenic smectite clay coats in CRP-3 drillcore, Victoria Land Basin, Antarctica, as a possible indicator of fluid flow: a progress report. *Terra Antartica*, **8,** 281-298.
Wooldridge, L.J., Worden, R.H., Griffiths, J., Thompson, A. and Chung, P. (2017a) Biofilm origin of clay-coated sand grains. *Geology*, **45,** 875-878.

Wooldridge, L.J., Worden, R.H., Griffiths, J. and Utley, J.E.P. (2017b) Clay-coated sand grains in petroleum reservoirs: Understanding their distribution via a modern analogue. *Journal of Sedimentary Research*, **87,** 338-352.
Wooldridge, L.J., Worden, R.H., Griffiths, J. and Utley, J.E.P. (2019a) Clay-coat diversity in marginal marine sediments. *Sedimentology*, **66,** 1118-1138.
Wooldridge, L.J., Worden, R.H., Griffiths, J. and Utley, J.E.P. (2019b) How to quantify clay-coat grain coverage in modern and ancient sediments. *Journal of Sedimentary Research*, **89,** 135-146.
Wooldridge, L.J., Worden, R.H., Griffiths, J., Utley, J.E.P. and Thompson, A. (2018) The origin of clay-coated sand grains and sediment heterogeneity in tidal flats. *Sedimentary Geology*, **373,** 191-209.
Worden, R.H., Armitage, P.J., Butcher, A.R., Churchill, J.M., Csoma, A.E., Hollis, C., Lander, R.H. and Omma, J.E. (2018a) Petroleum reservoir quality prediction: overview and contrasting approaches from sandstone and carbonate communities. *Geological Society, London, Special Publications*, **435,** 1-31.
Worden, R.H., Benshatwan, M.S., Potts, G.J. and Elgarmadi, S.M. (2016) Basin-scale fluid movement patterns revealed by veins: Wessex Basin, UK. *Geofluids*, **16,** 149-174.
Worden, R.H., Bukar, M. and Shell, P. (2018b) The effect of oil emplacement on quartz cementation in a deeply buried sandstone reservoir. *AAPG Bulletin*, **102,** 49-75.
Worden, R.H. and Burley, S.D. (2003) Sandstone diagenesis: the evolution from sand to stone. In: *Sandstone diagenesis, recent and ancient.* (Eds S.D. Burley and R.H. Worden), *International Association of Sedimentologists Reprint Series*, **4**, pp. 3-44, Oxford, United Kingdom.
Worden, R.H., French, M.W. and Mariani, E. (2012) Amorphous silica nanofilms result in growth of misoriented microcrystalline quartz cement maintaining porosity in deeply buried sandstones. *Geology*, **40,** 179-182.
Worden, R.H., Griffiths, J., Wooldridge, L.J., Utley, J.E.P., Lawan, A.Y., Muhammed, D.D., Simon, N. and Armitage, P.J. (2020a) Chlorite in sandstones. *Earth-Science Reviews*, **204,** 103105.
Worden, R.H. and Morad, S. (2000) Quartz cement in oil field sandstones: A review of the critical problems. *Quartz Cementation in Sandstones*, **29,** 1-20.
Worden, R.H. and Morad, S. (2003) Clay minerals in sandstones: Controls on formation, distribution and evolution. *In: Clay mineral cements in sandstones (eds. Worden, R.H. and Morad, S.) International Association of Sedimentologists Special Publications*, **34,** 3-41.
Worden, R.H., Needham, S.J. and Cuadros, J. (2006) The worm gut; a natural clay mineral factory and a possible cause of diagenetic grain coats in sandstones. *Journal of Geochemical Exploration*, **89,** 428-431.
Worden, R.H., Oxtoby, N.H. and Smalley, P.C. (1998) Can oil emplacement prevent quartz cementation in sandstones? *Petroleum Geoscience*, **4,** 129-137.
Worden, R.H., Utley, J.E.P., Butcher, A.R., Griffiths, J., Wooldridge, L.J. and Lawan, A.Y. (2020b) Improved imaging and analysis of chlorite in reservoirs and modern day analogues: new insights for reservoir quality and provenance. *Geological Society, London, Special Publications*, **484,** 189.
Xiang, F., Wang, Y., Feng, Q., Zhang, D. and Zhao, J. (2016) Further research on chlorite rims in sandstones: evidence from the Triassic Yanchang Formation in the Ordos basin, China. *Arabian Journal of Geosciences*, **9,** 507.
Xie, X.G., Byerly, G.R. and Ferrell, R.E. (1997) IIb trioctahedral chlorite from the Barberton greenstone belt: Crystal structure and rock composition constraints with implications to geothermometry. *Contributions to Mineralogy and Petrology*, **126,** 275-291.
Yamamuro, M. and Kayanne, H. (1995) Rapid direct determination of organic carbon and nitrogen in carbonate-bearing sediments with a Yanaco MT-5 CHN analyzer. *Limnology and Oceanography*, **40,** 1001-1005.
Yardley, B.W.D. (1989) *An Introduction to Metamorphic Petrology*. Longman, Harlow.
Young, B., Fortey, N.J. and Nancarrow, P.H.A. (1986) An occurrence of tungsten mineralisation in the Eskdale Intrusion, West Cumbria. *Proceedings of the Yorkshire Geological Society*, **46,** 15-21.

Young, K.E., Evans, C.A., Hodges, K.V., Bleacher, J.E. and Graff, T.G. (2016) A review of the handheld X-ray fluorescence spectrometer as a tool for field geologic investigations on Earth and in planetary surface exploration. *Applied Geochemistry*, **72,** 77-87.
Yu, Y., Lin, L.-B. and Gao, J. (2016) Formation mechanisms and sequence response of authigenic grain-coating chlorite: evidence from the Upper Triassic Xujiahe Formation in the southern Sichuan Basin, China. *Petroleum Science*, **13,** 657-668.
Yuan, G.H., Gluyas, J., Cao, Y.C., Oxtoby, N.H., Jia, Z., Wang, Y., Xi, K. and Li, X. (2015) Diagenesis and reservoir quality evolution of the Eocene sandstones in the northern Dongying Sag, Bohai Bay Basin, East China. *Marine and Petroleum Geology*, **62,** 77-89.
Yuan, Z., Cheng, Q., Xia, Q., Yao, L., Chen, Z., Zuo, R. and Xu, D. (2014) Spatial patterns of geochemical elements measured on rock surfaces by portable X-ray fluorescence: application to hand specimens and rock outcrops.
Zahid, M.A., Chunmei, D., Lin, C., Gluyas, J., Jones, S., Zhang, X., Munawar, M.J. and Ma, C. (2016) Sequence stratigraphy, sedimentary facies and reservoir quality of Es4s, southern slope of Dongying Depression, Bohai Bay Basin, East China. *Marine and Petroleum Geology*, **77,** 448-470.
Zarco-Perello, S. and Simões, N. (2017) Ordinary kriging vs inverse distance weighting: spatial interpolation of the sessile community of Madagascar reef, Gulf of Mexico. *PeerJ*, **5,** e4078.
Zhang, J., Wen Huang, W. and Chong Shi, M. (1990) Huanghe (Yellow River) and its estuary: Sediment origin, transport and deposition. *Journal of Hydrology*, **120,** 203-223.
Zhu, M.-X., Hao, X.-C., Shi, X.-N., Yang, G.-P. and Li, T. (2012) Speciation and spatial distribution of solid-phase iron in surface sediments of the East China Sea continental shelf. *Applied Geochemistry*, **27,** 892-905.
Zhu, S., Wang, X., Qin, Y., Jia, Y., Zhu, X., Zhang, J. and Hu, Y. (2017) Occurrence and origin of pore-lining chlorite and its effectiveness on preserving porosity in sandstone of the middle Yanchang Formation in the southwest Ordos Basin. *Applied Clay Science*, **148,** 25-38.
Ziegler, K. (2006) Clay minerals of the Permian Rotliegend Group in the North Sea and adjacent areas. *Clay Minerals*, **41,** 355-393.
Zwingmann, H., Clauer, N. and Gaupp, R. (1999) Structure-related geochemical (REE) and isotopic (K-Ar, Rb-Sr, δ18O) characteristics of clay minerals from Rotliegend sandstone reservoirs (Permian, northern Germany). *Geochimica et Cosmochimica Acta*, **63,** 2805-2823.

8. Appendix

The appendix present journal articles that Dahiru Muhammed co-authored during his PhD training program. The published papers are related to Dahiru Muhammed PhD project.

I. In this paper, Dahiru Muhammed performed a detailed core description of 20 cores, that aided in the understanding and interpretation of the Ravenglass stratigraphy and sedimentary evolution. Dahiru Muhammed also collected grain size data at every 5 cm, and conducted grain size analysis using Laser particle size analysis to examine how grain size and sorting in the basin have evolved through time, which contributed to the interpretation and writing of the manuscript.

Claire McGhee[1#], Dahiru Muhammed[2], Naboth Simon[2], Sanem Acikalin[1], James E. P. Utley[2], Joshua Griffiths[2,3], Luke Wooldridge[2,3], Iris T. E. Verhagen[2], Cees van der Land[1], Richard H. Worden[2], **Stratigraphy and sedimentary evolution of a modern macro-tidal incised valley – an analogue for reservoir facies and architecture** (published in sedimentology).

1. School of Natural and Environmental Sciences, Newcastle University, NE1 7RU, UK
2. School of Environmental Sciences, Liverpool University, L69 3BP, UK
3. BP Exploration, Chertsey Road, Sunbury-on-Thames, Middlesex, TW16 7LN, UK

II. In this paper, D. D. Muhammed performed pXRF analysis and mapped the distribution of iron that aided in understanding, the distribution of chlorite in sandstones, and contributed to the reviewing of the manuscript.

R. H. Worden[1*], J. Griffiths[1,2], L. J. Wooldridge[1,2], J. E. P. Utley[1], A. Y. Lawan[1,4], D. D. Muhammed[1], N. Simon[1], P. J. Armitage[1, 3], **Chlorite in sandstones** (published in earth-science reviews).

1. Department of Earth, Ocean and Ecological Sciences, University of Liverpool, Liverpool, L69 3GP, UK
2. BP Exploration, Chertsey Road, Sunbury-on-Thames, Middlesex, TW16 7LN, UK
3. BP Upstream Technology, Chertsey Road, Sunbury-on-Thames, Middlesex, TW16 7LN, UK
4. Department of Geology, Bayero University, Kano State, Nigeria.

III. In this paper, D. D. Muhammed performed grain size analysis and mapped the distribution of sediment textural parameters, that aided in understanding their relationship with sub-depositional environment, and contributed to the reviewing of the manuscript.

N. Simon[a], R. H. Worden[a, *], D. D. Muhammed[2], J. E. P. Utley[a], I. T. E. Verhagen[a], J. Griffiths[a,b], L. Wooldridge[a,c], **Sediment textural characteristics of the Ravenglass Estuary; Development of a method to predict palaeo sub-depositional environments from estuary core samples** (published in Sedimentary geology).

a) School of Environmental Sciences, Liverpool University, L69 3BP, UK
b) BP Exploration, Chertsey Road, Sunbury-on-Thames, Middlesex, TW16 7LN, UK
c) BP Upstream Technology, Chertsey Road, Sunbury-on-Thames, Middlesex, TW16 7LN, UK

Stratigraphy and sedimentary evolution of a modern macro-tidal incised valley – an analogue for reservoir facies and architecture

Claire McGhee[1#], Dahiru Muhammed[2], Naboth Simon[2], Sanem Acikalin[1], James E. P. Utley[2], Joshua Griffiths[2,3], Luke Wooldridge[2,3], Iris T. E. Verhagen[2], Cees van der Land[1], Richard H. Worden[2*]

1. *School of Natural and Environmental Sciences, Newcastle University, NE1 7RU, UK*
2. *School of Environmental Sciences, Liverpool University, L69 3BP, UK*
3. *BP Exploration, Chertsey Road, Sunbury-on-Thames, Middlesex, TW16 7LN, UK*

Abstract

Incised valley fills are complex as they correspond to multiple sea-level cycles which makes interpretation and correlation of stratigraphic surfaces fraught with uncertainty. Despite numerous studies of the stratigraphy of incised valley fills, few have focused on extensive core coverage linked to high fidelity dating in a macro-tidal, tide-dominated settings. For this study nineteen sediment cores were drilled through the Holocene succession of the macro-tidal Ravenglass Estuary in north-west England, UK. A facies and stratigraphic model of the Ravenglass incised valley complex was constructed, to understand the lateral and vertical stacking patterns relative to the sea-level changes. The Ravenglass Estuary formed in five main stages. First, incision by rivers (*ca* 11,500 to *ca* 10,500 yrs BP) cutting through the shelf during lowstand, which was a period of fluvial dominance. Secondly, a rapid transgression and landward migration of the shoreline (10,500 to 6,000 yrs BP). Wave action was dominant, promoting spit formation. The third stage was a highstand at *ca* 6,000 to *ca* 5,000 yrs BP, creating maximum accommodation and the majority of backfilling. The spits narrowed the inlet and dampened wave action. The fourth stage was caused by a minor fall of sea-level (*ca* 5,000 to *ca* 226 yrs BP), which forced the system to shift basinward. The fifth and final stage (226 yrs BP to present) involved the backfilling of the River Irt, southward migration of the northerly (Drigg) spit and merging of the River Irt with the Rivers Esk and Mite. The final stage was synchronous with the development of the central basin. As an analogue for ancient and deeply buried sandstones, most of the estuarine sedimentation occurred after transgression, of which the coarsest and cleanest sands are found in the tidal inlet, on the foreshore and within in-channel tidal bars. The best-connected (up to 1 km) reservoir-equivalent sands belong to the more stable channels.

Introduction

Incised valleys form as a result of basinward migration of the shoreline, inducing exposure of the shelf and promoting enhanced fluvial incision within the lower reaches of the coastal valleys. The valley fills during landward migration of the shoreline and contains the most complete record of lowstand, transgression and subsequent highstand deposition (Zaitlin *et al.*,1994). The stratigraphic expression of the deposits within the valley can promote sediment preservation that can result in highly economical oil and gas reservoirs and storage sites for carbon dioxide for CCS projects (Salem *et al.*, 2005; Hein, 2015; Wang *et al.*, 2019; Meng *et al.*, 2020). The understanding of reservoir facies and stratigraphic architecture of incised valley-fills is also critical for predicting a field's recoverable hydrocarbon potential (Hampson *et al.*, 1999; Slatt, 2013; Wang *et al.*, 2019) and reducing overall risk. The valley deposits are unique in that they represent the creation of accommodation space by one process (migration of shoreline) and the infill by a range of processes (wave, tide and fluvial) (Boyd *et al.*, 2011). In many modern and ancient examples of incised valleys, the sediment fill is typically composed of coarse-grained fluvial and alluvial beds at the valley base. Subsequent transgression and

sea-level highstand result in estuarine and marine sedimentation, of which the former appears to be the most common volumetrically (Allen & Posamentier, 1993; Chaumillon *et al.*, 2010; Garrison & Bergh 2006; Willis & Gabel, 2001). Estuarine sedimentation within the valley is complex in that the deposits are the product of river, tide and wave action causing a tripartite zonation of facies that corresponds to net bedload transport (Boyd *et al.*, 2011). Compound filling (corresponding to multiple phases of sea-level cycles) of such valleys results in complex architecture, resulting in extensive amalgamation of stratigraphic surfaces (Zaitlin *et al.*, 1994). Widely adopted conceptual facies models and stratigraphic frameworks have been developed to explain and predict the distribution of sediment within incised valleys during transgression (Allen & Posamentier 1993; Dalrymple *et al.*, 1992; Heap *et al.*, 2004; Zaitlin *et al.* 1994). A recent study by Wang, *et al.* (2020) demonstrated that 87 Quaternary incised valley fills showed similar stratigraphic organization comparable to the classic conceptual models (Dalrymple *et al.*, 1992b; Allen & H. W. Posamentier, 1993; Zaitlin *et al.*, 1994; Heap *et al.*, 2004; Virolle *et al.*, 2019) but displayed significant variability in the stratigraphic architecture of valley fills, related to continental margin type, inherited topography, river size, catchment area and shoreline hydrodynamics. Depending on the dominant hydrodynamics at the estuary mouth, two end-members have been recognized (Dalrymple *et al.*, 1992). Wave-dominated estuaries are typically described as possessing a tripartite zonation of facies; a barrier spit at the estuarine mouth, tidal inlet, a sheltered muddy central basin and a bayhead delta. In tide-dominated systems, the marine sand body is made up of elongate tidal bars in the inlet and the mouth. The meandering channel belt in tide-dominated settings is the equivalent to the central basin in the wave-dominated models. Typically, the inner estuarine facies above the sequence boundary in wave-dominated settings can be very muddy compared to sandy facies in the tide-dominated settings.

Despite a vast amount of literature regarding the stratigraphy of incised valley fills, few have focused on high resolution core coverage coupled with high fidelity dating within a macro-tidal tide-dominated setting. The Cobequid Bay–Salmon River estuary, located in the Bay of Funday (Tessier, 2012), is arguably one of the most cited modern examples of a tide-dominated valley fill (Dalrymple & Zaitlin, 1994) and represents the basis for the Dalrymple *et al.* (1992) classic conceptual model. The Gironde Estuary in France is also another commonly cited tide-dominated valley fill (Allen & Posamentier 1993; Fenies & Tastet 1998; Virolle *et al.* 2019). Ravenglass is a scaled down version of many modern estuaries discussed in the literature, covering an area of 5.6 km^2 (Chaumillon *et al.*, 2010a; Menier *et al.*, 2010). The Gironde Estuary (south-west France) and the tide-dominated palaeo-Changjiang in China have drainage basins that cover approximately 75,000 km^2 (Allen & Posamentier, 1993) and 1.8×10^6 km^2 (Hori *et al.*, 2001), respectively. Despite differences in scale and sediment supply, the three estuaries possess similar morphologies.

The lateral and vertical stacking patterns of the Holocene deposits of the Ravenglass estuary, north-west England, UK were investigated, in order to model facies distributions within a tide-dominated incised valley. According to Zaitlin *et al.* (1994), the deposits have formed a single, simple-fill in that most of the deposits correspond to one cycle of sea-level fall and rise during the Holocene (Lloyd *et al.*, 2013). The Ravenglass incised valley is a relatively small, modern day macro-tidal estuary with a multi-tributary system that extensive interpretation of the surface and shallow subsurface sediment (Griffiths *et al.*, 2018; Wooldridge *et al.*, 2018, 2019). Here, the study will examine the complete sedimentary in-fill of the Ravenglass valley, produce detailed facies descriptions and create high resolution correlations linking shoreline migration to style of sedimentation.

This study aims to address the following research questions, in order to summarize the evolution of the Ravenglass Estuary incised valley-fill:

1. What is the stratigraphic organization of infill for the Ravenglass Estuary?
2. What are the architectural elements of the infill for the Ravenglass Estuary?
3. What is the morpho-sedimentary evolution of the valley?
4. Is lateral and vertical correlation of facies possible over 100 m to 1,000 m scales?
5. How does the Ravenglass incised valley-fill compare to current stratigraphic models?

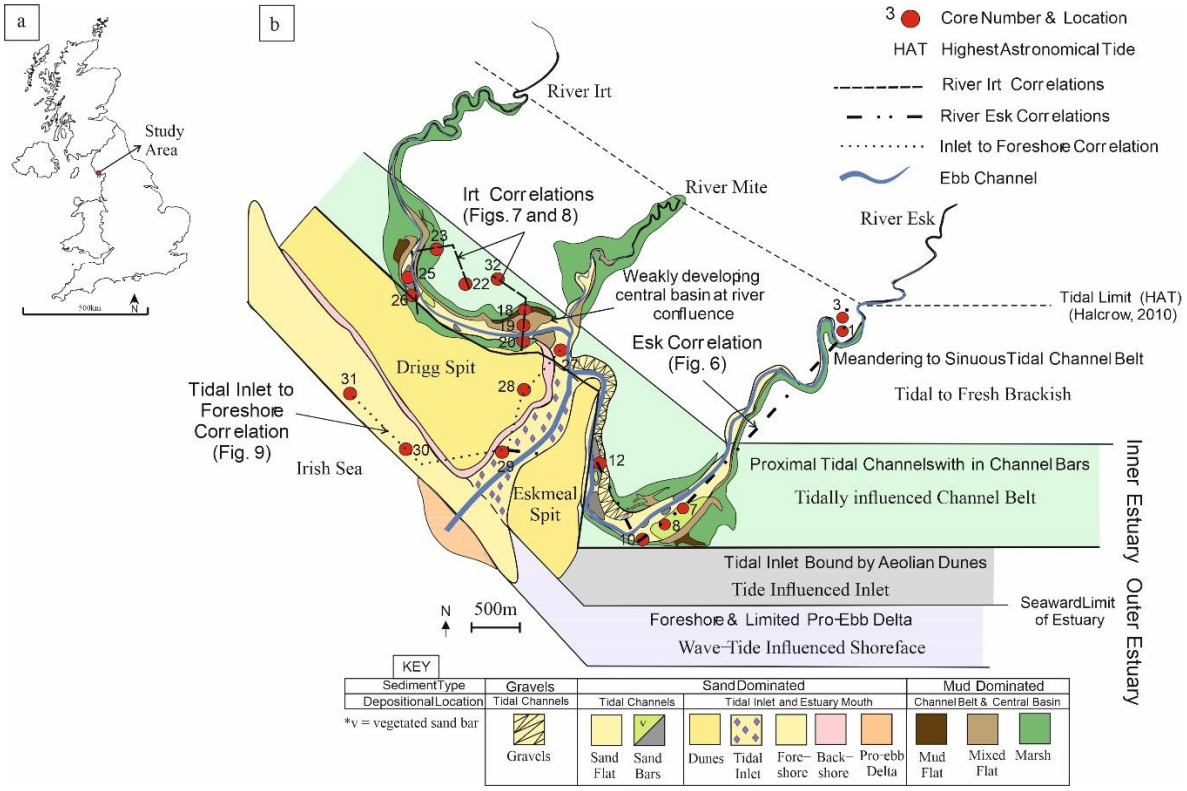

Figure 1: Location map indicating Ravenglass Estuary, Cumbria, UK with a red circle. (B) The present-day estuarine zones of Ravenglass Estuary. The outer estuary (purple and green) is defined by the landward limit of the tidal inlet (dashed line). The outer estuary consists of a tidal inlet bound by the Drigg and Eskmeal spits (grey) and a pro-ebb delta (purple). The inner estuary consists of proximal tidal channels (the rivers Irt, Esk and Mite) with a distal meandering tidal channel belt (green) and proximal tidal sand bars (yellow). The map also indicates the position of the 19 Holocene cores (red circles) used in the study. Correlation panels for the Holocene cores are shown by a single dashed line for the River Irt, dashed and dotted line for the River Esk and a dotted line for the tidal inlet to foreshore.

Geological setting and hydrodynamics

The Ravenglass Estuary is located in Cumbria, England (Fig. 1A), west of the Lake District mountains (maximum elevation of 980 m at Scafell Pike). It is one of the most natural and least developed

estuaries in the UK, with little industry and virtually no artificial coastal defences. The estuary lies on relatively flat low-lying coastal plain, occupying an area of 5.6 km^2, of which approximately 80% is intertidal (Bousher, 1999; Lloyd *et al.*, 2013; Wooldridge *et al.*, 2017a; Griffiths *et al.*, 2018, 2019; Wooldridge *et al.*, 2018). The estuary is a mixed energy, macrotidal system with a mean spring tidal range of >7 m, leaving the estuary nearly fully drained at low tide. The estuary is fed by three main rivers, the Irt, Mite and Esk. The River Irt flows at 3.4 m^3/s^{-1} and the River Mite flows at 0.4 m^3/s^{-1} (Bousher, 1999) The River Esk has an average flow rate of 4.2 m^3/s^{-1} (broadly similar with the River Irt) with suspended sediment concentrations of 20 to 70 gm^{-3} during spring tides and 5 to 20 gm^{-3} during neap tides (Assinder *et al.*, 1985). These westward-draining rivers cut through the steep hinterland topography of the English Lake District and meet at a point of confluence creating a single tidal channel (Fig. 1B). Restriction in the tidal inlet size can be attributed to the formation of the Drigg barrier spit to the north-west and the Eskmeal barrier spit to the south-east (Fig. 1B). Strong tidal asymmetry occurs due to the shallow bathymetric nature and short length of the estuary (Kelly *et al.*, 1991). Modern surface facies from the Ravenglass estuary consist of gravel, tidal flats, fluvial tidal bars (alternate bars) and dunes, tidal-inlet, backshore, foreshore and pro-ebb delta (Wooldridge *et al.*, 2017b; Griffiths *et al.*, 2018; Simon *et al.*, 2021).

The Ravenglass Estuary is underlain to the west of the Lake District Boundary Fault by Triassic Sherwood Group sandstones, and to the east by Devonian Eskdale Granites, Ordovician Borrowdale Volcanics and the Cambrian Skiddaw Group. The River Irt drains Borrowdale Volcanic Group andesites and Sherwood sandstones whereas the River Esk drains the Eskdale granite and granodiorite. The minor River Mite drains Eskdale granite and granodiorite and Borrowdale volcanic rocks.

Quaternary geology

Western Cumbria has been affected by periodic Quaternary glacial advance and retreat (Royd, 2002; Merritt & Auton, 2000), with the most recent event occurring during the Mid to Late Devensian (MLD), between 28,000 to 13,000 yrs BP (Moseley, 1978). During the MLD, Ravenglass lay in an ice-sheet convergence zone, fed by ice from both Scotland to the north and the Lake District to the east. Ice flow directions have been interpreted from the distribution of erratics (granite and greywackes from the Southern Uplands of Scotland) and drumlin orientation, which support the interpretation of Scottish Ice impinging on the Cumbrian coastline (Merritt & Auton, 2000).

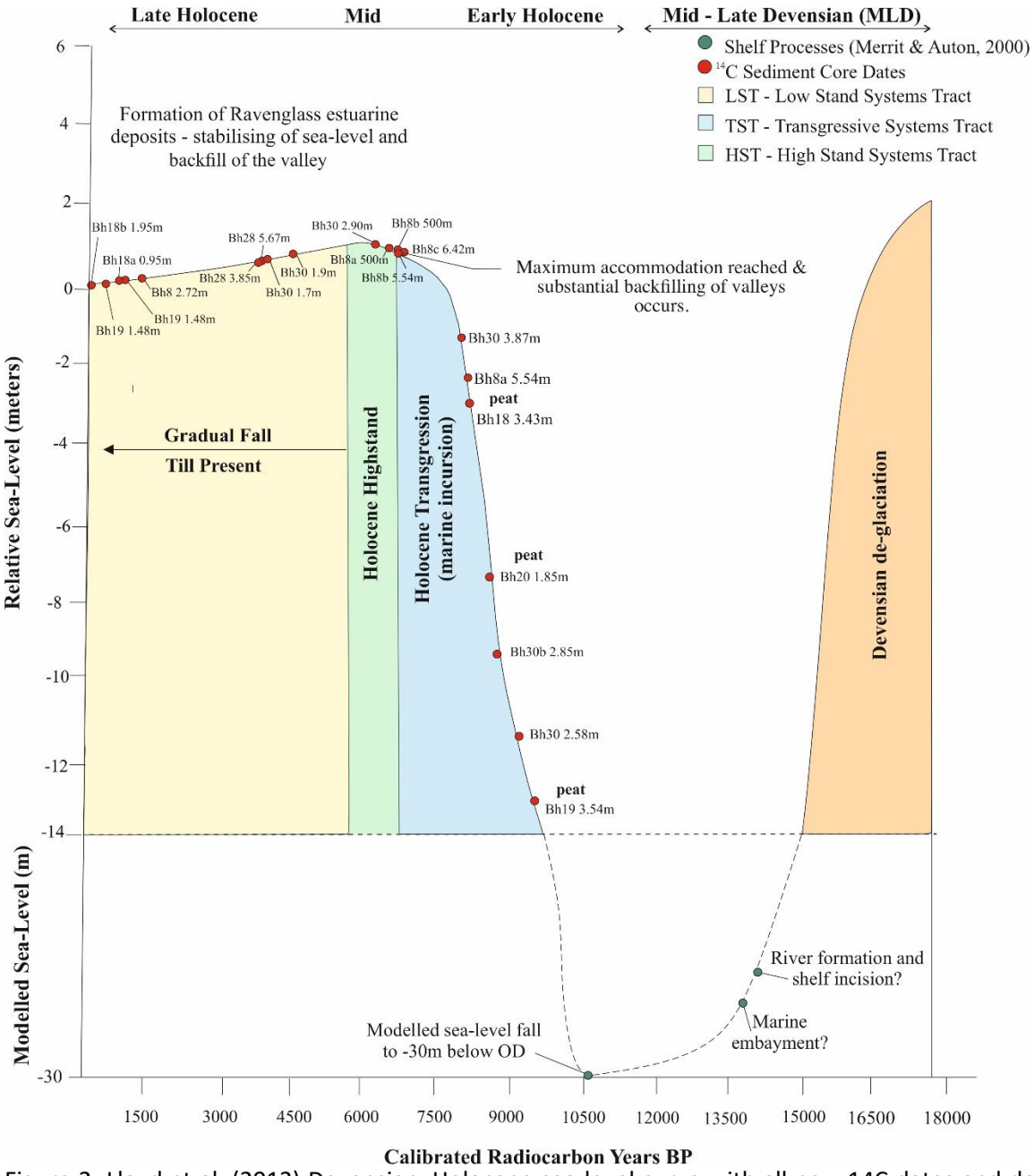

Figure 2: Lloyd et al. (2013) Devensian–Holocene sea-level curve with all new 14C dates and depths plotted from Ravenglass Estuary cores (red circles). The Devensian glacial lowstand, when isostatic rebound outstripped sealevel rise, between 12 000 and 10 500 yrs BP inducing enhanced fluvial incision in the lower valleys. This was followed by a rapid transgression, which was characterized by a phase of relative sea-level rise, occurring between ca 10 500 and 6000 yrs BP During this time, net sediment transport was landward. A minor fall in relative sea level from 5000 yrs BP to the present day, resulting in dominant estuarine conditions (adapted from Lloyd et al., 2013).

The evolution of the Cumbrian coastline and resulting sediment deposits have been greatly modified by post-glacial processes and changes in relative sea-level linked to spatially variable glacio-isostatic rebound (Zong & Tooley 1996). According to the lithostratigraphic and biostratigraphy study of central Cumbria, and specifically Ravenglass, the area underwent a sea-level highstand of approximately +2.3 m Ordnance Datum (OD) during the Late Devensian between 17,000 and 15,000 yrs BP. From 15,000 to 11,500 yrs BP, a rapid fall in sea-level below -5 m OD (modelled up to -30 m) occurred as glacio-isostatic rebound exceeded global sea-level rise. After the period of incision, a rapid marine

transgression began in the Early Holocene between 11,500 to 6,000 yrs BP, followed by a stabilized highstand, estimated at +2 m OD with a gradual fall until present (Lloyd *et al.*, 2013) (Fig. 2).

Samples and methods

To construct a facies architecture model of the Ravenglass Estuary Holocene sedimentary sequence, information on the age and depositional environments of the sediments was investigated. To do this, radiocarbon dating and detailed core descriptions from 19 cores were undertaken.

Core Acquisition

Nineteen cores were drilled through the Holocene succession as far as the Ravenglass Glacial Till Member, under tender by Geotechnical Engineering Ltd. All sites were subject to an initial desk study to estimate depth to glacial till based on previous reports and publications (Assinder *et al.*, 1985; Kershaw *et al.*, 1990; Halcrow Group, 2013; Coast & Area, 2015). All sites were subject to environmental impact assessment in conjunction with Natural England; several sites in, and around, the estuary required the presence of an independent ecologist to ensure there was no damage to protected species, such as natterjack toads and great crested newts. Due to more than 100 years of weapons testing from the Ministry of Defence-owned Eskmeals firing range (located on the southern spit with heavy-artillery firing out into the East Irish Sea) much of the beach and tidal inlet was flagged as high-risk for unexploded ordnance (UXO). The risk of UXO was mitigated by Lankelma Ltd who appraised each foreshore and pro-ebb delta site with a magnetometer probe mounted on a wide-tracked vehicle (Fig. 4D) immediately before coring. Core acquisition had to be timed around periods of low tide and at least two cores were collected at each site. Cores were acquired using either a Geotechnical 'P60' Rotary rig or a Geotechnical 'Pioneer' rotary rig. The Pioneer rig is a light-weight percussion rig that was used on soft substrates, such as mudflats (Fig. 4C) and vegetated tidal bars (Fig. 4A). The P60 is a heavier rotary rig which was used on hard substrates such as sandflats (Fig. 4B) and in areas of uneven land surface, such as the upper reaches of the Esk Estuary flood plain, as it is capable of operating on slopes of up to 45 degrees. The retrieved cores were 12 cm in diameter retained in a semi-rigid plastic liner and transported back to the University of Liverpool for subsequent analysis.

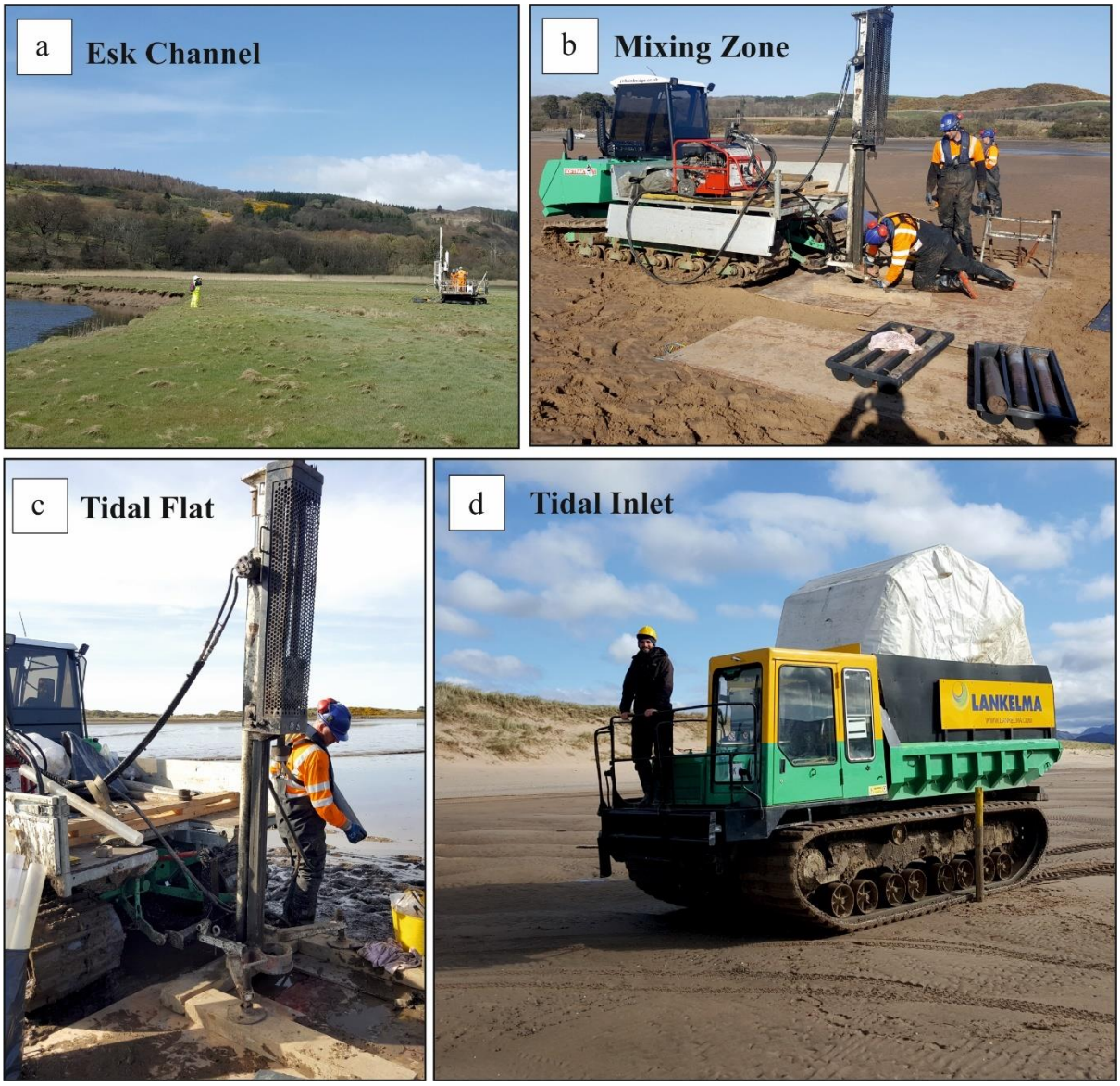

Figure 3: Drilling locations and rigs used to core the Ravenglass valley-fill. (A) River Esk tidal channel with Pioneer (B) mixing zone of the rivers (C) tidal flat and (D) tidal inlet. People for scale are ca 1.8 m tall.

Core descriptions

The 19 sediment cores were sliced and photographed wet, and after air-drying. Detailed logging of each core was undertaken, wet and then dry, at a scale of 1:5. Facies were described in terms of grain size, sorting, colour, sedimentary structures, bed thickness, presence of roots and shell fragments, bioturbation index and type of bioturbation.

Radiocarbon Dating (^{14}C)

Nineteen radiocarbon analyses were undertaken under contract by the Chrono Centre, which is part of Queen's University of Belfast, in Northern Ireland, UK. Samples of shell fragments and organic matter were taken from the cores as they were logged. The precise depth and type of material was carefully recorded (Table 1).

The shell fragments used for dating were identified as bivalves, such as oysters. Shells were classified as being thin or thick specimens. It was recognized that thick samples may have been able to withstand erosion from their initial site of deposition, followed by subsequent re-deposition; thick-shelled samples are therefore more liable to anomalous ages than thin-shelled samples. Organic matter subject to dating included leaf-bearing peat.

Samples from the top 1 m of sediment were not subject to radiocarbon dating since they were considered to be at risk of contamination from radionuclides, including ^{14}C, released accidentally from the Sellafield (previously known as Windscale) nuclear reprocessing site, 15 km north of Ravenglass, since its inception in 1947.

Table 1. Radiocarbon dating results, showing the samples for each facies association (FA), as well as sediment descriptions, sample depth (m), ^{14}C ages and the associated error (±).

FA	*Sample Type*	*Sediment Context*	*Depth (m)*	*^{14}C Ages*	*±*
Ravenglass Glacial Till Member (RGTM)	Nil	Nil	Nil	Nil	Nil
Alluvial Gravels	Nil	No ^{14}C datable material.	Nil	Nil	Nil
Peats	Peat fragments	Central basin peat beds overlying glacial till. Local depressions with no in-channel deposition.	3.54m	**9,309**	38
			1.85m	**8,416**	37
			3.43m	**8,094**	32
Tidal-Fluvial	Thin white bivalve shells	Medium to coarse grained, moderately sorted sands with shell fragments. Signifies the first sediment deposited within the valley	5.0m	**6,971**	30
			5.54m	**6566**	40
				7,948	
Aeolian Dunes	Medium white bivalve shell fragments	Fine to medium grained sediment with rare pebbles and shells.	3.85m	**3,910**	24
			5.67m	**4,341**	26
Tidal Meander and Central Basin	Oyster and thin white bivalve shells	Fine grained, poorly sorted sand and mud. Restricted to central basin samples. Upper 1m of sediment contaminated from Sellafield, a nearby nuclear power plant.	1.46m	**813**	20
			1.48m	**733**	21
			1.55m	**634**	26
			1.95m	**123**	24
Tidal Sand Bar	Thin white bivalve shells	Medium grain sands, moderate to well sorted with shelly horizons.	2.72m	**1,229**	20
Foreshore	White bivalves and blue oyster shells	Fine to medium grained sand with thicker gravel beds. Located between the Irt and Esk palaeo-channels and	2.58m	**9003**	
			2.90m	**6439**	
			1.91m	**3629**	
			1.91m	**3727**	

		potentially a zone of tidal ravinement.	1.70m 1.49m	**3307** **1890**	
Salt & Fresh Marsh	Nil	Nil		Nil	Nil
Upper Flow Regime	Nil	Nil		Nil	Nil

Post-glacial palaeo-topography

All available data related to the depth of the Ravenglass Glacial Till Member (RGTM) throughout the Ravenglass Estuary are collated in Fig. 3. Data from cores published by Merritt & Auton (2000) and a core from the British Geological Survey (BGS, 1939) data repository were also plotted on the palaeo-topographical map. The map further incorporates glacial till outcrop locality information from Ravenglass (Griffiths *et al.*, 2019). Based on the 28 spot depths to glacial till, a tentative palaeo-topographical map of the Ravenglass area has been drafted, prior to valley being infilled (Fig. 3).

The palaeo-Irt, in the north-west of the area, had a steep north-west-side with a relief of *ca* 22 m. South-east of palaeo-Irt, the land surface rose up, by *ca* 12 m, with a local 'high' in the area currently occupied by the central basin of the present-day estuary (Fig. 3). On this basis, the palaeo-Irt flowed directly into the Irish Sea rather than deviating to the south-east and joining the palaeo-Esk. The initial separation of the palaeo-Irt from the palaeo-Esk is supported by historical map information that shows that the Irt only merged with the Esk at approximately 270 yrs BP. A map by Speed from the year 1610 ME (Speed, 1610) shows the Irt flowed directly into the Irish Sea, while a map by Thomas Donald from the year 1774 ME (Donald, 1774) shows the estuary had adopted the current geomorphology with the River Irt deviating to the south-east and joining the Rivers Esk and Mite.

Based on the mapped contours to the glacial till, the palaeo-Esk followed the outline of the present-day River Esk, in that it deviated to the north-west and joined the much smaller River Mite (Fig. 3). It was previously suggested that the palaeo-Esk flowed directly into the Irish Sea (Halcrow Group, 2013) but there seems to be no evidence to support this interpretation. Moreover, there is archaeological evidence [signs of a Neolithic flint napping factory, possibly as old as 9,000 yrs BP; (Bonsall *et al.*, 1989; Clare *et al.*, 2001)] proving the existence of the Eskmeals spit immediately after the glacial retreat, supporting our interpretation of the trajectory of the palaeo-Esk.

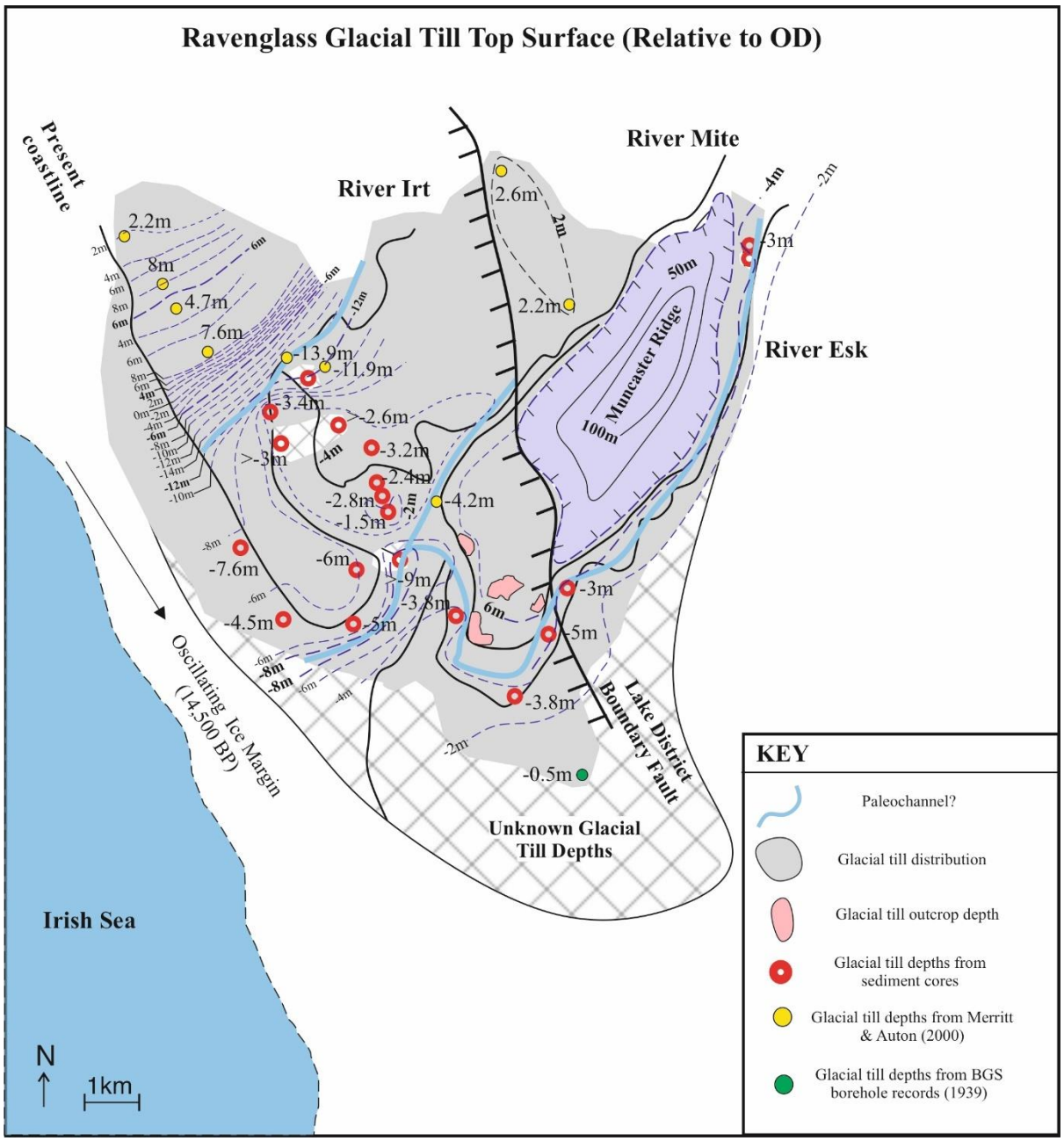

Figure 4: Contoured surface map of the Ravenglass Glacial Till Member (RGTM) based on outcrop data (pink), the drilled sediment cores (red circles), data from Merritt & Auton (2000; yellow) and the BGS repository (green). The white squared box under the present- day Eskmeal Spit is unknown depths to the RGTM. The blue lines indicate the palaeo-channels of the River Irt, Mite and Esk. Note the steep sided, deeper channel of the River Irt to the north-west and the topographical high between the River Irt and River Mite. The river Esk flows around an Ordovician Granitic fell (purple) known as Muncaster Ridge, bound by the Lake District Boundary Fault.

Facies analysis and interpretation

In this section, results are presented from field observations, aerial photography, core analysis in the form of sedimentary logs, facies characterization and radiocarbon dating, in order to assess the infill of the incised valley and to establish whether correlation over hundreds to thousands of metres is possible. This work also aims to build on the surface and 1 m core studies by Wooldridge *et al.* (2018).

The total thickness of the post-glacial sedimentary infill for Ravenglass Estuary is up to 9 m, close to the estuary mouth, thins to the east (landward) to between 4 m and 6 m in the cores (Figs 6, 7, 8 and 9). A total of nine facies were identified in the core and are illustrated in Fig. 4 and listed in Table 2.

Ravenglass Glacial Till Member (Seascale Glaciogenic Formation) (inner and outer estuary)

The Ravenglass Glacial Till Member (RGTM) underlies the majority of the Ravenglass estuary and is present in all cores except 18 and 27 (Figs 3 and 7). The till forms part of the Seascale Glaciogenic Formation (Merritt & Auton, 2000). The grey-brown, stiff, matrix-supported, silty clay represents the lowest part of the stratigraphy in many of the cores and also outcrops as knolls throughout the estuary. The till is poorly sorted and displays a chaotic structure with rare sedimentary and meta-sedimentary clasts and rare shell fragments. The till varies in thickness across the estuary based on core data (between 0.2 m and 1.0 m) and shows a sharp contact with the overlying facies. The distribution of glacial till within the valley is probably a product of the movement of meltwaters from the retreating and advancing ice-sheets to the north/north-west, that focused around the Esk and present-day foreshore (Delaney, 2003). It has been suggested that the tills are a result of proglacial lakes fed by glacial meltwaters during the Main-Late Devensian (MLD) (Merritt & Auton, 2000). The older, Late Devensian ('late glacial') set of tills, which occur sporadically around the Cumbrian coast, were formed during, and shortly after, retreat of MLD ice. The top of the RGTM represents the sequence boundary.

Table 2. Descriptions of Ravenglass Incised valley-fill facies associations (FA) including: thickness (m), texture and sedimentary structures, location and dominant sedimentary processes, relative sea-level and sequence boundaries.

Facies (FA1)	***Thickness (m)***	***Texture & Sedimentary Structures***	***Location & Processes***	***Sea-Level***
Ravenglass Glacial Till Member (RGTM)	0.15-1.0m	Grey to reddish in colour, very fine grained (0.063mm), very poorly sorted clay rich till. Commonly chaotic structure with some shell fragments and small clasts.	Inner, central and outer estuary. **Glacial to fluvial processes dominate**	Highstand?
Alluvial Gravels	0.10-1.0m	Gravel beds with mixed clasts of sandstone, volcanics and granite up to 7cm. Commonly shows sharp contact with Ravenglass Glacial Till Member.	Outer to inner estuary**. Alluvial processes dominate**	Lowstand to Transgressive. Base of gravels represents sequence boundary.
Brown-Black Peats	0.10-1.3m	Black to dark brown in colour, laminated and well consolidated. Commonly shows sharp contact with Ravenglass Glacial Till Member.	Inner estuary, central basin and tidal inlet. **Lowland raised bogs – limited fluvial processes.**	Transgressive Central basin shielded.
Inner Straight Tidal-Fluvial		Fine (0.25-0.125mm) to medium (0.25mm) grained sands, poorly sorted at base with pebbles and moderately to well sorted upwards Flaser beds, silty laminae and clay drapes common. Proximal settings are finer grained with higher heterogeneity.	Inner estuary tidal channel. **Estuarine processes dominate.**	Transgressive to Highstand
Tidal Sand Bar	3.0-5.0m	Orangey brown, fine (0.25-0.125mm) to medium (0.25-0.35mm) grained sandstones, moderate to well sorted with small disarticulated shell frags. Sands are commonly massive, structures limited to clay drapes no thicker than 10cm. Overall sands fine upwards.	Inner estuary tidal channel. **Estuarine processes dominate.**	Highstand
Tidal Meander	1.7-3.5m	Very fine (0.125mm) to medium (0.25mm) grained sands and silts. Commonly interbedded, heterogenous	Inner estuary. **Estuarine processes dominate.**	Highstand to Falling

		and finer in proximal settings. Commonly fines upwards.		

Table 2: Continued.

Salt & Fresh Marsh	0.30-1.9m	Light brown, very fine to fine (0.065-0.125mm) grained laminated silts, poorly sorted and commonly rooted in top 10cm. Overall, fining upwards grain size trend.	Inner estuary, representing the preferential deposition of fine-grained material in an inter-tidal environment. **Estuarine Processes dominate.**	Highstand to Falling
Upper Flow Regime Sands	Up to 1.2m	Fine to medium grained (0.125-0.25mm), well sorted sands, bioturbation near central basin channel.	Foreshore and backshore. **Marine processes dominate on foreshore and estuarine on backshore.**	Highstand to Falling
Aeolian Dunes	Up to 5.5m	Light brown, med (0.25mm) to coarse (0.5mm) grained, moderate to well sorted sands. Small pebbles present with charcoal fragments.	Foreshore and backshore. **Marine wave action & longshore drift forming spit. Wind processes dominate.**	HSST-FSST

Alluvial gravel and coarse sands

The gravel and coarse sands (cores 1, 3, 12, 27, 28 and 31; Figs 6, 7 and 9) commonly overlie the RGTM and vary in thickness (0.6 to 3.0 m). The gravels and coarse sands can be correlated over distances of 0.5 km in the outer estuary (Fig. 9). The clasts range from 3 to 7 cm in size, are angular to sub-angular and are sedimentary, meta-sedimentary and igneous, suggesting that the source is predominantly from the catchment area. Poor sorting, angularity and the absence of shell fragments suggest that the gravels are of fluvial–alluvial origin. Radiocarbon dating was not possible due to the absence of shells and peat. The occurrence of gravel beds beneath the estuarine deposits implies that a fluvial–alluvial system extended *ca* 15 to 20 km further west (seaward) than the present-day coastline. Merritt & Auton (2000) have suggested a relative sea-level fall of -30 m below ordnance datum at *ca* 10,200 yrs BP which could have resulted in the deposition of the gravels. The base of the fluvial gravels represents the sequence boundary within the valley.

Estuarine brown-black peats

Brown-black peat (cores 12, 18, 19, 20, 29 and 32; Figs 6, 8 and 9) is rich in indistinct, probably deciduous, leaves and other woody plant material and is likely terrestrial in origin. It also contains some silt and is well-consolidated. Peat thickness varies across the estuary between 0.1 m and 1.3 m (Figs 7, 8 and 9). Peat occurs directly on top of the glacial till at sites where fluvial–alluvial gravel and coarse sands are absent. In the inner estuary, the peats can be correlated over distances of 0.5 km but are commonly laterally discontinuous. This facies typically displays a sharp contact with the overlying

estuarine sands and underlying till or gravel and is mostly concentrated in the central basin and in the Esk channel.

As shown by the radiocarbon dating, the peat beds are the oldest Holocene sediments from the valley-fill that can be dated, since the underlying fluvial-alluvial gravels do not contain organic matter and shells. The peats are between 8,094 ± 32 and 9,309 ± 38 BP in age and conform to the Holocene transgression (Fig. 2; Table 1).

Considering their variable distribution, location between channels and contact with the fluvial deposits below, the peats represent the first deposits of the valley during the Holocene transgression. The transition from glacial–fluvial deposits below the peats, indicates that some areas of the valley were in isolated and sheltered locations of poorly drained topographical depressions (between palaeo-channels).

Salt and fresh marsh

Salt and fresh marsh sediment is present in cores 1, 3, 7, 8 and 10 (Fig. 6). Commonly distributed throughout the inner estuary and estuary limits, the marsh-related sediment is typically composed of planar laminated, poorly sorted, very fine silts and clays with vegetated tops, in the form of roots. Marsh thickness varies across the estuary from 0.25 to 2.0 m, with the thickest deposits at the proximal channel margins (Fig. 6), where they are continuously correlatable over 3.2 km.

Salt and fresh marsh commonly represent the final stages of the levelling of marine coastal plains and the presence of marsh above the meanders and sand bars in cores 1, 3, 7, 8 and 10 implies a phase of abandonment as rivers have migrated. Salt and fresh marsh sediment is either linked to transgression or regression; here the stratigraphic context leads to the interpretation that the salt and fresh marsh sediment represents falling sea level (regression).

Sand-dominated sediments

The sand-dominated sediment has been subdivided into a variety of sub-facies from geographic and stratigraphic positions, based on grain size, sorting, sedimentary structures, presence of shell and peat fragments, and presence of minor silt and mud laminae. Five sand-rich facies have been identified for the Ravenglass valley fill: tidal–fluvial deposits, tidal sand bar deposits, tidal meander deposits, outer estuary–shoreface deposits and dune deposits.

Tidal–fluvial channel sands

The tidal–fluvial sand facies (present in all cores except 28; Figs. 6, 7, 8 and 9) are present in most cores and throughout the estuary. They represent a landward thinning wedge of sandy estuarine sediment that, in terms of measured thicknesses in core (0.2 to 6.3 m), makes up less than a third of the Holocene valley-fill. The facies are composed of fine-medium (0.125 to 0.25 mm) grained sands with shell debris at the base and higher concentrations of silty-mud laminae in the inner estuary. This sandy facies commonly fines upwards, for example in cores 7, 8, 10 and 12. Pebbles and clay drapes are common at the base in the inner estuary sands and reworked peat clasts are common, particularly in the Irt channel and outer estuary. With a radiocarbon age of 7,848 ± 40-6,827 ± 31 yrs BP, they represent the first estuarine sands within the valley.

The presence of tidally-influenced fluvial sands above the RGTM, suggests that these facies were the first estuarine sand to be deposited within the valley during transgression. Thus, the tidally influenced fluvial sands were deposited as aggrading, transgressive to highstand-facies which onlap the lowstand fluvial deposits during landward migration of the shoreline. The shelly material (dominated by disarticulated bivalves) mixed with the tidal–fluvial sand implies that the sand possibly had a dominant marine source that was reworked by tidal currents, also suggested by Bousher (1999).

Tidal sand bars within tidal channels

The tidal sand bar facies (cores 7, 8, 12, 25 and 26; Figs 6, 8 and 9) are present above the RGTM and peat beds and are deposited along the sinuous section of the Rivers Esk and Irt. Tidal sand bar facies are composed of fine to medium (0.125 to 0.35 mm) grained sands, that are moderately to well-sorted with horizons of small, disarticulated shell debris. The tidal sand bars can be correlated up to 0.5 km in the tidal channels. Pebble beds with shell debris are common at the base and clay drapes are preferentially observed towards the top. Overall, the facies show a significant fining upward profile, at the multi-metre scale, from pebbly gravel, through medium grained sand capped with laminated silt and mud that is typically vegetated after abandonment.

The deposition of the sand bars symbolizes the time when sea-level stabilized, with the development of channel banks. The disarticulated shelly and pebble surfaces most likely reflect internal erosion and migration surfaces within the bar.

Tidal meander (inner estuary)

Tidal meander sediments (cores 1, 3, 10, 18, 19 and 20; Figs 6, 7 and 8), are restricted to the most proximal environments and are composed of planar to slightly inclined lamination, alternating very fine to medium (0.125 to 0.250 mm) grained sand and silt. Flaser bedding occurs in the mid to upper sections of the facies with localized clay drapes. Silt interbeds are common in most proximal settings and they are capped with root-rich fresh marsh. The heterolithic, silt-rich strata are indicative of floodplain development associated with a meandering river system; these facies are restricted to the top 3 m of upper estuary cores because it only developed once sediment had been stabilized by vegetation. The tidal meander sediments can be correlated 1.4 km downstream in the inner estuary.

Tidal sand-flat (outer estuary to upper wave-dominated shoreface)

The outer estuary zones represented by the foreshore, tidal inlet and backshore sediments are medium grained (0.25 mm), well sorted sands and show rippled to planar laminations; they are interpreted to represent tidal flats (cores 27, 28, 29, 30 and 31; Fig. 9). This type of sediment is currently present in the foreshore beach and main tidal channel bank sediments and can be correlated up to 1 km over the foreshore. Close to the main tidal channel, the sands form superimposed low-amplitude dunes that are constantly remobilized by tidal currents. Therefore, in the cores, these relatively coarse grained, rippled to planar laminated sediments are interpreted to result from the progradation of sands at, or on either side of, the mouth of the tidal inlet.

It is noteworthy that there is an absence of well-developed tidal bars in the main tidal channel of the modern Ravenglass Estuary; this is due to the relatively limited modern supply of sand-rich sediment from the rivers and the constant remobilization by tidal currents. The restricted sand-supply and constant remobilization probably lasted throughout the Holocene and resulted in limited occurrence of tidal bars in the sediment cores. The tidal inlet itself lacks modern accommodation for the development of well-developed bars (Fig. 1B).

Aeolian dunes (barrier spits to outer estuary)

The aeolian deposits (core 28; Fig. 9) are composed of medium to coarse grained (0.25 to 0.5 mm), moderate to well-sorted sands, with small pebbles and charcoal fragments (*ca* 3 cm) which are common throughout. The aeolian facies only occurs in the top five metres of one core, on the current Drigg Spit; the base of the aeolian deposits occurs after 3,910 ± 24 yr BP (Fig. 9; Table 2). The modern vegetated aeolian dunes, known as the Drigg Spit to the north-west and Eskmeal Spit to the south-east, separate the foreshore and the backshore, here defined as sand-rich shore to the main part of the inner estuary. The dune deposits subsequently constrict the tidal inlet.

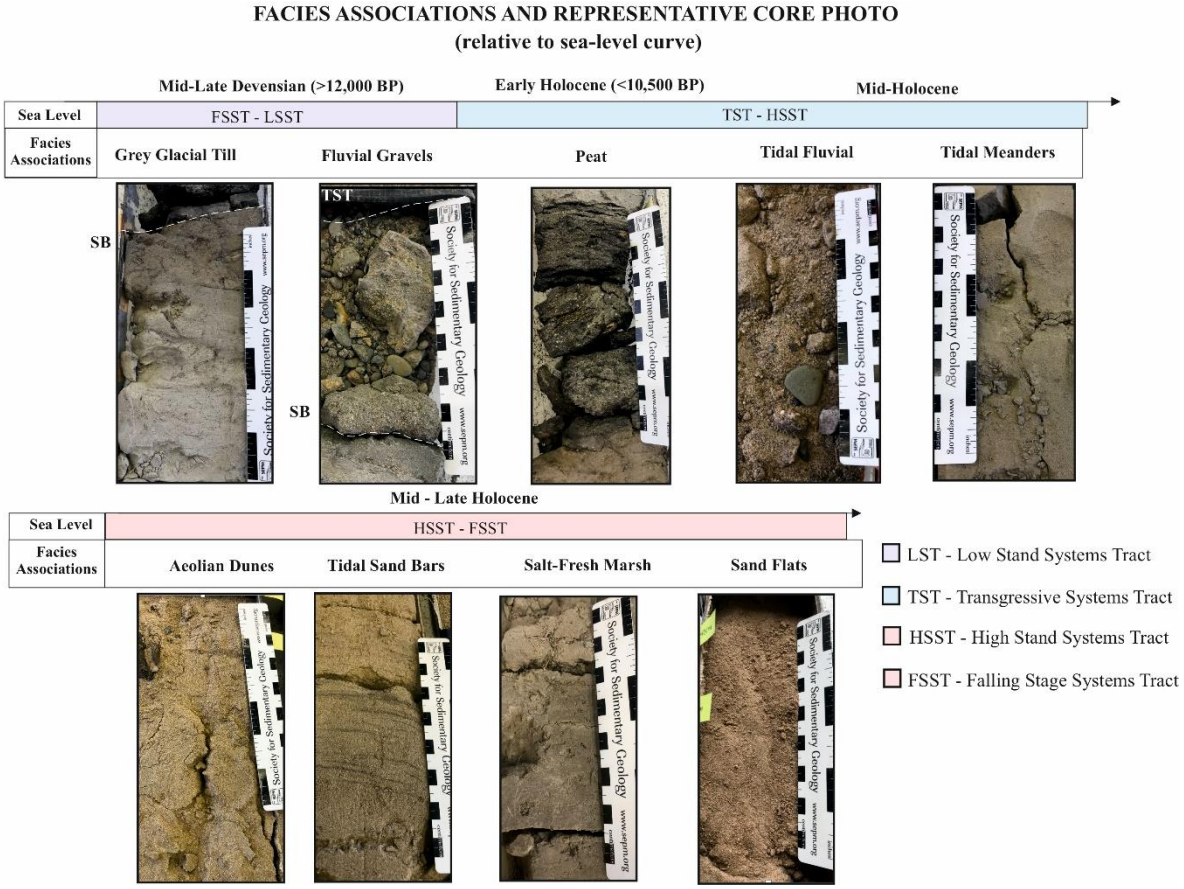

Figure 5: Facies associations (FA) and representative core photograph. From left to right (top to bottom): The Devensian RGTM, a grey diamicton till that is a poorly sorted with a chaotic internal structure. The fluvial gravels composed of gravel grade material and coarse sand. The laminated black to brown coloured peat is composed of leafy organic material. The tidal fluvial sands are composed of medium to coarse-grained sand with pebbles and disarticulated shell fragments. The aeolian dunes are composed of fine to medium-grained cross-bedded sands. The tidal meanders are fine to medium-grained, interbedded muds and sands that fine upward. The tidal sand bars show an overall fining upward profile from coarse-grained sands to interbedded muds and sand. Vegetated tidal sand bars are commonly capped with salt or fresh marsh. The marsh is composed of interbedded silt and mud

which is often moderately bioturbated and roots are present near the top. The sand flats are fine-grained with some disarticulated shell fragments.

Discussion

Controls on facies organization

The controls on facies organization of incised valley-fills are a function of the balance between sea-level rise and sediment supply, coupled with incised valley area and hydrodynamics (Garrison & Bergh, 2006; Davis & Dalrymple, 2010; Virolle *et al.*, 2019, 2020). The dominant controls on the Holocene facies expression and organization of the Ravenglass valley-fill mostly conform to those outlined in the wave to tide-dominated estuarine models by Allen & Posamentier (1993) and Dalrymple *et al.* (1992). Differences to these idealized models are expected due to local variations in estuarine settings, relative sea-level, climate, tectonics and scale. The Ravenglass valley owes its existence to the Devensian lowstand, and its fill to Holocene transgression and highstand. A complete fill through the valley (>9 m) shows that the sequence boundary is characterized by a gravel lag cutting through pre-existing till deposits. In the outer estuary (Fig. 2) the gravels are followed by coarse grained, cross-bedded sands that generally coarsen upward with some rare heterolithic bedding in the form of clay drapes (Fig. 9, cores 27, 29, 30. In the inner estuary (Fig. 2) the sands fine upwards into rhythmic heterolithic bedding and are commonly capped by marsh (Fig. 6, cores 1, 3, 7, 8 and 10) The aeolian dunes are not considered as part of the fill due to their low preservation potential. The evolution of this filled and associated hydrodynamics are discussed below.

Process-based classification of Ravenglass Incised Valley

The present-day surface of the Ravenglass valley-fill generally shows the typical tripartite zonation of facies with coarse sandy barrier spits/inlet, weakly developed central basin tidal (mud) flats and the common presence of sand bars towards the head of the estuary in the tidal inlet and the Irt and Esk arms systems (Fig. 1); this zonation is normally indicative of wave dominated systems (Dalrymple *et al.*, 1992). The central basin of Ravenglass estuary is weakly developed as it is limited to the extensive mud and mixed tidal flats that have been deposited around the confluence zone of the Rivers Irt and Mite. In terms of timing, these mud and mixed mud flats are fairly recent, dating *ca* 813 ± 20 yrs BP in the River Irt (Fig. 8). The deposition and expansion of the mud and mixed flats is also likely attributed to the development of the turbidity maximum at the point of river confluence, a zone containing higher proportions of suspended sediment (Geyer, 1993; Sanford *et al.*, 2001; Jalón-Rojas *et al.*, 2015). Inhibition of sediment transport via flood currents can also promote extensive central basin muds to form, such as the muds present in the funnel of the Gironde Estuary in south-west France (Allen & Posamentier, 1993; Wells, 1995; Virolle *et al.*, 2019, 2020). However, along the axis of the estuary (Fig. 10), grain size tends to increase seaward and decrease landward, suggesting that, throughout the valley fill, the flood currents promoted fluvial sediment transport rather than inhibited it.

The overall fill of Ravenglass can be categorized as a mixed tide/wave dominated system since the onset of the Holocene to the present day. Ravenglass estuary possesses some morphological features like that of wave-dominated estuaries, such as barrier spits and a central basin; however, a strong tidal signature of the facies prevails. The presence of the tidal inlet, tidal sand bars and tidal flats within the system (Figs 1B, 6, 7, 8 and 9) and the lack of a well-developed muddy central basin or bayhead delta, strongly support the interpretation of tide-dominance with wave influence. During the initial filling of the valley, tidal range was potentially limited compared to the >7 m present-day macro-tidal range, and fluvial and wave action were stronger. The reduced tidal range at the start of estuary filling is

supported by the presence of the wave-influenced coarse-grained cross-bedded sands above the sequence boundary in the outer estuary (Fig. 9, cores 27, 28 and 29). In the outer estuary, the sands above the sequence boundary show some evidence of tidal influence suggesting the tidal channels have always been restricted from wave action (Fig. 6, cores 1, 3 and 10). As the Drigg and Eskmeal spits were migrating to the south-east and north-west, ultimately narrowing the inlet, wave penetration within the valley was likely decreasing and tidal range increasing. This is evident from the transition of the wave-influenced coarse-grained sands to the medium grained clay draped sands present in cores 27, 29 and 31 at around -3 m OD (Fig. 9) and the development of sand flats above. Based on the coastal processes classification scheme by Ainsworth *et al.* (2011), Ravenglass valley was initiated as a dominantly fluvial system that dissected the coastal plain with the deposition of the gravels (cores 1, 3, 12, 27, 28 and 31; Figs 6, 7 and 9). Landward migration of the shoreline due to rising sea-level (Fig. 2) and the formation and migration of the Drigg and Eskmeal barrier spits (Fig. 9, core 28) represents a transition from a fluvial-dominated to wave-dominated system with secondary tide and fluvial influence. Possibly during and after the formation of the barrier spits and tidal inlet, tidal processes became dominant, resulting in extensive estuarine mud flats in the outer estuary (Figs 7 and 8, cores 18, 19, 20, 25 and 26) and sand flats within the inner estuary (Fig. 9, cores 27, 28, 30 and 31).

Throughout the Holocene, valley filling processes have been somewhat segregated, in that wave dominated processes have controlled deposition in the foreshore and tidal processes have dominated in the tidal inlet and tidal channels. The progradation of the present-day tidal inlet is likely to cut stratigraphically deeper and be less susceptible to later transgressive ravinements. This could lead to wave processes being under-represented in the sedimentary record since the tidal inlet is preferentially preserved. The majority of the valley fill of Ravenglass commenced at the end of the Holocene transgression (Fig. 1B) and tidal ravinement could have also contributed to the lack of wave-dominated facies present in the Ravenglass estuary cores (Fig. 9, cores 27, 28 and 29).

Correlation and architectural elements

The lateral and vertical distribution of the different facies identified from the core logs have here been correlated relative to the RGTM as it occurs throughout most of the inner and outer estuary (Figs 6, 7, 8 and 9). Overall, the architecture of the Ravenglass valley fill, above the sequence boundary, is expressed as a landward thinning wedge of sandy estuarine sediments. Correlation within the Ravenglass estuarine sediment is discussed below and shown in Figs 6, 7, 8 and 9.

Inner Estuary to River Esk

The Esk channel shows the most complete section of stratigraphy through the cores. The outer estuarine Esk channel correlation is represented by a set of cores along the channel, from core 3 and 1 (north-east, most upstream) to 7, 8, 10, 12 and 29 (south-west, most downstream) (Fig. 6), covering a distance of 2.5 km. The channel is composed of a distal meandering river system which becomes wider seaward. All the sediment cores are underlain by the correlatable RGTM which is overlain by fluvial gravel beds, with the exception of cores where the fluvial tidal sands directly overlay the RGTM (for example, in cores 7 and 8, Fig. 6). The lack of fluvial gravel beds in cores 7 and 8 suggests that the channel thalweg was not present here during the lowstand incision phase. The gravels are thickest in the most upstream, meandering section of the outer estuary (cores 1 and 3) and generally thin downstream (core 10, Fig. 6). The thick fluvial gravel, that accumulated during lowstand in the proximal floodplain, suggests that the River Esk was wider than it is today and appears to show no

time lag between progradation of the shelf during lowstand and upstream fluvial aggradation (Cattaneo & Steel, 2003). Fluvial gravel in core 1, drilled in the modern-day floodplain, is 25 cm thick while in core 3, only 185 m away, the fluvial gravel is 3 m thick (Fig. 6). The difference in the thickness of the fluvial gravel from the two cores from the tidal meander (cores 1 and 3; Figs 1 and 6) emphasizes the heterogeneity that can occur over short distances.

Tidal sand bars, up to 5 m thick, have accumulated in the straighter parts of the Esk channel and have good internal correlation over 500 m (cores 7 and 8, Fig. 6). However, sand bar facies cannot be correlated with cores 1.8 km upstream (cores 1 and 3).

Salt and fresh marsh now occurs and can be correlated in all cores in the upper Esk channel (cores 1, 3, 7, 8 and 10; Fig. 6) along the channel banks and caps abandoned channels and vegetated bars.

The River Irt and central basin

The River Irt is shown by two north-west – south-east correlation panels, the first highlights cores 22, 23, 25 and 26 (Figs 7 and 8) over 1.45 km. The RGTM is only penetrated in core 25 on panel 1 (Fig. 7) and is immediately overlain by a tidal sand bar (cores 25 and 26) (Fig. 1) that fine upwards to mud. The sands show reworked peat clasts implying erosion of pre-existing peat beds nearby. There are thick mud beds at the base of cores 22 and 23 which are overlain by tidal fluvial sands with rare clay drapes and flaser bedding. Tidal sand-flats, mixed-flats and mud-flats developed through time indicating the abandonment and reactivation of the River Irt palaeo-channel. The cores of the River Irt and central basin also show no gravel above the limited RGTM indicating that this was possibly a location near the top of the valley walls or interfluves. It is possible that the RGTM and gravels exist deeper in the palaeovalley of the River Irt (Fig. 2) but the boreholes never penetrated the thalweg of the palaeovalley. Lack of peat beds and shell fragments limited the potential for dating of these cores.

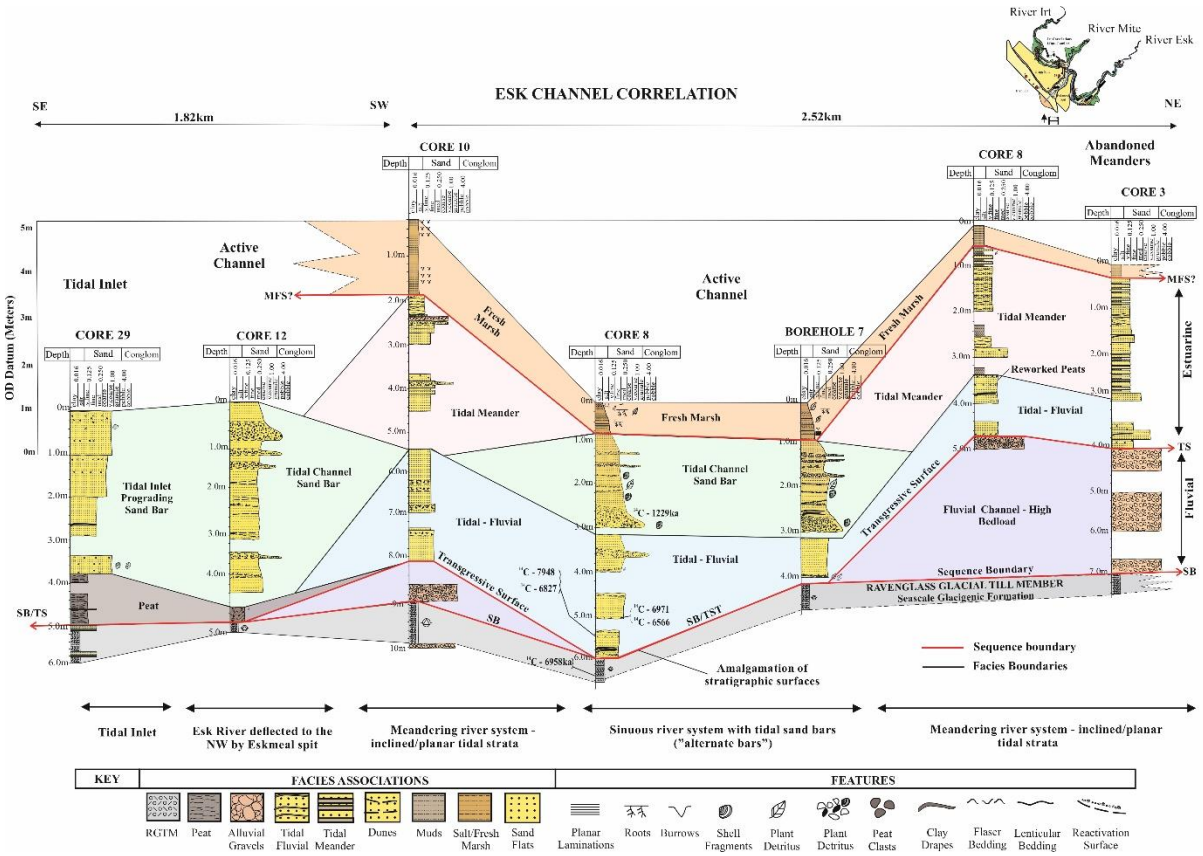

Figure 6: River Esk correlation panel from the Devensian to present-day highlighting inner estuarine facies and sequence stratigraphic boundaries marked by the dashed black lines. The red dashed lines highlight uncertainties in the correlation, especially associated with the tidal meander sediments. Also highlighted is the meandering–sinuous meander nature of the sediment with channel tidal bars (alternate bars) and upstream point-bars, indicative of tide dominated systems.

The second correlation panel of the Irt River arm covers a distance of 0.6 km and (Fig. 8) is shown by cores 18, 19 and 20, located in the active channel, and core 32, located in the floodplain (Fig. 1B). The underlying RGTM and the transgressive peat beds are overlain by tidal fluvial sands. The lack of gravel beds here suggests that the channel thalweg did not incise this location during sea-level fall. As the tidal–fluvial sands were the first estuarine sediment deposits above the peat and till and the coarsest of all sediment in these cores, most likely reflect the migration of the River Irt and ultimately the confluence of all three rivers. The ^{14}C date in the peat in core 18 is 8,094± 32 yrs BP, which implies the migration occurred after this. However, the subsequent sedimentation in the form of mixed-flats and mud-flats is much younger (*ca* 634 ± 26 yrs BP). The sequence of dates suggests that the recent formation of muddy estuarine deposits (*ca* 634 ± 26 yrs BP) was limited to mud and silt grade material, which is possibly a result of barrier spit formation and dampening of wave action that promoted the recent development of a newly developed central basin at the river confluence.

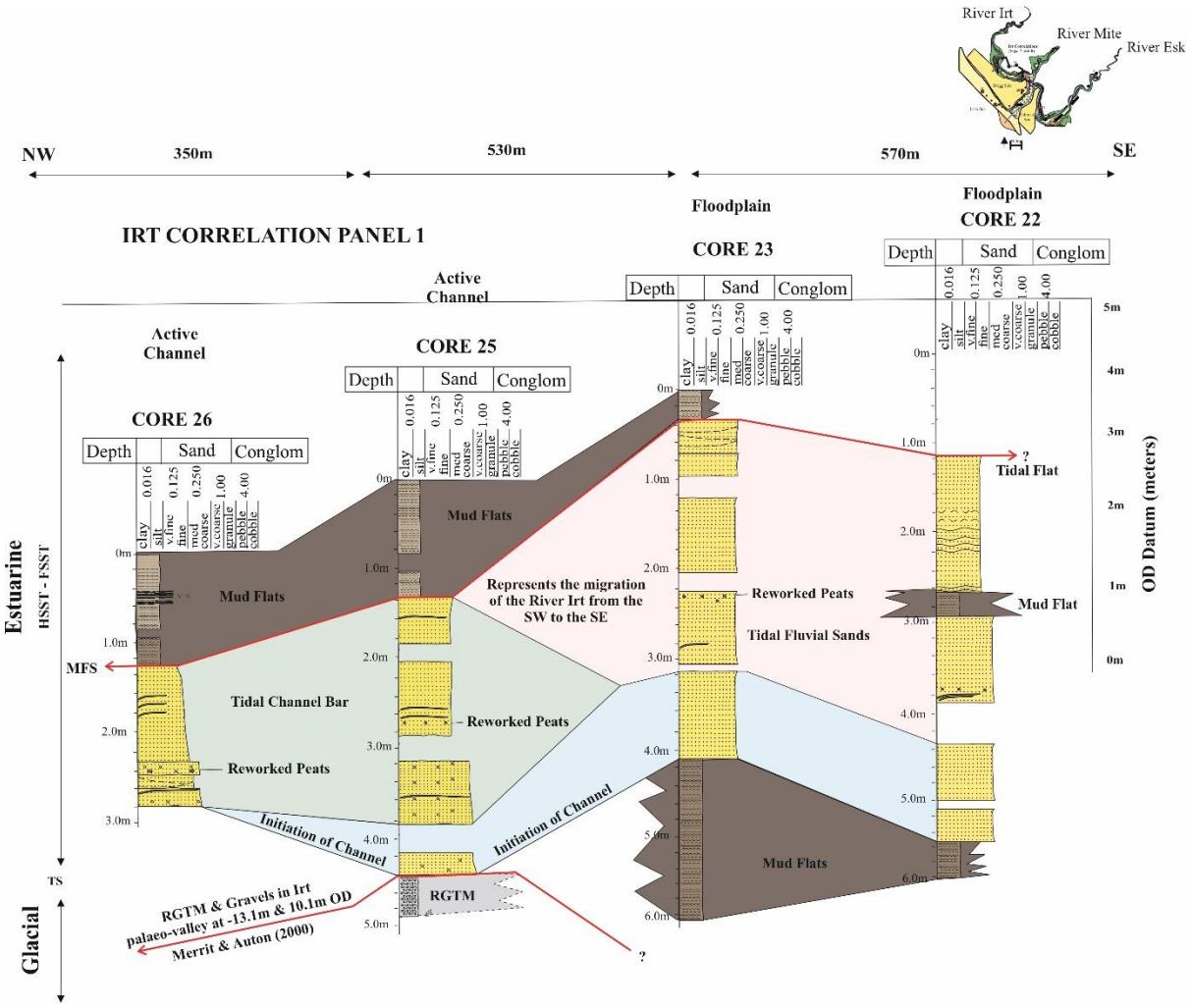

Figure 7: River Irt correlation panel 1. The River Irt panel shows the inner estuarine facies and sequence boundaries marked by the solid red lines. Note the lack of sequence boundaries with the exception of core 25 which has the RGTM. Above the RGTM are fluvial tidal bars between core 25 and 26, channel sands and mud flats in cores 22 and 23. The sequence boundary is located deeper in the Irt palaeo-channel at 13.1 m (OD) indicated by the red arrow (Merritt & Auton, 2000).

The recent development of tidal flats in the central basin also have been encouraged by the confluence of the three rivers. The correlation panels (Figs 7 and 8, cores 18, 19, 20, 25 and 26) show that, through the past *ca* 9,000 yrs BP, the central basin was located on a topographical high, near the valley wall, old palaeo-channels of the floodplain (cores 32, 22 and 23) are also present. The current channel shows the general sandy thalweg sands and off-channel mixed-flats to mud-flats through the surface deposition (Fig. 8, cores 18, 19 and 20).

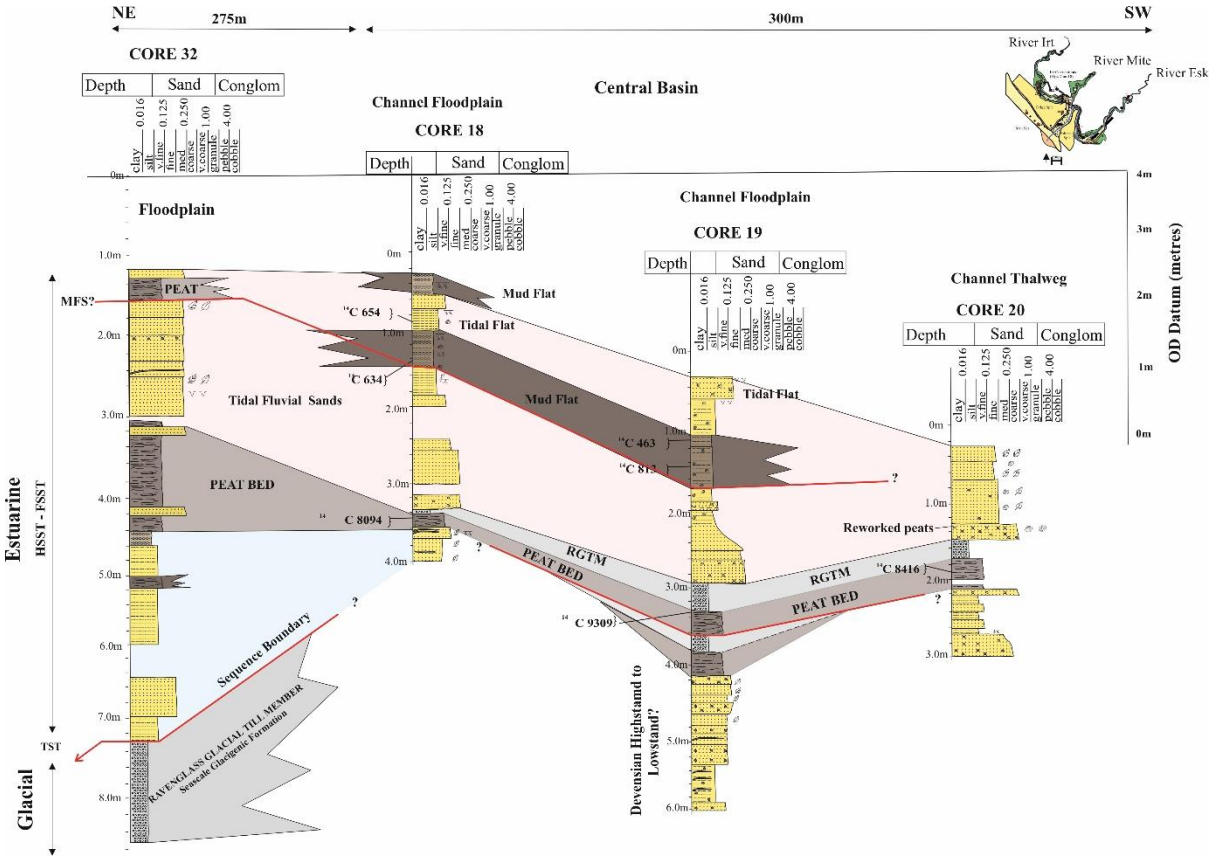

Figure 8: River Irt correlation panel 2. This panel indicates the River Irt and part of the central basin from the Devensian to present-day with sequence boundaries shown by a red solid line. The RGTM is partially correlatable between cores. The most abundant peat accumulations (14C 9309, 8416 and 8094 BP) and fine-grained sediment occur here, implying that it was a relatively sheltered area above the valley wall throughout most of the lowstand and Holocene transgression – also supported by the back of gravel beds above RGTM.

Outer estuary to foreshore, backshore and tidal inlet

The foreshore, backshore and tidal inlet are underlain by the RGTM and the gravel beds are limited to core 27 and core 28 (Fig. 9) which are interpreted to represent the River Esk palaeo-channel. The gravel beds are thought to be of fluvial origin as they are of a similar thickness to the gravel beds in the inner estuary meandering channel belt (Fig. 6, cores 1 and 3). Fluvial gravel beds are absent in cores 29, 30 and 31 for different reasons. Core 29 shows a sharp transition from the RGTM to peats, indicating that this was a sheltered depression along the Esk valley during sea-level rise. The RGTM in core 31 is immediately overlain by marine sands, potentially implying that a major Irt palaeo-channel existed here during the lowstand phase feeding a sand bar in core 31. This interpretation is supported by the mapped palaeo-river Irt in Fig. 3. The RGTM was deposited almost 4 m lower in core 31 compared to core 30, supporting the interpretation of a palaeo-channel in core 31 and a possible wave ravinement surface in core 30. The limited deposition of sand, and the presence of repeat gravel above the sand in core 30, may imply that this was an area of continued shoreface erosion during shoreline retreat. Wave action may have promoted a landward migration of gravels at this location. The presence of the peat bed and absence of gravels in core 29 above the RGTM (Fig. 9) also reveals that no major channel existed here until the Esk channel migrated as a result of the formation of the barrier spits. Core 30 shows very little in the way of correlation with core 31 over a distance of 0.5 km and their sediment bodies are quite different in both volume and character. The absence of the thicker

tidal sand bodies in core 30 suggests that this could have been a wave ravinement surface that progressively moved landward during shoreface retreat. The ravinement surface may have reworked previous deposits and surfaces such as the transgressive systems tract, therefore the wave ravinement surface may also become amalgamated with the sequence boundary. Evidence in the form of reworked peat clasts (Figs 7, 8 and 9) also suggests extensive reworking of peat beds during this time as channels migrated.

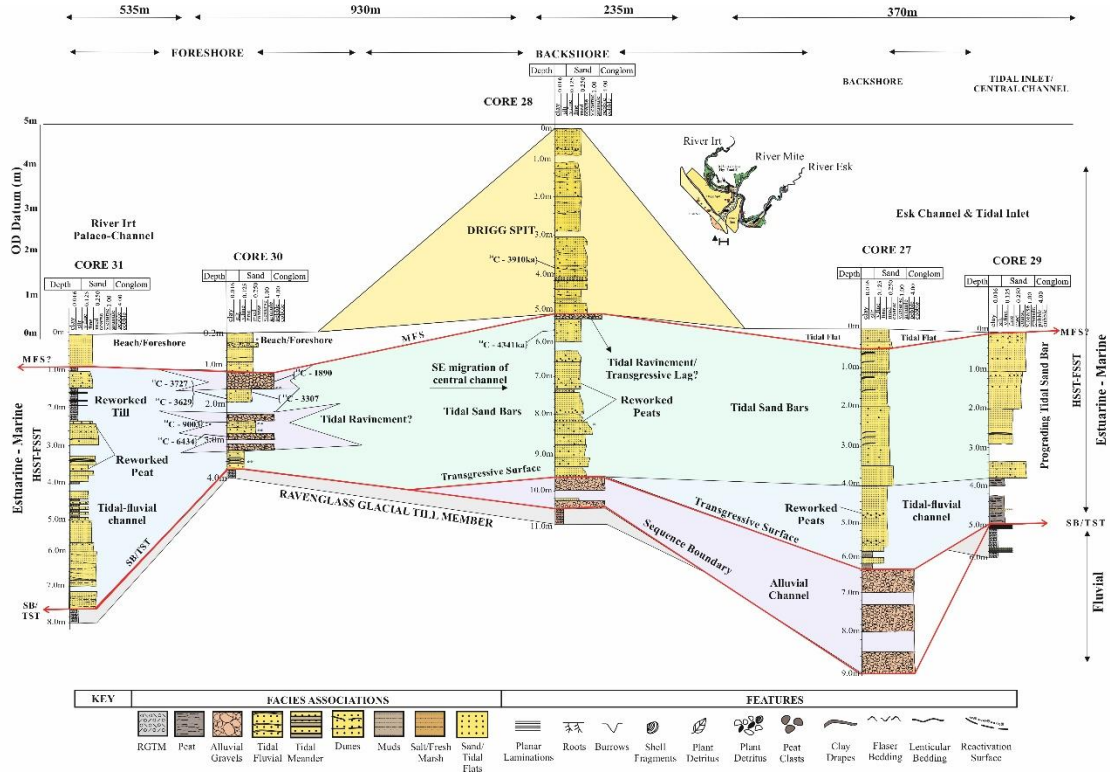

Figure 9: The foreshore and tidal inlet correlation panel highlighting the outer estuarine facies and sequence stratigraphic surfaces shown by the solid red line. The sequence boundary here becomes amalgamated with the transgressive surface near the valley highs shown by core 30 (potentially a point of tidal ravinement). Core 31 indicates the sequence boundary going deeper into the River Irt palaeo-channel also shown in the first River Irt correlation panel. Reworked peats are also limited to the Irt palaeo-channels. Cores 28 and 29 are in the tidal inlet and show the prograding sand bars. Core 28 shows the evolution of the Drigg Spit.

Summary of lateral and vertical connectivity

Connectivity within the Ravenglass incised valley sediments is best in the channels that have remained relatively stable during the Holocene transgression. The River Esk panel (Fig. 6) indicates that the initial fluvial–tidal channel sands can be correlated over 2.5 km from the inner to the outer estuary and range in thickness from 1 to 3 m. Tidally influenced sand bars within the channels can be correlated over 0.5 km and range from 3 to 5 m in thickness (Fig. 6, cores 7 and 8), showing similar sediment character but varying thicknesses. 1.8 km upstream of the sand bars, correlation of the fluvial-tidal sands becomes difficult due to the extensive meandering of the tidal channels upstream. The increased heterogeneity upstream is common to all three rivers that feed the system.

Peat beds are extensive and thickest in the River Irt floodplain (Fig. 8), ranging from 1.2 m thick in core 32 to 0.2 m downstream in cores 18, 19 and 20 (Fig. 8). Not all the peat beds can be correlated. The tidally-influenced fluvial sands, ranging from 0.8 to 1.5 m in thickness, may be correlated up to 1.4 km

between cores 22, 23, 25 and 32 (Figs 7 and 8). The tidally influenced fluvial sands thin towards the active Irt channel to 1.5 m (Figs 7 and 8) and are not present in cores 18, 19 and 20, located in the active floodplain. A tidally influenced sand bar ranging from 1.6 m to 2.6 m can be correlated *ca* 0.2 km along the River Irt (Fig. 7, cores 25 and 26) thinning downstream into tidal flats (Figs 8, 18, 19 and 20). The sand bar is capped with 1.3 m of muds that also thin to 0.5 m downstream towards the channel floodplain (Figs 7 and 8, cores 22, 23, 18 and 19). The lack of gravels and limited deposition of the RGTM within the cores suggests that the channel thalweg was never penetrated making correlation is more difficult.

In the outer estuary, the thickest (6 m) tidal fluvial sands are represented by the palaeo-Irt in core 31 and show little correlation with core 30, located 0.5 km to the south-east (Fig. 9). The sand bars within the tidal inlet show excellent correlation both laterally and vertically. The tidal sand bars range in thickness from 3.5 to 4.4 m and can be correlated over lengths of *ca* 1.5 km.

Synthesis of valley creation and fill

A synthesis of the Ravenglass valley creation, classification and fill throughout the Holocene to present is demonstrated in Fig. 10 and is summarized below.

According to existing estuary classification schemes (Boyd *et al.*, 2011; Dalrymple *et al.*, 1992; Davis & Dalrymple, 2010), the Ravenglass incised valley-fill is categorized as a small, macro-tidal, mixed wave to tide-dominated system that initially resulted from coastal plain incision and subsequent transgression. The incision cut through pre-existing glacial stratigraphy (Busby & Merritt, 1999). The creation of the Ravenglass incised valley occurred during the Late Devensian Period (17,000 to 12,000 yrs BP), attributed to changes in relative sea-level linked to glacio-isostacy (Figs 2 and 8A). When the maximum period of sea-level fall was reached between *ca* 12,000-10,500 yrs BP, the present-day coastline was exposed and incised by the Rivers Irt, Esk and Mite (Fig. 8A). According to modelled sea-level curves for the Ravenglass area, the period of incision lasted for 6,500 yrs, between *ca* 18,000 to 11,500 yrs BP (Lloyd *et al.*, 2013). During this initial phase of valley development, the proto-Drigg and Eskmeal sand spits must have been developing, suggesting a dominant role for wave activity over tidal or fluvial action. Despite the differences in the scale of estuaries, the duration of the Ravenglass incision period is broadly similar to those reported for the Holocene Gironde incised valley, which had an incision period of 8,000 yrs (Allen & Posamentier, 1993) and the Holocene Qiantang River estuary, which had an incision period of *ca* 5,000 yrs BP (Zhang *et al.*, 2014).

The presence of basal gravel beds (Figs 6 and 9) implies that the Early Holocene palaeo-Rivers Esk and Irt had a higher energy than the present-day rivers and a bedload that was capable of cutting through the shelf and forming the Ravenglass valley complex. The post-glacial vegetation may have also favoured rivers carrying gravels and glacial outwash (Kasse *et al.*, 2005). A straighter profile for the palaeo-Rivers Esk, Irt and Mite has been previously proposed by the Halcrow Group (2013). The Irt followed a roughly straight trajectory until at least 410 yrs BP, as evidenced by a historical map by John Speed, published in the year 1610 (Speed, 1610). By 1794, the River Irt had deviated from the south-west to north-east, following the present-day shoreline and merged with the River Mite (Cary, 1794). At present, there is no published historical map evidence for when the Esk deviated to the north but the absence of fluvial gravels in core 12 (Fig. 6) proves that the deviation happened long after the main Holocene incision phase. The peat bed towards the base of core 12, implies that no fluvial deposition occurred in this sheltered location and that the River Esk did not migrate into the central basin until after the transgressive peat had been deposited.

The deeper parts of cores 18, 19, 20 and 32 (Fig. 8) are dominated by peat with negligible sandy sediment. This suggests that the palaeo-River Irt feeding this area, the present-day central basin, had low flow volume and minimal bedload. The absence of fluvial gravel, repetition of peat beds and the young stratigraphic age of the sediment in the central basin (> 813 ± 20 yrs BP, cores 18, 19 and 20) can be used to infer that the River Irt, with its greater flow volume and presumably greater bed load, did not deviate its course to the south and merge with the diminutive River Mite 226 yrs ago.

There seems to be no evidence in the map of the depth to glacial till (Fig. 3) for an initial straight path for the Early Holocene palaeo-River Esk. The northward migration of the southern Eskmeals spit was probably responsible for the northward deviation of the larger River Esk and its subsequent merger with the smaller River Mite. The capture of the River Esk by the River Mite presumably contributed to the accumulation of the tidal–fluvial sands and the prograding tidal sands and muds in the upper parts of cores 18, 19 and 20 (Fig. 8).

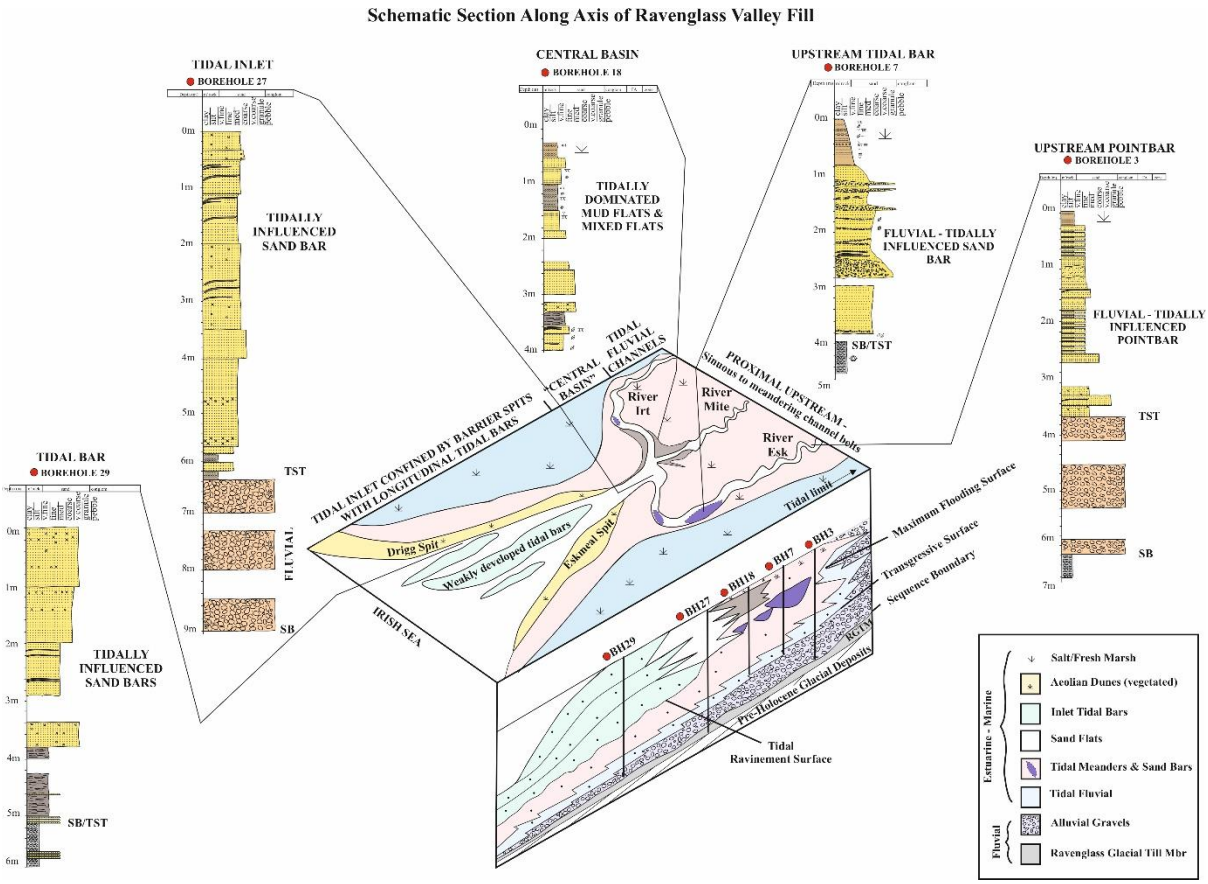

Figure 10: Schematic stratigraphic section along the axis of the Ravenglass incised valley fill with representative cores and facies distributions. The facies distributions are a result of an initial lowstand represented by the fluvial gravels, marking the sequence boundary. The valley underwent rapid landward migration of the shoreline and deposition was limited to the tidal fluvial channel sands. During highstand the system started prograding and most of the filling occurred in the form of tidal meanders, tidal sand bars, mudflats and mixed flats. Along the axis of the estuary, grain size tends to increase seaward (core 29) and decrease landward (cores 1 and 3).

Stratigraphic surfaces of Ravenglass Incised Valley

The stratigraphic organization and relative stratigraphic surfaces within the Ravenglass incised valley fill are shown in Fig. 10 and discussed below.

Sequence Boundary and Lowstand Systems Tracts – Gravels (LST)

The marine lowstand (12,000 to 10,500 yr BP) of the Late Devensian into the early Holocene (Fig. 2) is categorized as a time when isostatic rebound outstripped sea-level rise (Lloyd *et al.*, 2013; Merritt & Auton, 2000) (Figs 10 and 11A). In the Ravenglass valley, this stratigraphic surface is expressed by the fluvial–alluvial gravels and coarse sands, the base of which marks the sequence boundary with the RGTM. The fluvial gravels and sands have a high preservation potential due to the subsequent rapid onlapping of the transgressive estuarine sediments. During lowstand, sediment was bypassed through the valley and was most likely deposited seaward (west) of the present-day coastline. The rapid lowstand and transgression that the Ravenglass Valley underwent, prior to and into the Holocene, limited the amount of time possible for fluvial aggradation. The gravel beds are thicker in the outer than in the inner estuary (Figs 6 to 9) because the palaeo-valleys, on the glacial till surface (Fig. 3), were steeper than the present-day valleys. This resulted in high energy palaeo-rivers capable of carrying gravel further downstream.

Transgressive Systems Tract – Peat and Estuarine Tidal–Fluvial Sands (TST)

During transgression, after the deposition of the till and gravel, the incised valley was inundated (Figs 10 and 11B). This resulted in an accumulation of peat beds in sheltered areas between the main channels, and estuarine tidal–fluvial sands within the tidal channels. The base of the transgressive surface separates the lower fluvial gravels and coarse sands with estuarine peats, sands and muds (Figs 6 to 9). In the inner estuarine zone, the surface is well defined particularly along the palaeo-river Esk, however, in contrast, in the River Irt, central basin and outer estuarine zones, the transgressive surface becomes amalgamated with the sequence boundary along the palaeo-valley walls. Contrary to other Holocene estuaries, that typically show large-scale transgressive deposits (Martinsen, 1994; Hori *et al.*, 2001; Wilson *et al.*, 2007; Chaumillon *et al.*, 2010b), the Ravenglass estuary demonstrates that most of the backfill began at the end of transgression when maximum accommodation was achieved. Deposition continued into, and throughout, the highstand and falling stage systems tract. The limited accumulation of transgressive deposits within the Ravenglass valley-fill are most likely a result of the rapid transgression and coastal flooding, during which the rate of sea-level rise outpaced sediment supply. The rapid transgression limited the thickness of the aggrading, onlapping sediment within the valley during the landward migration of the coastline, evident in the Esk channel profile (Fig. 6).

Highstand Systems Tract (HSST) – Tidal Bar Channel Sands, Tidal Meanders, Central Basin Muds and Prograding Tidal Sand Bars

Post-glacial sea-level within the Ravenglass coastal area is estimated to have reached its peak of +2 m OD around 6,000 yrs BP (Lloyd *et al.*, 2013) and has fallen since (Figs 10 and 11C to E). At this peak stage of sea-level rise, accommodation within the valley achieved its maximum point (Figs 10, 11C and 11D). Consequently, infilling of the system mostly occurred during this time, and into, the sea-level regression (Figs 10, 11D and 11E). After 6,000 yrs BP, the falling sea-level formed a seaward-prograding, tide-dominated system consisting of meandering point bars with alternate sand bars, sand-flats, mud-flats, gravels and a small, restricted, muddy central basin with a prograding tidal inlet.

Due to the nature of progradation during the highstand-into-regression, the top of the highstand surface is downlapping onto the transgressive estuarine wedge (Figs 6 and 9). During this time of infilling, the upper estuary tidal limit migrated downstream, promoting fluvial gravel to gradually work its way downstream. This is prominent on the banks of the present day Esk Channel.

Reservoir implications

Ravenglass Estuary is a good analogue for assessing simple tide-dominated incised valley-fill models in terms of stratigraphic organization with the opportunity to analyse a single fill (corresponding to a single sea-level cycle). Although the present day Ravenglass Estuary appears to be mud-rich, the cores (Figs 6 to 9) show that majority of the infill is very much sand-dominated. The presence of sand above the sequence boundary implies that, the majority of the coarse-grained sand filling the tidal channels and inlet, is of marine origin. As previously mentioned, this is supported by the presence of shelly detritus hosted in medium to coarse-grained sands. Tidal processes have been dominant since the onset of transgression as double clay drapes are recorded in the first sand deposits after the sequence boundary in core 8 (Fig. 6) along the Esk channel. This study is a rare modern analogue of a sandy, tide-dominated estuary. Discussed below is the significance of the Ravenglass sedimentary system for building models of sand/mud ratios, grain size and sand body connectivity in subsurface reservoirs.

Sand/mud ratio and grain size

Based on the evidence from 19 Holocene sediment cores, the Ravenglass Estuary-fill is dominated by sand. It should be noted that this interpretation is based on the 19 cores acquired however parts of the subsurface remain unsampled. Although, the localised sand/mud ratio varies from upstream to downstream, sandy deposits typically represent 75% of all cores, the remainder being peat (5%), gravel (10%) and mud (10%) (Figs 6 to 9). The upstream meandering portions of the tidal channel system contain greater proportions of interbedded finer grained sand and mud compared to the cleaner, coarser grained sands in the downstream, sinuous portions of the channels (Figs 5 to 7). The downstream coarser sands lack well developed mud beds and have accumulated as thick, continuous sands with rare mud drapes (Figs 6 and 9).

The most abundant mud deposition occurred along the River Irt and within the central basin (Figs 7 and 8), which was a result of the backfilling of the River Irt valley and migration to the south-east to merge with the Rivers Mite and Esk. The confluence of all three rivers (Fig. 11D and E) allowed for the recent development of the classical tripartite zonation of facies (Boyd *et al.*, 2011; Dalrymple & Zaitlin, 1992); inner estuarine medium-coarse grained sandy tidal channels, mud-rich central basin and marine influenced sands at the estuary mouth.

The sand/mud ratio is highest within the marine-influenced tidal inlet and foreshore (Fig. 9). The tidal inlet hosts large incipient tidal bars (Fig. 11E) with limited mud quantities (Fig. 9) due to the remobilization of bar sediment by the ebb and flood tides. The sand/mud ratio in foreshore sediments is similar to the modern tidal inlet and lacks mud deposition. This lack of mud in the foreshore and tidal inlet can be attributed to the high energy shoreline processes remobilizing the sediment and lack of slack water within the tidal inlet.

Connectivity

By analogy to the subsurface, the connectivity of sand is heterogenous across the estuarine system but, as the estuary is sand-dominated, most of the sediment looks as if it has good connectivity. The Esk arm of the estuary represents good reservoir in terms of connectivity (Fig. 5). Tidal fluvial sands and tidally-influenced sand bars (cores 7, 8, 10, 12 and 29) are well connected up to 5.2 km through the river course. The tidal sand bars show varying thickness across the estuary between 4 to 6 m. The Esk system becomes less sandy upstream, promoting reservoir compartmentalization due to the presence of extensive mud and interfluves (cores 1 and 3). Even under the Saltcoats mudflats, in the River Irt cores 32, 18, 19 and 20 (Figs 1B and 7) have thin (30 to 150 cm) correlatable, sand-dominated deposits which become coarser grained towards the thalweg over 1.5 km. The outer Esk, typifying outer estuarine deposits, represents excellent connectivity (cores 27, 28 and 29; Figs 6 and 9) of sandy sediments ranging from 4 to 6 m . The connectivity of palaeo-Esk and Mite sands is excellent due to the interpretation that the flow path has been stable for about 10,000 yrs (Fig. 11A to E).

In contrast to the Esk-Mite system, the palaeo-Irt looks as if it has limited sand connectivity with the palaeo-Esk, as shown by tidal-ravinement deposits in core 30 (Fig. 9) and the palaeotopography map which reveals a high between the River Irt and Esk on the present-day foreshore and in the central basin (Fig. 3). The connectivity of palaeo-Irt and palaeo-Esk-Mite sands is limited due to the recent (between 410 to 226 yrs BP) merging of the Irt with the Esk-Mite channels (Fig. 11D and E). These observations indicate that channel migration can happen in a short time period (*ca* 10 ka), resulting in complicated reservoir architecture.

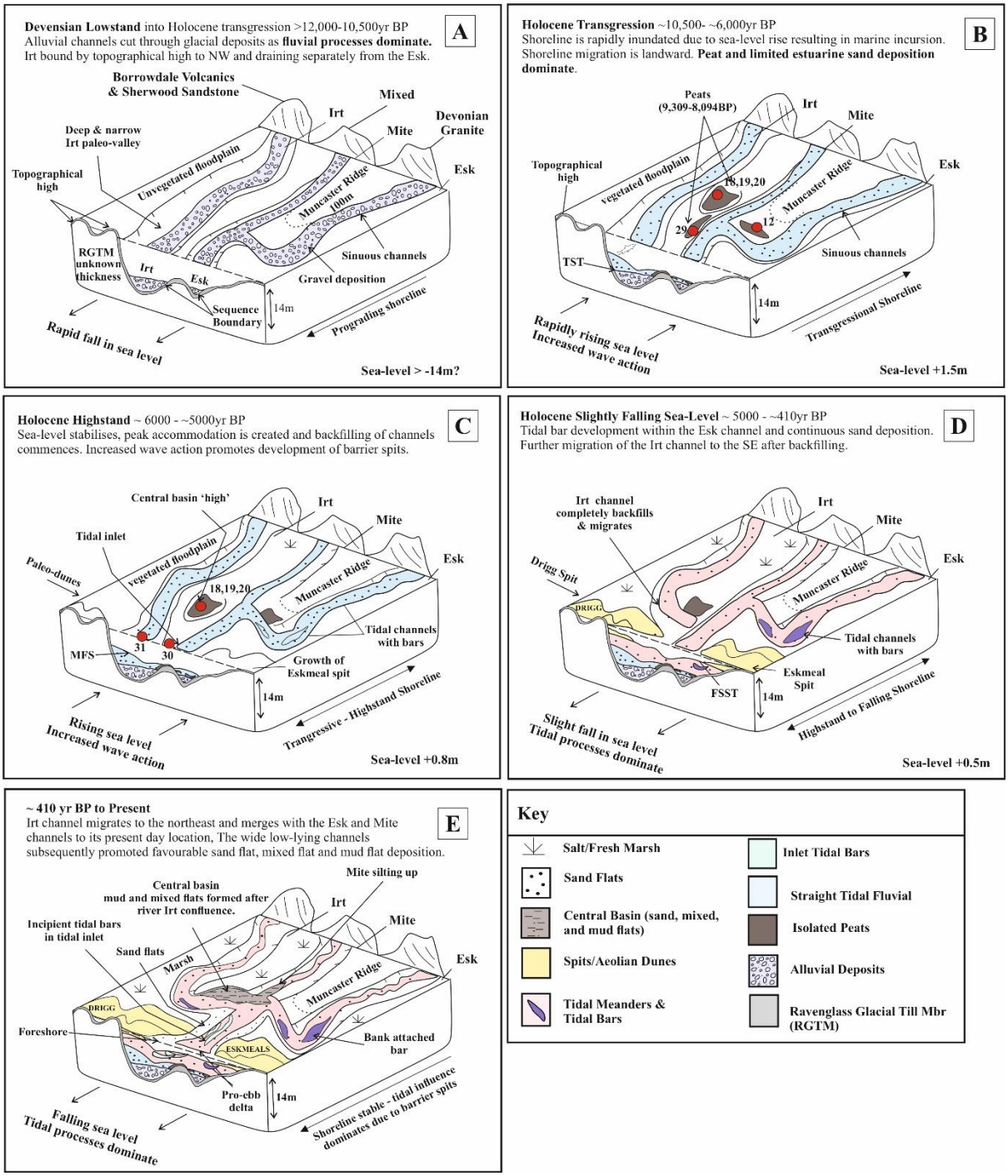

Figure 11: Morphological evolution and corresponding facies of Ravenglass Incised Valley since of onset and throughout the Holocene transgression. (A) Incision on the newly exposed post-glacial shelf during the Devensian lowstand (12 000 yrs BP) by a series of sinuous rivers depositing gravel and coarse sands. (B) Holocene transgression which began around 10 500 BP and continued to around 6000 BP. The initial flooding and landward migration of the shelf promoted peat bed deposition in sheltered areas between the sandy tidal channels. (C) The Holocene Highstand (6000 to 50 000 yrs BP) was a time of sea-level stabilization when peak accommodation is reached and backfilling of the valleys occurs. The palaeo-Drigg Spit began migrating to the south-east. (D) Sea level begins to fall from 5000 yrs BP to around 410 yrs BP and the migration of the Drigg Spit and backfilling of the River Irt forced migration to the south east. Tidal sand bars and meandering channel belts accumulated in the River Esk. (E) The River Irt migrates to the north-east and joins the Rivers Mite and Esk. The now

backfilled, wide and shallow channels have promoted favourable estuarine conditions resulting in the development of the muddy central basin.

Synthesis

This study of the Ravenglass incised valley, post-glacial fill provides a practical means of highlighting the facies distributions and stratigraphic differences of glacio-induced estuaries of macro-tidal, tide-dominated settings. This paper has revealed the characteristics of the estuary that have developed in the palaeo-Ravenglass incised valley during the last transgression. This has been achieved using 19 cores drilled into the Holocene estuarine sediment, and sediment facies analysis, sediment distribution and high-resolution ^{14}C ages.

It is proposed here that Ravenglass valley formed and subsequently filled in five identifiable stages:

1. The Devensian glacial lowstand, when isostatic rebound outstripped sea-level rise, between 12,000 to 10,500 yrs BP (Fig. 2). This promoted shelf incision represented by the fluvial–alluvial gravel overlying the Ravenglass Glacial Till Member (Figs 10 and 11A). Fluvial processes were dominant and net sediment was bypassed to the lowstand shelf. During this time there was a basinward shift in facies (Figs. 2, 10, 11a) .

2. The Early Holocene rapid transgression, which was characterized by a phase of relative sea-level rise, occurring between *ca* 10,500 to 6,000 yrs BP (Fig. 2). During this time, net sediment transport was landward with transgressive sediments onlapping alluvial gravels or the Ravenglass Glacial Till Member where the gravels were not present (Figs 10 and 11B). This resulted in estuarine deposition, with peats initially forming on locally isolated highs, between channels, and the transitional fluvial–estuarine sands subsequently filling the deepest part of the valleys. During this time, it is here suggested that much of the sand supplied to the estuary was of marine origin due to the presence of shelly debris. Sea-level rapidly outpaced sediment supply, limiting the amount of time for the transgressive estuarine deposits to form. The transgressive deposits are therefore relatively thin. As the first transgressive deposits are sandy, it implies a reasonable amount of sand was available on the shelf to be reworked into the valley by tidal currents.

3. The Holocene highstand, which occurred as sea-level stabilized, and accommodation reached its maximum point at around 6,000 to 5,000 yrs BP (Figs 10 and 11C). Back-filling of the Irt and Esk valleys continued at this time. The stabilizing of sea-level and dominant wave-action may have promoted the growth of the palaeo-Drigg and Eskmeals Spits. Despite increased wave action, tidal signatures were still prevalent in the estuarine sediment since the onset of deposition. The spits demonstrate that wave-dominated elements can play an important role in the evolution of tide-dominated systems.

4. A minor fall in relative sea level from 5,000 yrs BP to the present day, resulting in the estuarine system filling and prograding (Figs 10 and 11D). In-channel tidal bars started to build in the downstream tidal channels, upstream meanders prograded and the system stepped seaward. Radiocarbon dating suggests that most of the fill occurred during the highstand to falling stage systems tract, highlighting that not all estuarine sedimentation corresponds to the transgressive phase.

5. Complete backfill of the Irt and Esk channels is the final stage (*ca* 410 to 226 yrs BP, Fig. 11E). This was possibly coincident with the southward migration of the Drigg spit which closed off the mouth River Irt which thus forced the merging of the Irt with the Rivers Mite and Esk to adopt the present-day morphology.

These stages of evolution within the Ravenglass incised valley system have resulted in a particular facies organization not widely discussed in the literature. The stratigraphic relationships and facies models (Figs 6 to 9) enable the construction of a detailed depositional model of the Ravenglass incised valley-fill.

The results of this study can be used to interpret the development of several other, mixed energy macrotidal estuaries in the stratigraphic rock record, that may also correspond to late transgressive – highstand conditions. It may also be used to predict reservoir architecture, lateral and vertical connectivity and sand quality within such a system.

The work presented here can be used to predict connectivity and sand-quality within incised valley-fill sediments. The Esk–Mite system has very good connectivity and sand quality, largely due to the stability of the flow path of the rivers. The Irt, in contrast, is poorly connected to the Esk–Mite system because of the relatively recent southward deflection of the flow path and consequent merging of the rivers. Sand–mud ratios decrease upstream in both the Irt and Esk estuarine fills. The coarsest and cleanest sands are found in the tidal inlet and on the foreshore.

References

Ainsworth, R.B., Vakarelov, B.K. and Nanson, R.A. (2011) Dynamic spatial and temporal prediction of changes in depositional processes on clastic shorelines: Toward improved subsurface uncertainty reduction and management. *AAPG Bulletin*, 95, 267–297.

Allen, G.P. and H. W. Posamentier (1993) Sequence Stratigraphy and Facies Model of an Incised Valley Fill: The Gironde Estuary, France. *SEPM Journal of Sedimentary Research*, Vol. 63, 378–391.

Assinder, D.J., Kelly, M. and Aston, S.R. (1985) Tidal variations in dissolved and particulate phase radionuclide activities in the Esk estuary, England, and their distribution coefficients and particulate activity fractions. *Journal of Environmental Radioactivity*, 2, 1–22.

Bonsall, C., Sutherland, D., Tipping, R. and Cherry, J. (1989) The Eskmeals Project: late Mesolithic settlement and environment in north-west England. *The Mesolithic in Europe*, 175–205.

Bousher, A. (1999) Ravenglass Estuary: Basic characteristics and evaluation of restoration options. *RESTRAT Technical Deliverable TD*, 12.

Boyd Ron, Robert W. Dalrymple, K.C. and Zaitlin, B.A. (2011) Estuarine and Incised-Valley Facies Models. 171–235 pp.

Busby, J.P. and Merritt, J.W. (1999) Quaternary deformation mapping with ground penetrating radar. *Journal of Applied Geophysics*, 41, 75–91.

Cattaneo, A. and Steel, R.J. (2003) Transgressive deposits: A review of their variability. *Earth-Science Reviews*, 62, 187–228.

Chaumillon, E., Tessier, B. and Reynaud, J.-Y. (2010a) Stratigraphic records and variability of incised valleys and estuaries along French coasts. *Bulletin de la Société Géologique de France*, 181, 75–85.

Chaumillon, E., Tessier, B. and Reynaud, J.Y. (2010b) Stratigraphic records and variability of Incised valleys and estuaries along French coasts. *Bulletin de la Societe Geologique de France*, 181, 75–85.

Clare, T., Clapham, A.J., Wilkinson, D.M. and Haworth, E.Y. (2001) The Mesolithic and Neolithic landscapes of Barfield Tarn and Eskmeals in the English Lake District: some new evidence from two different wetland contexts. *Journal of Wetland Archaeology*, 1, 83–105.

Coast, D. and Area, S. (2015) Drigg Coast SAC , Ravenglass Estuary Intertidal Survey.

Dalrymple, R.W., Canada, O.K.L. and Zaitlin, B.A. (1992a) Estuarine Facies Models: Conceptual Basis and Stratigraphic Implications: PERSPECTIVE. *Journal of Sedimentary Petrology*, 62, 1130–1146.

Dalrymple, R.W. and Zaitlin, B.A. (1994) High-resolution sequence stratigraphy of a complex, incised valley succession, Cobequid Bay — Salmon River estuary, Bay of Fundy, Canada. *Sedimentology*, 41, 1069–1091.

Dalrymple, R.W., Zaitlin, B.A. and Boyd, R. (1992b) Estuarine facies models; conceptual basis and stratigraphic implications. *Journal of Sedimentary Research*, 62, 1130–1146.

Davis, R.A. and Dalrymple, R.W. (2010) Principles of tidal sedimentology. 1–621 pp.

Delaney, C. (2003) The last glacial stage (the Devensian) in northwest England. *North West geography*, 3, 27–37.

Fenies, H. and Tastet, J.P. (1998) Facies and architecture of an estuarine tidal bar (the Trompeloup bar, Gironde Estuary, SW France). *Marine Geology*, 150, 149–169.

Garrison, J.R. and Bergh, T.C.V. Van Den (2006) Effects of sedimentation rate, rate of relative rise in sea level, and duration of sea-level cycle on the filling of incised valleys: examples of filled and "overfilled" incised valleys from the upper Ferron Sandstone, Last Chance Delta, east-central Utah. 239–279 pp.

Geyer, W.R. (1993) The importance of suppression of turbulence by stratification on the estuarine turbidity maximum. *Estuaries*, 16, 113–125.

Griffiths, J., Worden, R.H., Wooldridge, L.J., Utley, J.E.P. and Duller, R.A. (2018) Detrital Clay Coats, Clay Minerals, and Pyrite: A Modern Shallow-Core Analogue For Ancient and Deeply Buried Estuarine Sandstones. *Journal of Sedimentary Research*, 88, 1205–1237.

Griffiths, J., Worden, R.H., Wooldridge, L.J., Utley, J.E.P., Duller, R.A. and Edge, R.L. (2019) Estuarine clay mineral distribution: Modern analogue for ancient sandstone reservoir quality prediction. *Sedimentology*, 66, 2011–2047.

Halcrow Group (2013) Ravenglass Estuary Complex Sefton Council.

Hampson, G.J., Da Vies, S.J., Elliott, T., Flint, S.S. and Stollhofen, H. (1999) Incised valley fill sandstone bodies in Upper Carboniferous fluvio-deltaic strata: Recognition and reservoir characterization of Southern North Sea analogues. *Petroleum Geology Conference Proceedings*, 5, 771–788.

Heap, A.D., Bryce, S. and Ryan, D.A. (2004) Facies evolution of Holocene estuaries and deltas: A large-sample statistical study from Australia. *Sedimentary Geology*, 168, 1–17.

Hein, F.J. (2015) The Cretaceous McMurray oil sands, Alberta, Canada: A world-class, tidally influenced fluvial-estuarine system-An Alberta government perspective, 1st edn. *Elsevier B.V.*, 561–562 pp.

Hori, K., Saito, Y., Zhao, Q., Cheng, X., Wang, P., Sato, Y. and Li, C. (2001) Sedimentary facies of the tide-dominated paleo-Changjiang (Yangtze) estuary during the last transgression. *Marine Geology*, 177, 331–351.

Jalón-Rojas, I., Schmidt, S. and Sottolichio, A. (2015) Turbidity in the fluvial Gironde Estuary (southwest France) based on 10-year continuous monitoring: Sensitivity to hydrological conditions. *Hydrology and Earth System Sciences*, 19, 2805–2819.

Kasse, C., Hoek, W.Z., Bohncke, S.J.P., Konert, M., Weijers, J.W.H., Cassee, M.L. and van der Zee, R.M. (2005) Late Glacial fluvial response of the Niers-Rhine (western Germany) to climate and vegetation change. *Journal of Quaternary Science*, 20, 377–394.

Kelly, M., Emptage, M., Mudge, S., Bradshaw, K. and Hamilton-Taylor, J. (1991) The relationship between sediment and plutonium budgets in a small macrotidal estuary: Esk estuary, Cumbria, UK. *Journal of Environmental Radioactivity*, 13, 55–74.

Kershaw, P.J., Woodhead, D.S., Malcolm, S.J., Allington, D.J. and Lovett, M.B. (1990) A Sediment History of Sellafield Discharges. *Journal of Environmental Radioactivity*, 12, 201–241.

Lloyd, J.M., Zong, Y., Fish, P. and Innes, J.B. (2013) Holocene and Lateglacial relative sea-level change in north-west England: Implications for glacial isostatic adjustment models. *Journal of Quaternary Science*, 28, 59–70.

Martinsen, O.J. (1994) Evolution of an incised-valley fill, the Pine Ridge Sandstone of southeastern Wyoming, USA: systematic sedimentary response to relative sea-level change. *Incised Valley Systems: Origin and Sedimentary Sequences, SEPM Special Publication*, 109–128.

Meng, J., Holubnyak, Y., Hasiuk, F., Hollenbach, J. and Wreath, D. (2020) Geological characterization of the Patterson CO2 storage site from 3-D seismic data. *Midcontinent Geoscience*, 1, 52–90.

Menier, D., Tessier, B., Proust, J.N., Baltzer, A., Sorrel, P. and Traini, C. (2010) The Holocene transgression as recorded by incised-valley infilling in a rocky coast context with low sediment supply (southern Brittany, western france). *Bulletin de la Societe Geologique de France*, 181, 115–128.

Merritt, J.W. and Auton, C.A. (2000) An outline of the lithostratigraphy and depositional history of Quaternary deposits in the Sellafield district, west Cumbria. *Proceedings of the Yorkshire Geological Society*, 53, 129–154.

Royd, D.O. (2002) Chapter 19: The glaciation of the Lake District. *Geological Society Memoir*, 25, 255–269.

Salem, A.M., Ketzer, J.M., Morad, S., Rizk, R.R. and Al-Aasm, I.S. (2005) Diagenesis and Reservoir-Quality Evolution of Incised-Valley Sandstones: Evidence from the Abu Madi Gas Reservoirs (Upper Miocene), the Nile Delta Basin, Egypt. *Journal of Sedimentary Research*, 75, 572–584.

Sanford, L.P., Suttles, S.E. and Halka, J.P. (2001) Reconsidering the physics of the Chesapeake Bay estuarine turbidity maximum. *Estuaries*, 24, 655–669.

Simon, N., Worden, R.H., Muhammed, D.D., Utley, J.E.P., Verhagen, I.T.E., Griffiths, J. and Wooldridge, L.J. (2021) Sediment textural characteristics of the Ravenglass Estuary; Development of a method to predict palaeo sub-depositional environments from estuary core samples. *Sedimentary Geology*, 418, 105906.

Slatt, R.M. (2013) Fluvial deposits and reservoirs. 283–369 pp.

Tessier, B. (2012) Stratigraphy of Tide-Dominated Estuaries. In: *Principles of Tidal Sedimentology*, 2012, 109–128.

Virolle, M., Brigaud, B., Luby, S., Portier, E., Féniès, H., Bourillot, R., Patrier, P. and Beaufort, D. (2019) Influence of sedimentation and detrital clay grain coats on chloritized sandstone reservoir qualities: Insights from comparisons between ancient tidal heterolithic sandstones and a modern estuarine system. *Marine and Petroleum Geology*, 107, 163–184.

Virolle, M., Féniès, H., Brigaud, B., Bourillot, R., Portier, E., Patrier, P., Beaufort, D., Jalon-Rojas, I., Derriennic, H. and Miska, S. (2020) Facies associations, detrital clay grain coats and mineralogical characterization of the Gironde estuary tidal bars: A modern analogue for deeply buried estuarine sandstone reservoirs. *Marine and Petroleum Geology*, 114, 104225.

Wang, R., Colombera, L. and Mountney, N.P. (2019) Geological controls on the geometry of incised-valley fills: Insights from a global dataset of late-Quaternary examples. *Sedimentology*, 66, 2134–2168.

Wang, R., Colombera, L. and Mountney, N.P. (2020) Quantitative analysis of the stratigraphic architecture of incised-valley fills: A global comparison of Quaternary systems. *Earth-Science Reviews*, 200, 102988.

Wells, J.T. (1995) Chapter 6 Tide-dominated estuaries and tidal rivers. *Developments in Sedimentology*, 53, 179–205.

Willis, B.J. and Gabel, S. (2001) Sharp-based, tide-dominated deltas of the {Sego} {Sandstone}, {Book} {Cliffs}, {Utah}, {USA}. *Sedimentology*, 48, 479–506.

Wilson, K., Berryman, K., Cochran, U. and Little, T. (2007) A Holocene incised valley infill sequence developed on a tectonically active coast: Pakarae River, New Zealand. *Sedimentary Geology*, 197, 333–354.

Wooldridge, L.J., Worden, R.H., Griffiths, J., Thompson, A. and Chung, P. (2017a) Biofilm origin of clay-coated sand grains. *Geology*, 45, 875–878.

Wooldridge, L.J., Worden, R.H., Griffiths, J. and Utley, J.E.P. (2019) Clay-coat diversity in marginal marine sediments. *Sedimentology*, 66, 1118–1138.

Wooldridge, L.J., Worden, R.H., Griffiths, J. and Utley, J.E.P. (2017b) Clay-Coated Sand Grains In Petroleum Reservoirs: Understanding Their Distribution Via A Modern Analogue. *Journal of Sedimentary Research*, 87, 338–352.

Wooldridge, L.J., Worden, R.H., Griffiths, J., Utley, J.E.P. and Thompson, A. (2018) The origin of clay-coated sand grains and sediment heterogeneity in tidal flats. *Sedimentary Geology*, 373, 191–209.

Zaitlin, B.A., Dalrymple, R.W. and Boyd, R. (1994) The Stratigraphic Organization of Incised-Valley Systems Associated with Relative Sea-Level Change. Incised-Valley Systems: Origin and Sedimentary Sequences 51:0.

Zhang, X., Lin, C.M., Dalrymple, R.W., Gao, S. and Li, Y.L. (2014) Facies architecture and depositional model of a macrotidal incised-valley succession (Qiantang River estuary, eastern China), and differences from other macrotidal systems. *Bulletin of the Geological Society of America*, 126, 499–522.

Zong, Y. and Tooley, M.J. (1996) Holocene sea-level changes and crustal movements in Morecambe Bay, northwest England. *Journal of Quaternary Science*, 11, 43–58.

Sediment textural characteristics of the Ravenglass Estuary; Development of a method to predict palaeo sub-depositional environments from estuary core samples

N. Simon[a], R. H. Worden[a, *], D. D. Muhammed[2], J. E. P. Utley[a], I. T. E. Verhagen[a], J. Griffiths[a,b], L. Wooldridge[a,c].

a) School of Environmental Sciences, Liverpool University, L69 3BP, UK
b) BP Exploration, Chertsey Road, Sunbury-on-Thames, Middlesex, TW16 7LN, UK
c) BP Upstream Technology, Chertsey Road, Sunbury-on-Thames, Middlesex, TW16 7LN, UK

Abstract

Here we present a new way to automatically classify the exact sub-environment of deposition of sediment from estuarine sediment cores. It can be challenging to define the exact sub-environment of deposition in core as sediment of a given appearance, or facies, can be found in multiple settings. This issue is important given that petrophysical, geomechanical and reservoir quality properties of sedimentary rocks are typically strongly influenced by the specific sub-environment of deposition. Here, using a ten-fold classification of depositional sub-environments, we have determined the sub-environments of 482 sample sites from the Ravenglass Estuary, in NW England, UK. We then analysed the textural characteristics of each of these samples using laser particle size analysis. A novel automatic textural classification scheme was then developed using a combination of visual discrimination of gravel and vegetated surfaces, principal component analysis and recursive partitoning routine (RPART) in Rstudio. The new automatic textural classification scheme can resolve eight of the ten sub-environments of deposition: gravel beds, salt-marsh, mud flat, mixed flat, sand flat, tidal inlet, combined south foreshore/ebb tidal delta and combined tidal inlet/north foreshore. Our scheme cannot differentiate the spatially adjacent tidal inlet and north foreshore sediments as they are texturally identical. Similarly, the scheme cannot differentiate the spatially adjacent ebb tidal delta and southern foreshore sediments as they also are texturally identical. We have applied our surface-calibrated method to a 3 m Holocene core drilled through fine-grained surface sandflats into interbedded fine- and coarse-grained sands in the Ravenglass Estuary and successfully defined palaeo-environments of deposition. Our automatic approach to the definition of palaeo-environment of deposition approach supersedes a simple lithofacies-based approach for the Ravenglass Holocene core as we can define, cm-by-cm, how the exact estuarine sub-environments evolved over the last 10,000 years. This approach could also be applied to other modern estuaries and could be trialled for use with ancient and deeply buried sedimentary rocks deposited in equivalent marginal marine estuarine environment.

Introduction

Grain size is a fundamental property of sediments that affects sediment's entrainment, transport and deposition (Blott and Pye, 2001) and has a huge impact on sandstone petrophysical properties (Tiab and Donaldson, 2015). Using largely descriptive approaches based on core and outcrop, sedimentologists have, for many years, attempted to use a supervised learning approach and grain size variations to help determine sedimentary environments and the processes that were responsible for sediment deposition (Folk, 1966; Folk, 1968). However, grain size analysis of modern sediment has also been used to provide clues to the mode of transportation and the energy condition of the transporting medium; Table 2.1 lists numerous studies that have attempted to use textural characteristics to help establish overall environment of modern clastic sediments. For example, there have been attempts to use sediment textural characteristics to discriminate modern sedimentary environments such as beach, dune and river sands (Sevon, 1966), beach, coastal dune, inland dune, and fluvial sands (Moiola et al., 1974), beach, dune and aeolian environments (Biederman, 1962; Mason and Folk, 1958), dune, beach and river sands (Friedman, 1961). Greenwood (1969) used multivariate discriminant analysis on sediment properties (average grain size, sorting, skewness and kurtosis) to differentiate between wave lain sand and aeolian sand. Moiola and Spencer (1979) and Zubillaga and Edwards (2005) used discriminant analysis to differentiate between inland aeolian and coastal aeolian sands. Recently, there have been attempts to use modern data analysis approaches, such as principal component analysis (Flood et al., 2015), and data transforms (Purkait and Das Majumdar, 2014), to try to define statistically different depositional environments and facies from surface sediments and cores in modern environments. With several criteria available to discriminate environments of deposition and depositional processes, clastic sediment textural studies can provide evidence to help in the interpretation of clastic deposits of unknown origin (Visher, 1969). This approach provides the basis for the next step towards a truly genetic classification of sedimentary textures.

The petrographic characteristics of modern sands in their present environments can potentially be used to help determine depositional environment to interpret the genesis of ancient clastic deposits (Friedman, 1961). However, a possible problem in the analysis of grain size is that the same transport and depositional process can occur within a number of environments and the resulting textural response can be similar (Visher, 1969). To complicate things still further, sediment can be reworked and redeposited, there may post-depositional processes such as infiltration and there may be diagenetic processes (Worden and Burley, 2003) all of which may serve to obscure the relationship between depositional environment and sediment texture.

The ability to relate the textural characteristics of ancient sediments and sedimentary rocks to their specific sub-environment of deposition would be extremely useful in developing an understanding of sedimentary architecture. For example, interpretation of sedimentary sub-environment is the objective of core logging from oil and gas fields and sites planned for carbon capture and storage (Blackbourn, 2012). Assessment of the sum of a sediment's characteristics is used to design groups, known as facies, with a common set of attributes which are then assembled into facies associations that are, in turn, interpreted in terms of environment of deposition. By this approach, the interpretation of environment of deposition is indirect and sometimes struggles to result in interpretations of specific sub-environments. Areas of mixing in tidal-fluvial depositional environments, e.g., estuaries, present an interesting extra problem due to (1) multiple sources of sediment (2) the mobility of sediment and possible movement in and out of the estuary basin and (3)

the relative susceptibility to relative sea-level changes and the consequent rapid changes from fluvial to estuarine to marine, and the reverse (Dalrymple and Choi, 2007).

Table 1: Summary of previous work on discrimination of sedimentary environment from sediment textural characteristics.

Author and year	**Depositional environment**	**Method**	**Data interpretation method**
Flood et al., (2015)	Deltaic	LPSA	Compositional data analysis (CODA) associated with a multivariate statistical framework (PCA and Cluster analysis (CA))
Purkait and Majumdar, (2014)	Deltaic	Sieving	Log-normal, log-skew-Laplace and discriminant analysis
Kasper-Zubillaga and Carranza-Edwards, (2005)	Desert and coastal dunes	LPSA	Linear discriminant analysis and ANOVA
Friedman, (1979)	Beach, inland and nearshore dune sands	Sieving	Bivariate analysis
Moiola and Spencer, (1979)	Inland aeolian and coastal aeolian sands	Sieving	Discriminant analysis
Moiola, Spencer, and Weiser (1974)	Beach, coatal dune, inland dune, and river sands	Sieving	Discriminant analysis
Greenwood, (1969)	Marine and aeolian sands	Sieving	Linear discriminant analysis
Visher, (1969)	Coastal	Sieving	Log-prbability grain size distribution curves
Sevon, (1966)	Fluvial, beach and aeolian sands	Sieving	Discriminant analysis
Klovan (1966)	Coastal	Sieving	Factor analysis
Biederman, (1962)	Beach, dune, lagoon and marsh sediments	Sieving	Histogram and bivariate analysis
Friedman, (1962)	Beach from river sands	Sieving	Bivariate analysis and mathematical computation
Friedman, (1961)	Aeolian, beach and river sands	Sieving	Bivariate analysis
Shepard and Young, (1961)	Aeolian and beach sands	Sieving/microscope	Bivariate analysis
Mason and Folk, (1958)	Aeolian, beach and river sands	Sieving	Bivariate analysis
Keller, (1945)	Aeolian and beach	Sieving	Ratio

Here we have developed a supervised learning approach that relates specific categories of depositional sub-environments to quantitative textural attributes. We have produced a classification diagram that can take grain size, and other attributes, from any sediment from the Ravenglass Estuary and automatically define the exact sub-environment of deposition. To achieve this, we have mapped the Ravenglass Estuary to define depositional sub-environments, collected 482 surface sediment samples from the range of sub-environments and defined texture using laser particle size analysis. The Ravenglass Estuary was chosen for this study because of its accessibility, its macro-tidally (7.55 m) influenced environment, and the wide range of estuarine sub-environments. The aim was to study textural attributes of each estuarine sub-environment and to determine if there are statistically significant differences between sediments from the various sub-depositional environments. This categorical classification approach to the Ravenglass Estuary sediments has been applied to a Holocene core drilled into the Ravenglass Estuary but it might serve as aid for the discrimination of sub-environments in ancient and deeply buried estuarine sediments. This approach was developed as the majority of a suite of Holocene cores, drilled during the overarching research project, were sand-rich and lacked diagnostic sedimentary structures. Many of the cores simply had metre after metre of relatively bland sand that we struggled to relate to the top-surface depositional environments.

This study addresses the following research questions, focused on the estuarine sediments of the Ravenglass Estuary (Fig. 1):

1. What depositional sub-environments and ranges of grain size, and other textural characteristics are present within the Ravenglass Estuary?

2. What controls the distribution of grain size, and other textural characteristics, in estuarine settings?

3. Is it possible to develop a classification scheme to enable prediction of depositional environment from sediment textural attributes?

4. Can grain size characteristics from Holocene, or older, sediment cores be used to predict or discriminate palaeo-estuarine environments?

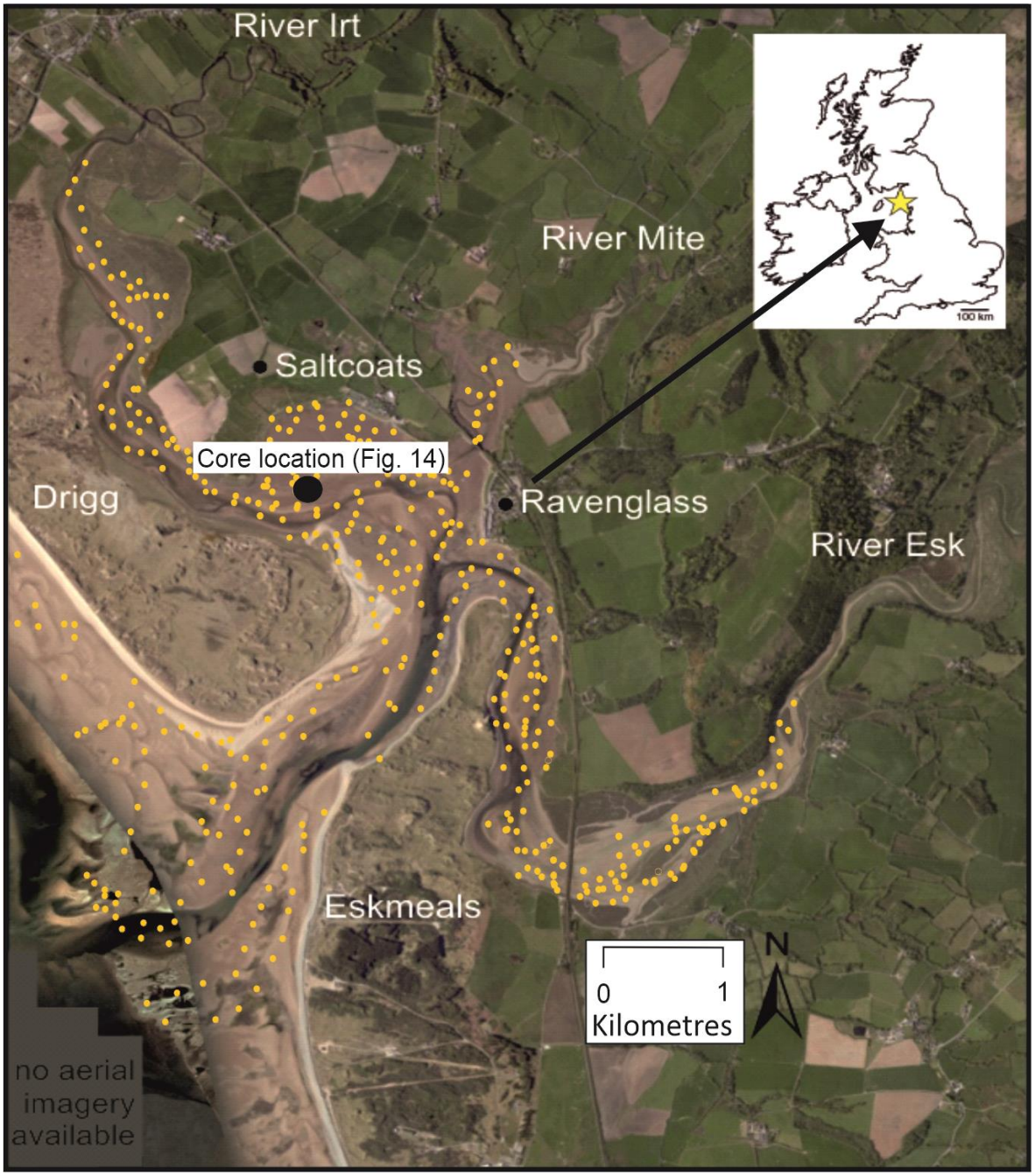

Figure 1: Location map of the Ravenglass Estuary, north-west England with inset map of location of estuary in the UK. Surface sediment (<2 cm) sample sites highlighted by yellow dots. The geotechnical core location (Figures 2.9 and 2.14) is also marked for reference.

Study Site: Ravenglass Estuary

The Ravenglass Estuary is on the west coast of Cumbria, in north west England, United Kingdom. The estuary covers an area of about 5.6 km^2 and is a macro-tidal environment, of which 86% is intertidal, with a maximum tidal range of about 7.55 m (Bousher, 1999; Griffiths et al., 2018a; Lloyd et al., 2013; Wooldridge et al., 2017b). Sediment in the Ravenglass Estuary is quartz-dominated but contains variable quantities of clay minerals (Daneshvar and Worden, 2018; Griffiths et al., 2019; Wooldridge et al., 2017b; Wooldridge et al., 2019; Wooldridge et al., 2018) and so the estuary may be a good

analogue for ancient and deeply buried sandstone petroleum reservoirs that contain chlorite-coated grains. For example, it may be an analogue for the tidally-influenced, shallow marine-deltaic Tilje Formation, Norway (Ehrenberg, 1993), the shallow marine to deltaic Lower Vicksburg Formation U.S.A. (Grigsby, 2001), and the braid-delta margin with foreshore and shoreface deposits of Garn Formation, Norway (Storvoll et al., 2002).

The Holocene sedimentary succession that has filled the Ravenglass Estuary sits on top of Devensian glacial till that is directly overlain either by peat beds or fluvial gravel beds. The glacial tills and the peat beds have distinctive clasts of the underlying bedrocks that have allowed lithostratigraphical divisions and ice-movement patterns to be discerned (Merritt and Auton, 2000). Changes in relative sea level during the Holocene were predominantly caused by glacio-eustatic sea-level change and spatially-variable glacio-isostatic crustal-rebound resulting from deglaciation (Lloyd et al., 2013; Merritt and Auton, 2000).

The Ravenglass Estuary has three rivers that feed the main estuary (Fig. 1): the Rivers Esk, Mite, and Irt. These rivers have average discharge rates of 4.2 m^3s^{-1} for the River Esk, 3.4 m^3s^{-1} for the River Irt, and 0.4 m^3s^{-1} for the River Mite (Bousher, 1999). In the lower Esk arm of the estuary (Fig. 2.1), the maximum discharge measured during the ebb tidal flow (estuary emptying) is slightly lower 4.99 m^3s^{-1} than the flood tidal flow (estuary filling) 5.41 m^3s^{-1}; the slightly lower ebb drainage was reported to be a result of the short length of the Ravenglass Estuary (Kelly et al., 1991).

The estuary is connected to the Irish Sea through a single, 500 m-wide tidal inlet (Fig. 1) that flows between two dune-topped barrier systems, the Drigg spit to the north and Eskmeals spit to the south (Wooldridge et al., 2017b). The estuary has previously been divided into discrete zones, which have been grouped into four categories based on the dominant physical processes active in each zone (Griffiths et al., 2018a; Griffiths et al., 2019) (and see Figs. 1 and 2): (1) the fluvial zones for the Esk, Mite, and Irt, which are freshwater dominated; (2) the brackish zones of the tide-dominated inner estuary parts of the Irt, Mite, and Esk; (3) the relatively mixed-energy (mainly tide- and wave-influenced) zone of the central basin with near-seawater salinity; and (4) the outer zone including the tidal channel (between the Drigg and Eskmeals barrier spits), foreshore and ebb-tidal delta, which are dominated by seawater with wave and/or tidal currents. The fluvial-to-estuarine Esk, Mite and Irt, their overbank deposits, the estuary central basin, the tidal inlet, the foreshore, and the ebb-tidal delta complex, together provide a complete fluvial to marine transect that has already been extensively studied in terms of depositional environments, compositional variation, detrital clay mineralogy, detrital clay coat abundance, and detrital clay coat mineralogy (Daneshvar and Worden, 2018; Griffiths et al., 2018b; Griffiths et al., 2019; Verhagen et al., 2020; Wooldridge et al., 2017a; Wooldridge et al., 2017b; Wooldridge et al., 2019; Wooldridge et al., 2018; Worden et al., 2020).

The Ravenglass Estuary has some of the morphological characteristics of a wave-dominated estuary, e.g., the presence of the Drigg and Eskmeal barrier spits and the mud-rich central basin (Griffiths et al., 2019). Wave-dominated estuaries usually have a well-defined tripartite zonation; (i) a high energy, coarse-grained, outer-estuary, marine-dominated region, (ii) a low energy, fine-grained, central region with mixed marine- and fluvial-influences and (iii) a high energy, coarse-grained, fluvial-dominated, inner region (Bokuniewicz, 1995; Dalrymple et al., 1992). However, the Ravenglass Estuary does not wholly conform to this simple pattern as the central region is relatively sand-rich and the inner estuary is not especially coarse-grained (Griffiths et al., 2019). This deviation from a simple model might plausibly be due to one or more of: (i) strong tidal currents that pass beyond the low-energy, central basin into the inner parts of the estuary, thus producing extensive tidal bars and tidal dunes complexes

(Griffiths et al., 2019), (ii) the Ravenglass Estuary is in the later stages of filling, as shown by the presence of a ebb-tidal delta, because ebb-tidal deltas have been reported to reduce the significance of the energy-minimum in the central part of an estuary (Posamentier and Walker, 2006), or (iii) as tidal energy increases relative to wave energy, marine-derived sand can be transported greater distances up-estuary, and the otherwise muddy central basin has been replaced by sandy tidal channels that are flanked by marshes (Dalrymple et al., 1992).

Samples and Methods

To study the relationship between grain size distribution and depositional environment, sub-depositional estuarine environments were first defined by describing surface sediment characteristics, detailed ground surveys, aerial imagery, then surface sediment samples were collected (Fig. 2.1) for grain size analysis and finally the data were statistically modelled to examine links between sediment textural attributes and sub-depositional estuarine environments.

Field-Based Mapping and Sample Collection

Eleven sub-depositional environments were initially mapped and defined across the estuary, using aerial imagery and detailed surveys based on geomorphology of estuarine feature and sediment type (Fig. 2.2 and 2.3). These estuarine sub-environments are gravel beds (De1), tidal flats (De2-4), tidal bars (De5), tidal inlets (De6), backshore deposits (De7), foreshore deposits (NDe8) that were split between northern (NDe8), southern foreshore (SDe8), ebb-tidal delta deposits (De9) and salt marsh (De10). Using a classification scheme initially proposed by Brockamp and Zuther (2004), tidal flats (De2-4) have been split into three sub-divisions using laboratory-derived sand percentages into: mud flat (De2: 15 to 50% sand), mixed flat (De3: 50 to 90% sand) and sand flat (De4: 90 to 100% sand). The small area occupied by the backshore deposits (De7), the diminutive number of samples collected (two) and the low preservation-potential of this sub-environment, led us to remove this category from the classification scheme. We chose to exclude the dune-topped spit environments (nominally De11) from the scheme as they have negligible preservation-potential.

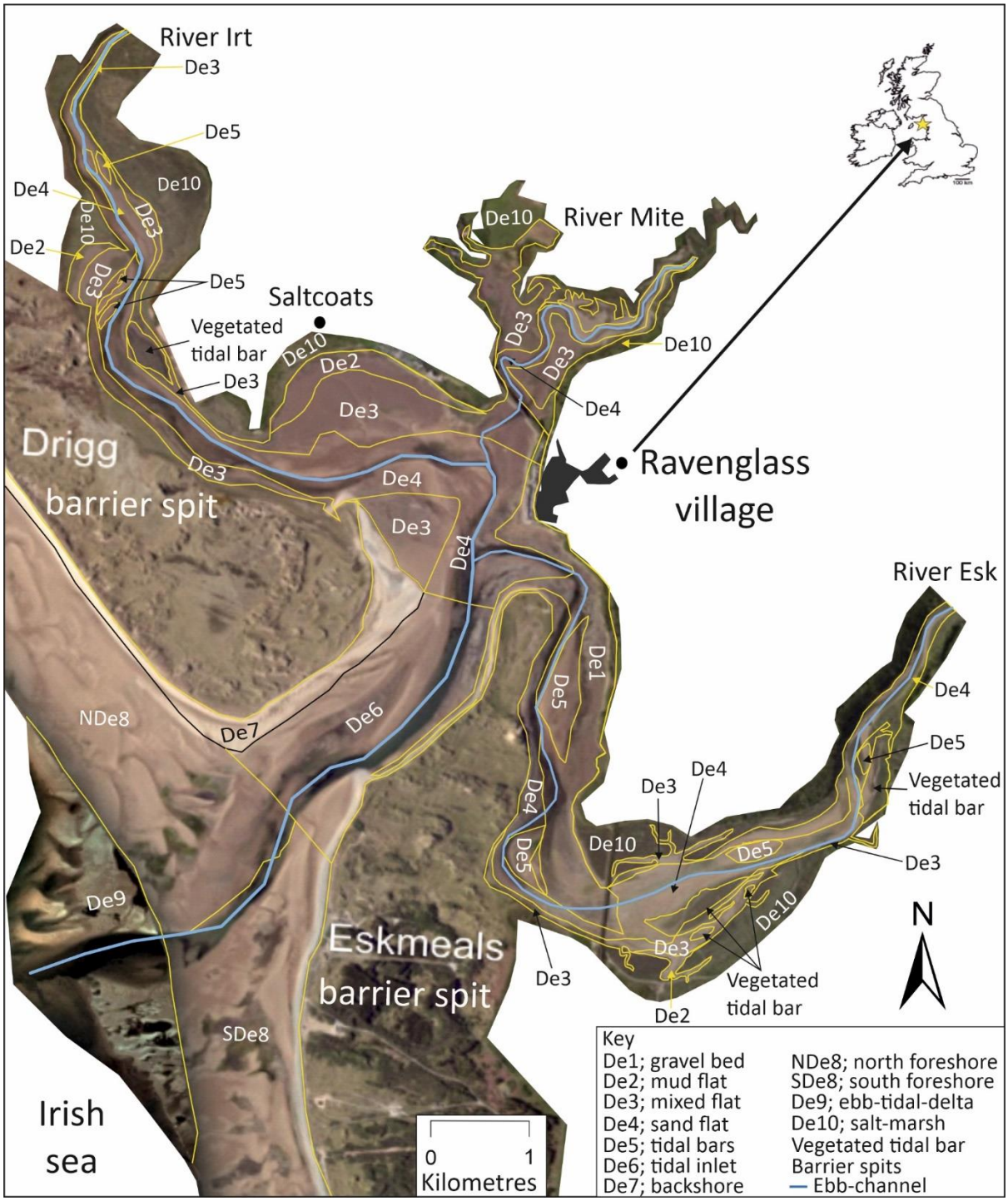

Figure 8: Distribution of depositional-environments in the Ravenglass Estuary. Depositional environments are labelled; De1, gravel-bed; De2, mud-flat; De3, mixed-flat; De4, sand-flat; De5, tidal bars and dunes; De6, tidal-inlet; De7, backshore; De8, foreshore (northern and southern areas); De9, ebb-tidal delta; and De10, salt marsh. Tidal flats have been sub-divided by lab-derived sand percentages into sand flat (90-100% sand), mixed (sand-mud) flat (50–90% sand), and mud flat (15–50% sand). The classification is modified from the scheme initially proposed by Brockamp and Zuther (2004).

A total of 482 surface sediment samples (here defined as sediment from the top 2 cm) were collected from the estuary and nearby coast, at low tide, that provide a complete fluvial to marine transition (Fig. 1). As the estuary almost totally empties (86%) at low tide during which most channels are no more than 1 m deep, we had access to the entire estuary sediment surface, with the exception of the channel in the main tidal inlet. The sediment samples were placed in airtight plastic bags in the field and air-dried in the laboratory at the University of Liverpool for further study.

Grain size analysis using Laser Particles Size Analysis (LPSA) and GRADISTAT© soft-ware

Prior to automated grain size analysis, coarse materials and organic matter was removed. The Laser Particle Size Analyser (LPSA) only accepts particles up to 2 mm in size; therefore, samples containing, for example, pieces of shell, algae, wood, or grit, were passed through a 2 mm sieve. The relative mass of the > 2 mm fraction was noted, and the coarse fraction sample was retained. About 10 to 20 mL of loose sediment was transferred into a 100 mL Pyrex beaker. 30 mL of 6 % hydrogen peroxide was added to remove organic matter from each sample that contained organic matter. The samples were transferred onto a hotplate at 70 °C in a fume cupboard to aid digestion, and to evaporate the fluid. Each sample stood for at least one hour until all signs of oxidative reaction of organic matter had ceased. Clay- and organic-rich samples, in some cases, required additional hydrogen peroxide to ensure full removal of organic matter. Surfactant ethanol was added to minimise fizzing and so prevent sediment sample-loss. The organic digestion process was repeated until all signs of organic digestion had ceased. The sides of the Pyrex beaker were rinsed with a fine jet of distilled water to wash down any residue and guarantee preservation of the whole sediment sample. A small amount of Calgon was added to convert the dried sediment into a paste on a watch glass for mixing and homogenisation.

Laser particle size analysis was conducted on the entire dispersed sediment sample using a Beckman Coulter counter. The LPSA results were analysed using GRADISTAT© software (Blott and Pye, 2001) for the quantification of grain size distribution, mean grain size, grain size sorting, skewness, kurtosis, sand, silt and clay abundance, and the calculation of the proportions of specific sediment grain size fractions. Statistical parameters used in describing the grain-size sorting (σg) scale of the sediments are those proposed by Folk and Ward (1957), in which high values are indicative of poorly-sorted sediment. Grain-size sorting classes, as defined by the GRADISTAT© software (Blott and Pye, 2001) are as follows: 1.27–1.41 (well-sorted), 1.41–1.62 (moderately well-sorted), 1.62–2.0 (moderately-sorted), 2.0–4.0 (poorly-sorted), and 4–16 (very poorly-sorted).

Spatial Mapping

Spatial distribution maps of various textural attributes were plotted (Figs. 4-8) using an inverse distance weighted (IDW) interpolation function in ArcGIS to avoid the formation of valleys, ridges of extreme and unrepresentative values or spurious negative values (e.g., for grain size) (Watson and Philip, 1985). To ensure that the interpolated values on either side (marine versus estuarine) of the coastal barrier spits did not influence each other despite their relative spatial proximity, a polyline was drawn through the long axes of the Drigg and Eskmeals spits (Griffiths et al., 2018b).

Holocene core

A 3 m sediment core was drilled through the Holocene succession in the tidal flats at Saltcoats in the Ravenglass Estuary under tender by Geotechnical Engineering Ltd (Fig. 9). This core was acquired using a Geotechnical light-weight "Pioneer" rotary rig since the on soft and environmentally sensitive surfaces heavy drilling rigs tend to have trouble safely traversing the terrain. The retrieved core was 12 cm in diameter, thus permitting extensive study. 1 m segments of core were retained in a semi-rigid plastic liner ready to enable transport back to the University of Liverpool for subsequent analysis. The sediment core segments were sliced and photographed wet and air-dried. Following this, detailed visual logging of each core segment was undertaken at a scale of 1:5. Facies associations were described in terms of grain size, colour, sedimentary structures, bed thickness, presence of roots and shell fragments, bioturbation index and type of bioturbation. The core was then subject to LPSA analysis using techniques described above, from samples taken every 5 cm.

Statistical Analysis

Multivariate statistical techniques (Principal Component Analysis)

Principal component analysis (PCA) was employed to look for clusters in the textural data. PCA is a statistical procedure that converts a set of observations of possibly correlated variables into a set of values of linearly uncorrelated variables, called principal components (PCs). This multivariate statistical technique has been used repeatedly to investigate variability in large data sets (Cheng et al., 2006; Dempster et al., 2013; Grunsky and Smee, 1999; Klovan, 1966). Each principal component represents a certain amount of variability in the data and the first two principal components (PC1 and PC2) typically account for most of the variation within the whole dataset (Reimann et al., 2008). Only principal components with eigenvalues > 1 are used when using PCA, as they account for most of the variance in the data.

Table 1: Summary of the eigenanalysis and discrimination proportion of each principal component.

Eigenanalysis of the Correlation Matrix				
Eigenvalue	2.476	1.112	0.279	0.133
Proportion	0.619	0.278	0.070	0.033
Cumulative	0.619	0.897	0.967	1.000

Mean grain size, grain size sorting, skewness and kurtosis data (phi unit) from the Ravenglass Estuary were imported into MINITAB© 17 for PCA analysis. The PCA produces an analysis of the PCA (Table 2.2) and eigenvectors (Table 3), also referred to as principal component coefficients, or loadings, which describe the relative significance of a given component.

The derived principal component values for each sample were then linked to their specific sub-environment categories. Cross-plots of the principal components, with data categorised by sub-environment, was employed (Fig. 10) to assess whether the approach could be employed to reveal the environment of deposition of the Ravenglass Estuary samples from unknown environments (e.g., from core samples).

Table 2: Summary of eigenvectors of each principal component.

Eigenvectors				
Variable	PC1	PC2	PC3	PC4

Mean grain size	0.546	-0.348	-0.585	0.488
Grain size Sorting	0.600	-0.158	-0.001	-0.784
Skewness	0.561	0.245	0.694	0.379
Kurtosis	0.165	0.891	-0.419	-0.053

ANOVA and Post Hoc Tests

As we will show, principal component analysis was helpful for discriminating the three types of tidal flat environments, but it lumped all the sand-dominated sub-depositional environments into one area of a cross plot of PC1 versus PC2. We therefore employed other approaches to establish whether textural data can be used to discriminate the sand-dominated sub-depositional environment. The statistical significance of textural differences between various pairs of sand-dominated sub-depositional environment was investigated using an Analysis of Variance (ANOVA) approach. Following ANOVA, post-hoc Tukey's honestly significant difference (HSD) test was also employed to highlight the numerical significance of differences between each sand-dominated sub-environment for each sediment textural characteristic. The difference between each pair for each textural attribute is defined as being significant if the "p" value is less than 0.025. ANOVA and post-hoc Tukey tests (Table 2.4) were performed in R statistical software (R Core Team, 2016).

Bivariate analysis, and boxplots and classification trees

Bivariate plots of sediment textural parameters for discrimination of sedimentary environments have been used by numerous authors for many years (Friedman, 1961; Friedman, 1979; Mason and Folk, 1958; Shepard et al., 1961). Plots of grain size sorting against skewness were used here to try to discern estuarine sub-environments (Fig. 11).

Boxplots, produced using ggplot2 in Rstudio (Wickham, 2016) were employed to visualise some of the key differences between environments of deposition in terms of sedimentary parameters (Fig. 12). Key value, indicated by the node points in the classification tree (see next) as a function of depositional environments, were added to the boxplots. The boxplots are best examined in conjunction with the output from the ANIOVA analysis (Table 4).

Table 3: Collation of some of the significance values resulting from the ANOVA analysis and post-hoc Honestly Significant Difference (HSD) tests for the characteristics of the sand-dominated sedimentary environments. We have excluded differences that are at best marginally significant (when $P < 0.1$). We have here listed significant difference when $P < 0.05$ (*), very significant differences when $P < 0.01$ (**), and extremely significant differences when $P < 0.001$ (***).

Depositional environment discrimination	**Discriminatory variable**	**P-values**	**Useful for 1st order discrimination of sub-environments in this study**
De6-De5	Grain size	0.0000015***	Y
N-De8-De5	Grain size	0.0000007***	Y
De9-De6	Grain size	0.0014742**	Y
S-De8-De6	Grain size	0.0000010***	Y
N-De8-De9	Grain size	0.0052703**	Y
S-De8-N-De8	Grain size	0.0000025***	Y
De6-De5	Medium sand fraction	0.0094279**	
N-De8-De5	Medium sand fraction	0.0029329**	

S-De8-De5	Medium sand fraction	0.0005359***	Y
S-De8-De6	Medium sand fraction	0.0000001***	
S-De8-De9	Medium sand fraction	0.0002193***	Y
S-De8-N-De8	Medium sand fraction	0.0000000***	
De9-De5	Kurtosis	0.0257901*	Y
N-De8-De5	Kurtosis	0.0115690*	
De6-De5	Sorting	0.0183192*	
De9-De5	Sorting	0.0186735*	
N-De8-De5	Sorting	0.0028333**	
De6-De5	Skewness	0.0274987*	
N-De8-De5	Skewness	0.0000049***	
S-De8-De5	Skewness	0.0293121*	

Classification of the environments of deposition (categorical data) was undertaken using the numerical descriptions of sedimentary texture (continuous data) that were used to characterise each environment and the Recursive Partitioning and Regression Tree (RPART) package (Therneau and Atkinson, 2019), that is available in R statistical software (R Core Team, 2016). Using RPART, a classification tree can be developed by the following process: first the single variable (e.g., grain size) is found which best splits the data into two groups. The data are separated at the decision node, and then this process is repeated separately to each sub-group with further decision nodes, and so on, repeatedly, until no more improvement can be made. RPART results in "leaf" (or terminal) nodes that represent the optimum final classification down that branch. Each leaf node lists the quantity of samples in that specific classification category (and all other categories), listed as a fractional quantity. The ideal is 100% certainty that the classification is correct, which is indicated by a fractional value of 1.00. If the fractional value is less than 1.00, this shows that the classification has some uncertainty. Uncertainty is the result of some samples from different categories (in this case environments of deposition) falling in overlapping parts of multi-dimensional classification space, i.e., there are some categories of depositional environments that have overlapping attributes, even when four or six dimensions are considered. In the Ravenglass Estuary, case we applied an initial RPART classification tree to the output from the Principal Component Analysis, which neatly separated each of De2, De3 and D4 from De5-De9 (for example see Fig. 10 for a bivariate slice through the data). We then applied a second RPART classification tree to mean grain size, sorting, skew, kurtosis, the medium sand fraction, and the silt fraction to optimally-separate De5, De6, NDe8, SDe8 and De9 (for example see Fig. 2.12 for how textural variables separate the data, one-by-one).

Results

Depositional environments in the estuary

The distribution of sub-environments is illustrated in Figure 2 and the appearance of each sedimentary sub-environment is illustrated in Figure 3.

Inner estuary

The inner estuary is comprised of (i) gravel beds (De1), localised to the lower part of the Esk arm, and is dominated by a loose aggregate of rock fragments, (ii) localised vegetated salt marsh (De10) in the

lower Esk arm, dominated by salt-tolerant plants, (iii) tidal bars (De5), which are sand bars in the intertidal zone that have their long axis (crest) oriented approximately parallel to the direction of the main current (Figs. 2 and 3).

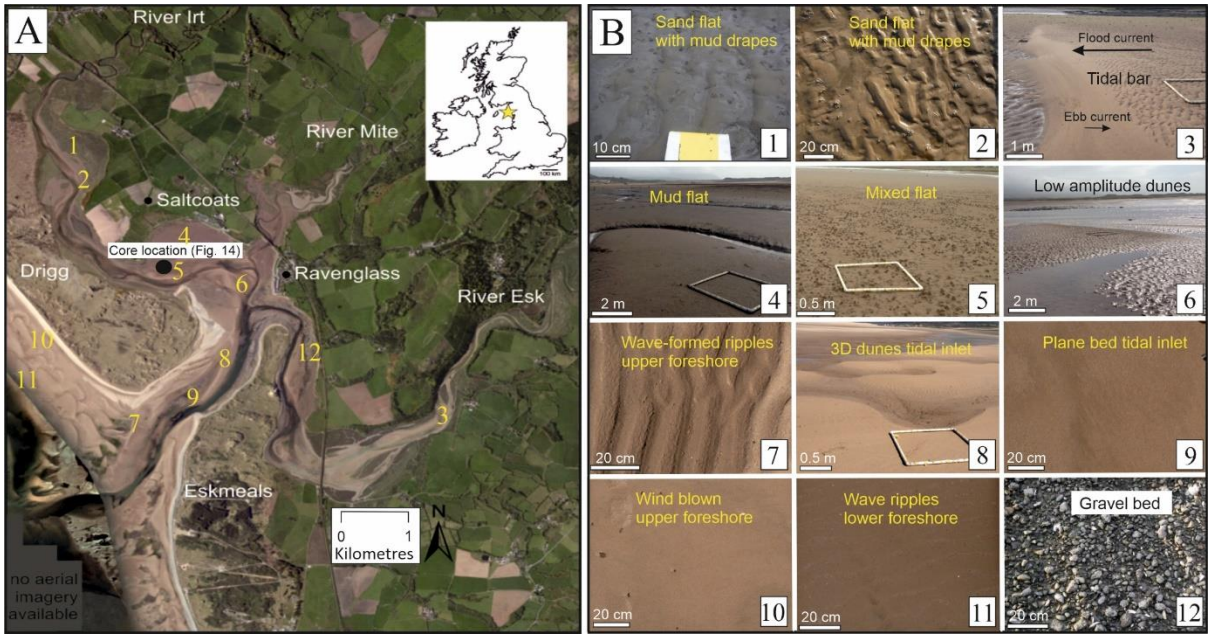

Figure 2: (A) image revealing characteristics of depositional environment; each site image in part B marked by the large yellow numbers. (B) Compilation of surface photographs taken throughout the Ravenglass Estuary. 1 and 2) inner estuarine sand-flats with mud-drapes. 3) inner estuary flood-dominated tidal-bar. 4) central basin mud-flat. 5) central basin, highly-bioturbated (Arenicola marina), mixed-flat. 6) central-basin low amplitude dunes. 7) upper-foreshore/tidal-inlet wave-formed ripples. 8) tidal-inlet, migratory 3D dunes. 9) tidal-inlet upper-phase plane bed, proximal to the ebb-channel. 10) wind-blown, upper-foreshore sediment. 11) lower-foreshore wave-ripples, with subtle shell-debris lag deposits. 12) gravel-bed, exposed in the inner-Esk Estuary.

Tidal flats

The central basin and parts of the inner estuary consist of sand flat (De4, 90-100% sand), (ii) mixed flat (De3, 50–90% sand), (iii) mud flat (De2, 15–50% sand) and (iv) fully vegetated salt marsh (De10) (Figs. 2.2 and 2.3). The tidal flat sediment subdivision follows the scheme defined by Wooldridge et al. (2017b), which was adapted from the subdivisions initially proposed by Brockamp and Zuther (2004). The mud flat (De2) lies furthest away from the tidal inlet (De6) and is dominated by fallout of suspended sediment. The mixed flat (De3) lies between the sand flat and mud flat and is characterised by alternating bedload sedimentation and fallout from suspension. The sand-flat (De4) is an intertidal flat relatively close to the tidal inlet (De6) and is dominated by bedload transport of sand grade sediment. The salt marsh (De10) is a supratidal zone, or upper coastal intertidal zone, that is subjected to daily or occasional flooding by salt water or brackish water and is dominated by a dense stand of salt-tolerant plants.

Outer estuary

The outer estuary is comprised of (i) the tidal inlet (De6), (ii) the backshore (De7), (iii) the foreshore (De8), and (iv) the ebb-tidal delta (De9) (Figs. 2 and 3). The tidal inlet (De6) dissects Eskmeals and Drigg barrier spits and connects the open ocean and the coastal environments to the central and inner

zones of the estuary (Fig. 2). The diminutive backshore area (De7) is tidally inundated only during spring tide and storm events and fringes the dunes sitting on the barrier spits. The foreshore (De8) is the section of beach between the backshore and the mean-low-water line. The foreshore splits between the northern foreshore (NDe8) and southern foreshore (SDe8) since the two areas have radically different grain sizes (Fig. 4). The ebb-tidal delta is exposed during spring tides (Fig. 2). The paucity of backshore (De7) samples and their negligible preservation potential have led us to exclude this environment from the classification scheme.

Estuarine sediment characteristics

The mapped distribution of grain size and sorting for the whole of the Ravenglass Estuary are presented in (Figs. 4 and 5). Skewness (Fig. 6) is defined as the asymmetry of a distribution from the mean of a data set (Brown, 1997). Kurtosis (Fig. 7) is defined as a measure of the relative peakedness or flatness of a distribution compared to the normal distribution (Brown, 1997). The distribution patterns of the proportions of different sand fractions are presented in Figures 8A to 8E, and silt plus clay fraction distributions is presented in Figure 8F. The following text describes the distribution of sediment parameters in the sub-environments.

Inner and central estuary mud flats (De2) are poorly-sorted and very fine-grained (Figs. 2, 4, 5). Sediments in mixed flats (De3) are heterogeneous and poorly-sorted, containing both mud and sand. Within the inner and central estuary, there is a gradational change from the poorly-sorted, very fine to fine-grained mixed flat to moderately well-sorted to moderately-sorted, fine to medium-grained, sand flat (De4).

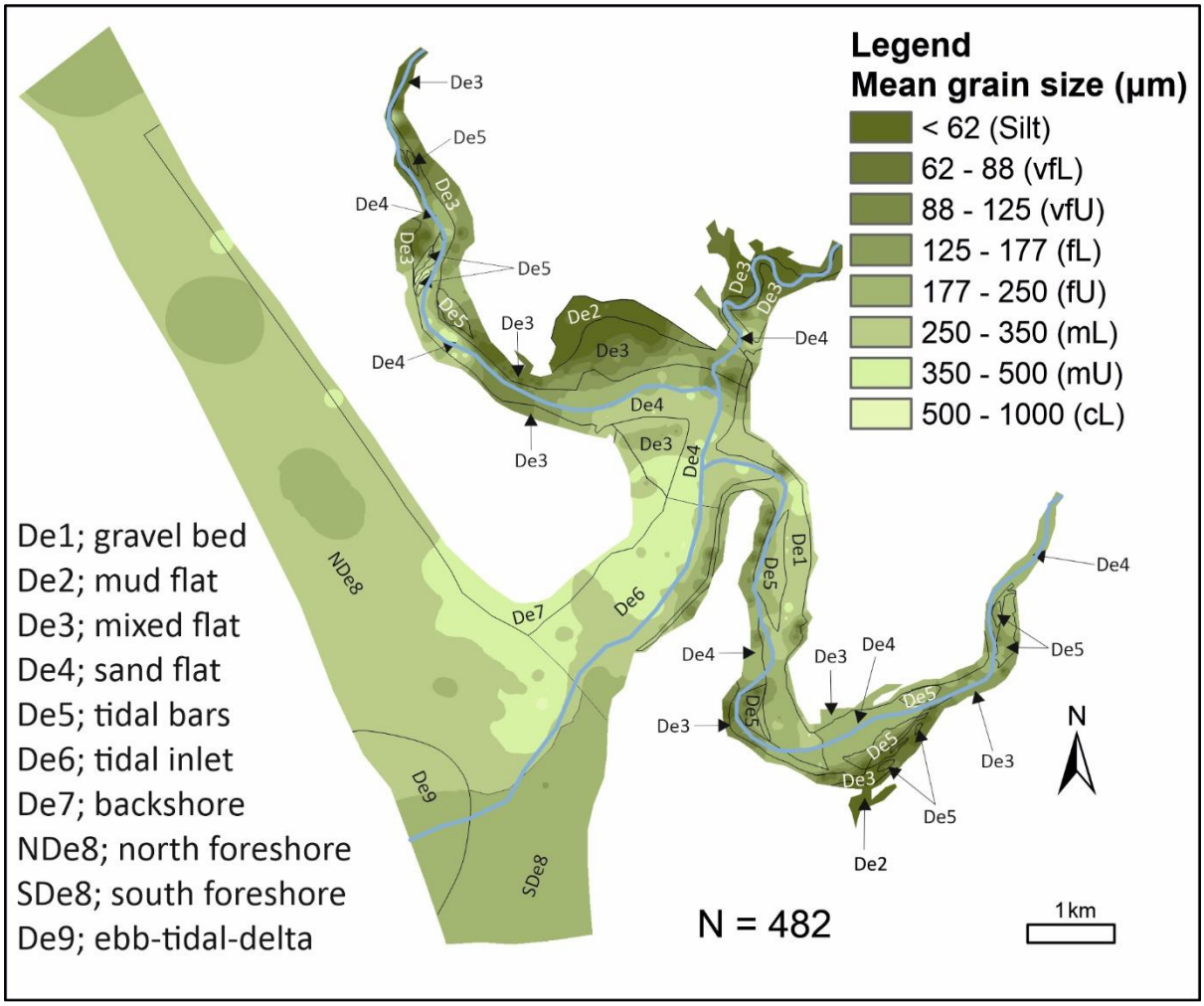

Figure 3: Grain size (µm unit) distribution in the Ravenglass Estuary. With units defined by GRADISTAT© software (Blott and Pye, 2001). Boundaries between different environments of deposition have been taken from Figure 2.2. Note that mean grain size decreases toward the margins of the inner estuary and central basinwell-sorted. Mean grain-size classes are labelled accordingly: silt; lower very fine sand (vfL); upper very fine sand (vfU); lower fine sand (fL); upper fine sand (fU); lower medium sand (mL); upper medium sand (mU); lower coarse sand (cL).

Tidal bars sediments (De5) are moderately well-sorted to well-sorted, and fine- to medium-grained (Figs. 2, 4, 5). The gravel beds in the Esk arm (De1) are moderately well-sorted and fine- to medium-grained. The salt marsh sediments in the Esk arm (De10) are poorly- to moderately-sorted, very fine- to medium-grained. Tidal inlet sediment (De6) is typically moderately well-sorted and medium-grained. Sediments in the southern foreshore (SDe8) and in ebb-tidal delta (De9) are finer grained and better sorted than the sediments within the northern foreshore (NDe8) (and the backshore sediment, De7). Grain sizes are most coarse in the tidal inlet and the northern foreshore nearest the mouth of the estuary.

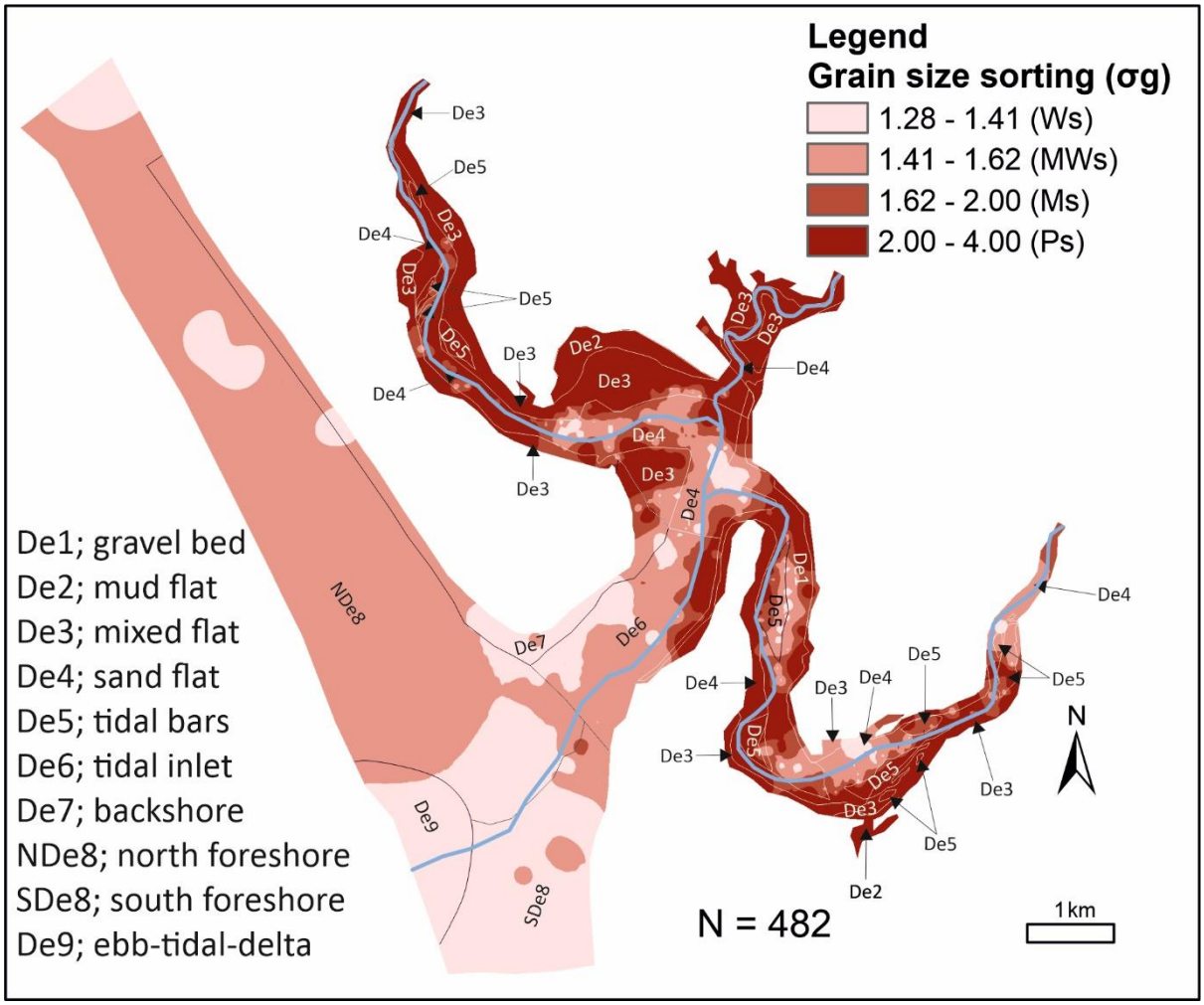

Figure 4: Sorting distribution in the Ravenglass Estuary, with units defined by GRADISTAT© software (Blott and Pye, 2001). Boundaries between different environments of deposition have been taken from Figure 2. Note that textural maturity decreases toward the margins of the inner estuary and central basin, sandy sub-environments in the marginal marine settings are moderately to well-sorted. Grain-size sorting classes are labelled accordingly: well-sorted (Ws); moderately well-sorted (MWs); moderately-sorted (Ms); and poorly-sorted (Ps).

Grain size and degree of sorting across the estuary tend to increase down channel and decrease toward the margin of the inner estuary and central basin (Figs. 4, 5). Kurtosis is heterogeneously distributed, and sediment skewness becomes positive upstream and in the central basin, and negative down channel (Figs. 6, 7). There is a heterogenous distribution of grain sizes in the estuary with a dominance of fine- and very fine-sand fractions in the inner estuary (De2, De3) and southern foreshore and ebb delta (SDe8 and De9) (Figs. 8D, 8E). The medium sand fraction is dominant in the tidal bars (De5), central basin sand flats (De4), tidal inlet (De6) and northern foreshore (NDe8) (Fig. 8C). Coarse-grained sand is most abundant in the tidal inlet (De6), the proximal part of the northern foreshore and in parts of the tidal bars (De5) (Fig. 8B). Very coarse sands are rare (Fig. 8A).

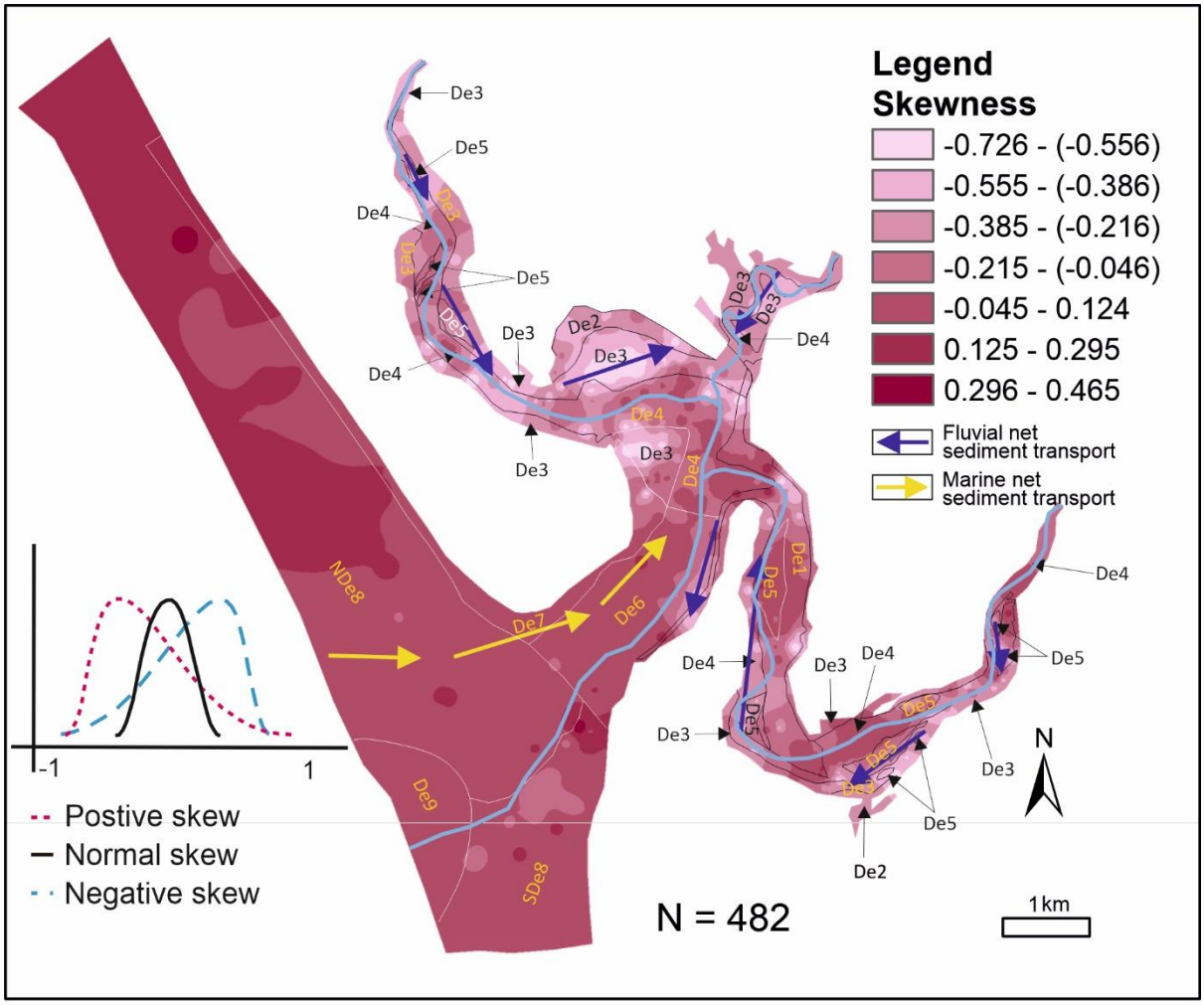

Figure 5: Skewness of grain size distribution in the Ravenglass Estuary. Boundaries between different environments of deposition have been taken from Figure 2. Note that the sediments skewed positively upstream and central basin and skewed negatively down channel.

Grain size and kurtosis in Ravenglass Estuary are heterogeneous (Figs. 4 and 7). Ravenglass sediment in the main parts of the estuary tends to be negatively skewed (Fig. 6). The sediment evolves to being slightly positively skewed along the tidal inlet (De6) towards the open sea (Fig. 6). Towards the head of the arms of the estuary and in mud flats (De2) and mixed flats (De3), the sediment tends to become increasingly positively skewed. The sediment in the Ravenglass Estuary is well- to moderately well-sorted in the tidal inlet and foreshore sub-depositional environments (De6 and De8; Figs. 2 and 5). In the three inner arms of the Ravenglass Estuary (Irt, Mite and Esk), sedimentary deposits are poorly-sorted, e.g., where there are mud flat (De2) and mixed flat (De3) sub-depositional environments. In contrast the sediment is moderately well-sorted along the channel of the Irt inner arm, and tidal bars (De5) and sand flats (De4) of the inner Esk arm (Figs. 2 and 5).

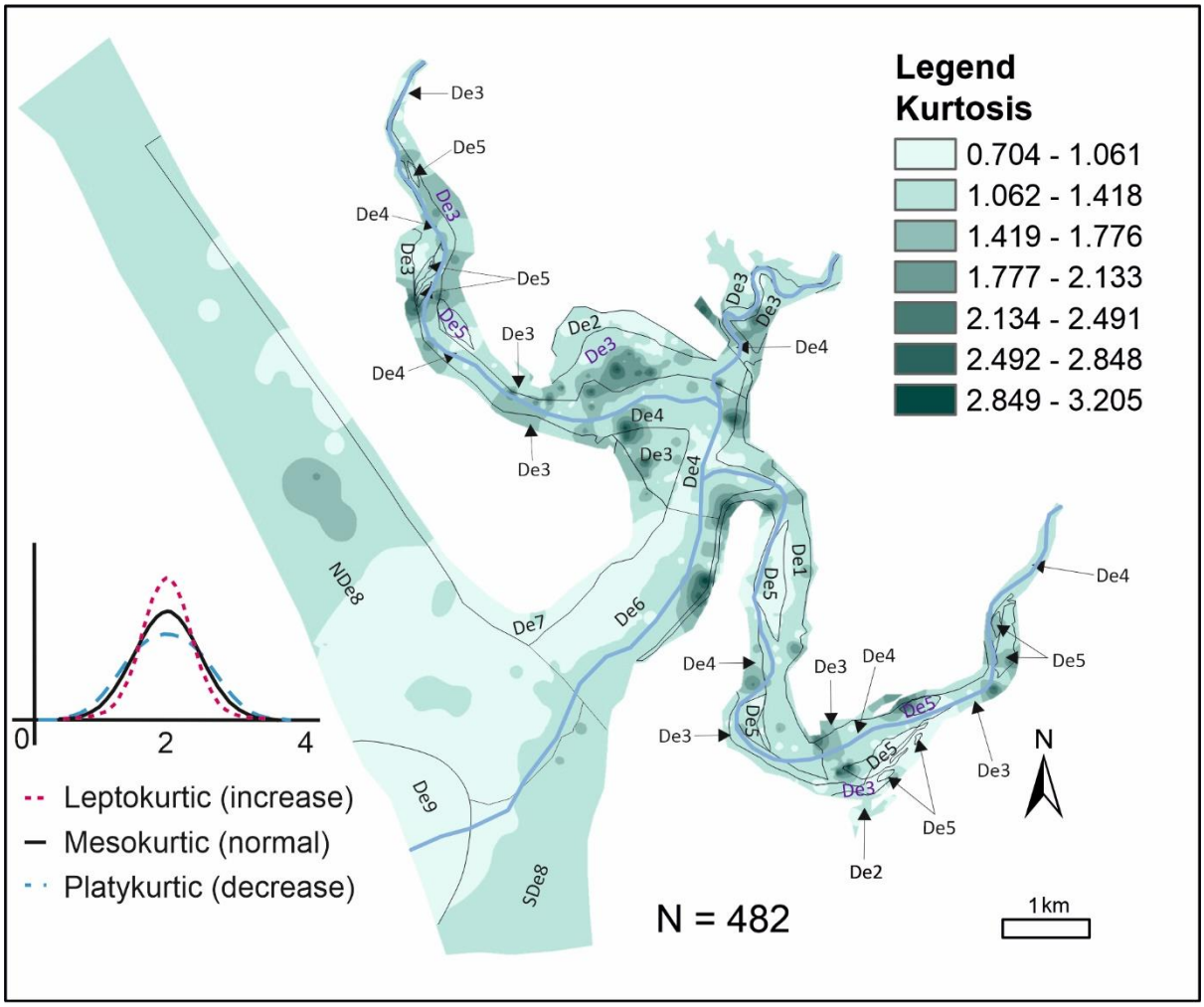

De1; gravel bed De2; mud flat De3; mixed flat De4; sand flat De5; tidal bars De6; tidal inlet
De7; backshore NDe8; north foreshore SDe8; south foreshore De9; ebb-tidal-delta

Figure 6: Kurtosis of the grain size distribution in the Ravenglass Estuary, where kurtosis is defined as a measure of the relative peakedness or flatness, or tail magnitude of a distribution compared to the normal distribution (Brown, 1997). Boundaries between different environments of deposition have been taken from Figure 2. A high kurtosis value means that there are more outsize grains than samples with a low kurtosis value. Kurtosis is heterogeneously distributed.

The distribution of different grain size classes (Fig. 8) reveals that there is no simple correspondence between grain size and position in the estuary. Coarse sand is located along the tidal inlet (De6) and in the northern foreshore (NDe8) just to the north of the tidal inlet (De6, Fig. 8B). Medium sand is also located along the tidal inlet (De6), along most of the northern part of the foreshore (NDe8) and in tidal bars (De5) in the mid Irt and Esk estuaries (Fig. 8C). Fine sand has a distinctly different distribution than the medium sand and is concentrated in the southern foreshore (SDe8) and in the sand (De4), mixed (De3) and mud (De2) flats in the Irt and Esk Estuaries (Fig. 8D). Very fine sand, silt and clay tend to be concentrated in the upper parts of the Irt and Mite estuaries and in the margins of the Esk Estuary (Figs. 8E and 8F).

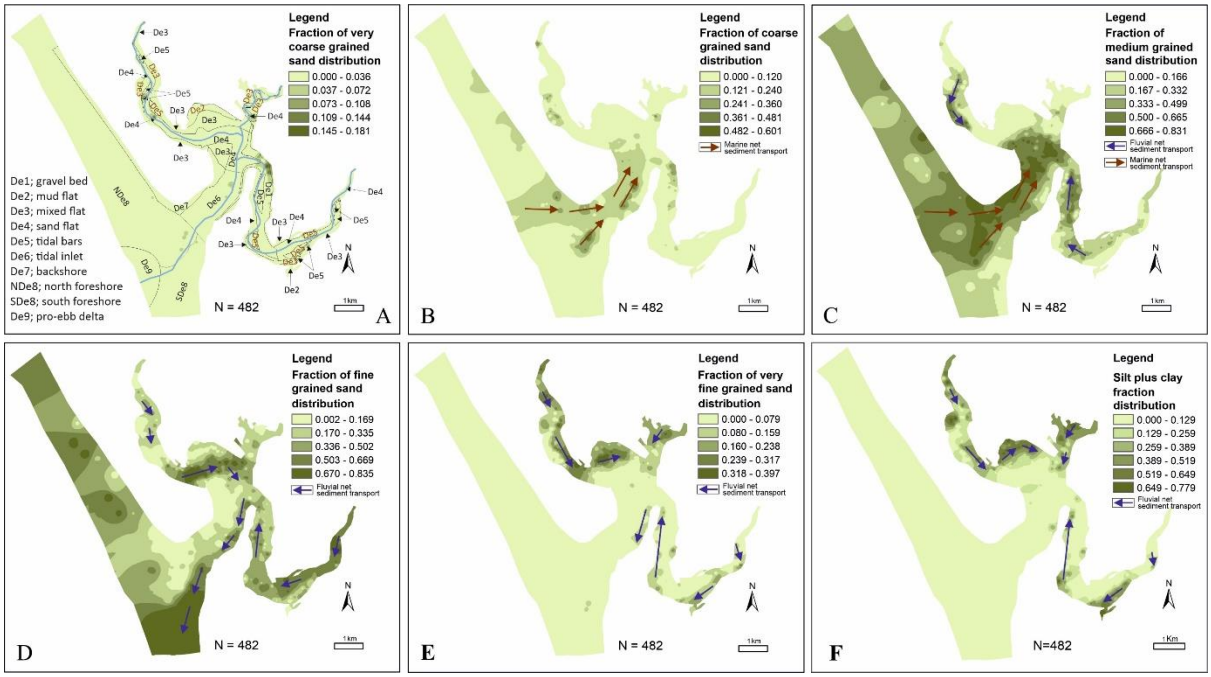

Figure 7: Mapped sand fraction distribution patterns in the Ravenglass Estuary, (A) Fraction of very coarse-grained sand, (B) Fraction of coarse-grained sand, (C) Fraction of medium-grained sand, (D) Fraction of fine-grained sand, and (E) Fraction of very fine-grained sand, (C) Fraction of medium-grained sand, (D) Fraction of fine-grained sand, and (E) Fraction of very fine-grained sand. (F) Fraction of all silt fractions plus clay. Boundaries between different environments of deposition have been taken from Figure 2 and added to part A.

Holocene core

Based on visual description, it was possible to identify various grades of sand in the geotechnical core drilled into the sandflats near Saltcoats (Fig. 9). Even though the core was drilled into tidal flat sediment and much of the sediment is composed of fine-grained sand, there are coarse-grained intervals that would not automatically be expected to be associated with sandflats. There was a distinct lack of sedimentary structures typically associated with estuarine sediment (mud drapes, bi-directional current ripples, etc) and a lack of trace fossils that might have been diagnostic of specific sub-environments. Based on core description alone, it was not possible to unambiguously define the palaeo-depositional environments of the sand, even 1 m below the surface. The Holocene core was analysed using LPSA, which informed the final interpretation of the palaeo-environments of deposition. The grain size, sorting, skewness, kurtosis and medium sand fraction and mud fraction output data from the LPSA have been added to Figure 9.

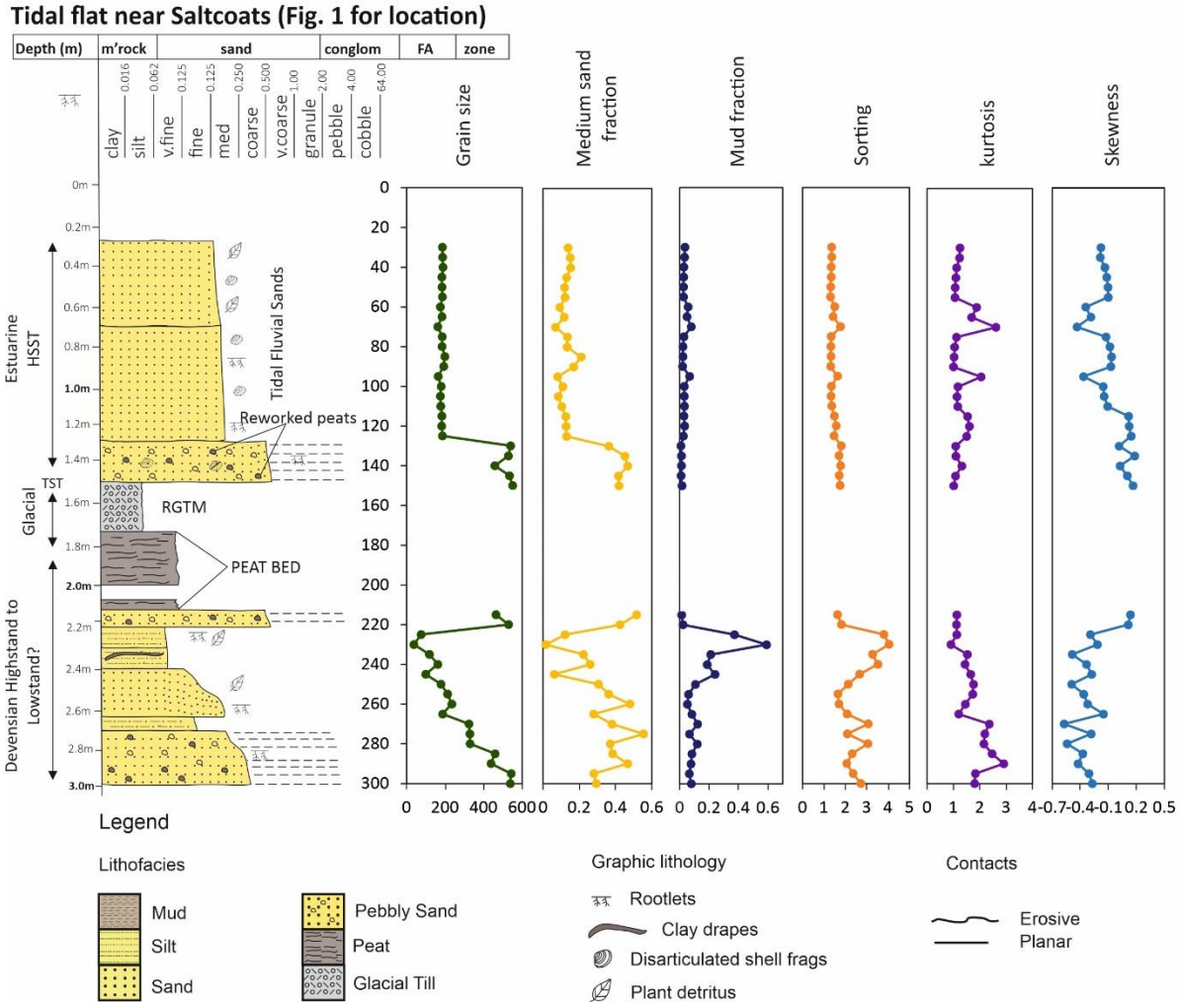

Figure 8: Graphic log of the 3 m core drilled in the tidal flats adjacent to the central basin of the Ravenglass Estuary with illustration of the variation of grains size, sorting, skewness, kurtosis (µm unit), the medium sand fraction and the silt fraction, all derived from LPSA analysis.

Discussion

Controls on sediment texture

Estuaries are variably influenced by tides (Dalrymple and Choi, 2007) and greater tidal influences will give rise to greater marine sediment flux into estuaries (Dalrymple et al., 1990; Dalrymple et al., 1992). Tidal activity mixes fresh-river and saline-marine waters and can cause flocculation and deposition of clay minerals (Allen, 1991). Tidal activity also re-suspends and transports sediments, creates bedforms, and scours channels (Wells, 1995).

Distribution of sediment grain sizes in the Ravenglass Estuary

Most of the coarse-grained sand is within, or near, to the tidal inlet (De6; Fig. 8B). This area is where the tidal flow velocities will be highest. The flood tide tends to have a higher flow rate than the ebb tide (Kelly et al., 1991), so it is understandable that coarse marine sand is preferentially flushed into the estuary instead of flushed out (Dalrymple and Choi, 2007; Dalrymple et al., 2012). We have added

schematic net sediment transport vectors to Figure 8B to 8F to illustrate sand grain size movement patterns in the estuary. Note that the coarse sand tends to be absent in the central basin, probably as the flow rate will diminish when the flooding tide spills, or dissipates, into the wider basin from the narrower tidal inlet.

The medium-grained sand distribution shows a pattern similar to the coarse sand with medium sand being flushed into the tidal inlet (De6) part of the estuary from a marine source (NDe8) (Dalrymple and Choi, 2007; Dalrymple et al., 2012; Dalrymple et al., 1992) (Fig. 8C). However, there is also a substantial quantity of medium-grained sand associated with tidal bars (De5) in the Irt and Esk estuaries, separated from the medium sand in the tidal inlet, suggesting that some medium-grained sands have been transported into the estuary from the two main fluvial sources (Esk and Irt). It is possible that high fluvial discharge rates linked to storm events have been responsible for the influx of medium-grained fluvial sand (Dalrymple and Choi, 2007).

There is a strong contrast between the distributions of fine- and medium-grained sand (Figs. 8C and D). Much of the fine-grained sand seems to have been brought into the estuary from the two main fluvial sources (Rivers Irt and Esk) as fine sand has highest concentrations in Esk and Irt sand flats (De4) in the inner estuary. There is also a substantial proportion of fine sand in the tidal inlet (De6) but it preferentially sits along the south side, whereas the medium sand sits preferentially along the north side. This suggests that fine sand is transported from the fluvial environment, via the central basin and out into the marine setting along the southern side of the tidal inlet (De6), where it supplies sediment to the west of the Eskmeals spit on the southern foreshore (SDe8).

The very fine sand distribution (Fig. 8E) suggests either that very fine sand is fluvially-supplied nto the estuary or that the very fine sand tends not to be deposited in foreshore environments. The distribution of silt plus clay mimics the distribution of very fine-grained sand suggesting that clay and silt are predominantly derived from fluvial sources (Fig. 8F).

Sediment in the marine-dominated parts of Ravenglass Estuary, i.e., the tidal inlet (De6) and foreshore (SDe8 and NDe8) sub-depositional environments, tend to be negatively skewed with a relatively greater proportion of coarser than finer grains in the same sample (Figs. 2 and 6). Sediment in the central estuary and towards the margin of the inner estuary, i.e., mud flat (De2) and mixed flat (De3) sub-depositional environments, tends to be positively skewed with a relatively greater proportion of finer than coarser grains in the same sample (Figs. 2 and 6). This skewness pattern, together with the interpreted sediment transport patterns illustrated in Figure 8, suggests that the marine sediment supply is predominantly medium-grained and that the positive skew to finer sediment may be a consequence of minor mixing with the finer-grained, fluvial sediment (Fig. 6). Conversely, the fluvial sediment supply is predominantly fine-grained from the Esk and very fine-grained from the Irt, and that the negative skew in both to coarser sediment may be the result of minor mixing with the coarser-grained, marine sediment (Fig. 6).

Sorting is generally poor in the inner parts of Irt and Esk estuaries except for tidal bars (De5) and sand flats (De4) where the sediment is moderately well-sorted (Figs. 2 and 5). This suggests that the higher flow velocities required to create tidal bars and sand flats are responsible for more unimodal and more organised sediment. The tidal inlet (De6), much of the foreshore (SDe8, NDe8) and ebb delta (De9) are well-sorted or moderately well-sorted suggesting that the higher energy of the marine realm is better at developing unimodal and more organised sediment than the inner estuarine realm.

Discrimination of depositional sub-environments using sediment textural parameters

Textural parameters of sediments, e.g., mean grain size, sorting (standard deviation), kurtosis and skewness, have been used previously to attempt to discern environments of sediment deposition but most studies have focussed on sands from completely different depositional settings; e.g. fluvial and marine-paralic sands from the Texas River, USA (Rogers and Strong, 1959), dune, beach and aeolian sands from Mustang Island, Texas, USA (Mason and Folk, 1958), and foreshore, backshore and aeolian sands from Barnstaple Bay, UK (Greenwood, 1969). These approaches were predicated upon the assumption that sediment's quantitative textural parameters reflect depositional environment because these experience different modes of sediment transport and deposition. The published approaches (Table 1) were able to discern large-scale differences in environment of deposition (e.g., marine versus fluvial), but most of them were not designed to differentiate sub-environments in the same overall setting (e.g., within an estuary). The existing schemes and models listed in Table 1 do not consider complex mixing at the interface between marine and fluvial depositional environment. Here, we provide, for the first time, a classification scheme that relates grain size characteristics to estuarine depositional sub-environments.

The ability to identify the exact sub-environment of deposition in ancient and buried sandstones, e.g., from core samples, would enable a detailed understanding of how a given sand body accumulated and evolved laterally and stratigraphically. The ability to identify the exact sub-environment of deposition was a prime objective of this study of sediment from the core drilled through the Holocene succession at the Ravenglass Estuary. The aim was to enable the confident definition of the sub-environment of deposition rather than just to provide a general description of lithofacies.

Visual discrimination of gravel beds and vegetated salt marsh samples

For the first step in classification of sub-environments, it is important to realise that gravel beds (De1) and vegetated salt marsh (De10) Holocene surfaces can be identified visually from each sample without the need for any further sophisticated analysis of the material. Gravel beds have easily identified gravel and salt marsh samples have abundant roots. The first step in any classification therefore involved only visual classification. For clarity, we have excluded the dune-topped spits from the classification scheme because their preservation potential in estuarine sedimentary settings is negligible (Mountney and Thompson, 2002).

Principal component analysis discrimination of mud-, mixed and sand-flat samples from all remaining environments

The next stage in the classification involved principal component analysis of the textural data: grain size, sorting, skewness, kurtosis. Because we have not used the entire spectrum of grain size data, where the full spread of grain sizes must equal 100%, there was no need to apply any sort of data transformation before we undertook principal component analysis to avoid the problems of closed datasets (Park and Jang, 2020; Sahoo et al., 2020; Zhou et al., 1991). The first two principal components in the Ravenglass Estuary sample set have eigenvalues > 1 (Table 2) accounting for the vast majority (89.7 %) of the variance of the entire dataset. For the Ravenglass Estuary sediment texture dataset, PC1 accounts for 61.9 % of the variance and PC2 for 27.8% of the variance. Principal component-1 and principal component-2 from the grain size distribution and sub-environment dataset are illustrated in a bivariate plot (Fig. 10) which demonstrates that some groupings of

sedimentary sub-environments can be easily discerned using this approach. Figure 10 differentiates mud flats (De2), mixed flats (De3) and sand flats (De4). However, the left-hand cluster of data-points shows that this approach struggles to differentiate the sand-dominated sub-depositional environments, i.e., tidal bar (De5), tidal inlet (De6), foreshore (De8) and ebb-tidal delta (De9) sub-environments. The overlap of sand-dominated sub-environments could possibly be a consequence of being deposited under broadly similar energy conditions leading to these sediments apparently having similar textural parameters. Some sand flat (De4) samples fall in the mass of other sand-dominated sub-depositional environments (De5-De9), and vice versa, suggesting that a two-dimensional approach to prediction would probably have some degree of inaccuracy. Backshore sediment environments (De7) are not included in the statistical analysis as they are aerially restricted and very few samples were collected.

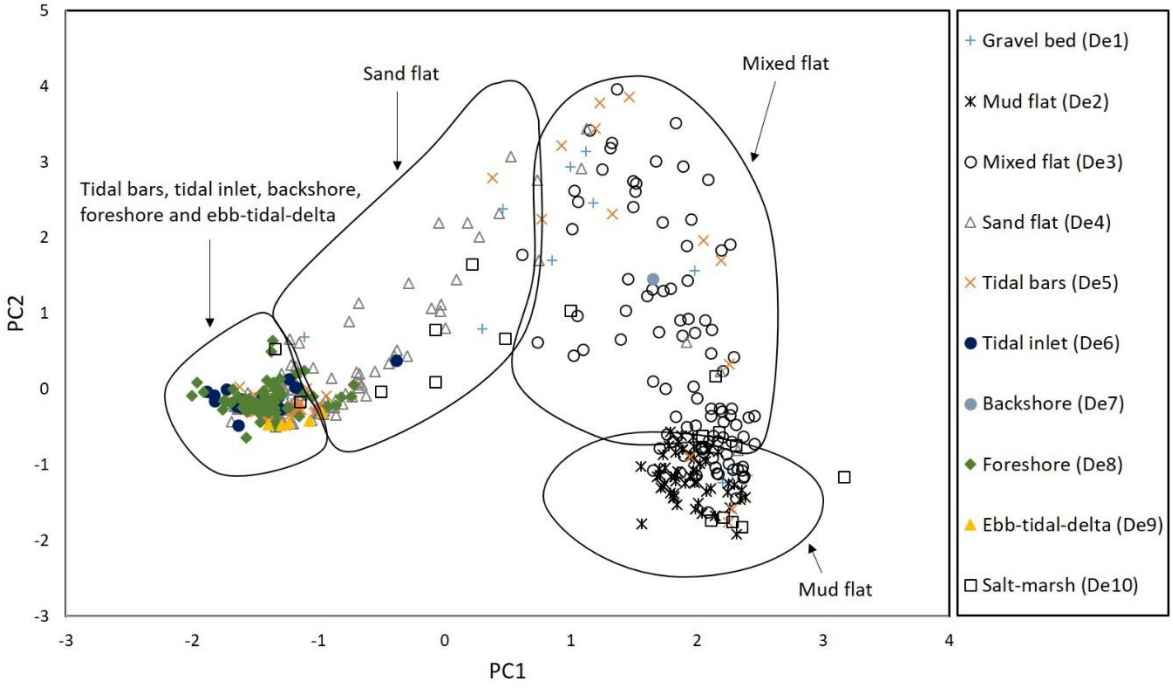

Figure 9: Interpreted bivariate plot of multivariate Principal Component Analysis (PCA) from all 482 samples from the Ravenglass Estuary using grain size data (mean grain size, sorting, skewness and kurtosis, phi unit). The dominant principal components, PC1 and PC2, discriminate the loading score of each sample and groupings of sedimentary environments can be discerned. The collection of data points to the lower left of the diagram shows that multivariate analysis struggles to differentiate the sand-dominated sedimentary environments (De5-De9). Backshore (De7) sediment is not included in the final sub-environment classification as there were too few data points and there is negligible preservation potential.

Previous attempts to differentiate sub-environments have employed a simpler bivariate approach comparing, for example, sorting and skewness (Friedman, 1961; Friedman, 1962; Friedman, 1979; Mason and Folk, 1958; Shepard et al., 1961). We have here mimicked this approach in Figure 11 which seems able to broadly differentiate mud flats (De2), mixed flats (De3), sand flats (De4), a discrete grouping of gravel beds (De1) and vegetated saltmarsh (De10), and the collection of sand-dominated environments (Fig. 11). The lower left-hand cluster of data-points in Figure 11 reveals that the sorting and skewness bivariate approach also struggles to differentiate the sand-dominated sub-depositional environments (De5 to De9).

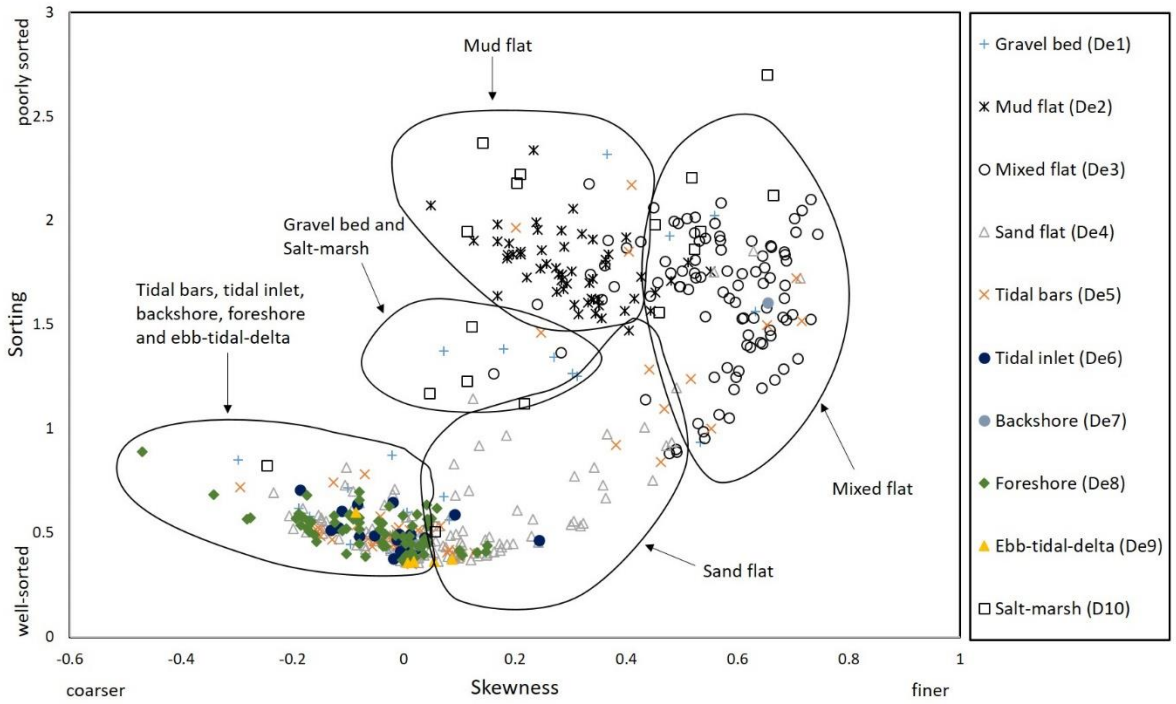

Figure 10: Bivariate plot of sorting and skewness (phi unit) showing that different groups of sub-environments can be partly discriminated. The collection of data points to the lower left of the diagram shows that this bivariate analysis cannot differentiate the sand-dominated sedimentary environments (De5-De9). Backshore (De7) samples are not included in the final sub-environment classification as there were too few data from a small area of sediment that has negligible preservation potential.

ANOVA and Tukey HSD tests help discriminate tidal bars, tidal inlet, foreshore and ebb-tidal delta samples

To advance our ability to differentiate the sand-dominated tidal bar (De5), tidal inlet (De6), northern foreshore (NDe8), southern foreshore (SDe8) and ebb-tidal delta (De9) sub-depositional environments, we have employed quantitative textural data from the LPSA and subjected them to Analysis of Variance (ANOVA) and post hoc Tukey Honestly Significant Different (HSD) statistical tests using R. The significance of the difference is defined by the derived "p" value where p greater than 0.1 represents an insignificant, p less than 0.05 represents a significant difference, p less than 0.01 represents a very significant difference, and p less than 0.001 represents an extremely significant difference. The pairs of sub-environments, the quantitative textural data used to assess the difference and the p values for differences that are at least significant are defined in Table 4. We have here avoided reporting non-significantly different pairs of environments.

The distribution maps in Figures 4 to 8 show that there are major differences in textural attributes across the estuary and these are spatially related to the origin of the sediment. The differences, and similarities, in quantitative textural data between the various sandy sub-environments, apparent using ANOVA and HSD tests can be visualised using boxplots, here plotted using ggplot2 in R (Wickham, 2016). We have here illustrated the mean grain size (Fig. 4), medium sand fraction (Fig. 8C), kurtosis (Fig. 7), skewness (Fig. 6), sorting (Fig. 5) and silt fraction (Fig. 8F) using boxplots (Figs 12A to F).

Mean grain size effectively discriminates tidal inlet (De6) and northern foreshore (NDe8) from tidal bar (De5), ebb delta (De9) and southern foreshore (SDe8) sediments (Fig.12A, Table 4). The medium

sand fraction (Fig. 12B, Table 4) can be used to discriminate southern foreshore (SDe8) from tidal bar (De5) and ebb delta (De9) sediments. Kurtosis values (Fig. 12C, Table 4) can be used to discriminate tidal bar (De5) and ebb delta (De9) sediments. Skewness can be used to differentiate tidal bar (De5) from tidal inlet (De6) and the two foreshore sub-environments (SDe8 and NDe8) but the differences are only marginally significant (Fig. 12D, Table 4). Sorting is generally not a good discriminator of estuarine sub-environments except that some northern foreshore (NDe8) sediments are especially poorly-sorted (Fig. 12E). Silt fraction values discriminate depositional environments De5 to De9 better than sorting, as well as being a key to differentiating De2-4 from De5-9 (Fig. 12F).

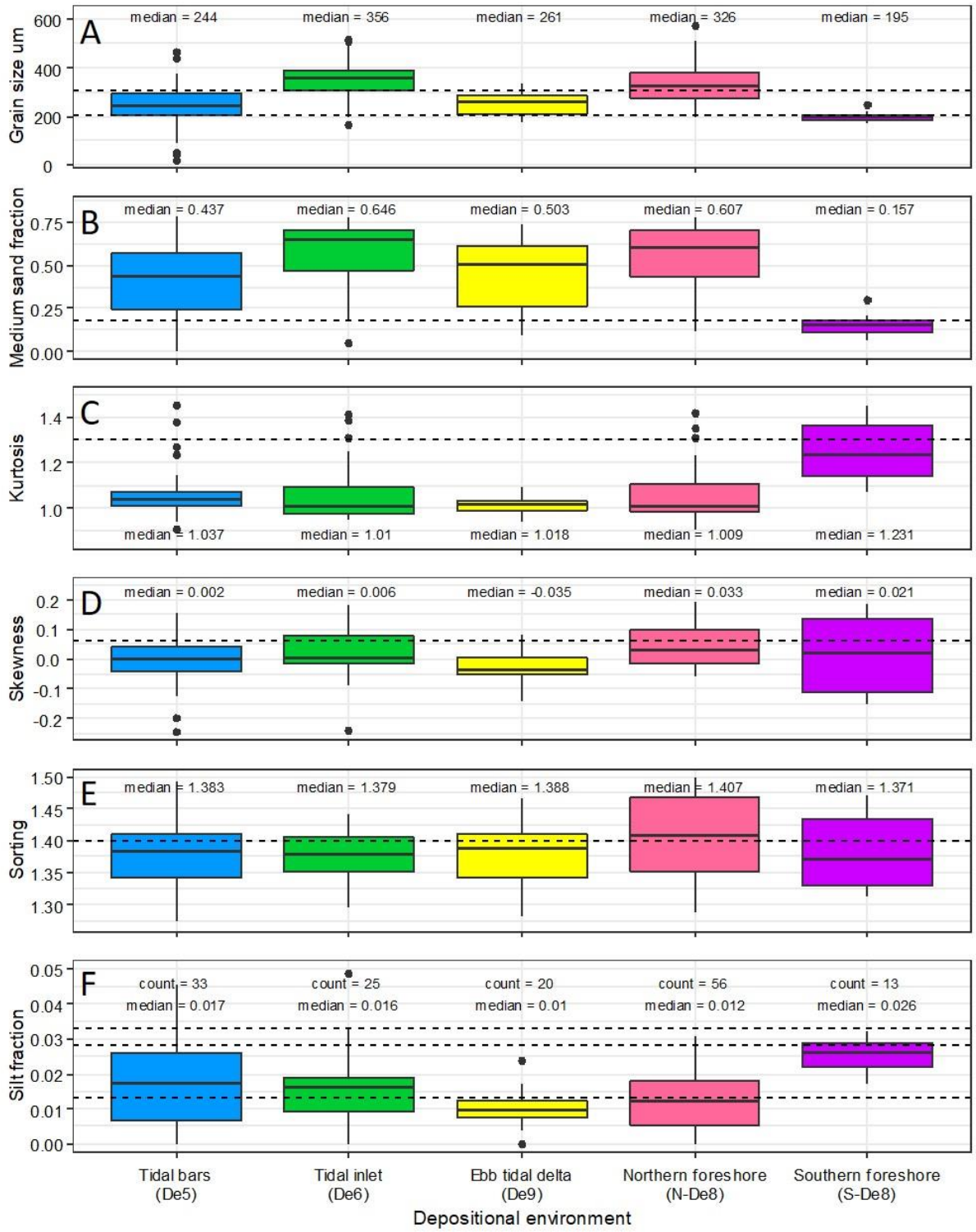

Figure 11: Boxplots of textural attributes of the sand-dominated sub-environments that clustered together in Figures 2.10 and 2.11. Boxplots contain the median and upper and lower quartile ranges. Outliers are defined as > (or <) 1.5 times the interquartile range, above the upper and below the lower quartiles. (A) Grain size of the five sand-dominated sedimentary environments with the median value defined (and in Parts B to F). (B) Medium sand fraction. (C) Kurtosis. (D) Skewness. (E) Sorting. (F) Silt fraction with the number of samples (count) and the median value defined. This figure should be examined in conjunction with Table 4 to reveal the most important differentiators between sub environments. The critical values for parts A to F have been taken from the machine learning-derived decision nodes in Figure 13.

Other differences and similarities are apparent from the collection of boxplots and the p values in Table 4. Based on the study of statistically significant differences between sub-environments and the cut-off values between them for the various textural parameters, it is looks as if it possible to discriminate between several of the five sand-dominated sub-environments.

Recursive partitioning and the development of the classification tree using RPART

The combination of visual analysis, and principal component analysis (PCA) followed by the machine learning approach of recursive partitioning in Rstudio (RPART) allows the construction of a method for the discrimination of eight out of the ten depositional sub-environments (Fig. 13). The RPART package (Therneau and Atkinson, 2019), available in R studio software (R Core Team, 2016), was applied to the PCA and sediment attribute data. Each decision node in Figure 13 splits the data using one data type. In each leaf (terminal) node, the classification (depositional environment) is first listed, followed by the quantity of samples in the training dataset in that specific classification category, listed as a fractional quantity. RPART can report the fraction of samples in each leaf node in each category but in Figure 13 we have simplified the classification tree by only reporting the fraction al amount of the dominant class to allow the diagram to be readable. Finally, RPART also reports the total percentage of the whole sample set that lies in each leaf node.

Using the PCA output data plus the fractional quantity of silt, the machine learning approach separated De2, De3 and De4 from the remaining environments, De5 to De9, (Fig. 13). Mudflats (De2) are nearly perfectly classified (note that the fraction of mudflats in that category is 0.98 in the training dataset). Mixed flats (De3) are also well differentiated (with a fraction of 0.84) but sand flats (De4) are less well differentiated, having a fractional quantity of 0.74 in the training dataset. This can be read as 74% probability of samples ending in this leaf node being sand flat samples.

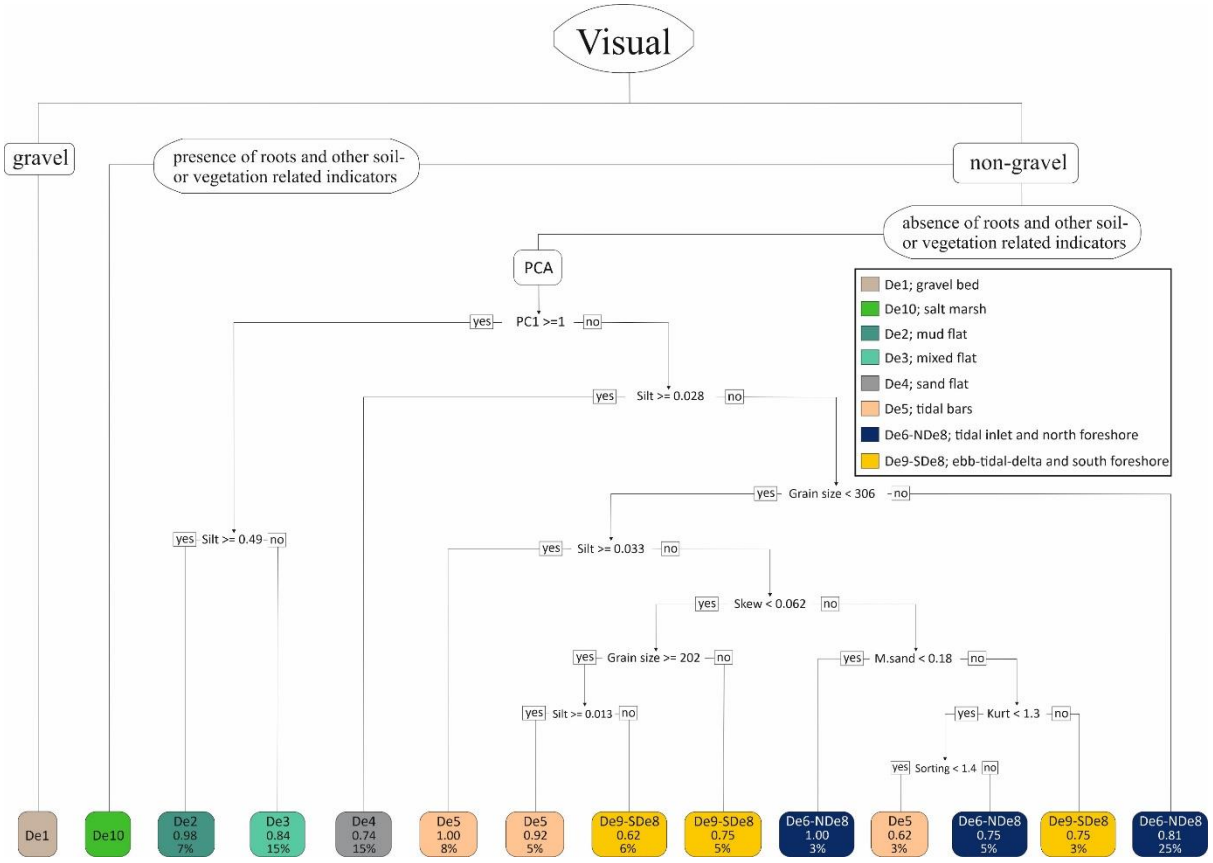

Figure 12: Discrimination diagram for the discrimination of depositional sub-environments, based on samples collected from the Ravenglass Estuary, developed through a combination of visual analysis (Fig. 3), differentiation of the principal component data and plus grain size, sorting, skew, kurtosis, medium sand fraction and silt fraction data (Figs. 10, 11, 12), using supervised classification and the recursive partitioning package, RPART (Therneau and Atkinson, 2019), available in R studio software (R Core Team, 2016). Each machine-learning-derived decision node splits the data using one data type. In each leaf (terminal) node, the classification (in this case, the depositional environment) is first listed. The second value is the quantity of samples in that specific classification category, listed as a fractional quantity; high fractional quantities show that the classification has a high degree of certainty. Finally, the third value that RPART reports in the leaf nodes is the total percentage of the whole sample set that lies in each leaf node. This approach separated De2, De3 and De4 from De5 to De9 using the PCA output data plus the fractional quantity of silt. De5, De6-NDe8 and De9-SDe8 were subjected to RPART classification based on grain size, sorting, skew, kurtosis, silt fraction and medium sand fraction data. The pairs De6-NDe8 and De9-SDe8 were merged during feature engineering as the classification approach proved to be incapable of differentiating them. Each leaf (terminal) node lists the fraction of the samples in that specific classification category as a fractional quantity. Uncertainty, visible by fractional values less than 1.00, is the result of some samples falling in overlapping parts of multi-dimensional classification space, i.e., there are some categories (of depositional environments) that have overlapping attributes, even when four or six dimensions are considered.

Based on the grain size, sorting, skew, kurtosis, medium sand fraction and silt fraction, due to the great degree of similarity in the textural attributes of the tidal inlet (De6) and northern foreshore (NDe8) (Figs. 4, 5, 6, 7, 8, 11, 12), these environments were merged for the RPART classification. Similarly, the ebb-tidal delta (De9) and southern foreshore (SDe8) were merged. Grain size, sorting, skew, kurtosis, silt fraction and medium sand fraction data were run through RPART for De5, De6-NDe8 and De9-SDe8. The classification diagram (Fig. 13) shows that there are different ways to

achieve a classification of De5, De6-NDe8 and De9-SDe8, each with a different fractional degree of certainty ranging from a perfect 1.00 to a less good 0.62.

We have added the machine learning-derived decision node criteria to the boxplots in Figure 12 to show how the automated collective analysis of six variables translates into the critical values in terms of the single variables. For example, a grain size of greater than 306 μm is one of the main ways of defining the combined tidal inlet and northern foreshore (De6-NDe8) (Fig. 12A).

This proposed method, calibrated using surface sediments from known estuarine sub-environments, can be used to interpret grain size distribution data from cores from the Holocene succession at the Ravenglass Estuary, it could be possibly applied to other estuaries that have similar geomorphological histories and potentially it could be used to interpret the exact sub-environments of cores from ancient and deeply buried sandstones.

Application of the classification method to the Holocene core

Using the classification (decision tree) diagram in Figure 13, based on visual inspection, principal component analysis and the recursive partitioning routine RPART, we have been able to uniquely discriminate mudflat, mixed-flat and sandflat sub-environments throughout most of the core (Fig. 14B). The base of the succession, from 300 cm to about 235 cm, is composed of interbedded mixed flat (De3) and sand flat (De4) sediment. This is overlain by 10 cm of mud flat sediment (De2). From 225 to 215 cm, there is tidal inlet-northern foreshore sediment (De6-NDe8). From 215 up to about 150 cm, there is peat and glacial till, which are not here defined as estuarine sub-environments. From 150-130 cm, the sediment is classified into the combined tidal inlet-northern foreshore (De6-NDe8) category (Fig. 13). The top 130 cm represents a sand flat sub-environments (De4), which is the same as the present day depositional sub-environment at the surface. In Figure 14, the sediment that was either tidal inlet or northern foreshore sediment (De6-NDe8) beds is most likely tidal inlet sediment (De6) because, at the present day, tidal inlet sediments juxtapose sand flat (De4) and mud flat (De2) sediments whereas foreshore sediments nowhere directly juxtapose sand flat sediment (Fig. 2).

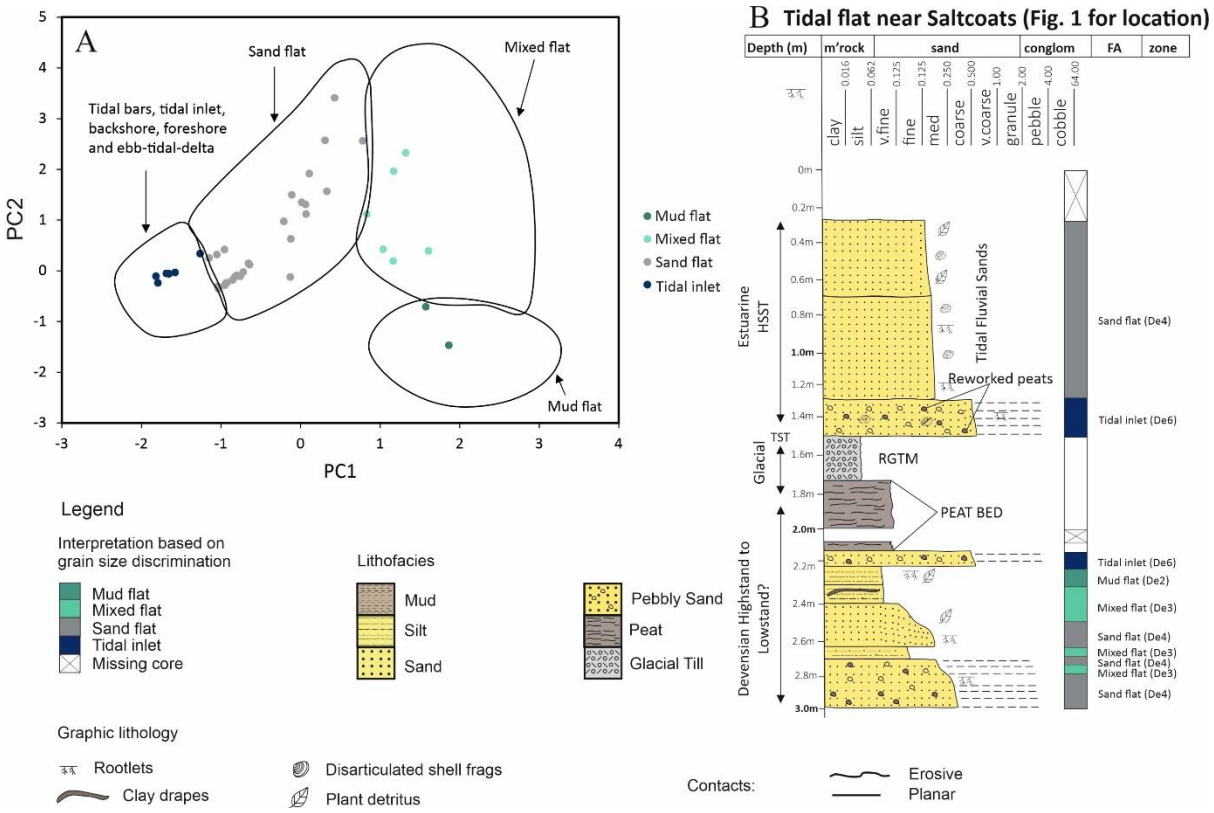

Figure13: Schematic sedimentary log of central basin tidal flats deposits with appluication of the classification tree in Figure 2.13. A) Graphic log of a core from a sand flat in the central basin, near the hamlet of Saltcoats, with the sub-environments defined in the column to the right of the graphic log following application of the classification diagram (Fig. 2.13). B) Interpreted bivariate plot of replicated multivariate Principal Component Analysis (PCA) of samples from Holocene cores across Ravenglass Estuary, PC1 and PC2 discriminating loading score of each sampled, Ravenglass Estuary grain size data (mean grain size, sorting, skewness and kurtosis, phi unit). The replicated PCA shows the colour coded of each sampled within different sub-depositional environments.

The overall evolution of sediment in this core was from sand flat, via mixed flat to mud flat with evolving depositional environments leading to the tidal inlet migrating to this point in the estuary. This was followed by up to several meters of primary peat accumulation, assuming substantial compaction has affected the 60 cm of peat in the core (van Asselen et al., 2009), followed by a late glacial event. More tidal inlet sediment was then superseded by sandflats, presumably as the pattern of environments migrated towards the present-day coastline. The application of the discrimination diagram in Figure 13 to a modern core has allowed us to make a much finer interpretation of the sequence of estuarine depositional sub-environments (Fig. 14) than would have been possible based only on visual analysis and description of the relatively bland sand-rich core that has few of the expected estuarine sedimentary structures and is trace fossil-poor (e.g., Fig. 9).

Conclusions

1. This work is the first high-resolution study of grain size distribution as a function of sedimentary sub-environments in a modern marginal–shallow marine setting. This work was undertaken at the Ravenglass Estuary, NW England, United Kingdom.

2. Ten estuarine sub-environments, that are likely to be preserved in the sedimentary record, were defined, and mapped across the estuary; these are gravel bed, salt marsh, mud flat, mixed flat, sand flat, tidal bars, tidal inlet, northern-foreshore, southern foreshore, and ebb-tidal delta (Fig. 2.2).

3. Sediment at the surface of the Ravenglass Estuary was derived from both marine and fluvial sources. The marine sediment is coarse- to medium-grained and is dominant at the north side of the tidal inlet, just into the central basin and on the northern part of the foreshore. The fluvial sediment is fine- to very-fine-grained and is dominant in the inner arms of the estuary, on the south side of the tidal inlet and on the southern side of the foreshore. Net sediment transport patterns in the estuary have been interpreted on this basis.

4. Grain size data from 482 surface sediment samples were used to create a classification diagram to facilitate the discrimination of depositional sub-environments through a combination of the careful mapping of sedimentary sub-environments, visual sample description, laser particle size analysis, principal component analysis, and a recursive partitioning classification model (RPART) produced in the Rstudio environment. The approach permits the identification of eight out of the ten estuarine sub-environments based solely on the sediment's textural characteristics. With this approach, we can identify whether the environment of deposition of a Ravenglass Estuary sample was gravel bed, salt marsh, mud flat, mixed flat, sand flat, tidal bars, southern foreshore-plus-ebb tidal delta, and tidal inlet plus northern-foreshore sediment.

5. The method developed in this study has been applied to a core drilled into a present-day sand flat, through the Holocene succession at Ravenglass. The application of the machine-learning-derived classification tree has uniquely identified a range of Holocene estuarine palaeo-sub-environments, at the core site, responsible for the accumulation of 3 m of sediment.

6. The approach developed here, using grain size distribution from the Ravenglass Estuary to discriminate depositional sub-environments, could potentially be used in other estuaries or possibly in ancient and deeply buried estuarine sedimentary rocks where textural characteristic may need to be defined by petrographic techniques if the rock is cemented.

REFERENCES

Allen, J.R.L. (1991) Fine sediment and its sources, Severn Estuary and inner Bristol Channel, southwest Britain. *Sedimentary Geology*, **75,** 57-65.

Biederman, E.W. (1962) Distinction of shoreline environments in New Jersey. *Journal of Sedimentary Research*, **32,** 181-200.

Blackbourn, G.A. (2012) *Cores and core logging for geoscientists*. Whittles Publishing, Dunbeath, UK, 160 pp.

Blott, S.J. and Pye, K. (2001) GRADISTAT: a grain size distribution and statistics package for the analysis of unconsolidated sediments. *Earth Surface Processes and Landforms*, **26,** 1237-1248.

Bokuniewicz, H. (1995) Sedimentary systems of coastal-plain estuaries. In: *Developments in Sedimentology*, **53**, pp. 49-67. Elsevier.

Bousher, A. (1999) Ravenglass Estuary: basic characteristics and evaluation of restoration options. *Restrad-Td*, **12,** 03.

Brockamp, O. and Zuther, M. (2004) Changes in clay mineral content of tidal flat sediments resulting from dike construction along the Lower Saxony coast of the North Sea, Germany. *Sedimentology*, **51,** 591-600.

Cheng, Q., Jing, L. and Panahi, A. (2006) Principal component analysis with optimum order sample correlation coefficient for image enhancement. *International Journal of Remote Sensing*, **27,** 3387-3401.

Dalrymple, R.W. and Choi, K. (2007) Morphologic and facies trends through the fluvial–marine transition in tide-dominated depositional systems: a schematic framework for environmental and sequence-stratigraphic interpretation. *Earth-Science Reviews*, **81,** 135-174.

Dalrymple, R.W., Knight, R.J., Zaitlin, B.A. and Middleton, G.V. (1990) Dynamics and facies model of a macrotidal sand-bar complex, Cobequid Bay—Salmon River Estuary (Bay of Fundy). *Sedimentology*, **37,** 577-612.

Dalrymple, R.W., Mackay, D.A., Ichaso, A.A. and Choi, K.S. (2012) Processes, morphodynamics, and facies of tide-dominated estuaries. In: *Principles of tidal sedimentology*, pp. 79-107. Springer.

Dalrymple, R.W., Zaitlin, B.A. and Boyd, R. (1992) Estuarine facies models; conceptual basis and stratigraphic implications. *Journal of Sedimentary Research*, **62,** 1130-1146.

Daneshvar, E. and Worden, R.H. (2018) Feldspar alteration and Fe minerals: origin, distribution and implications for sandstone reservoir quality in estuarine sediments. In: *Reservoir Quality of Clastic and Carbonate Rocks: Analysis, Modelling and Prediction* (Eds P.J. Armitage, A.R. Butcher, J.M. Churchill, A.E. Csoma, C. Hollis, R.H. Lander, J.E. Omma and R.H. Worden), *Geological Society Special Publication*, **435**, pp. 123-139.

Dempster, M., Dunlop, P., Scheib, A. and Cooper, M. (2013) Principal component analysis of the geochemistry of soil developed on till in Northern Ireland. *Journal of Maps***,** 373.

Ehrenberg, S.N. (1993) Preservation of anomalously high porosity in deeply buried sandstones by grain-coating chlorite: examples from the Norwegian continental shelf. *AAPG Bulletin*, **77,** 1260-1286.

Flood, R., Orford, J., McKinley, J. and Roberson, S. (2015) Effective grain size distribution analysis for interpretation of tidal–deltaic facies: West Bengal Sundarbans. *Sedimentary geology*, **318,** 58-74.

Folk, R.L. (1966) A review of grain-size parameters. *Sedimentology*, **6,** 73-93.

Folk, R.L. (1968) *Petrology of sedimentary rocks*, Austin, Texas: Hemphill.

Folk, R.L. and Ward, W.C. (1957) Brazos River bar [Texas]; a study in the significance of grain size parameters. *Journal of Sedimentary Research*, **27,** 3-26.

Friedman, G.M. (1961) Distinction between dune, beach, and river sands from their textural characteristics. *Journal of Sedimentary Research*, **31,** 514-529.

Friedman, G.M. (1962) On sorting, sorting coefficients, and the lognormality of the grain-size distribution of sandstones. *Journal of Geology*, **70,** 737-753.

Friedman, G.M. (1979) Differences in size distributions of populations of particles among sands of various origins: addendum to IAS Presidential Address. *Sedimentology*, **26,** 859-862.

Greenwood, B. (1969) Sediment parameters and environment discrimination: an application of multivariate statistics. *Canadian Journal of Earth Sciences*, **6,** 1347-1358.
Griffiths, J., Worden, R.H., Wooldridge, L.J., Utley, J.E.P. and Duller, R.A. (2018a) Compositional variation in modern estuarine sands: predicting major controls on sandstone reservoir quality. *AAPG Bulletin*.
Griffiths, J., Worden, R.H., Wooldridge, L.J., Utley, J.E.P. and Duller, R.A. (2018b) Detrital clay coats, clay minerals, and pyrite: a modern shallow-core analogue for ancient and deeply buried estuarine sandstones. *Journal of Sedimentary Research*, **88,** 1205-1237.
Griffiths, J., Worden, R.H., Wooldridge, L.J., Utley, J.E.P., Duller, R.A. and Edge, R.L. (2019) Estuarine clay mineral distribution: Modern analogue for ancient sandstone reservoir quality prediction. *Sedimentology*.
Grigsby, J.D. (2001) Origin and growth mechanism of authigenic chlorite in sandstones of the lower Vicksburg Formation, South Texas. *Journal of Sedimentary Research*, **71,** 27-36.
Grunsky, E.C. and Smee, B.W. (1999) The differentiation of soil types and mineralization from multi-element geochemistry using multivariate methods and digital topography. *Journal of Geochemical Exploration*, **67,** 287-299.
Kelly, M., Emptage, M., Mudge, S., Bradshaw, K. and Hamilton-Taylor, J. (1991) The relationship between sediment and plutonium budgets in a small macrotidal estuary: Esk Estuary, Cumbria, UK. *Journal of Environmental Radioactivity*, **13,** 55-74.
Klovan, J. (1966) The use of factor analysis in determining depositional environments from grain-size distributions. *Journal of Sedimentary Research*, **36,** 115-125.
Lloyd, J.M., Zong, Y., Fish, P. and Innes, J.B. (2013) Holocene and Lateglacial relative sea-level change in north-west England: implications for glacial isostatic adjustment models. *Journal of Quaternary Science*, **28,** 59-70.
Mason, C.C. and Folk, R.L. (1958) Differentiation of beach, dune, and aeolian flat environments by size analysis, Mustang Island, Texas. *Journal of Sedimentary Research*, **28,** 211-226.
Merritt, J. and Auton, C. (2000) An outline of the lithostratigraphy and depositional history of Quaternary deposits in the Sellafield district, west Cumbria. *Proceedings of the Yorkshire Geological Society*, **53,** 129-154.
Moiola, R. and Spencer, A. (1979) Differentiation of aeolian deposits by discriminant analysis. *US Geological Survey Professional Paper***,** 53.
Moiola, R.J., Spencer, A.B. and Weiser, D. (1974) Differentiation of modern sand bodies by linear discriminant analysis. *Gulf Coast Association of Geological Societies Transactions*, **24,** 321-326.
Mountney, N.P. and Thompson, D.B. (2002) Stratigraphic evolution and preservation of aeolian dune and damp/wet interdune strata: an example from the Triassic Helsby Sandstone Formation, Cheshire Basin, UK. *Sedimentology*, **49,** 805-833.
Park, N.W. and Jang, D.H. (2020) Geostatistical Classification of Intertidal Surface Sediments Using Log-ratio Transformation and High-resolution Remote Sensing Imagery. *Journal of Coastal Research***,** 157-165.
Posamentier, H.W. and Walker, R.G. (Eds)(2006) *Facies models revisited*. SEPM Special Publication, Oklahoma.
Purkait, B. and Das Majumdar, D. (2014) Distinguishing different sedimentary facies in a deltaic system. *Sedimentary Geology*, **308,** 53-62.
R Core Team (2016) R: A Language and Environment for Statistical Computing. R Foundation for Statistical Computing, Vienna, Austria.
Reimann, C., Filzmoser, P., Garrett, R.G. and Dutter, R. (2008) *Statistical Data Analysis Explained*. John Wiley & Sons Ltd., Chichester, UK.
Rogers, J.J. and Strong, C. (1959) Textural differences between two types of shoestring sands. *Gulf Coast Association of Geological Societies Transactions*, **9,** 167-170.
Sahoo, P.K., Dall'Agnol, R., Salomao, G.N., Ferreira, J.D., Silva, M.S., Souza, P., da Costa, M.L., Angelica, R.S., Medeiros, C.A., da Costa, M.F., Guilherme, L.R.G. and Siqueira, J.O. (2020) Regional-

scale mapping for determining geochemical background values in soils of the Itacaiunas River Basin, Brazil: The use of compositional data analysis (CoDA). *Geoderma*, **376**.
Sevon, W. (1966) Distinction of New Zealand beach, dune, and river sands by their grain size distribution characteristics. *New Zealand Journal of Geology and Geophysics*, **9,** 212-223.
Shepard, F.P., Manar, R.Y. and Young, R. (1961) Distinguishing between beach and dune sands. *Journal of Sedimentary Research*, **31,** 196-214.
Storvoll, V., Bjørlykke, K., Karlsen, D. and Saigal, G. (2002) Porosity preservation in reservoir sandstones due to grain-coating illite: a study of the Jurassic Garn Formation from the Kristin and Lavrans fields, offshore Mid-Norway. *Marine and Petroleum Geology*, **19,** 767-781.
Therneau, T.M. and Atkinson, E.J. (2019) An Introduction to Recursive Partitioning Using the RPART Routines, **2021**. Comprehensive R Archive Network.
Tiab, D. and Donaldson, E.C. (2015) *Petrophysics, 4th edition*. Elsevier, Amsterdam, 894 pp.
van Asselen, S., Stouthamer, E. and van Asch, T.W.J. (2009) Effects of peat compaction on delta evolution: A review on processes, responses, measuring and modeling. *Earth-Science Reviews*, **92,** 35-51.
Verhagen, I.T.E., Crisostomo-Figueroa, A., Utley, J.E.P. and Worden, R.H. (2020) Abrasion of detrital grain-coating clays during sediment transport: Implications for diagenetic clay coats. *Sedimentary Geology*, **403,** 105653.
Visher, G.S. (1969) Grain size distributions and depositional processes. *Journal of Sedimentary Research*, **39**.
Watson, D.F. and Philip, G.M. (1985) Comment on "a nonlinear empirical prescription for simultaneously interpolating and smoothing contours over an irregular grid" by F. Duggan. *Computer Methods in Applied Mechanics and eEngineering*, **50,** 195-198.
Wells, J.T. (1995) Tide-dominated estuaries and tidal rivers. In: *Developments in Sedimentology*, **53**, pp. 179-205. Elsevier.
Wickham, H. (2016) *ggplot2: Elegant graphics for data analysis*. Springer, Switzerland, 226 pp.
Wooldridge, L.J., Worden, R.H., Griffiths, J., Thompson, A. and Chung, P. (2017a) Biofilm origin of clay-coated sand grains. *Geology*, **45,** 875-878.
Wooldridge, L.J., Worden, R.H., Griffiths, J. and Utley, J.E.P. (2017b) Clay-Coated Sand Grains In Petroleum Reservoirs: Understanding Their Distribution Via A Modern Analogue. *Journal of Sedimentary Research*, **87,** 338-352.
Wooldridge, L.J., Worden, R.H., Griffiths, J. and Utley, J.E.P. (2019) Clay-coat diversity in marginal marine sediments. *Sedimentology*, **66,** 1118-1138.
Wooldridge, L.J., Worden, R.H., Griffiths, J., Utley, J.E.P. and Thompson, A. (2018) The origin of clay-coated sand grains and sediment heterogeneity in tidal flats. *Sedimentary Geology*.
Worden, R.H. and Burley, S.D. (2003) Sandstone diagenesis: the evolution of sand to stone. *Sandstone diagenesis: Recent and ancient*, **4,** 3-44.
Worden, R.H., Griffiths, J., Wooldridge, L.J., Utley, J.E.P., Lawan, A.Y., Muhammed, D.D., Simon, N. and Armitage, P.J. (2020) Chlorite in sandstones. *Earth-Science Reviews*, **204,** 103105.
Zhou, D., Chen, H.Z. and Lou, Y.L. (1991) The logratio approach to the classification of modern sediments and sedimentary environments in northern South China Sea. *Mathematical Geology*, **23,** 157-165.
Zubillaga, J.J.K. and Edwards, A.C. (2005) Grain size discrimination between sands of desert and coastal dunes from northwestern Mexico. *Revista Mexicana de Ciencias Geológicas*, **22,** 383-390.